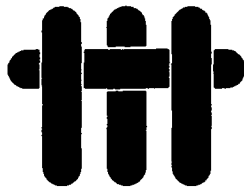


AD-A216 145

(1)

ANNUAL REPORT
University Research Initiative
Contract No.: N00014-86-K-0753
September 15, 1988-September 14, 1989



The Processing and Mechanical
Properties of High Temperature/
High Performance Composites

DTIC
ELECTE
DEC 26 1989
S D

by
A. G. Evans & R. Mehrabian
University of California,
Santa Barbara

Arizona State University
Cambridge University
Harvard University
Stanford University
Washington State University
University of Wisconsin-Madison

DISTRIBUTION STATEMENT A
Approved for public release
Distribution Unlimited

Sponsored by: The Defense Advanced Research Projects Agency
Monitored by: Office of Naval Research

Book 5 of 6

Section 4: PROCESSING: Matrices and Composites

Part 1 of 2

89 12 21 038

SUMMARY

of

TABLE OF CONTENTS

EXECUTIVE SUMMARY

SECTION 1: COATINGS AND INTERFACES Book 1

SECTION 2: STRENGTH AND FRACTURE RESISTANCE

Part 1 Book 2

Part 2 Book 3

SECTION 3: FLOW AND CREEP STRENGTH Book 4

SECTION 4: PROCESSING: Matrices and Composites

Part 1 Book 5

Part 2 Book 6

| | |
|---------------------|----------------------|
| Accession No. | |
| NTIS GRANT # | |
| DTIC TAB | |
| Uncontrolled | |
| Justification | |
| By <i>PJ, CG</i> | |
| Date <i>10/1/87</i> | |
| Availability Status | |
| Dist | A copy of Special |
| A 1 | |



BOOK 5

SECTION 4: PROCESSING: Matrices and Composites

Part 1 of 2

Intermetallics

| | | |
|-----|--|---|
| 59. | Materials Processing/Rapid Solidification/ Thermodynamics and Reactions at Interfaces | T.C. Jewett J.C. Mishurda W. Allen L.E. Seitzman N.R. Bonda J.H. Perepezko Y.A. Chang |
| 60. | Microstructural Analysis of Rapidly Solidified Ti-Al-X Powders | C. McCullough J.J. Valencia C.G. Levi R. Mehrabian |
| 61. | Solidification Paths in Ta-Ti-Al Alloys | C. McCullough J.J. Valencia C.G. Levi R. Mehrabian M. Maloney R. Hecht |

EXECUTIVE SUMMARY

The third annual report of the University Research Initiative project at UCSB on High-Temperature, High-Performance Composites consists of sections compiled in a total of six books. The first section in Book 1 is concerned with the properties and structure of bimaterial *interfaces* and the related problem of *coating* decohesion and cracking. The second section describes research on the *strengths and fracture resistance* of brittle matrix composites manufactured with fibers, whiskers and ductile phases. This information is presented in Books 2 and 3. The third section addresses the *flow and creep strength* of reinforced systems, with emphasis on effects of aspect ratio and the incidence of damage, and is offered in Book 4. The fourth section, Books 5 and 6, describes work on processing of intermetallic and ceramic matrices and composites, as well as numerical modelling of the melt-spinning process. (K+T)X

SECTION 4: PROCESSING: Matrices and Composites

INTERMETALLICS

PHASE EQUILIBRIA - The assessment of the binary TiAl phase diagram has been completed through combined efforts on thermodynamic modelling, differential thermal analysis and annealing experiments (Mishurda et al.), as well as high-temperature X-ray diffractometry and controlled solidification experiments (McCullough et al.). In particular, the liquid-solid equilibrium in the vicinity of the equiatomic composition and the boundaries of the high temperature α -(Ti) field are now well-established. The revised diagram and corollary thermodynamic

information has been instrumental not only in elucidating the microstructural evolution paths of binary Ti-Al intermetallic alloys, but also in permitting the systematic evaluation and computer calculation of related ternary systems, notably Ti-Al-Nb, Ti-Al-Ta and Ti-Al-B.

Substantial progress has been made on the Ti-Al-Nb ternary system. Extensive solidification experiments have been combined with the binary diagram information to define the approximate shape of the liquidus surface and the boundaries of the different primary phase fields (Jewett et al.). The α -(Ti) liquidus on the Ti-Al binary shrinks with the addition of Nb and is totally encroached by the β and γ -(TiAl) fields at ~ 18at%Nb. All other regions on the liquidus surface have temperatures that decrease from the Nb-Al binary toward the Ti-Al binary. Significant problems still exist in the vicinity of the Ti_2NbAl composition, where two ternary phases (T1 and T2) had been detected (Jewett et al., Boettinger et al.). Both phases have B2 structures at 1200°C and decompose upon cooling to rather complex microstructures involving α_2 , γ and a $B8_2$ phase.

Phase equilibria studies on the Ti-Al-Ta system have been initiated. Solidification work suggests that the shape of the liquidus surface in the vicinity of γ is quite similar to that reported for Ti-Al-Nb with the α -(Ti) field shrinking with Ta additions until it is encroached by the β -(Ti) and γ -(TiAl) fields (McCullough et al.), but the liquidus temperatures are generally higher than those for Nb additions. High temperature X-ray diffraction has been extensively used to study the phases present in the vicinity of the 50at%Al isoconcentrate (McCullough et al.). In addition, a preliminary isothermal section at 1100°C has been delineated based on the X-ray evidence combined with diffusion couples and isothermal annealing experiments developed under other DARPA sponsored programs.

SOLIDIFICATION - The fundamental understanding of the solidification of Ti-Al alloys developed in the previous funding period was systematically applied to elucidate the microstructure evolution of rapidly solidified powders produced by the industrial participants (McCullough et al., Jewett et al.). Microstructures of powders produced by containerless processing (PREP) were in general consistent with the trends established by the controlled solidification experiments, wherein β was found to be the kinetically preferred primary phase at high supercoolings, even in the composition range where α and/or γ are thermodynamically favored (45-55at%Al). In contrast, atomization processes involving graphite crucibles and/or nozzles (XSR) were found to yield powders with a large proportion of primary α -(Ti) phase, even at compositions where β is the equilibrium primary phase. This was ascribed to carbon contamination of the melt (~ 0.5at%C), which seems to shift the α / β liquidus boundary (McCullough et al.). Furthermore, the solidification behavior of dilute (\geq 5at%Nb or Ta) ternary alloys in the α_2 - γ range was found to proceed essentially as in the binary Ti-Al alloy of the same aluminum content (Jewett et al., McCullough et al.).

Studies on the effects of cooling rate after solidification using binary and dilute (\geq 5at%Nb or Ta) ternary alloys (McCullough et al., Jewett et al.), revealed that diffusion-controlled lath transformation is sensitive to quenching. Indeed, γ precipitation may be completely suppressed by decreasing the Al content or adding ternary elements (Nb or Ta) that exhibit strong partitioning between the α_2 and γ phases. It was also found that the $\alpha \rightarrow \alpha_2$ ordering is not suppressible by quenching.

The solidification of γ -TiAl base alloys containing 10 to 28at%Ta (McCullough et al.) revealed that primary β -(Ti) forms with γ segregates in the interdendritic spaces. The leaner alloys appear to go through the double peritectic cascade

previously reported for the binary system $L + \beta \rightarrow \alpha$ and $L + \alpha \rightarrow \gamma$, but the extent of α formation is reduced with increasing Ta content and most probably eliminated in the richer alloys. All these alloys exhibit strong partitioning of Ta toward the dendrite cores. This severe "coring" would require long homogenization treatments and its presence may lead to erroneous conclusions when mechanical and oxidation behavior studies are conducted on as-cast materials. Furthermore, the Ta-rich cores appear to follow a different transformation path in the solid state than the rest of the dendrites, substantially complicating the analysis of the phase sequencing and microstructure evolution during the post-solidification cooling. The scale of segregation can be refined by approximately one order of magnitude using melt-spinning or splat-quenching instead of arc melting. Homogenization has then been accomplished in a few hours.

CONSOLIDATION - HIP consolidation of titanium aluminide powders produced by Rapid Solidification Rate (RSR) and Rotating Electrode Process (REP) were studied (Choi et. al) and compared to computer model predictions (Ashby). In a corollary effort a high temperature sensor was developed (Paden et. al) for in-situ monitoring of the consolidation process. Characterization of the starting powders; RSR Ti-48%Al-2.5%Nb-0.3%Ta, and REP Ti-50%Al-2%Nb, showed dendrites with primarily hexagonal symmetry, indicative of α -phase formation from the liquid. These microstructures were consistent with solidification studies reported above - e.g. carbon contamination in the RSR process strongly favors the formation of primary α . Good agreement was obtained between the predicted HIP maps and the experimental data during later stages of densification (>85%) and longer times (4 and 16 hours). The power law creep mechanism predicted by the model is in best agreement with the experiments. However, discrepancies arise at the earlier stages. At lower temperatures, the model predicts much faster consolidation, indicating a

required adjustment to the model. At higher temperatures and short times (1 hour), the model predicts a slower densification. Direct in-situ sensing, using an eddy current sensor, provided an explanation for the latter discrepancy. It was found that significant consolidation occurred during the pressurization process which the model does not take into consideration.

COMPOSITES - The composite processing facet of this research has explored using alloying additions that develop reinforcements in titanium aluminides, through suitable control of the chemistry and solidification parameters. The compounds of most interest are those which exhibit strongly anisotropic growth from the melt, either because of their crystal structure and/or interfacial tension characteristics. Plate reinforcements have been readily grown in the Ti-Al-C system, where the phase in equilibrium with γ -TiAl is Ti_2AlC , a hexagonal structure with a rather complicated stacking sequence along the c-axis (Valencia et al.). Plates $\sim 1 \mu m$ thick with aspect ratios of ~ 20 and up to 12% by volume have been grown as primary phases in Ti-(48–51at%)Al-3at%C. Significant increases (20–60%) in creep strength were observed in these alloys when compared with unalloyed γ , but there are indications that some of the strengthening is due to dissolved C in the matrix.

Borides appear more promising as reinforcing phases for γ -TiAl; they offer flexibility for microstructural control and relatively straightforward processing conditions. The structures of interest are all based on the trigonal prismatic coordination of 6 metal atoms around each B, which may be arranged in close-packed (TiB_2), columnar (TiB) or lamellar (TaB, NbB) arrays. The boride in equilibrium with the binary γ -TiAl is TiB_2 , which forms a mixture of plates, needles and highly convoluted flakes when solidifying as a secondary phase. Major progress has been made in the understanding of these different morphologies and their dependence on alloy composition and solidification rate (Hyman et al.), but

TiB_2 may not lend itself to the production of appreciable volume fractions of reinforcements with the desirable morphologies. However, controlled additions of Ta or Nb change the structure of the stable primary boride to TiB, with Ta or Nb partially substituting for Ti. These borides grow as rods ~ 1 to $5 \mu m$ in diameter with aspect ratios of 20 or larger, as expected from crystallographic considerations, and have been produced in volume fractions up to 15% (Valencia et al.). Current studies are focused on optimizing the scale and distribution of these reinforcements, as well as on exploring alloy compositions which may produce platelike phases based on the structure of TaB.

PLANAR FLOW CASTING - High-speed, high-magnification video techniques were used to investigate the geometry and stability of the puddle during planar flow casting of aluminum alloys. Puddle oscillations and surface instabilities are correlated to macroscopic defects in the ribbon. The process was modelled numerically using fluid mechanics and heat transfer to establish thermal profiles in the solidifying puddle. Although not specifically reported herein, the system has been upgraded and used to produce ribbons of titanium aluminides for some of the solidification studies in this report.

CERAMICS

Pressureless densification of ceramic powders containing reinforcements has been emphasized as needed to understand processing limitations and to develop new methods for processing ceramic composites. Two major problems have been studied: the forming of powder compacts containing reinforcements and the constrained densification of the matrix powder. It has been shown that pressure filtration can be used to pack powder within a fiber preform provided: a) repulsive forces exist between particles and between the reinforcement and particles and b) the

particle size to fiber diameter ratio is ≤ 0.01 . The latter requirement not only provides for the flow of particles through preform channels, but also for high packing density within the preform. Densification of the powder matrix is constrained by the reinforcement. Studies of this problem have emphasized powders containing a non-connected network of inert particles, viz., Al_2O_3 -SiC plates and Al_2O_3 - ZrO_2 inclusions. Shrinkage measurements, mercury porosimetry, and microstructural observations illustrate the sequential events: sintering and shrinkage occurs until an interconnected dense network forms that surrounds lower density regions. Coarsening of grains within the lower density regions causes voids within these regions to grow and dissipate the sintering potential. *Higher particle packing density results in less differential shrinkage and higher composite density.*

Studies concerning sintering via vapor phase transport have been initiated with the goal of strengthening the powder matrix without the shrinkage associated with other modes of material transport. Studies have also been initiated in which precursor ZrO_2 fibers are incorporated into powders which also shrink, either more or less than the powder, depending on their prior heat treatment.

Materials Processing/Rapid Solidification/
Thermodynamics and Reactions at Interfaces

Third Annual Report

(September 17, 1988 - September 18, 1989)

T. C. Jewett, J. C. Mishurda, W. Allen, L. E. Seitzman,
N. R. Bonda, J. H. Perepezko, and Y. A. Chang

Department of Materials Science and Engineering
University of Wisconsin-Madison
Madison, WI 53706

University Research Initiative

Supported by DARPA through ONR Contract N00014-86-K-0753 to the University of California, Santa Barbara with a subagreement to the University of Wisconsin-Madison (P.O. VB38640-0).

September 1989

1.0 Introduction

2.0 Binary Ti-Al

2.1 Expansion of Ti-Al Alloys Investigated

- Additional Alloys Investigated
- Alternate DTA Crucible Materials

2.2 Ti-Al Phase Diagram Determination

- Characterization of Starting Materials
- Differential Thermal Analysis
- Microprobe Analysis
- Discussion of Results

2.3 Model and Calculations of Ti-Al Binary

3.0 Ternary Ti-Al-Nb

3.1 Experimental Determination of Ternary Ti-Al-Nb System

- Liquidus Projection of the Ternary Nb-Al-Ti System
- 1200°C Isothermal Section of the Ti-Al-Nb System
- Investigation of T_1 and T_2
- $\text{Al}_3\text{Ti}-\text{Al}_3\text{Nb}$ Pseudobinary System
- Phase Equilibria in the Nb-Rich Corner of the Nb-Al-Ti System

3.2 Diffusion Couples - Kinetic Implications

3.3 Model and Calculations for the Ti-Al-Nb Ternary System

3.4 Powder Processing

- $\text{Ti}_3\text{Al}+\text{Nb}$ Results (Alloys B and C)
- $\text{Ti}_3\text{Al}+\text{Nb}$ Discussion (Alloys B and C)
- $\text{TiAl}+\text{Nb}$ Results (Alloys D, E, and G)
- Discussion of $\text{TiAl}+\text{Nb}$ for the Ti (Alloys D and E)
- Discussion of $\text{TiAl}+\text{Nb}$ for the Al (Alloy G)
- Summary of Powder Processing Results

4.0 Summary and Conclusions

1.0 Introduction

As a result of the recent activity on high temperature alloy development, intermetallic compounds including a number of aluminides such as those in Ni, Fe, Nb and Ti systems have received considerable attention. In the development and evaluation of mechanical properties and high temperature structural stability, it has become evident that it is essential to consider also the strong influence of materials processing throughout all stages. Among the most fundamental data needed for the development of a new processing operation or the improvement of an existing one are the relevant phase diagrams, the characteristic diffusivities and the possible solidification reaction pathways.

The research activities in materials processing at the University of Wisconsin-Madison include several interrelated efforts which are focused in rapid solidification and powder processing, phase equilibrium thermodynamics and interdiffusion reactions at interfaces. A major effort is being directed towards the production of novel microstructures in high temperature intermetallic alloys in powder form. In conjunction with the experimental studies several approaches are being examined to develop models for the analysis of microstructural evolution and to provide a basis for predictive capability. A central objective in the processing studies is the production of composite systems with the well controlled microstructural features that have been identified in the micromechanics model analysis efforts.

The processing efforts are directed to examining phase selection, solidification pathways and thermal stability of solidification products to provide a basis for microstructural development and alloy design in high temperature intermetallics in titanium and niobium base alloys systems. The formation of alternate phases is controlled by the operative phase selection kinetics which are being identified in Ti-Al, Nb-Al and Ti-Al-Nb alloys. Powder samples that have been produced by atomization or processed in a containerless drop tube facility serve as useful experimental samples for the analysis of nucleation kinetics control. In addition, further work has been conducted with laser pulse melting (in collaboration with Drs. P. S. Peercy and D. M. Follsteadt of Sandia National Labs) to provide new insight into the competitive growth kinetics control of phase selection in γ phase Ti-Al alloys.

While good progress has been made in clarifying the binary equilibrium diagrams for the aluminides; especially in the case of the Ti-Al system, a good deal of the current alloy design and processing developments make it clear that ternary phase equilibria information will be essential. For example, dispersed phases of various types in an intermetallic matrix are being examined for strengthening, toughening, oxidation resistance and high temperature creep resistance applications. Monolithic alloy designs are being supplemented by intermetallic matrix composites where again ternary phase equilibria as well as interdiffusion data are needed in order to understand and to control possible interfacial reactions.

Some of the most attractive aluminides from the viewpoint of low density and high temperature potential are those in the Ti-Al system (Ti_3Al , $TiAl$, $TiAl_3$) and also in the Nb-Al system (Nb_3Al , $NbAl_3$). In fact, a few alloy compositions based upon Ti_3Al with Nb additions have been developed and are being examined in high temperature applications. Much of this alloy development has been hampered by the absence of a clear understanding of the phase relations in Ti-Al-Nb alloys. For the most part this is due to the lack of systematic and complete studies of the ternary equilibria such as the current investigation.

The development of an effective consolidation procedure for particulates and the long term stability of microstructures to elevated temperature exposure are key elements in the production of advanced intermetallic composite structures. These issues have been examined in terms of the influence of solidification processing and alloy composition in Ti-Al alloys. New information on microstructural changes is available in the ternary Ti-Al-Nb systems for certain alloys based on phase diagram studies. A further investigation of thermal stability has focused on the use of diffusion couples to assess the effect of high temperature annealing on dispersed phase/intermetallic matrix interfaces in Ti-Al-Nb alloys.

The final composite microstructure represents the combined influence of the phase selection, the solidification pathway, phase equilibria, the thermal stability and the diffusional interactions. The analysis of processing and

microstructure development is summarized in the following sections. The initial studies which are discussed in the previous report focused on the binary Ti-Al alloys. The experimental studies in the binary system are now essentially completed. In addition the results from new studies on Ti-Al-Nb alloys and the Nb-Al system have developed to the point where it is now possible to identify some new opportunities for microstructure control and processing that are being pursued in the continuing research effort.

2.0 Binary Ti-Al2.1 Expansion of Ti-Al Alloys InvestigatedAdditional Alloys investigated

As reported previously, special ingots provided by Pratt & Whitney (identified as 163-1 - 163-4 in Table I) were selected as the starting material for the phase diagram investigation due to the increased homogenization as a result of the hot deformation, the larger volume of material available for duplication of tests, and the overall high quality of the material. Additional ingots identified as 8, and 9 in Table I were produced by arc melting at the University of Wisconsin to supplement the alloys previously investigation. Metallography, x-ray analysis and chemical analysis were used to accurately characterize these starting materials. Special emphasis was placed on identifying the impurity contents of specimens during the investigation.

The primary tool selected for the equilibrium investigation of the phase diagram was differential thermal analysis (DTA). DTA has already proved useful in helping to sort out phase boundaries in the titanium-aluminum system [Shu84] [Sir86]. Microprobe analysis was used to identify the composition of the two phases in equilibrium in the α_2 - γ two phase field and thus pin the two phase field boundaries.

Alternate DTA Crucible Materials

Some interactions with the Al_2O_3 crucibles have been observed for sum of the previous DTA tests with 44, 46, 48, and 50 at.% Al. An alternate DTA crucible material was sought to

establish the influence of the crucible material on the DTA results.

The literature indicates a variety of materials have been examined for use as crucibles for molten titanium including oxides, carbides, nitrides, sulfides, borides, and silicides [Web57] [Gar65] [Lyo73] [Bla78]. No material was found to be inert to molten titanium. Materials such as Al_2O_3 , ZrO_2 , HfO_2 , ThO_2 , BeO and others have more negative free energies of formation than the titanium oxides. However, due to titanium's high affinity for interstitials and large solubilities, the true evaluation of the crucible materials requires an examination of the chemical stability of the ceramic material versus solution in titanium [Lyo73]. Yttria (Y_2O_3) was found to be among the best materials for containing molten titanium, although with long exposure times some reaction and dissolution can occur, resulting in the precipitation of flower shaped yttria particles [73Lyo] [78Bla,b]. The use of yttria (Y_2O_3) crucibles should help minimize oxygen pick up (below 1500 ppm) from the crucible [73Lyo]. As a result of the available literature the alternate DTA material selected was Y_2O_3 .

Another important aspect in DTA of titanium alloys is the potential for oxygen contamination from the gas environment during testing. Special care was given to maintain the lowest level of interstitial elements possible for the DTA 1700 system. A Ti-getter furnace was used to further purify the argon. Prior to performing the DTA analysis argon was allowed to flow for 4 hours or more (50 cc/min) to reduce the initial oxygen level in the DTA

chamber. The actual oxygen levels were measured using an oxygen gas analyzer to be 8 ppm (by wt) both before and after DTA testing.

2.2 Ti-Al Phase Diagram Determination

Characterization of Starting Materials

The chemical composition of the four HIP/Forged alloys and the two arc melted/annealed alloys used previously in the phase equilibria investigation for this study are provided in Table II. X-ray analysis indicated only the presence of α_2 and/or γ phases in all the binary alloys investigated. The two supplementary arc melted ingots, 8 and 9, had higher oxygen contents than the HIP/forged alloys (see Table II). The arc melted/annealed ingots contained trace amounts of Si (0.012 wt.%), C(0.041-0.026 wt.%), H(0.0012-0.002 wt.%) and N(0.029-0.032 wt.%).

Microstructural examination of ingot 9 (34.97 Al) revealed a coarse acicular α_2 structure. The microstructure of ingot 8 (40.24 Al) consisted of a plate like α_2 microstructure. The ingots were quartered and samples prepared for DTA from the center regions of the ingots. Four representative DTA specimens (3 mm diameter) could be obtained from each ingot.

Differential Thermal Analysis

Some of the results from DTA analysis of the ingots are presented in Table III through Table VIII. Selected representative thermograms are presented in Figure 1 through Figure 3. Second heating cycles were generally not employed for the specimens tested in the Al_2O_3 DTA crucibles since reactions with the crucible after melting would result in an increase in

aluminum and oxygen contents of the specimen. This would not a problem for the Y_2O_3 DTA crucibles. After melting the expected oxygen level is 1500 ppm (by wt%).

The level of oxygen in the argon gas exiting the DTA sample chamber was measured both before and after DTA analysis to be 8 ppm (by weight). The DTA samples had a surface discoloration which ranged from a gold tint to a blue surface layer on corners and exposed surfaces. Post oxygen analysis of some of the DTA specimens revealed an order of magnitude increase in the oxygen level after melting (see Table IX). The control sample showed the small size specimens yielded higher oxygen contents by 100 to 200 ppm (by wt%). Oxygen levels in the samples heated to temperatures just below the solidus were found to be five to six times higher than the initial oxygen content. While the sample is still in the solid form, a gradual increase in the oxygen content occurs with temperature. However, most of the oxygen content occurs after melting.

A comparison of a specimen of sample 163-1 heated to above the melting temperature (1547°C) with a specimen heated to below the melting temperature (1442°C) showed the microstructures were similar. Both specimens contain large prior β grain boundaries with lamellar structure inside the grains (see Figure 4). No dendritic structure was visible except for the shrinkage porosity near the top of the specimen heated to 1547°C . A comparison of a specimen of 163-4 heated above the melting temperature (1595°C) (see Figure 5) to a specimen heated below the melting temperature (1424°C) shows greater contrast between

the microstructures (Figures 5 and 6). The specimen heated to 1575°C has a dendritic structure with 60° orientation of the secondary dendrite arms. The microstructure consist of dendrites with an internal lamellar structure with a darkly etched uniform layer around the dendrite and an interdendritic region which is lighter in etching response away from the dendrite arms. The specimen heated to 1424°C has very fine equiaxed grains with some grains containing a lamellar structure while others have no internal structure.

The use of a Y_2O_3 DTA cup rather than a Y_2O_3 coated specimen tested in an Al_2O_3 cup resulted in less crucible - melt reactions and a decreased level of noise in the thermograms (see Figure 7). This first Y_2O_3 crucible was provided by Pratt and Whitney. Examination of the DTA sample after testing indicated a clean ingot and DTA cup surfaces with no visible reaction. The DTA specimen tested in the Y_2O_3 DTA cup was cut in half and tested for oxygen content (see Table IX). The oxygen levels of the two pieces were 1200 ppm and 3600 ppm (by wt.%).

Additional Y_2O_3 DTA cups were produced by a hot press, machine, and sinter process and the other alloys were tested. All the transformations observed during the DTA analysis using Al_2O_3 crucible were also observed using the Y_2O_3 crucible (see Figures 8-11). The bottoms of the Y_2O_3 crucibles were thicker than the desired size, resulting in a slight decrease in the expected magnitude of the transformation peaks. The transformation temperatures observed with DTA analysis using Y_2O_3 crucibles were within the range of values obtained from the DTA

analysis using the Al₂O₃ crucibles (see Table III - Table VIII). The DTA results were generally repeatable on a second heating cycle, except for solidification segregation effects (Figure 10). The Y₂O₃ crucibles had to be broken to remove the specimens due to adhesion of the melted samples to the crucible wall. The surface of the post-DTA specimens which melted, were concave indicating a high angle of wetting. Post oxygen analysis of a melted specimens indicated an oxygen level of 1700 ppm (by wt) on the bottom half and 3700 ppm (by wt) for the top half after the first melt (see Table IX). After the 2nd melt the oxygen level rose to a uniform level around 3750 ppm (by wt) (average). The higher oxygen levels in the top portion of the post-DTA specimen tested in the Y₂O₃ DTA crucible is an indication the oxygen pick up occurs during the 1 to 2 minutes the sample is in the molten state. Otherwise, the oxygen levels would be uniform throughout the sample. No differences were noted in the theromograms as a result of the increased oxygen level from the first cycle to the second cycle. An oxygen level of 1500 ppm would be expected due to melt contact with the Y₂O₃ crucible, the rest of the oxygen is likely from residual oxygen in the argon (8 ppm by wt). Molten titanium is more efficient at gettering oxygen than solid titanium heated to 750-800°C.

Microprobe Analysis

A specimen from ingot 163-1 (44.83 Al) was heated to 1100°C and held for 6 hours in the DTA system. Microprobe analysis across the lamellar structure gave a maximum aluminum content for the aluminum-rich phase of 47.16 at.% Al (see Figures

12 and 13) and a minimum aluminum content of the titanium-rich phase of 37.2 at.% Al (see Figure 14). Accelerating voltage used was 15 keV with a probe step size of 1 micron.

The lamellar structure observed in the dendrites of the post-DTA specimen 163-4 (50.94 Al) heated to 1556°C was also examined using microprobe analysis (see Figures 15 and 16). The maximum aluminum content of the lamellar structure was 51.33 at.% Al and the minimum was 42.45 at.% Al. The average composition of the dendritic area as determined by an area scan of the dendrite was 49.55 at.% Al.

Discussion of Results

The two supplementary arc melted ingots had higher oxygen levels (approx. 2000 ppm by wt.%) than the first four alloys examined. The expected affect of the higher oxygen content is to increase slightly the $\alpha \Rightarrow \beta$ transformation temperature and to broaden the two phase field. Overall the arc melted ingots should provide a useful first measurement of the Ti-Al phase equilibria. The four P&W alloys are considered superior starting materials when compared to the arc melted ingots due to their lower oxygen content, refined two phase microstructures and larger availability of representative samples. However, the DTA results from the additional compositions are complimentary to the previous data.

It is evident from all the DTA that only one solid-state invariant reaction exists instead of two. Thus the DTA results of the alloys with compositions between TiAl and Ti_3Al agree more closely with recently proposed diagrams

containing the high temperature α phase field.

A general interpretation of the average transition temperatures of all the thermograms for each alloy are presented in Table X. There are good agreement of the measured DTA transition temperatures for a given alloy analyzed in either an Al_2O_3 crucible (Y_2O_3 coated specimen) or a Y_2O_3 crucible (no coating). The agreement of transition temperatures supports the assumption that the first cycle of specimens tested in the Al_2O_3 crucibles are reliable and representative of the alloys, with a maximum oxygen content of 1700-1800 ppm (by wt.%) (worst case assumption). Most of the oxygen contamination observed in the post-DTA specimens occurred after melting. Figure 9 shows the effect of increasing the oxygen content from 1700 ppm (by wt.%) at end of the first cycle to 3750 ppm (by wt.%) at the end of the second cycle.

Supporting evidence for the interpretation presented in Table X is provided by the post-DTA metallography samples. Both samples 163-1 and 163-2 showed signs of rapid diffusion rates as no evidence of dendritic segregation was observable, and both samples contained large equiaxed grains with an internal structure of parallel plates of $\alpha_2\text{-}\gamma$. This structure is suggestive of grain growth and decomposition of a high temperature phase. A similar microstructure was observed in the DTA specimen (163-1) heated to 1442°C below the solidus (see Figure 4). These results are an indication the alloys (163-1 and 163-2) passed through a β single phase field during heating. On the other hand, both samples 163-3 and 163-4 showed signs of

dendritic segregation with 60° orientation (in 163-4) between primary and secondary dendrite arms indicating α formation from the melt (see Figure 5). The microstructure of specimen (163-4) heated to 1444°C provides additional evidence supporting the suggestion that an α - γ two phase field exists; the grains with the high temperature α phase decomposed on cooling to form grains with α_2 and γ parallel plates while the γ grains remained unchanged (see Figure 6).

Complimentary to the DTA data which provided transformations temperatures for a given composition, the microprobe data provided compositional information for samples annealed at a given temperature. Assuming a penetration depth of 3 microns and using a 1 micron step, the microprobe data (see Figures 12-14) should give the same measured composition at no less than three consecutive points for this concentration to be representative of a specific phase. Sample 163-1 (44.83 Al) was annealed (6 hours at 1100°C) just below the eutectoid reaction $\alpha=\alpha_2+\gamma$, and the microprobe data should provide information on the location of the boundaries at 1100°C of the α_2 - γ two phase field. It was easier to obtain three consecutive microprobe points at the same composition level for the aluminum rich phase (γ), which is an indication alloy 163-1 is on the aluminum-rich side of the lever arm (the 50-50 two phase composition point is towards the titanium rich side of alloy 163-1). The aluminum content of the γ phase is 47 at.% according to Figures 12b and 13b. The slope on the left side of the aluminum rich peaks in Figure 14b is an indication the γ phase is undercut by some α_2 phase within the 3

micron limit (i.e., the electron beam is not parallel to the plane of γ) which would account for the maximum aluminum content of only 45.5 at.% Al. The aluminum content of the titanium-rich phase (α_2) can only be assumed to be less than 39 at.% Al from Figures 12b and 13b. A more accurate number of 37.25 at.% Al can be obtained from Figure 14b since a number of areas had consecutive points with the same composition level for the titanium-rich phase (α_2). Thus the aluminum composition of the α_2 and γ phases in equilibrium at 1100°C are 37.25 at.% Al and 47 at.% Al respectively.

Microprobe analysis of the parallel plates of α_2 and γ in the decomposed primary α dendrites of the post-DTA sample 163-4 provide additional information on the eutectoid decomposition. The γ phase with 51 at.% Al and the α_2 phase with less than 42.5 at.% Al (see Figure 1e), did not agree with the composition limits determined from the annealed sample 163-1. This can be explained by noting that the parallel plates of γ and α_2 are not formed as a result of a classical eutectoid decomposition which involves the simultaneous growth of structurally dissimilar phases (incoherent interfaces) but, rather as a result of the structural relationship between the γ and α_2 phases ((001) α_2 parallel to (111) γ , [210] α_2 parallel to [110] γ) [Gra87]. Thus, as the α dendrite (average composition 47.5 at.% Al) cools it encounters the α - γ two phase field and γ starts precipitating with a composition of 51 at.% the γ phase grows at the expense of the α phase which decreases in aluminum content, until the eutectoid is reached and the remaining α phase

converts to the α_2 phase plus a small amount of γ phase (which would not be expected to be resolvable in the microprobe data). This description of the decomposition of the α dendrites is compatible with the DTA data.

The average transformation temperatures from the DTA results and composition data from microprobe analysis, are compatible with the version of the Ti-Al phase diagram with a high temperature α phase field [Mis89] [McC88].

The establishment of the high temperature α phase field in the Ti-Al phase diagram has a significant influence on the interpretation of the levels of undercooling required for the formation of different phases during rapid solidification processing. Thus high levels of undercooling are not necessary to obtain solidification of α phase from the melt. The Ti-Al phase diagram data here is being used as an additional guide in the phase diagram calculations currently under way.

2.3 Model and Calculations of Ti-Al Binary

The data obtained from the experimental investigation of the binary phase equilibria are being incorporated into a final iteration of the modeling parameters for the calculations of the binary Ti-Al system. The adjustments to the modeling parameters are still under way and the results have not been finalized. Initial results indicate changes in some phase boundaries and nature of reactions. For example the separation of the β - α two phase field from the α - α_2 two phase field and the L- γ + ϵ eutectic may be a L- γ - ϵ peritectic reaction. A new calculated phase diagram will be available after changes to the modeling

parameters have been finalized.

Table I
Alloys Used to Investigate the Binary Ti-Al System

| ID# | Composition (at. %) | Produced By |
|-------|------------------------|---------------------|
| 163-1 | Ti-44Al | Drop cast/HIP/Forge |
| 163-2 | Ti-46Al | Drop cast/HIP/Forge |
| 163-3 | Ti-48Al | Drop cast/HIP/Forge |
| 163-4 | Ti-50Al | Drop cast/HIP/Forge |
| 9 | Ti-35Al | Arc melt/anneal |
| 8 | Ti-40Al | Arc melt/anneal |

Table II
Composition of Alloys Used in Phase Diagram Study

| Alloy ID | Condition | Composition (at.%) | | |
|--------------------------|------------|--------------------|-------|------|
| | | Ti | Al | O* |
| 163-1 | HIP/Forged | 55.17 | 44.83 | 320 |
| 163-2 | HIP/Forged | 53.13 | 46.87 | 320 |
| 163-3 | HIP/Forged | 51.35 | 48.65 | 390 |
| 163-4 | HIP/Forged | 49.06 | 50.94 | 270 |
| Ingot 8 1300°C/6 days | Annealed | 60.36 | 39.64 | 1880 |
| Ingot 9 1300°C/6 days | Annealed | 64.58 | 35.42 | 2290 |

* = Values are based on ppm by wt.%

Table III
DTA Results for 163-1 (44.83 Al)
Observed Reactions (°C)

| Al_2O_3 Test 1 8 Jun 88 (#) | Al_2O_3 Test 2 20 May 88 (#) | Al_2O_3 Test 3 28 Oct 88 (##) | Al_2O_3 Test 4 24 Oct 88 (##) | Y_2O_3 Test 1 25 Feb 89 (##) |
|---|---|--|--|---|
| 15°C/min | 30°C/min | 15°C/min | 30°C/min | 30°C/min |
| O: 1120 P: 1129 | O: 1120 P: 1133 | O: 1126 P: 1141 | O: 1125 P: 1145 | O: 1123 P: 1138 |
| O: ---- P: 1288 | O: ---- P: 1282 | O: ---- P: 1297 | O: ---- P: 1302 | O: ---- P: 1302 |
| O: 1432 P: 1446 | O: 1418 P: 1444 | O: 1441 P: 1456 | O: 1433 P: 1458 | O: 1433 P: 1451 |
| O: 1492 P: 1514 P: 1535 | O: 1492 | O: 1502 P: 1518 P: 1544 | O: 1506 S: 1532 P: 1555 | O: 1493 S: 1513 P: 1547 |
| O = Onset Temperature P = Peak Temperature S = Slope Change | | # = Argon Purification R13 Catalyst ## = Ti-Gettered Argon System | | |

Table IV
DTA Results For 163-2 (46.87 Al)
Observed Reactions (°C)

| Al_2O_3 Test 1 7June 88 (#) | Al_2O_3 Test 2 23May 88 (#) | Al_2O_3 Test 3 27Oct 88 (##) | Al_2O_3 Test 4 25Oct 88 (##) | Y_2O_3 Cycle 1 20Aug 89 (##) | Y_2O_3 Cycle 2 20Aug89 (##) |
|--|--|---|---|---|--|
| <hr/> | | | | | |
| 15°C/min | 30°C/min | 15°C/min | 30°C/min | 30°C/min | 30°C/min |
| O: 1145 P: 1165 | O: 1136 P: 1163 | O: 1142 P: 1157 | O: 1146 P: 1169 | O: 1173 P: 1190 | O: 1147 P: 1160 |
| O: ---- P: 1227 | O: ---- P: 1330 | O: 1243 P: 1314 | O: ---- P: 1313 | O: 1239 P: 1335 | O: ---- P: 1343 |
| O: 1247 P: 1320 | O: ---- P: ---- | O: ---- P: ---- | O: ---- P: ---- | O: ---- P: ---- | O: ---- P: ---- |
| O: 1469 S: 1478 P: 1492 S: 1502 | O: 1470 S: 1485 P: 1494 | O: 1465 S: 1482 P: 1501 S: 1528 | O: 1471 S: 1482 P: 1497 P: 1509 | O: 1472 S: 1480 P: 1492 S: 1512 S: 1532 | O: 1474 S: 1488 P: 1496 S: 1510 |

O = Onset Temperature # = Argon Purification R13 Catalyst
 P = Peak Temperature ## = Ti-Gettered Argon System
 S = Slope Change

Table V
 DTA Results for 163-3 (48.65 Al)
 Observed Reactions (°C)

| Al_2O_3 | Al_2O_3 | Al_2O_3 | Al_2O_3 | Y_2O_3 | Y_2O_3 |
|-------------------------|-------------------------|-------------------------|-------------------------|------------------------|------------------------|
| Test 1 | Test 2 | Test 3 | Test 4 | Cycle 1 | Cycle 2 |
| 7June88 | 23May88 | 27Oct88 | 25Oct88 | 20Aug89 | 20Aug89 |
| (#) | (#) | (##) | (##) | (##) | (##) |
| 15°C/min | 30°C/min | 15°C/min | 30°C/min | 30°C/min | 30°C/min |
| O: ---- | O: 1185 | O: 1172 | O: 1208 | O: 1200 | O: ---- |
| P: ---- | P: 1218 | P: 1221 | P: 1248 | P: 1215 | P: ---- |
| O: 1279 | O: 1311 | O: 1306 | O: 1311 | O: 1305 | O: 1284 |
| P: 1378 | P: 1338 | P: 1386 | P: 1396 | P: 1386 | P: 1370 |
| O: ---- | O: 1331 | O: ---- | O: ---- | O: ---- | O: 1427 |
| P: ---- | P: 1386 | P: ---- | P: ---- | P: ---- | P: 1440 |
| O: 1452 | O: 1454 | O: 1466 | O: 1468 | O: 1460 | O: 1458 |
| P: 1485 | O: 1492 | P: 1496 | P: 1502 | P: 1500 | P: 1503 |

O = Onset Temperature # = Argon Purification R13 Catalyst
 P = Peak Temperature ## = Ti-Gettered Argon System
 S = Slope Change

Table VI
DTA Results for 163-4 (50.94 Al)
Observed Reactions (°C)

| Al ₂ O ₃ Test 1 7 June 88 (#) | Al ₂ O ₃ Test 2 24 May 88 (#) | Al ₂ O ₃ Test 3 26 Oct 88 (##) | Al ₂ O ₃ Test 4 26 Oct 88 (##) | Y ₂ O ₃ Test 1 21 Aug 89 (##) |
|--|--|---|---|--|
| 15°C/min | 30°C/min | 15°C/min | 30°C/min | 30°C/min |
| O: 1346 P: 1409 | O: 1344 P: 1419 | O: 1357 P: 1420 | O: 1358 P: 1426 | O: 1342 P: 1418 |
| O: 1431 P: 1440 | O: 1406 P: 1443 | O: 1432 P: 1450 | O: 1432 P: 1453 | O: 1439 P: 1448 |
| O: 1438 P: 1474 | O: 1435 P: 1483 | O: 1447 P: 1485 | O: 1449 P: 1492 | O: 1458 P: 1490 |

O = Onset Temperature # = Argon Purification R13 Catalyst
 P = Peak Temperature ## = Ti-Gettered Argon System
 S = Slope Change

Table VII
DTA Results for Ingot 8 (40,24 Al)
Observed Reactions (°C)

| Al_2O_3 Test 1 18 Jun 89 | Al_2O_3 Test 2 18 Jun 89 | Y_2O_3 Test 1 22 Aug 89 |
|--|--|---|
| 15 °C/min | 30 °C/min | 30 °C/min |
| O: 1104 P: ---- | O: 1121 P: ---- | O: 1081 P: 1104 |
| O: ---- P: 1172 | O: 1128 P: 1158 | O: 1124 P: 1159 |
| O: 1353 P: 1400 | O: 1320 P: 1394 | O: 1347 P: 1384 |
| O: 1549 P: 1584 | O: 1554 P: 1590 | O: 1549 P:>1582 |

O = Onset Temperature

A Ti-Gettered Argon System was used.

P = Peak Temperature

S = Slope Change

Table VIII
DTA Results for Ingot 9 (34.97 Al)
Observed Reactions (°C)

| Al_2O_3 Test 1 19 June 89 (##) | Al_2O_3 Test 2 19 Jun 89 (##) | Y_2O_3 Test 1 21 Aug 89 (##) |
|---|--|---|
| 15°C/min | 30°C/min | 30°C/min |
| O: 1173 | O: 1171 | O: 1169 |
| P: 1185 | P: 1189 | P: 1182 |
| O: 1245 | O: 1253 | O: 1246 |
| P: 1260 | P: 1267 | P: 1260 |
| O: 1570 | O: 1564 | |

O = Onset Temperature # = Argon Purification R13 Catalyst
 P = Peak Temperature ## = Ti-Gettered Argon System
 S = Slope Change

Table IX
Post Oxygen Analysis of DTA Samples
Based on Single Test of One Specimen

| Sample ID | Crucible Material | Date of DTA Test | Maximum Temperature | Oxygen Content ppm (wt.%) |
|-----------|----------------------------------|------------------|---------------------|---------------------------|
| 163-1 | Al ₂ O ₃ | 6 Jun 88# | 1590°C* | 4400 |
| 163-3 | Al ₂ O ₃ | 7 Jun 88# | 1570°C* | 3500 |
| 163-3 | Al ₂ O ₃ | 7 Jun 88# | 1582°C* | 5300 |
| 163-4 | Al ₂ O ₃ | 7 Jun 88# | 1563°C* | 3200 |
| 163-1 | Al ₂ O ₃ | 28 Oct 88 | 1571°C* | 11000 |
| 163-2 | Al ₂ O ₃ | 27 Oct 88 | 1548°C* | 3300 |
| 163-3 | Al ₂ O ₃ | 27 Oct 88 | 1527°C* | 3100 |
| 163-4 | Al ₂ O ₃ | 26 Oct 88 | 1513°C* | 3700 |
| 163-2 | Al ₂ O ₃ | 24 Feb 89 | 1450°C | 1800** |
| 163-3 | Al ₂ O ₃ | 24 Feb 89 | 1441°C | 1900** |
| 163-1 | Y ₂ O ₃ | 25 Feb 89 | 1592°C* | 1200/3600** |
| 163-4 | Y ₂ O ₃ | 21 Aug 89 | 1 melt* | 3700/1700** Top/Bottom |
| 163-2 | Y ₂ O ₃ | 20 Aug 89 | 2 melts* | 3700/3800** Top/Bottom |
| 163-3 | Not Tested in DTA Control Sample | | | 400/500** |

* = Heated above melting temperature

**= Based on two test of same sample

= Argon Purification Train System, all others used a Ti-gettered Argon system

Note: The specimens were coated with Y₂O₃ when tested in the Al₂O₃ crucibles

Table X
Interpretation of DTA Results
For Binary Ti-Al Alloys*

| Alloy (at.% Al) | | | | | | Proposed Reaction |
|-----------------|----------|----------|----------|---------|-------|--|
| Ingot 9 | Ingot 8 | 163-1 | 163-2 | 163-3 | 163-4 | |
| 34.97 | 40.24 | 44.83 | 46.87 | 48.65 | 50.94 | |
| 0:1171 | | | | | | $\alpha_2 \Rightarrow \alpha$ |
| \pm 2 | | | | | | |
| C:1185 | | | | | | |
| \pm 4 | | | | | | |
| 0:1102 | 0:1123 | 0:1150 | 0:1191 | | | $\alpha_2 + \gamma \Rightarrow \alpha$ # |
| \pm 16 | \pm 3 | \pm 12 | \pm 14 | | | |
| C:1107 | C:1137 | C:1168 | C:1224 | | | |
| \pm 4 | \pm 6 | \pm 11 | \pm 13 | | | |
| 0:---- | 0:---- | 0:---- | 0:1300 | 0:1349 | | $\gamma \Rightarrow \alpha$ |
| \pm -- | \pm -- | \pm -- | \pm 14 | \pm 8 | | |
| C:1163 | C:1294 | C:1328 | C:1388 | C:1418 | | |
| \pm 8 | \pm 9 | \pm 12 | \pm 7 | \pm 6 | | |
| | | | 0:1428 | | | $\gamma \Rightarrow \alpha + L$ # |
| | | | \pm 13 | | | |
| | | | C:1447 | | | |
| | | | \pm 5 | | | |
| | | 0:1460 | 0:1445 | | | $\alpha \Rightarrow L$ |
| | | \pm 6 | \pm 9 | | | |
| | | C:1496 | C:1485 | | | |
| | | \pm 7 | \pm 7 | | | |
| 0:1248 | 0:1340 | 0:1431 | 0:1470 | | | $\alpha \Rightarrow \beta$ |
| \pm 4 | \pm 18 | \pm 8 | \pm 3 | | | |
| C:1262 | C:1393 | C:1451 | C:1483 | | | |
| \pm 4 | \pm 8 | \pm 6 | \pm 5 | | | |
| 0:---- | | | | 0:---- | | $\alpha \Rightarrow \beta + L$ # |
| | | | | --- | | |
| | | | | C:1495 | | |
| | | | | \pm 3 | | |
| 0:1567 | 0:1551 | 0:1497 | 0:---- | | | $\beta \Rightarrow L$ |
| \pm 4 | \pm 3 | \pm 7 | \pm -- | | | |
| C:---- | C:1587 | C:1545 | C:1529 | | | |
| \pm -- | \pm 4 | \pm 8 | \pm 2 | | | |

* = Transformation Temperatures in °C

= Invariant Transformation, difference between onset and completion are in indication of the thermal lag

O = Onset Temperature of Transformation

C = Completion Temperature of Transformation

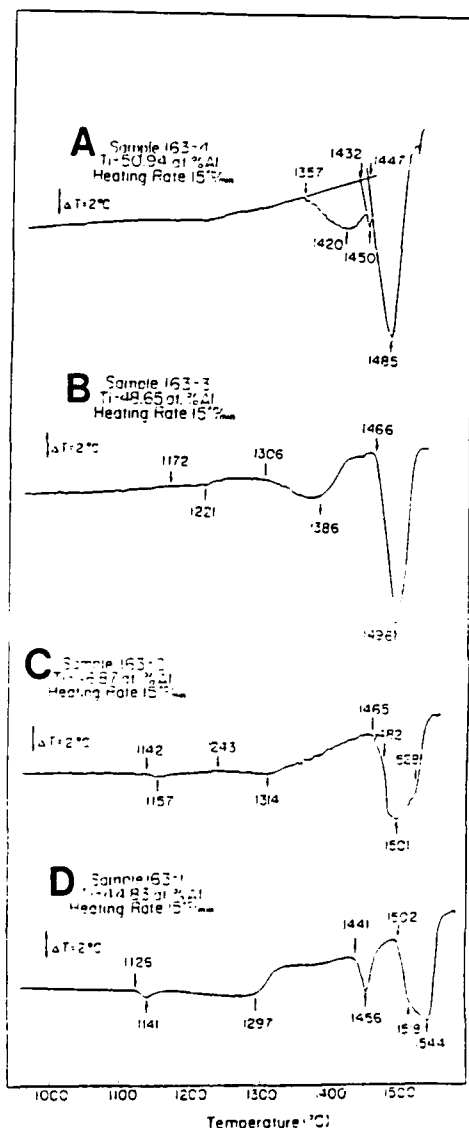


Figure 1

DTA Thermograms for Ti-Al Binary Alloys
 Note: Al_2O_3 DTA cup with Y_2O_3 coated sample.
 a) Sample 163-1 (Ti-44.83Al)
 b) Sample 163-2 (Ti-46.87Al)
 c) Sample 163-3 (Ti-48.65A).
 d) Sample 163-4 (Ti-50.94Al).

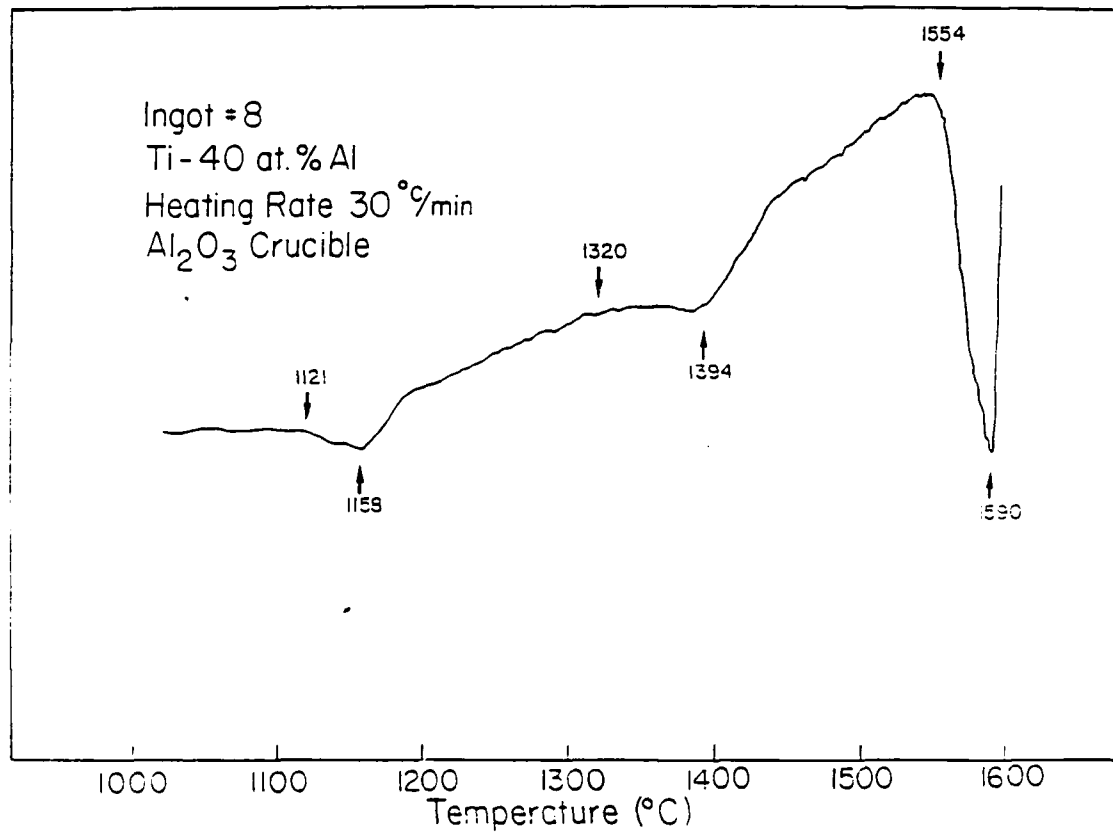


Figure 2 DTA Thermogram, Ingot 8 (Ti-40Al)
 Al_2O_3 DTA cup with Y_2O_3 coated sample.

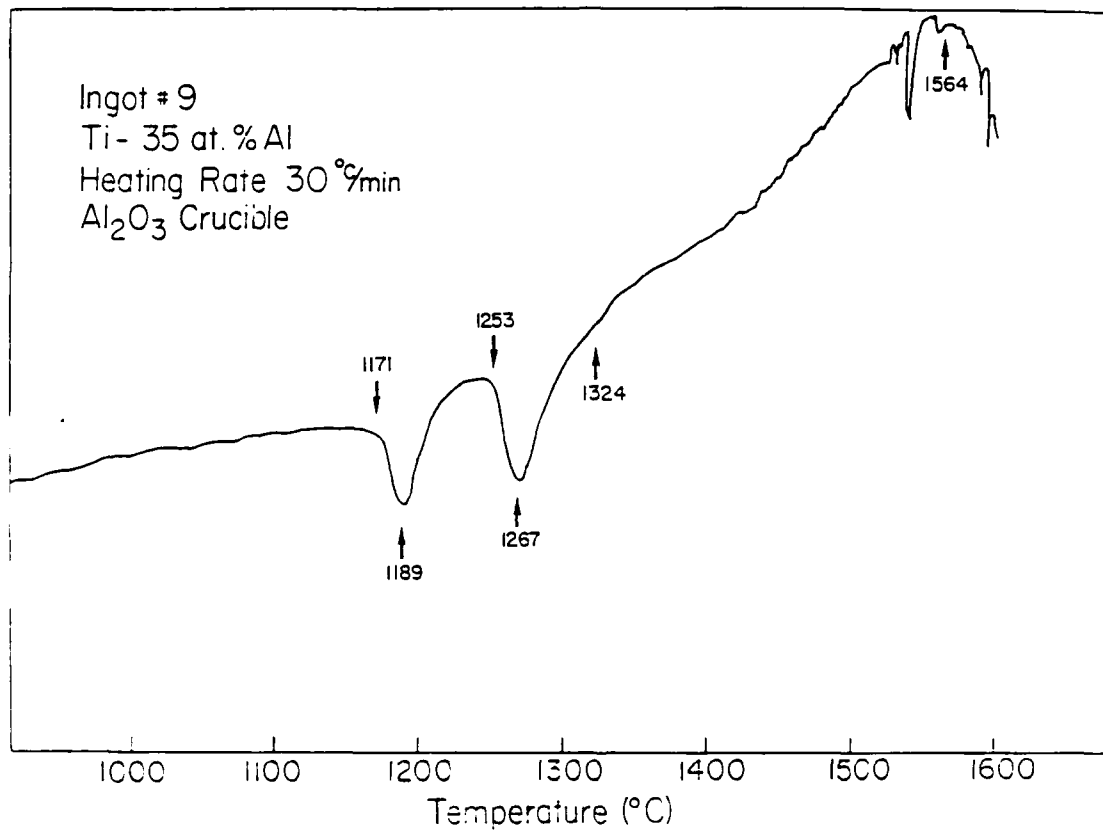


Figure 3 DTA Thermogram, Ingot 9 (Ti-35Al)
 Al_2O_3 DTA cup with Y_2O_3 coated sample.



Figure 4 Microstructure, Sample 163-1 (Ti-44.83Al)
After DTA Analysis, $T_{max} = 1422^\circ\text{C}$.

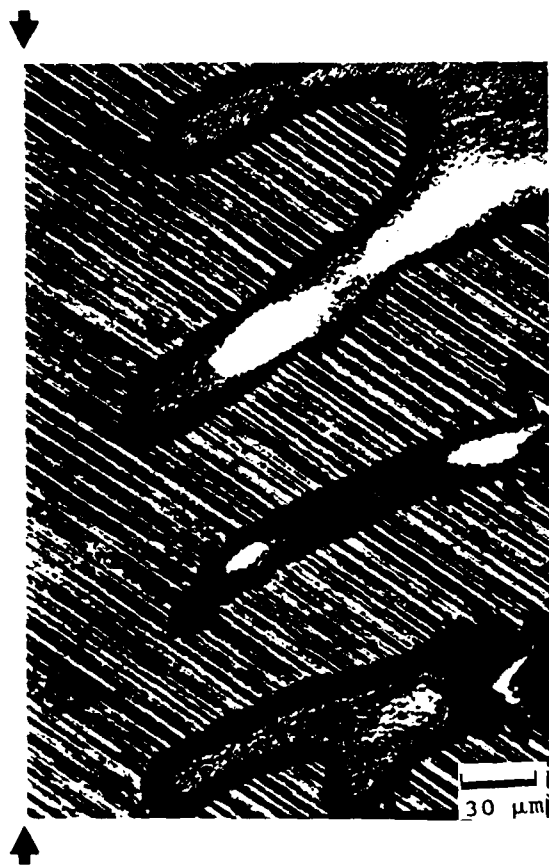


Figure 5

Microstructure of Sample 163-4 (Ti-50.94Al)
After DTA Analysis, $T_{max} = 1595^{\circ}\text{C}$.
Note: Arrows indicate center of dendrite arm,
secondary dendrites form 60°C angle.



Figure 6 Microstructure of Sample 163-4 (Ti-50.94Al)
After DTA Analysis, $T_{max} = 1444^{\circ}\text{C}$.

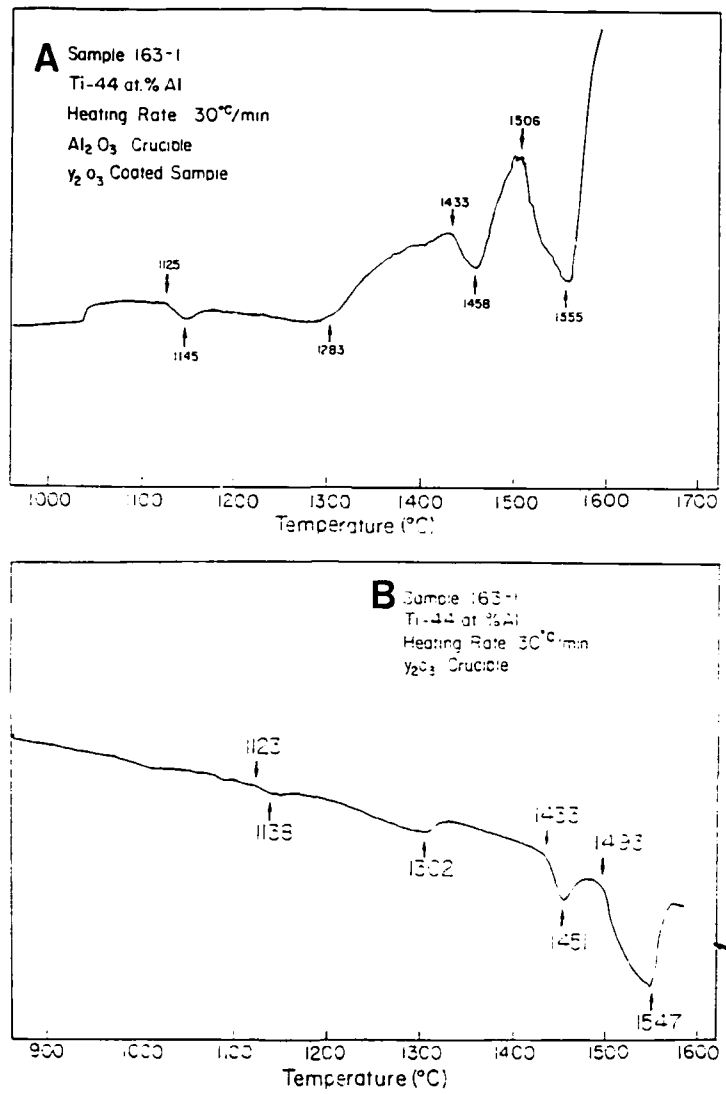


Figure 7

DTA Thermogram, Sample 163-1 (Ti-44.83Al),
 a) Al_2O_3 DTA Crucible and Y_2O_3 Coated Sample
 b) Y_2O_3 DTA Crucible

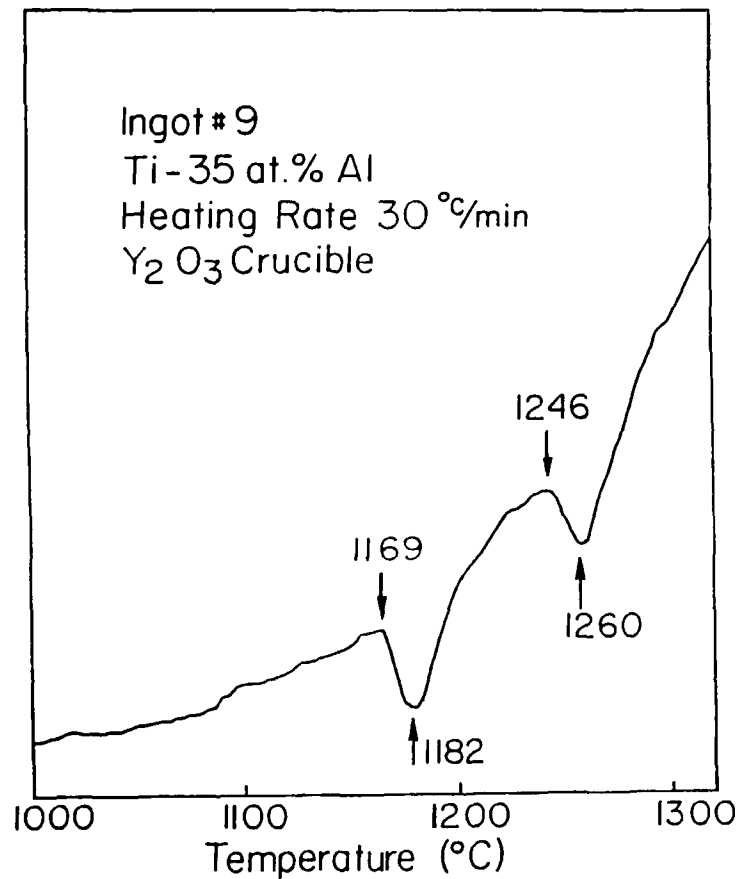


Figure 8 DTA Thermogram, Ingot 9 (Ti-35Al)
 Y_2O_3 DTA Crucible.

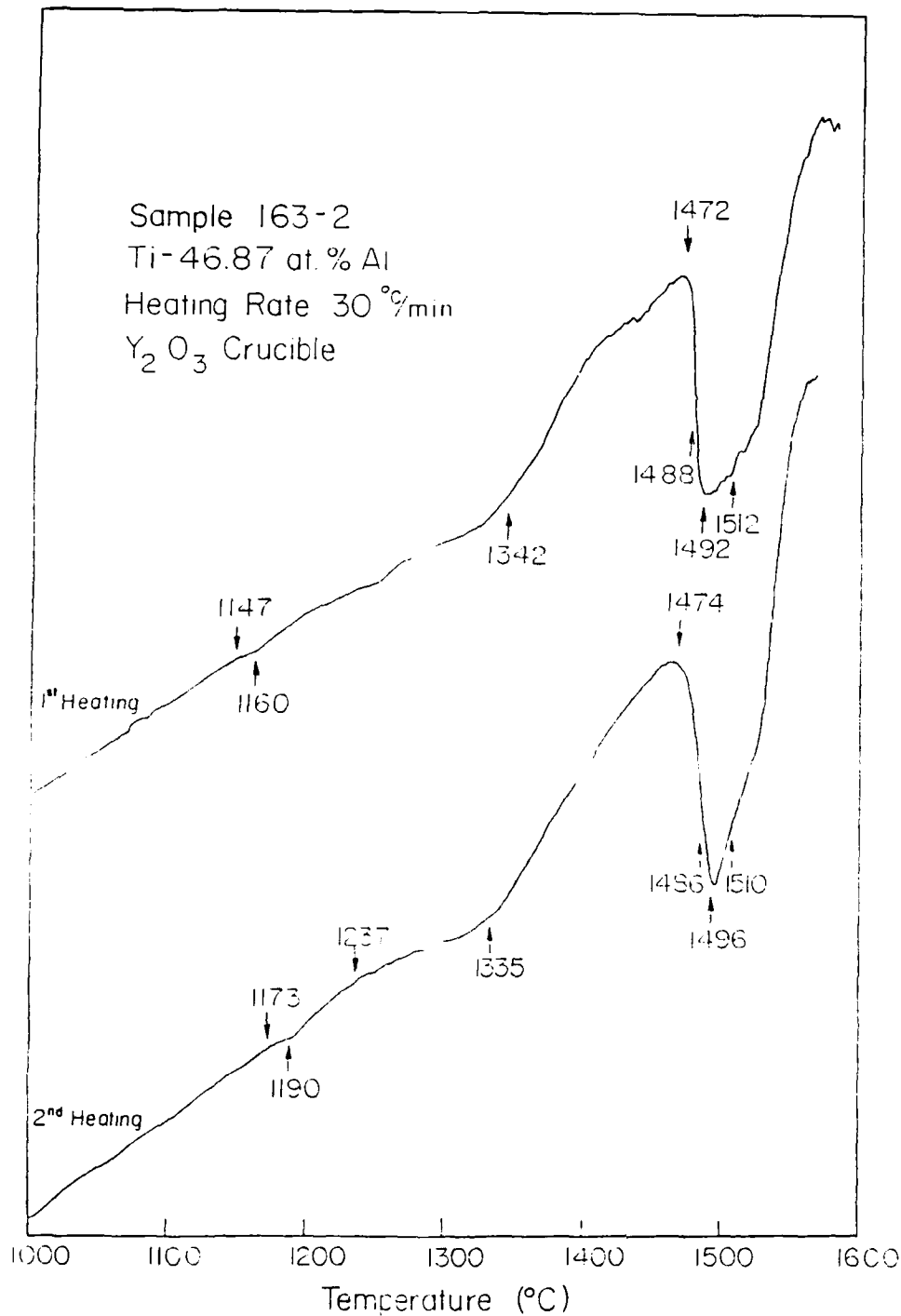


Figure 9 DTA Thermogram, Sample 163-2 (Ti-46.87Al)
 Y_2O_3 DTA Crucible.

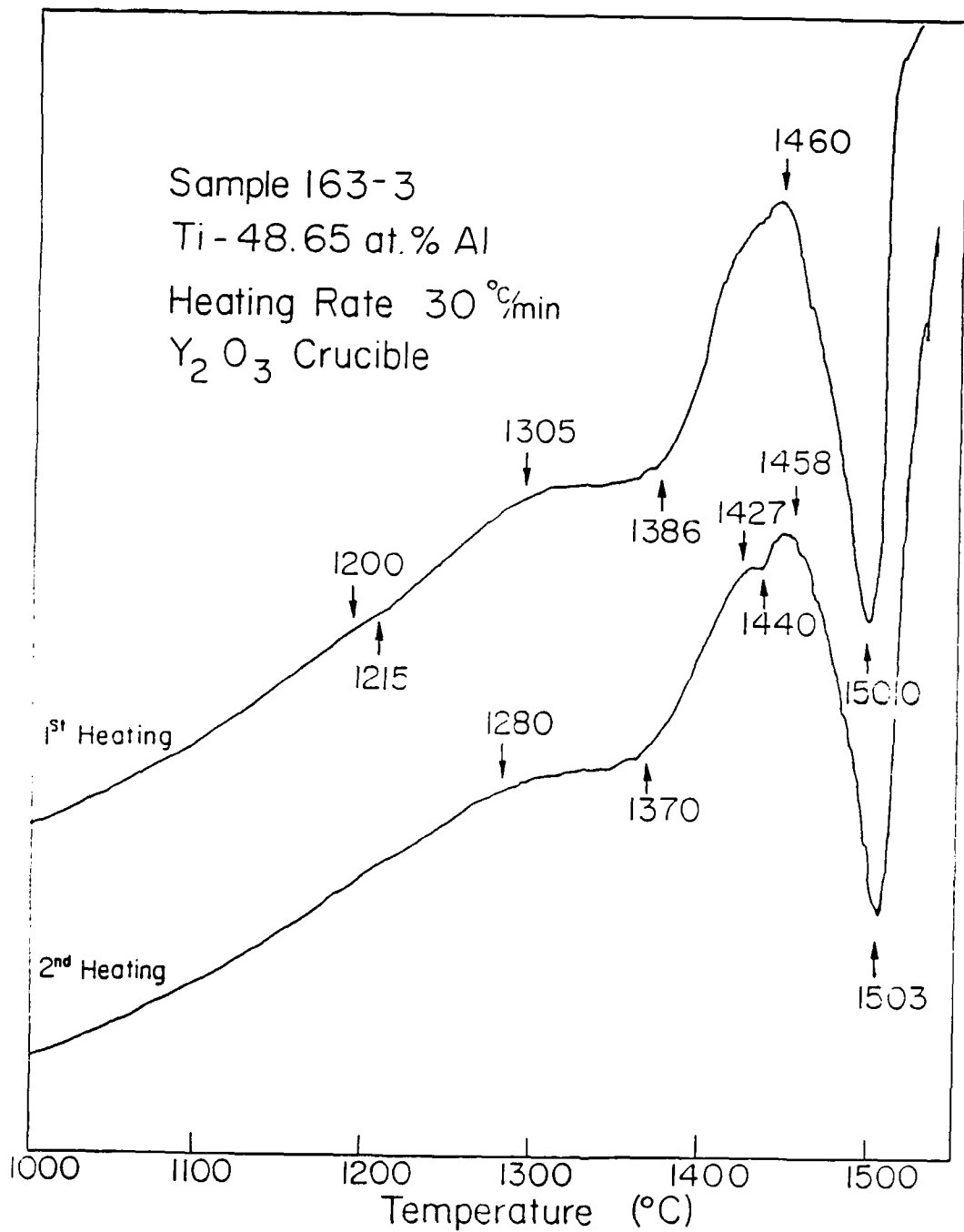


Figure 10 DTA Thermogram, Sample 163-3 (Ti-48.65Al)
 Y_2O_3 DTA Crucible.

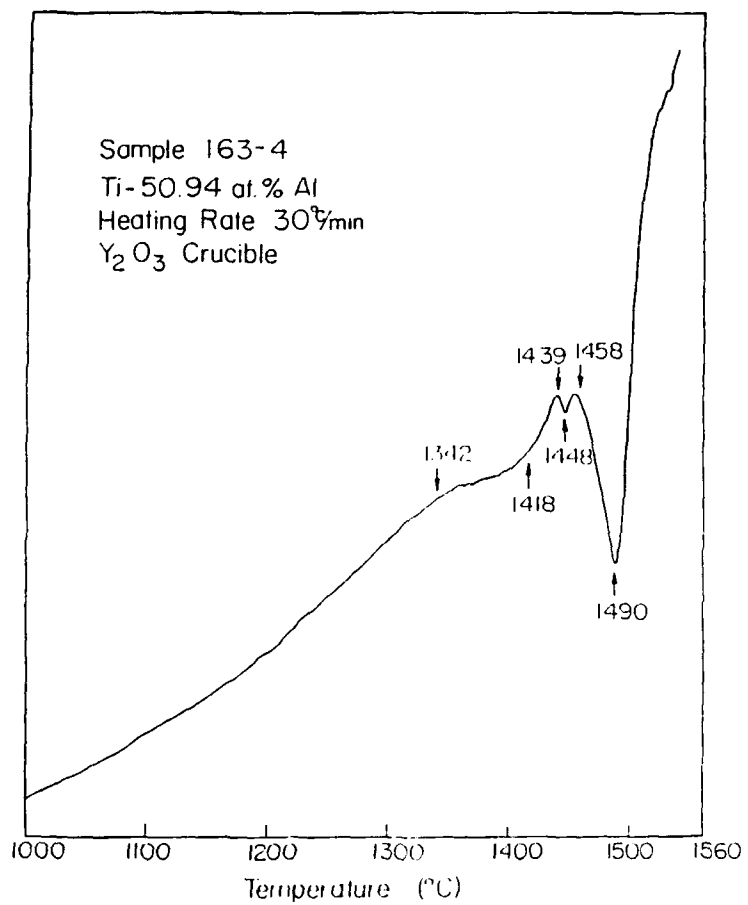
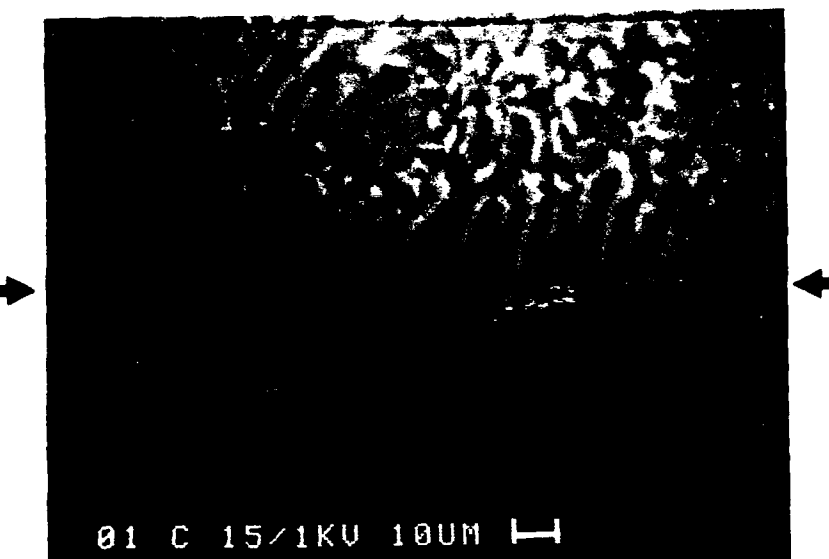
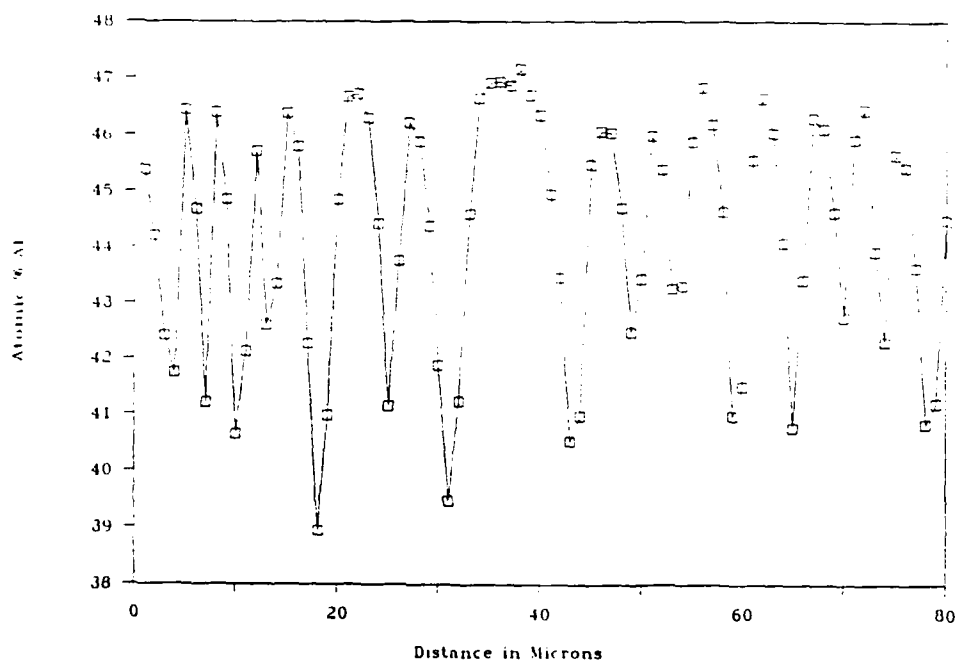


Figure 11 DTA Thermogram, Sample 163-4 (Ti-50.94Al)
 Y_2O_3 DTA Crucible.

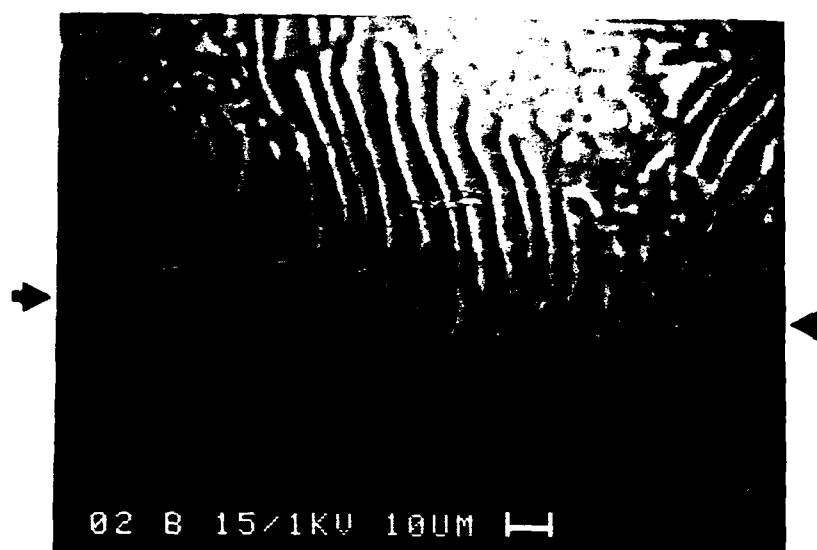


a) Microprobe Scan, arrows indicate scan line.

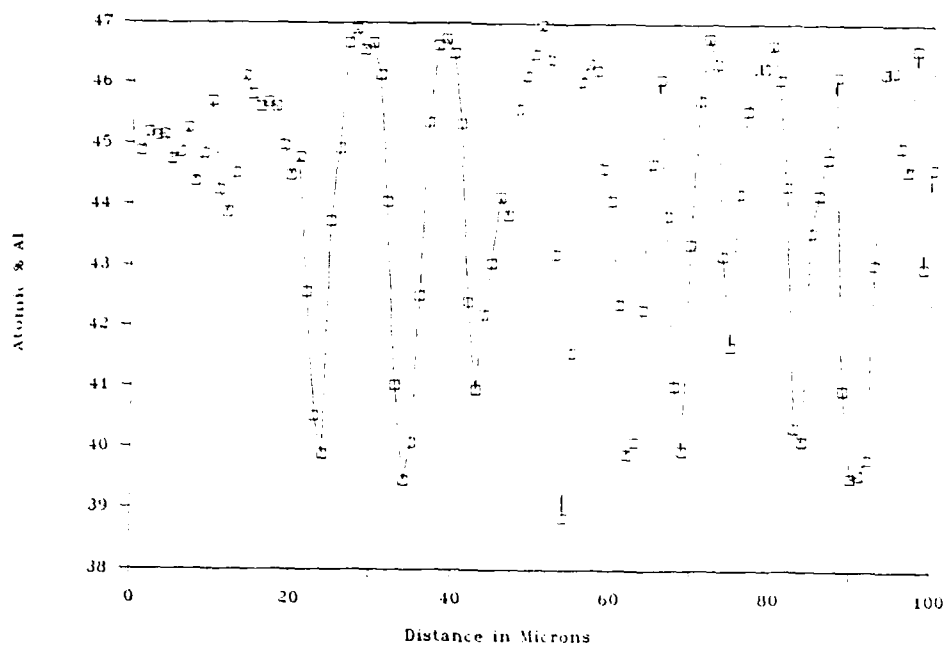


b) Microprobe Scan Data as a Function of Distance

Figure 12 Area #1, Sample 163-1 (Ti-44.83Al),
Annealed at 1100°C for 6 hours.



a) Microprobe Scan, arrows indicate scan line.

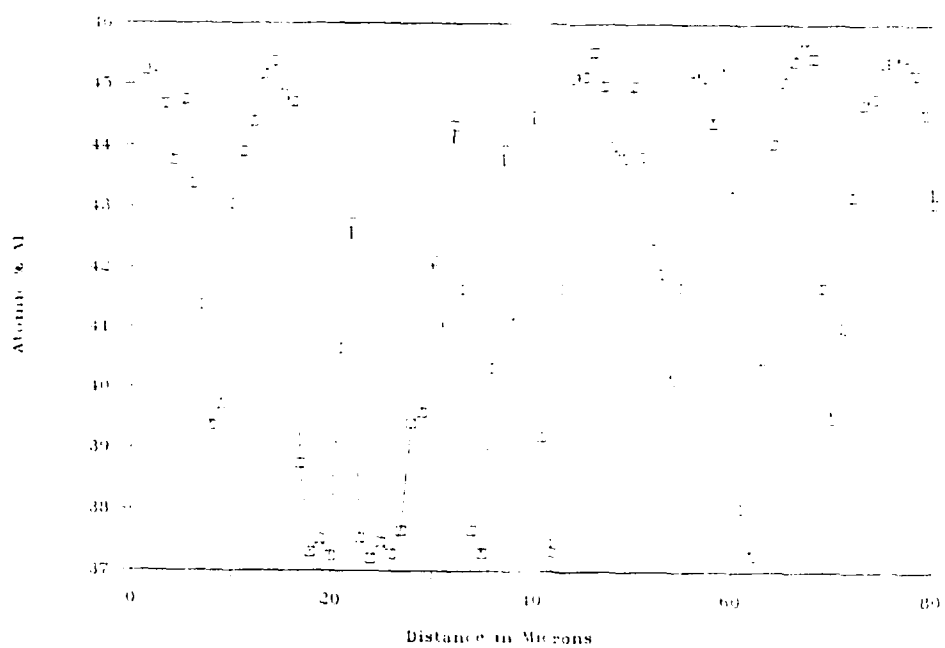


b) Microprobe Scan Data as a Function of Distance

Figure 13 Area #2, Sample 163-1 (Ti-44.83Al),
Annealed at 1100°C for 6 hours.



a) Microprobe Scan, arrows indicate Scan Line.



b) Microprobe Scan Data as a Function of Distance

Figure 14 Area #3, Sample 163-1 (Ti-44.83Al),
Annealed at 1100°C for 6 hours.



a) Area of Microprobe Scan



a) Microstructure of Area Subjected to Microprobe Analysis

Figure 15 Sample 163-4 (Ti-50.94Al), Post-DTA, Tmax = 1576°C.

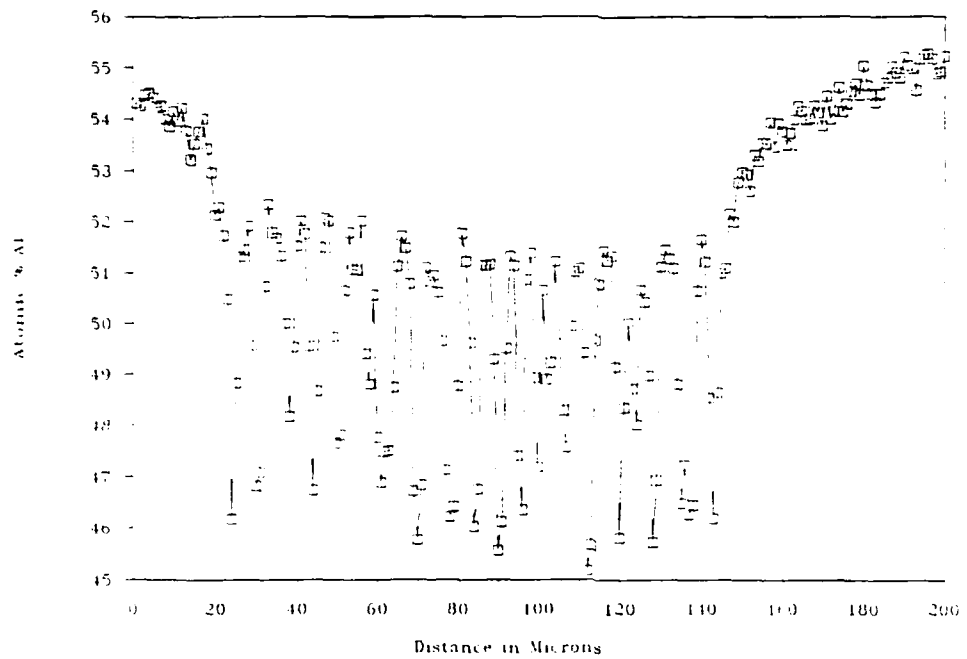


Figure 16 Microprobe Scan Data as a Function of Distance
 Sample 163-4 (Ti-50.94Al), Post DTA, Tmax = 1576°C.

3. Ternary Ti-Al-Nb3.1 Experimental Determination of Ternary Ti-Al-Nb SystemLiquidus Projection of the Ternary Nb-Al-Ti System

The liquidus projection given in Figure 17 is estimated on the basis of 24 ternary samples. The format of presentation for the liquidus projection follows that adopted by Chang et.al. [Cha79]. The binary invariants such as the peritectics and eutectics are denoted by p_1 , p_2 ... and e_1 , e_2 counterclockwise from the Nb-corner. The congruent melting points are denoted by solid circles and saddle points by open circles. The directions of the slopes for the liquidus valleys, i.e. the univariant equilibria, are indicated by arrows inscribed upon the lines toward the lower temperatures. The four-phase equilibria are indicated by type I, II and III according to Rhines [Rhi56]. A subscript 1, 2, ... is used to denote the various four-phase equilibria of the same type, with the subscript 1 indicating the highest temperature. For instance, II_1 , II_2 , denote type II four-phase equilibria with II_1 corresponding to the highest temperature type II four-phase equilibrium. The compositions of the 24 samples are summarized in Table XI and are also indicated on Fig 17. The primary phases of solidification obtained from the as-cast (by arc-melting) samples were determined by optical microscopy, scanning electron microscopy (SEM), electron probe microanalysis (EPMA), and x-ray diffraction. The binary invariant equilibria, i.e. the temperatures and compositions of the liquid phase for the binary peritectics, p_1 , p_2 , ... and eutectics, e_1 , e_2 , are taken from the literature. The data

for the binary Nb-Al system were taken from the DARPA report by Boettigner et.al. [Boe89]. The data for the Ti-Al binary were taken from Mishurda et.al. [Mis89]. Since the melting temperatures for only seven samples, i.e. nos. 49, 9, 35, 141, 142, 144 and 149 (see Table XI) were measured by DTA, the temperatures of the invariant equilibria as well as the types of the four phase equilibria are not known. Nevertheless, on the basis of the melting points of the binary peritectics and eutectics as well as the measured melting temperatures of the aforementioned seven samples, the types of the invariant equilibria (see Table XII) and directions of the slopes for the liquidus valleys (see Figure 17) are estimated.

The liquidus valley involving the L- σ - η three-phase equilibrium originates from binary eutectic e_1 . As given in Table XI, the primary phase of solidification from samples 141 and 144 is σ , that from sample 5 is η , and that from samples 37, 63, 142 and 149 is γ . Figure 18 shows a photomicrograph of sample 141 in the as-cast condition (Figure 19). This photomicrograph shows primary σ as verified by x-ray diffraction. Figure 20, on the other hand, shows a photomicrograph of sample 63 also in the as-cast condition. It shows primary γ , also supported by x-ray data (Figure 21). Figure 22 shows a photomicrograph of sample 5, displaying primary η , also verified by x-ray diffraction (see Figure 23). These three samples in addition to sample 149 place the composition of the liquid phase for the L= $\sigma+\eta+\gamma$ four-phase equilibrium at ~38.5at% Nb, ~52at% Al and ~9.5at% Ti. This four-phase equilibrium is believed to be

type II, occurring at a temperature of $\sim 1469^\circ\text{C}$. Differential thermal analysis of samples 141 and 144 to a maximum temperature of $\sim 1570^\circ\text{C}$ and $\sim 1590^\circ\text{C}$ respectively showed no signs of primary phase melting (see Table XI). Samples 144 and 149 both indicate initial melting occurs at $\sim 1469^\circ\text{C}$, which has been attributed to the II_2 four phase equilibrium. As the $\text{L}-\sigma-\eta$ equilibrium originates from e_1 (1590°C), this suggests that the liquidus valley, although decreasing in temperature with Ti additions is fairly flat. Preliminary DTA results of sample 142 and 149 indicate that the liquidus valley decreases towards the $\text{L}-\eta-\sigma-\gamma$ four phase equilibrium. The $\text{L}-\gamma-\sigma$ liquidus valley is believed to decrease away from the four phase equilibrium.

In the Nb-Al binary, the temperatures for p_1 and p_2 are 2060°C and 1940°C respectively while in the Al-Ti binary p_5 and P_6 are 1450°C and 1480°C respectively. Since the reaction temperatures of P_1 and P_2 are much higher than both P_6 and P_7 it is reasonable to expect that the $\text{L}-\beta-\delta$ extends into the ternary region with decreasing temperature. Furthermore, as the melting temperatures of sample 35, 9 and 49 decrease with decreasing Nb content, it is expected that the $\text{L}-\beta-\gamma$ liquidus valley decreases in temperature from the $\text{L}-\beta-\sigma-\gamma$ four phase equilibrium towards the Ti-Al binary. As type III four phase equilibria are quite rare in metallic systems it can thus be inferred that the $\text{L}-\beta-\sigma-\gamma$ four phase equilibria is type II with the down temperature directions as indicated in Figure 17.

It is also reasonable to expect the $\text{L}-\beta-\alpha$ liquidus valley originating at P_7 to decrease in temperature as it

approaches the L- β - α - γ four phase equilibria. This will then result in another type II equilibria, with the exiting down temperature liquidus valley being the L- α - γ liquidus valley which moves down temperature to P_6 . This results in the formation of the following type II four phase equilibria, II_1 , II_2 , II_3 and II_4 as indicated in Figure 17.

The phase equilibria involving the ϵ -phase in the Al-Ti binary are not known with certainty. Recent thermodynamic modelling and phase diagram calculations show the ϵ phase to form via a peritectic reaction. Efforts are currently underway to obtain experimental verification of this melting behavior. Four samples with compositions in the vicinity of ϵ , i.e. samples 46, 52, 53 and 60 (see Figure 17 and Table XI), were examined. Sample 53 in the as cast condition shows solidification of primary η phase. The preliminary results of samples 46, 52 and 60 are not conclusive. In the discussion of the L- σ - η - γ four-phase equilibrium, the temperature of the L- η - γ liquidus valley decreases in temperature toward the II_2 invariant point. Since the temperature of P_4 and P_5 (see Figure 17) are $\sim 1350^\circ\text{C}$ and $\sim 1370^\circ\text{C}$ respectively, there must be a saddle point along the L- η - γ liquidus valley. This suggests that there may exist a pseudo-binary eutectic between η and γ . Since there is no conclusive experimental data in the region involving ϵ , no attempt is made even to estimate the composition of the liquidus valley involving L- ϵ - γ .

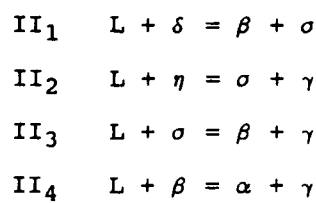
The region where β is indicated as the primary phase of solidification was constructed based on x-ray diffraction data

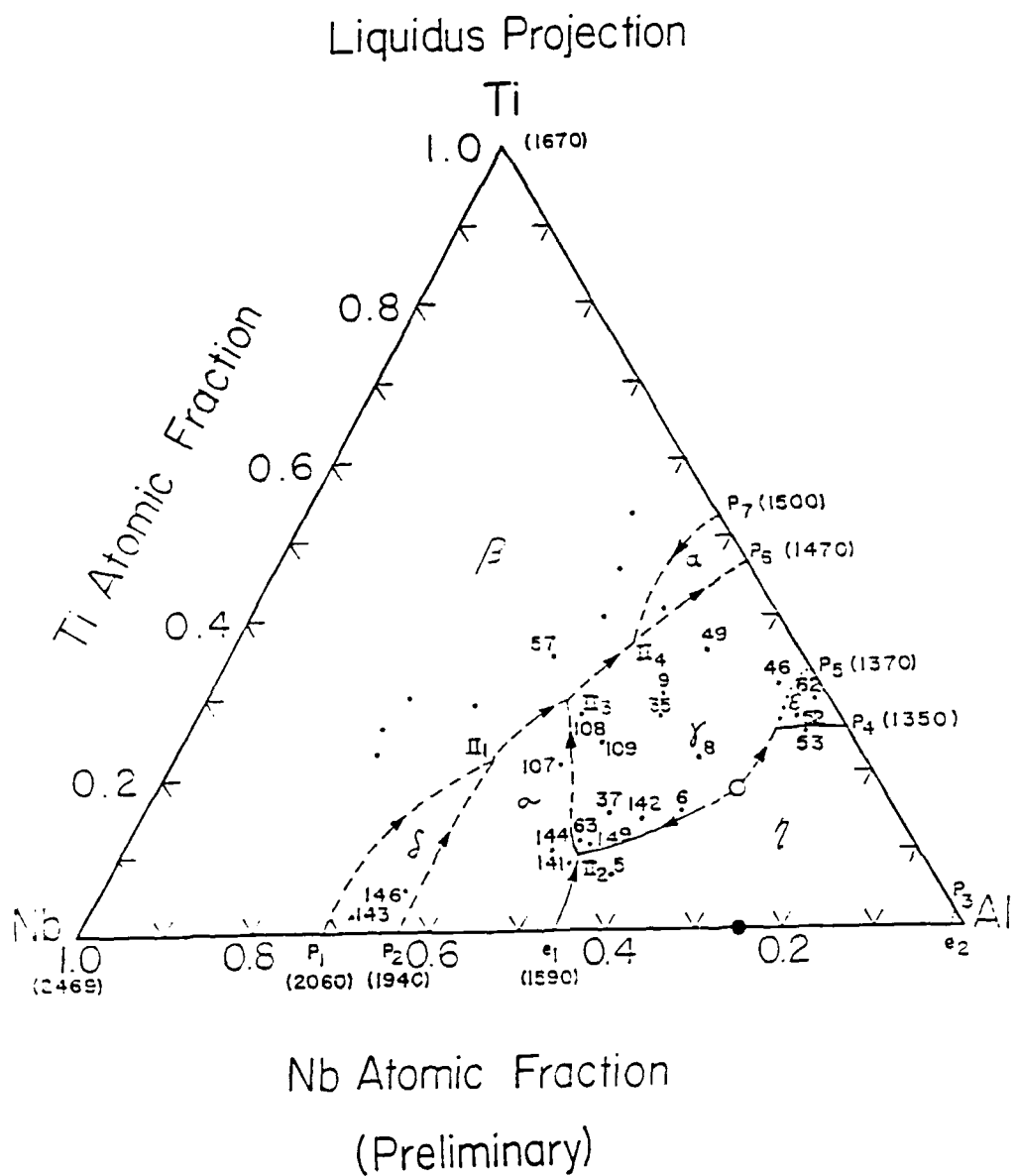
and optical microscopy. All alloys within this region had similar microstructures, consisting of large equiaxed grains with traces of dendritic concentration gradients within the grains (see Figure 24). However, throughout this region the intragranular morphology varied depending on the solid state reactions that took place upon cooling. In the Nb rich corner, X-ray diffraction and back-scattered electron imaging indicate that a massive $\beta \Rightarrow \delta$ transformation occurs for alloys in a portion of this region. Figure 25 shows the formation of δ at the β grain boundaries. In contrast to this, the transformation of alloys in the general region of Ti - 40 at.% Al - 15 at.% Nb involve the precipitation of needle shaped particles throughout the equiaxed β grains (See Figure 26). The existence of a massive $\beta \Rightarrow \delta$ transformation in the Nb-Al binary system has been well documented [Lio 87] [Lum 66]. The possibility exists that the ordered phase, i.e. B2 phase, may be stable all the way up to the melting point in some composition range within the β region. However, no evidence has been obtained to indicate this possibility.

Table X
A Summary of Various Samples Showing the Primary Phase of Solidification

| Alloy # | Nb | Al | Ti | Primary Phase |
|---------|------|------|------|----------------------------------|
| 5 | 34.6 | 57.9 | 7.5 | η |
| 37 | 31.7 | 53 | 15.3 | γ |
| 63 | 36.9 | 51.7 | 11.4 | γ |
| 141 | 39.9 | 51.4 | 8.8 | σ no melting up to 1570°C |
| 142 | 28.5 | 57 | 14.5 | γ |
| 144 | 41.6 | 48.7 | 9.7 | σ no melting up to 1590°C |
| 149 | 37.2 | 52.3 | 10.5 | γ |
| 57 | 27.8 | 37.2 | 35 | β |
| 107 | 33.9 | 44.2 | 21.9 | σ |
| 108 | 28.4 | 43.6 | 28 | γ |
| 109 | 25.5 | 49.4 | 25.1 | γ |
| 49 | 10.5 | 54 | 35.5 | γ melting at ~1462 |
| 9 | 18 | 52 | 30 | γ melting at ~1470 |
| 35 | 20 | 53 | 27 | γ melting at ~1500 |
| 46 | 5 | 64 | 31 | |
| 52 | 5.1 | 68.0 | 26.9 | |
| 53 | 5 | 71.1 | 23.9 | η |
| 60 | 2.2 | 68.3 | 29.5 | |
| 143 | 68 | 30 | 2 | δ |
| 146 | 61 | 32 | 7 | δ |

Table XII
Estimated Invariant Equilibria





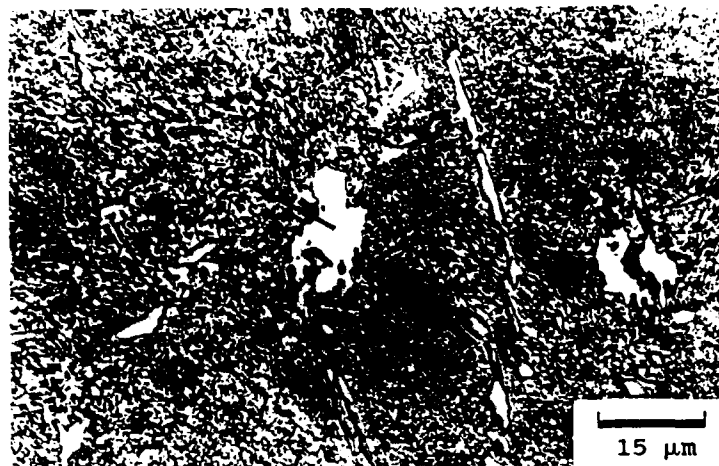


Figure 18 Photomicrograph of sample 141 (as cast) showing the primary phase of solidification σ .

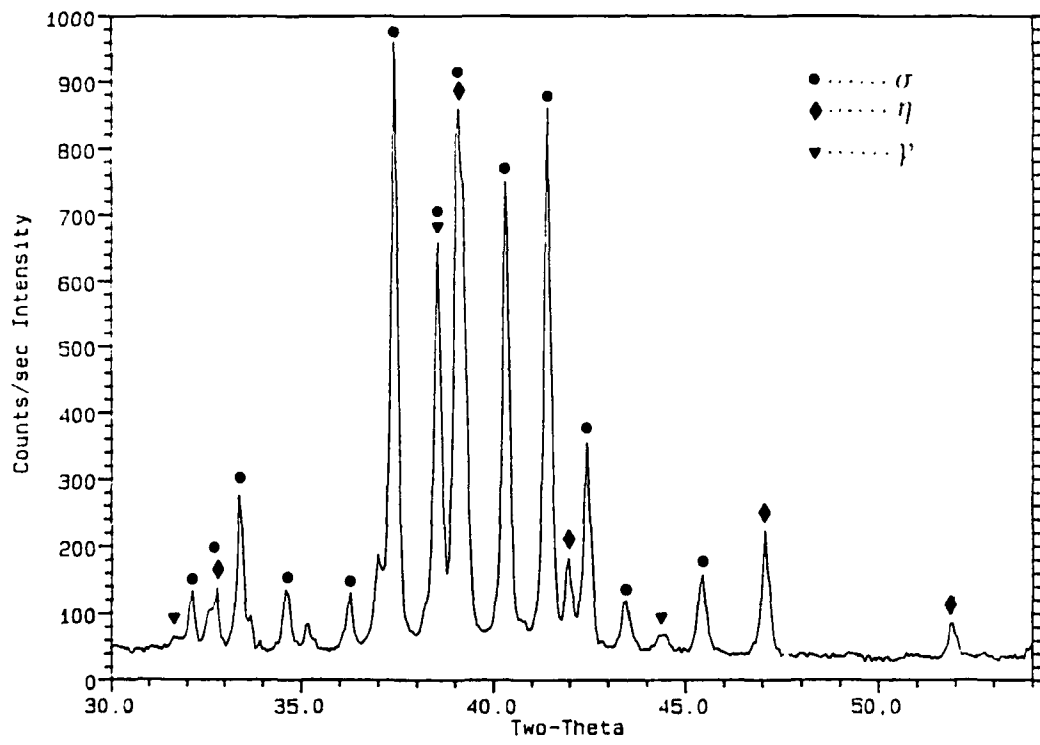


Figure 19 X-ray diffraction pattern of 141 (as cast), characteristic major peaks are identified.



Figure 20 Photomicrograph of sample 63 (as cast), showing cellular dendrites of primary γ .

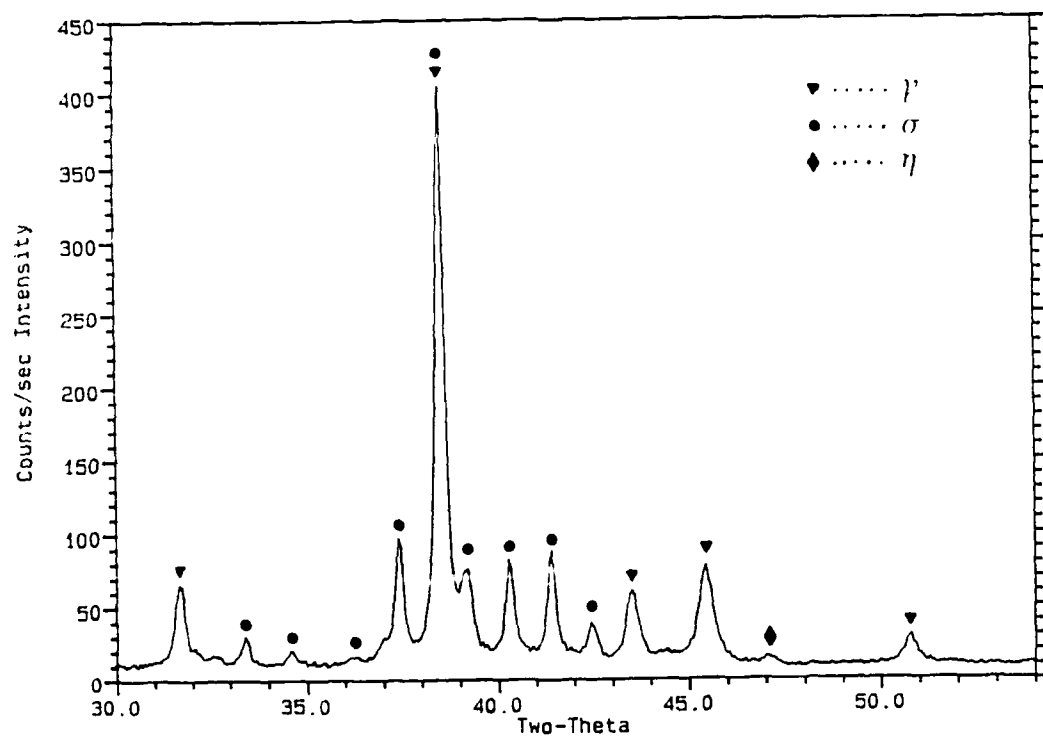


Figure 21 X-ray diffraction pattern of sample 63 (as cast), characteristic major peaks are indicated.

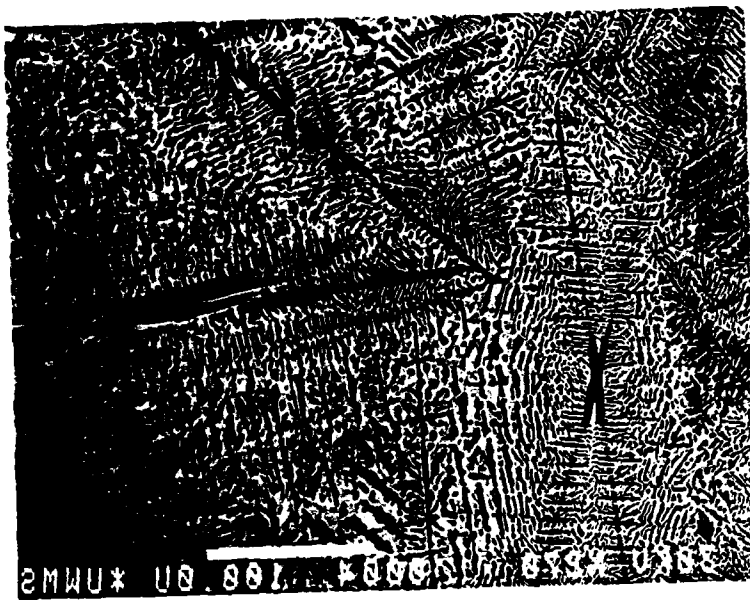


Figure 22 Photomicrograph of sample 5 (as cast), showing η dendrites and an η - σ eutectic like "matrix".

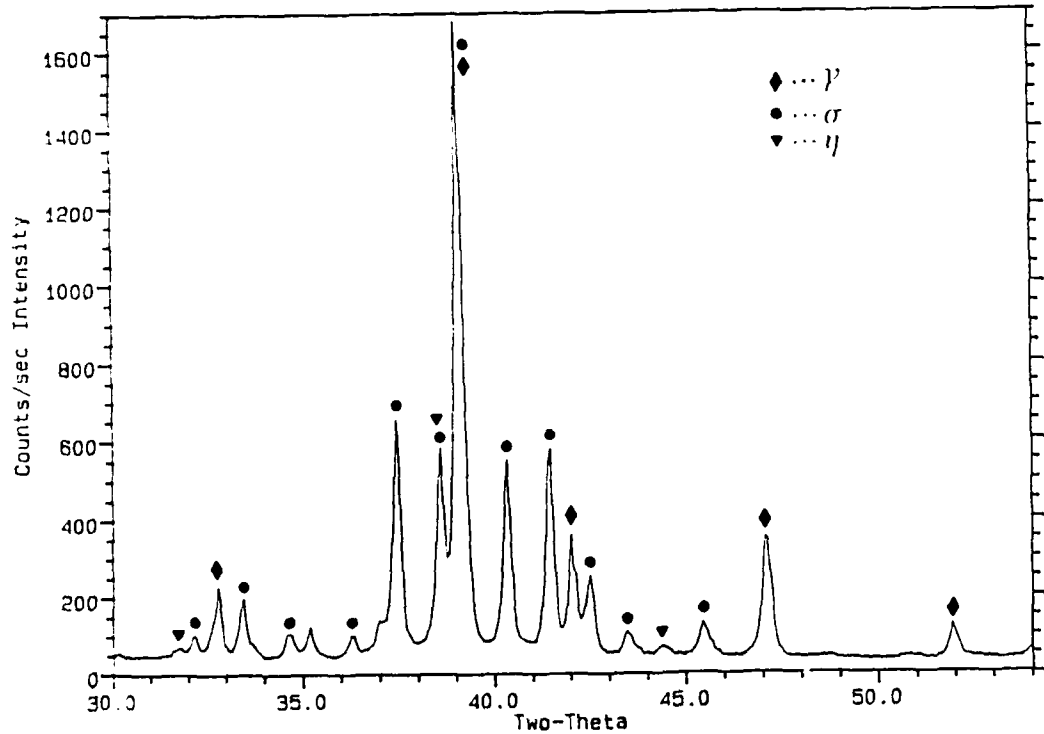
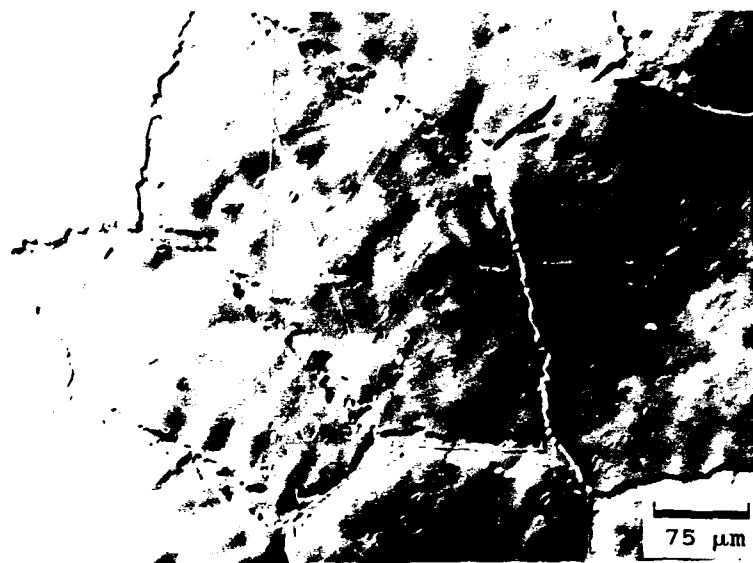


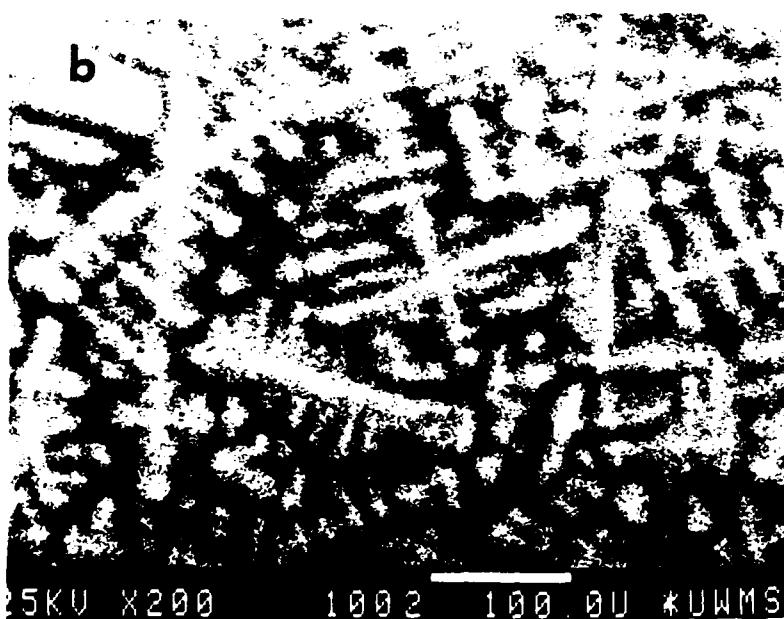
Figure 23 X-ray diffraction pattern of sample 5 (as cast), characteristic, major peaks are indicated.



Figure 24 Photomicrograph of sample 57 (as cast) showing the characteristic equiaxed β microstructure in as cast samples.



a) As-arc melted



b) SEM micrographs imaged with BSEI.

Figure 25 Nb₅₄Ti₂₃Al₂₃ As-cast

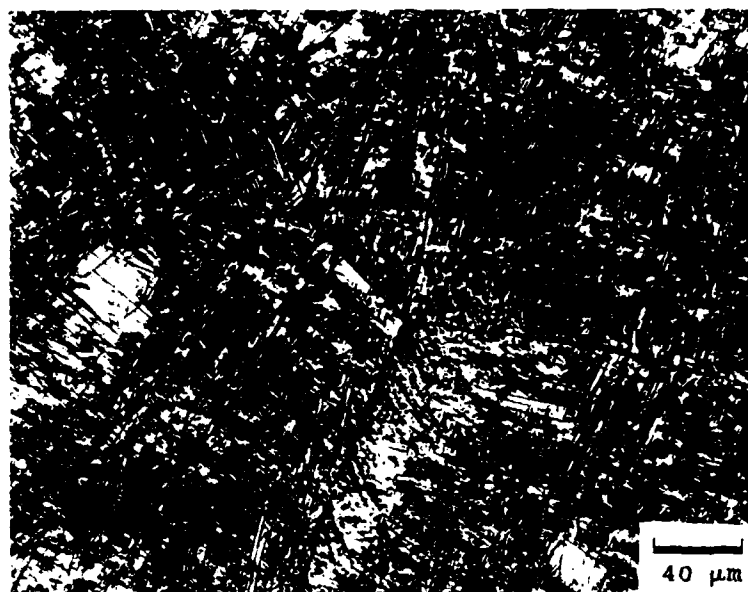


Figure 26 Decomposition of the β phase into needle-like morphology in the as-cast sample 33.

1200°C Isothermal Section of the Ti-Al-Nb system

Progressing into the ternary system from the η phase (See Figure 27) the first multiphase region encountered is the $\gamma-\eta$ two phase field. The tie lines in this region have been established from EPMA of samples 6, 8 and 42 (See Table XIII). Differentiation between the two phases can be made by optical microscopy using plane polarized light. This is possible due to the more intense interaction of polarized light with the η phase as compared to the γ phase. X-ray diffraction confirms the existence of only two phases, the η and γ phases. The sluggish diffusivity of the η phase in this region results in the retention of some metastable γ phase during solidification in alloys that should be single phase η . Although the γ phase eventually decomposes to the η phase, evidence of the solidification segregation is still evident in the morphology of the η phase (See Figure 28), even after annealing in excess of 2 weeks at 1200°C. Similar behavior is observed for sample 55 (See Figures 29 and 30).

The γ phase has been determined to have an extensive range of solubility, about 30 at.% along the 50 at.% Al direction. Further, lattice parameters calculated from X-ray diffraction show an increase of about 0.7% in the c/a ration with niobium additions along the 50 at.% Al composition line and a decrease of about 0.3% in the c/a ratio across the width of the γ phase field with decreasing aluminum content.

The $\gamma-\sigma-\eta$ tie triangle has been determined from sample 37 (See Figure 31) which consists of a γ matrix with σ and η

precipitates. The identities of the phases were established by X-ray diffraction (see Figure 32) and composition information was obtained for the γ and σ using EPMA (Table XIII). Due to the small size of the η precipitates, the composition of the third point of the tie-triangle was estimated based on near by binary tie lines from the η - σ two phase field (sample 5) and the η - γ two phase field (sample 6).

The solubility of the σ phase has been determined to extend about 30 at.% Ti into the ternary system along the 35 at.% Al compositional line. The width of the σ phase has been found to be about 10 at.%, varying from about 30 at.% Al to 40 at.% Al. The solubility limit along the γ - σ two phase field has been set in part by samples 10 and 11 (See Figure 27). The maximum solubility of Ti in the σ phase is set by the σ - γ -B2 tie triangle. The compositions of the tie-triangle σ - γ -B2 was determined by EPMA of sample 162 (See Figure 33). EPMA of the phase with the decomposed microstructure showed the composition to be that of B2 as shown in Figure 27, while X-ray diffraction indicated the B2 phase decomposed into the γ and α_2 phases upon cooling (See Figure 34).

The tie-lines for the σ -B2 two phase region have been determined from samples 12, 56 and 170. Sample 170 (See Figures 35 and 36) reveals σ precipitates in a matrix of transformed B2. The precipitates were fractured during metallographic sample preparation as a result of the brittleness of this phase. The basket-weave or tweed-like structure of the transformed B2 phase is typical of most alloys found in the regions between the σ - δ - β

and σ - γ -B2 tie-triangles and extending up into the regions of primary β and B2 phase fields.

The σ - δ - β tie-triangle has been determined from sample 4. The BSEI photograph (See Figure 37) clearly indicates the presence of three phases. The region of lightest shading contained the greatest amount of Nb and can therefore be identified as the δ phase. Likewise similar assignments can be made for the other regions based in their Nb content. X-ray diffraction of this sample confirms the presence of the δ and σ phases (see Figure 38). However, due to the low volume fraction of the β phase and the overlapping of the primary β peaks with σ and δ peaks, the X-ray diffraction pattern of the β phase is not observed.

Table XIII

| Sample ID | Bulk Alloy Composition | | | Phases Present | Phase composition | | |
|-----------|------------------------|------|------|---------------------------------|----------------------|----------------------|----------------------|
| | Al | Nb | Ti | | Al | Nb | Ti |
| 8 | 62 | 16 | 22 | γ η | 57.9 70 | 14 17 | 28.1 13 |
| 6 | 61 | 23 | 16 | γ η | 54.5 70.7 | 23.3 23.6 | 22.2 5.7 |
| 37 | 53 | 31.7 | 15.3 | γ η σ | 49.3 72 39.1 | 28 24 49 | 22.7 4 11.9 |
| 5 | 57 | 36 | 7 | σ η | 72.5 40.6 | 24.1 49.6 | 3.4 9.8 |
| 11 | 42 | 30 | 28 | γ σ | 45.5 34 | 20 40.8 | 34.5 25.2 |
| 162 | 41.5 | 21 | 37.5 | γ σ B2 | 45.5 34.5 -- | 17 35.4 -- | 37.5 30.1 -- |
| 12 | 27.5 | 35 | 37.5 | σ B2 | 30.0 24.6 | 43.5 33.0 | 26.5 42.4 |
| 56 | 30.7 | 40.8 | 29 | σ B2 | 29.7 22.3 | 43.5 33.6 | 26.7 44.1 |
| 170 | 30.2 | 40.1 | 29.7 | σ B2 | 29.5 24.6 | 43.4 32.3 | 27.1 43.1 |
| 4 | 25 | 50 | 25 | σ δ β | 28.4 20.5 19.5 | 48.5 55.7 47.2 | 23.1 23.8 33.3 |
| 50 | 50 | 12 | 38 | γ T ₂ | 49.0 44.0 | 12.8 13.1 | 38.2 42.9 |
| 15 | 37 | 10 | 53 | α_2 T ₂ | 34.5 45.6 | 9.5 7.4 | 56 47 |
| 33 | 39.1 | 14 | 46.9 | B2 T ₂ | 38 43.5 | 17.5 12 | 45.5 43.5 |
| 36 | 33 | 17 | 50 | α_2 B2 | 30.7 32.5 | 12.2 19.7 | 57.1 47.8 |
| 10 | 47 | 30 | 23 | σ γ | 36.8 48.9 | 44.5 24.0 | 18.7 27.1 |
| 55 | 59 | 15 | 26 | γ - | 58 -- | 14 -- | 28 -- |

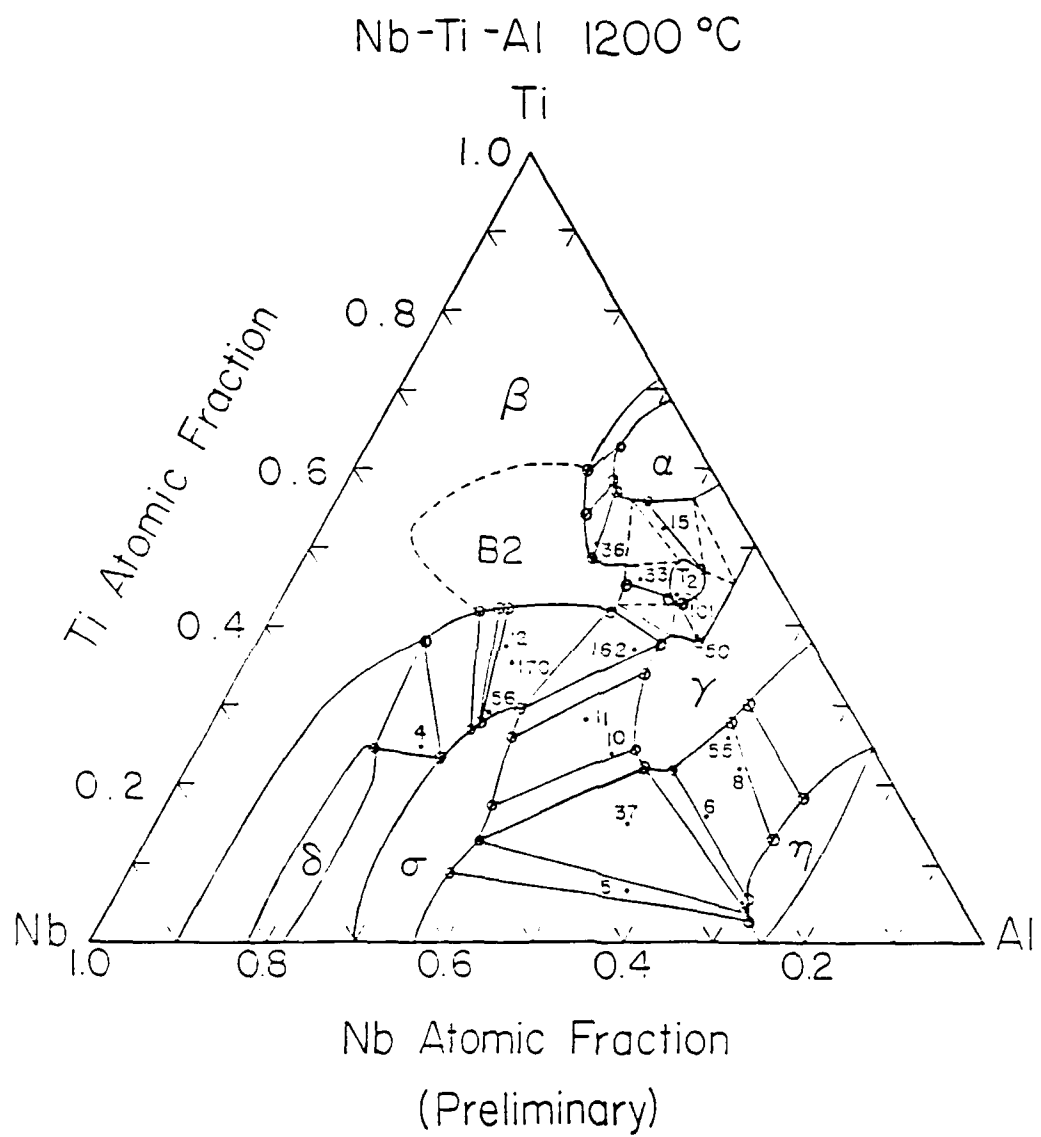


Figure 27 1200 °C isothermal section of the Nb-Ti-Al ternary system with the compositions of the samples from Table XIII plotted.



Figure 28 Photomicrograph of the sample 8 showing the dendritic morphology is retained after annealing at 1200°C for 16 days.



Figure 29 Photomicrograph of sample 55 annealed 8 days at 1200°C showing the decomposition of the γ dendrites into η plates in a γ matrix.

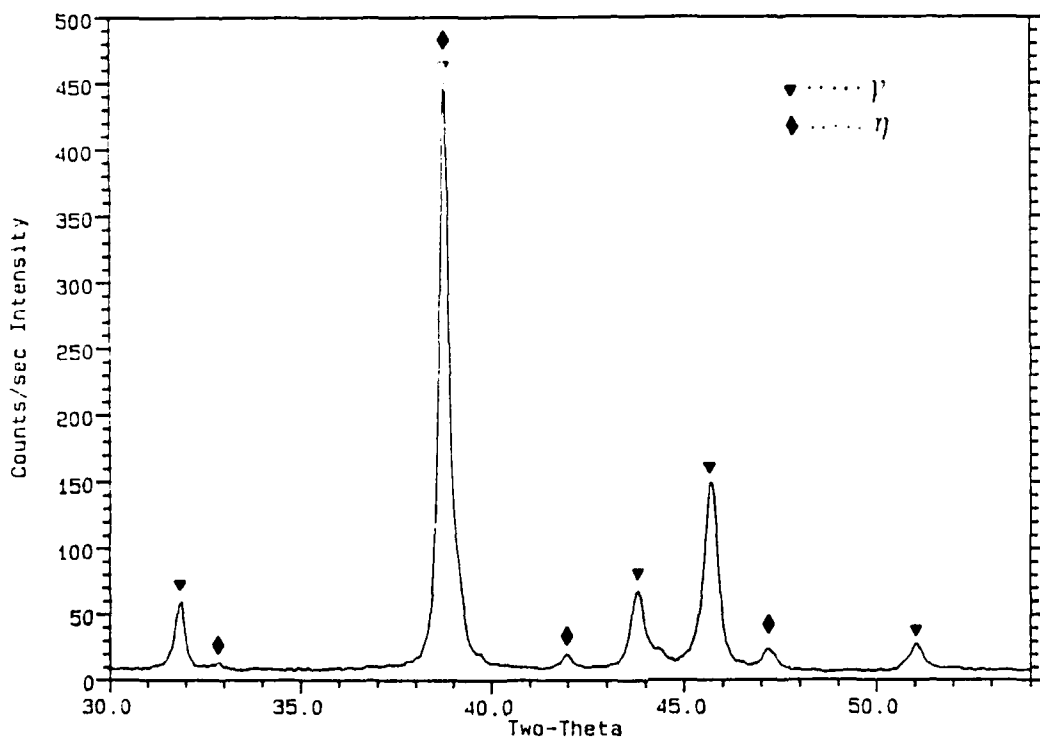


Figure 30 X-ray Diffraction of sample 55, annealed 8 days at 1200°C.

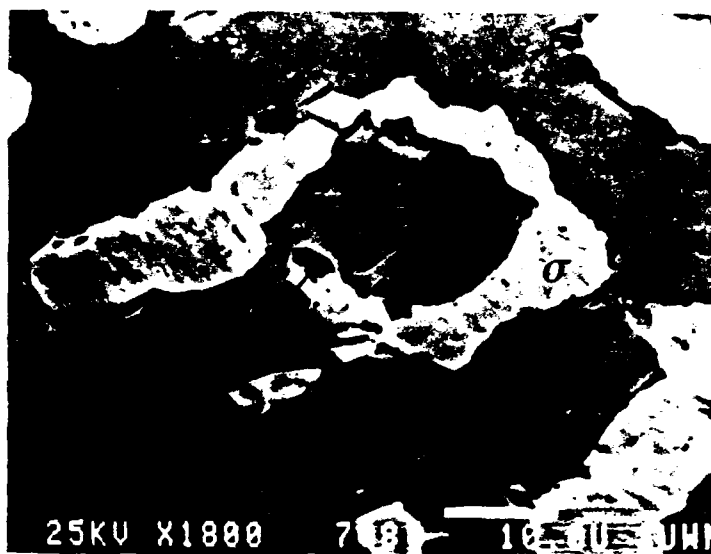


Figure 31 Photomicrograph of sample 37, annealed at 1200°C for 14 days, showing three phase mixtures of the σ , γ and η phases.

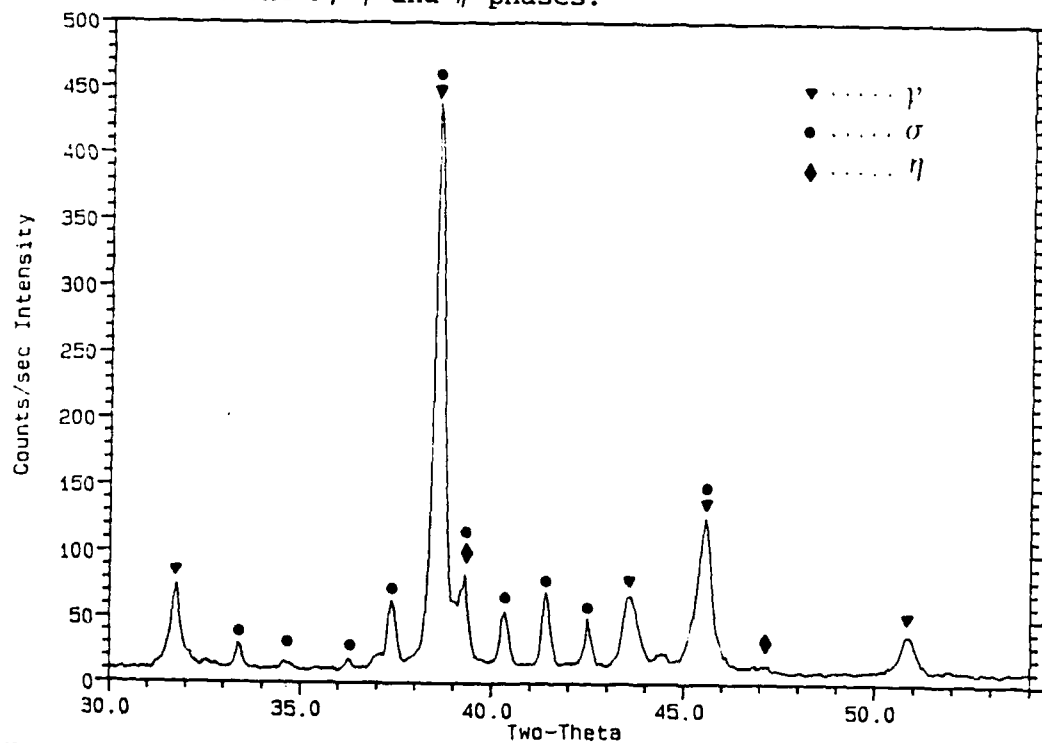


Figure 32 X-ray diffraction of sample 37, annealed for 14 days at 1200°C, characteristic σ , γ and η peaks are labeled.



Figure 33 Photomicrograph of sample 162, annealed at 1200°C for 7 days, showing a three phase mixture of the σ , γ and decomposed B2 phase.

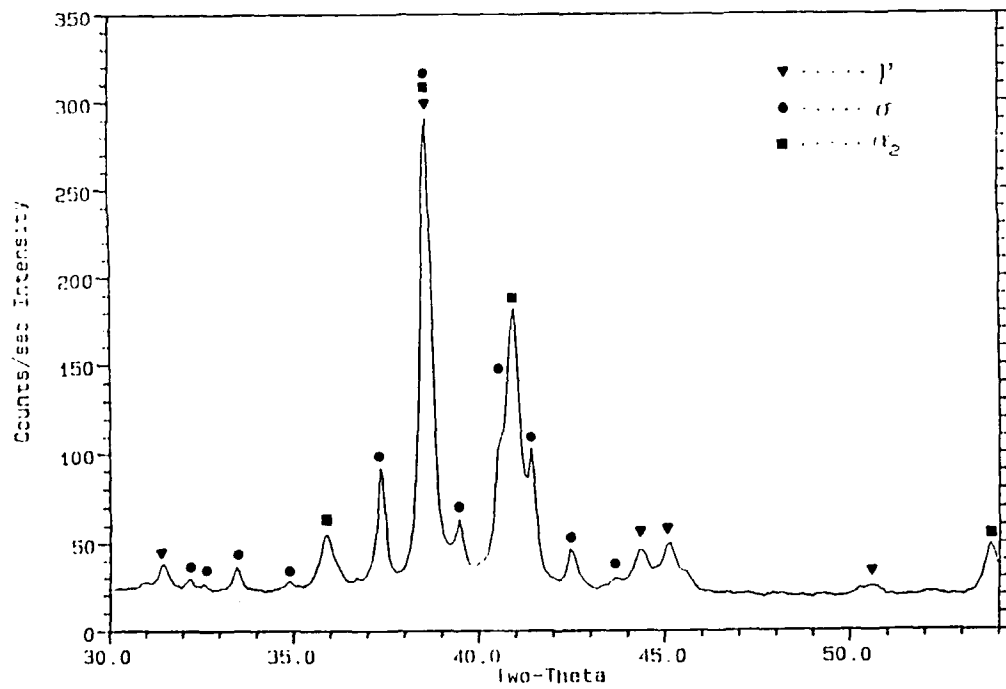


Figure 34 X-ray diffraction pattern of sample 162, annealed at 1200°C for 7 days with characteristic σ and γ peaks identified and the 100% peak of the as yet unidentified decomposition product from the B2 phase.



Figure 35 Photomicrograph of sample 170, annealed at 1200°C for 7 days, showing a mixture of the γ and B2 phases.

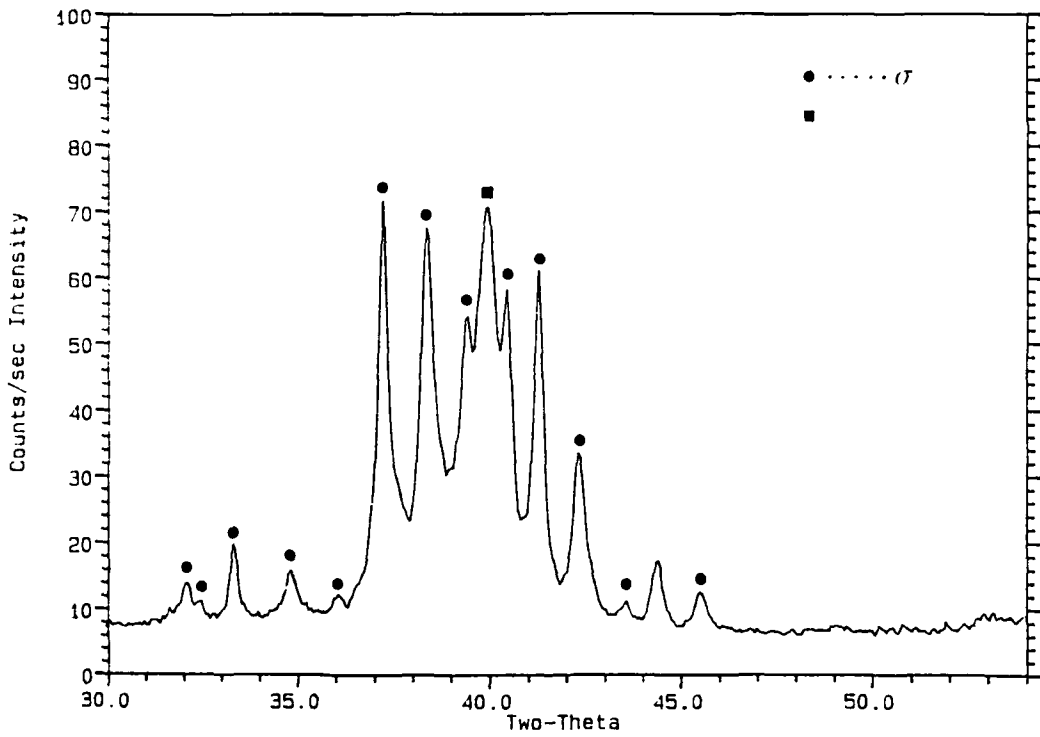
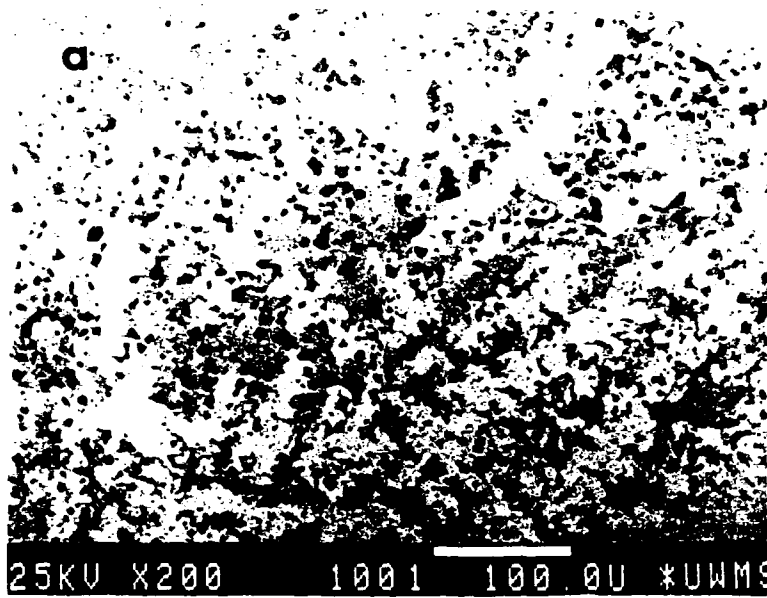
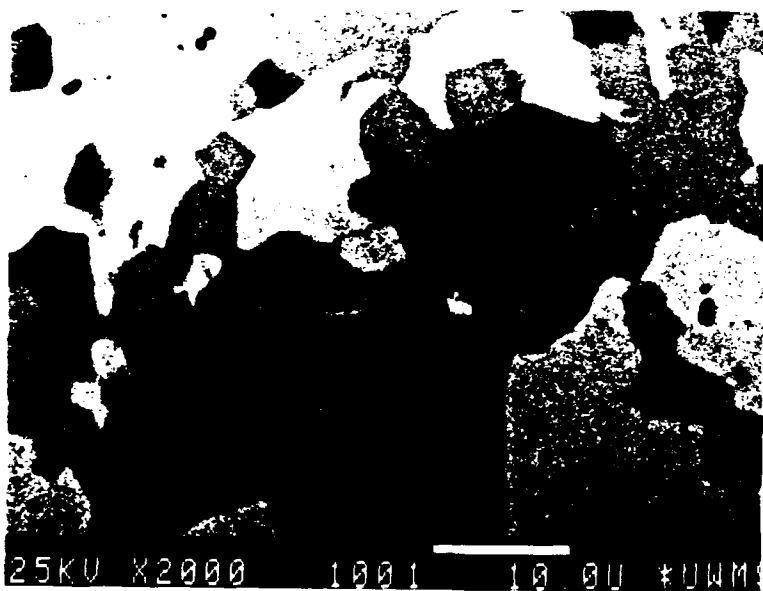


Figure 36 X-ray diffraction pattern of sample 170, annealed at 1200°C for 7 days.



a)



b)

Figure 37 BSEI image of sample 4, annealed at 1200°C for 16 days

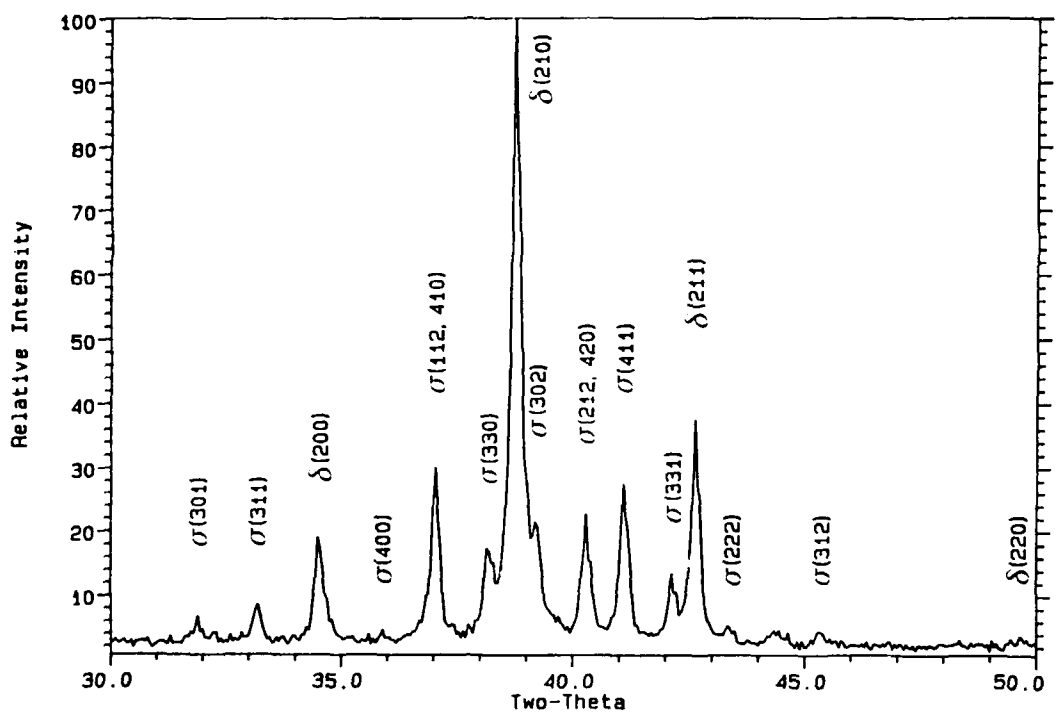


Figure 38 X-ray Diffraction scan of Sample 4,
annealed at 1200°C for 16 days.

Investigation of T₁ and T₂

In the central region of the isothermal section at 1200°C, a previous report indicated the presence of two ternary single phase regions that were labeled T₁ near Ti₄₅Al₃₅Nb₂₀ and T₂ near Ti₄₅Al₄₅Nb₁₀ [Jew89]. The evidence that supported the existence of T₁ and T₂ at 1200°C was based mainly upon EPMA analysis of several well-annealed bulk ingots and the presence of a ternary single phase layer in a diffusion couple between pure Nb and a binary γ phase alloy as the measured diffusion path passed through the T₁ phase region. The definition of the phase boundary for the T₂ region was established by the tie lines for different two phase mixtures such as α -T₂ from alloy 15, γ -T₂ from alloy 50 and T₁-T₂ from alloy 33. For example, the micrograph in Figure 39 for an Ti₄₆Al₃₉Nb₁₅ alloy after an anneal at 1200 °C for two weeks illustrates the morphology of the T₁-T₂ two-phase mixture. However, in the previous report no detailed information on the phase relations between the T₁ phase and the β phase was available.

In the present work the tie line for the two-phase mixture in alloy 33 has been confirmed, new tie line relations between the α phase and the β field and between the σ phase and the β field have been established and a three phase equilibrium between σ - γ -T₁ (i.e. σ - γ -B₂ in Figure 27) has been determined at 1200°C. As noted previously the alloys with compositions in the central region of the phase diagram undergo various solid state reactions upon cooling so that the resulting phases and microstructures appear to be sensitive to cooling rate. Under

these conditions complete identification of the structures of the ternary phases by XRD is difficult. Therefore, transmission electron microscopy (TEM) was employed to evaluate the structural identity of the phases present in alloys 15, 33, 36, 50 and 101.

Evidence for the existence of an ordered bcc phase is found in alloy 36. The microstructure of alloy 36, shown in Figure 40, is composed of clear grains and grains containing a high density of fine precipitates. The clear grains are identified by selected area diffraction (SAD) as the α_2 phase. Energy dispersive x-ray (EDX) in the TEM yields an average composition of $Ti_{59}Al_{30}Nb_{11}$ for the α_2 phase in this material while EMPA of the bulk ingot yields an α_2 composition of $Ti_{57}Al_{31}Nb_{12}$. The precipitate-bearing grains were identified by SAD and by convergent beam electron diffraction (CBED) as having the B_2 structure, while the precipitates were identified by SAD as having the $B8_2$ structure. The $B8_2$ phase is one of several decomposition products of the B_2 phase [Str88] [Ban88]. EDX of the $B_2/B8_2$ grains yields a composition of $Ti_{56}Al_{28}Nb_{16}$ while EMPA yields $Ti_{48}Al_{33}Nb_{19}$. The presence of precipitates in B_2 indicates that some transformation has occurred during cooling of the alloy after withdrawal from the annealing furnace. Therefore, it is possible that the B_2 phase may also be a decomposition product of a disordered bcc phase that existed at 1200°C. However, no evidence of antiphase domains is found in the B_2 grains.

The high temperature form of T_2 at 1200°C also appears

to be the bcc-type structure. The initial boundary of the T_2 phase was defined by tie lines, based on EMPA, of three alloys, $Ti_{53}Al_{37}Nb_{10}$ (alloy 15), $Ti_{46}Al_{39}Nb_{15}$ (alloy 33), and $Ti_{38}Al_{50}Nb_{12}$ (alloy 50). Examination of alloy 50 reveals large γ grains, occasionally separated by narrow regions composed of alternating α_2 and γ lathes. These lathes have a distinct orientation relationship, $(0001) \alpha_2 || \{111\}\gamma$ and $\langle1120\rangle\alpha_2 || \langle110\rangle\gamma$. This structure is common in binary alloys with a composition in the two-phase region between γ and α_2 [Bla69]. The microstructure of alloy 15, shown in Figure 41, is composed of two phases. One phase in alloy 15 appears smooth and clear. Based on SAD and CBED, this is the α_2 phase, $Ti_{56}Al_{34}Nb_{10}$ by EMPA and $Ti_{61}Al_{37}Nb_{11}$ by EDX. Figure 41a shows that the second phase, corresponding to T_2 , has decomposed during cooling. The decomposition structure, fig. 41b, is made up of alternating lamella. The clear lamella are identified as α_2 while the spotted lamella are identified as the B_2 parent and $B8_2$ precipitate structure.

The evidence from alloy 15 indicates that the T_2 phase present at $1200^\circ C$ undergoes rapid and complex transformation during both rapid and slow cooling. To address this problem, an alloy 101, in the center of the T_2 phase field was examined and the microstructure of this alloy, is shown in Figure 42. The Alloy 101 is composed primarily of large grains filled with unidirectional lathes. These lathes, Figure 43a, represent an alternating α_2 and γ (or γ_{TWIN}) structure which are found in alloys 101 and 50. The characteristic diffraction pattern is

shown in Figure 43b. Alloy 101 also contains a small volume fraction of γ grains (upper left corner of Figure 43a).

In order to determine whether the α_2/γ lathe structure reflects very slow kinetics for equilibration during annealing or rapid decomposition during cooling, a slice of ingot 101 coated with Y_2O_3 , was encapsulated in an evacuated quartz tube and subject to an annealing and quenching treatment. The alloy was annealed at $1000^{\circ}C$ for one hour, then annealed at $1200^{\circ}C$ for 20 minutes. The sample was then water quenched (and the quartz broken). The optical microstructure of this quenched material, alloy 101Q, is shown in Figure 42b. The major difference between alloys 101, Figure 42a, and 101Q, Figure 42b, is the presence of a few clear, blocky regions inside the lathe-filled grains of the quenched material. A TEM image of 101Q, Figure 44, also shows small clear regions in this interior of the lathe-filled grains. SAD and CBED were used to identify these regions as B_2 . Regions a, c-f in Figure 44a have the same orientation. This indicates that either each region nucleated independently with the same orientation during annealing or that the B_2 regions are remnants of the same parent that existed at higher temperatures. The latter explanation is more likely based upon diffusion analysis. The lathe structure diffraction pattern is the same as that from other lathe-containing alloys (i.e. α_2 and γ). However, when the B_2 regions are included in the selected area, the diffraction pattern of Figure 45 is obtained. This pattern shows a definite orientation between the B_2 and the lathe structure, given by $(0001)\alpha_2||\{110\}B_2$ and $\langle 1120 \rangle\alpha_2||\langle 111 \rangle B_2$. It should be noted that

a small volume fraction of γ grains also exists in alloy 101Q.

The EDX results on the B_2 remnants yield a composition of $Ti_{48}Al_{38}Nb_{14}$. EDX results were also obtained from the lathes in alloys 50 and 101Q by aligning the α_2/γ interface parallel to the electron beam. A few consecutive series of lathes in different regions were probed for an identical time. The results on lathes of the same type in a material always fell within a spread of ± 2 atomic percent. The γ lathes have a composition of $Ti_{38}Al_{49}Nb_{13}$ in alloy 50 and $Ti_{41}Al_{48}Nb_{11}$ in alloy 101Q. This is very near the single phase γ boundary in the ternary system, $\sim Ti_{37}Al_{50}Nb_{13}$. However, the α_2 lathes have a composition of $Ti_{47}Al_{41}Nb_{12}$ in alloy 50 and $Ti_{47}Al_{42}Nb_{11}$ in alloy 101Q. This is very different from the single phase α_2 boundary, $\sim Ti_{56}Al_{35}Nb_9$, which indicates that the α_2 lathes formed during cooling. This also is consistent with the rapid decomposition of the T_2 phase to the lath structure in alloy 101 and 50 and that T_2 is bcc-type at 1200°C. Antiphase domains have not been found in the B_2 phase which may indicate that the B_2 structure is stable at 1200°C or that it forms from a disordered phase during quenching and displays very rapid antiphase coarsening. Based upon the combined evidence from alloys 15, 50, 101 and other observations, it appears most likely that the T_2 phase is a B_2 structure at 1200°C.

Although the additional tie-line information and the new structural information available from TEM examination has resulted in a considerable clarification of the central region of the 1200°C isothermal section, there are several remaining

questions to be resolved and are under current study. For example, the current results indicate that the T_1 phase has a B2 structure. The approximate boundary between the β and B2 fields has been sketched in Figure 27 as a dashed curve which is preliminary, but is consistent with the relationships suggested by Boettigner and Bendersky at 1100°C and 1400°C [Ben]. Moreover, based on the tie line from the well developed two-phase microstructure in alloy 33, the T_2 phase field appears to be a separate isolated region. However, since the structure of T_2 also appears to be a bcc-type and is likely to have B2 order, the isothermal section at 1200°C contains two bcc-type phase fields. The relative thermodynamic competition between the α , γ and B2 phases allows for the possibility of two bcc-type phase fields. This feature is under continued study. In addition, the TEM observations indicate that the decomposition of the T_2 phase is sensitive to composition and the presence of other phases (i.e. γ or α) as well as cooling rate. As a result, there are a number of reaction pathways that can be examined for controlled microstructure variations.

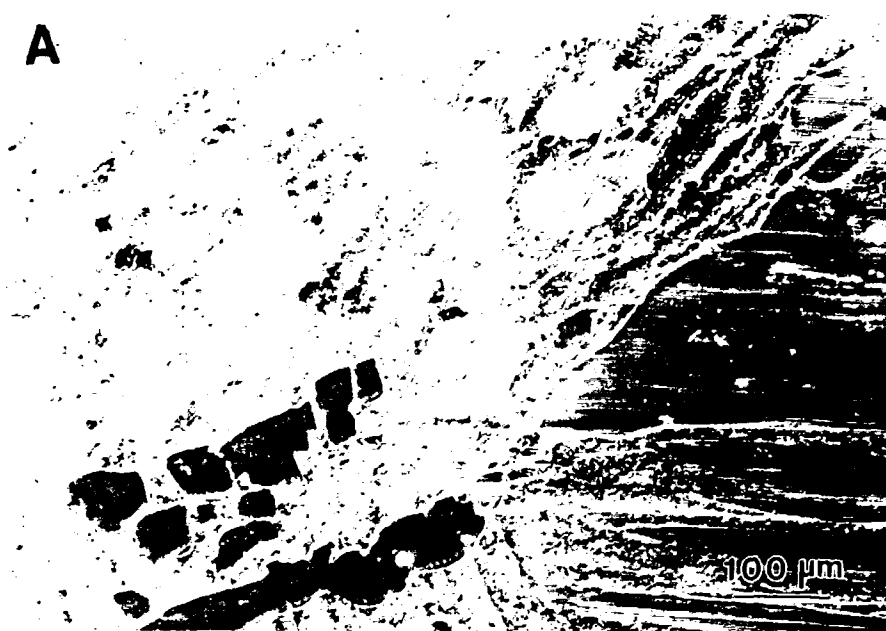


Figure 39 Photomicrograph of alloy 33 annealed at 1200°C
for 14 days

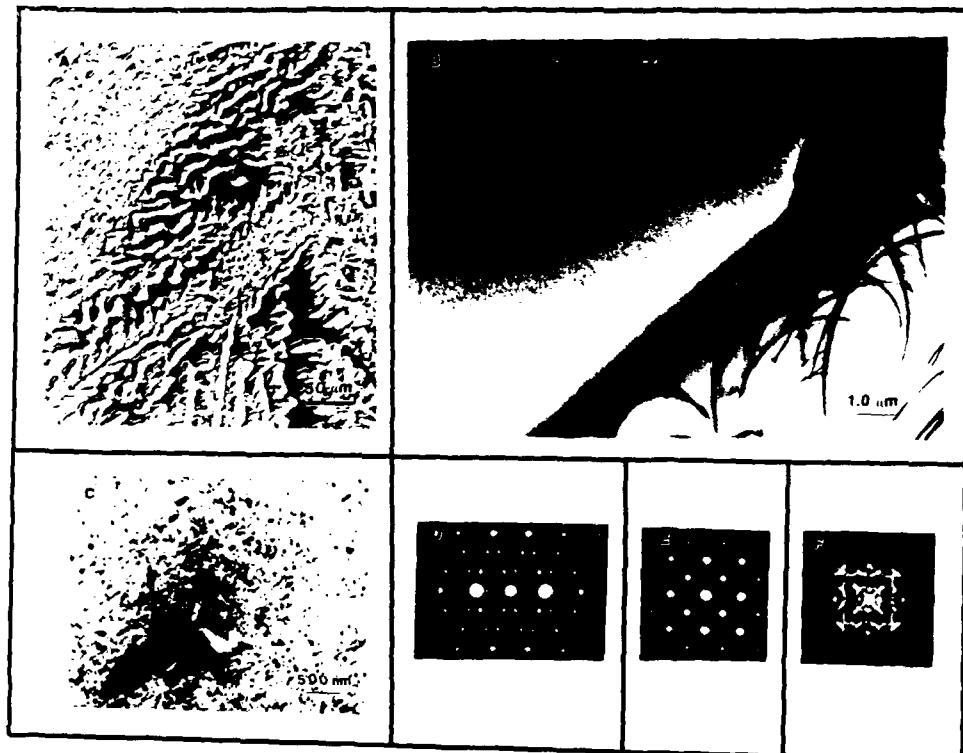


Figure 40

Structure of alloy 36

- a. Optical micrograph
- b. TEM micrograph
- c. Enlargement of precipitate-bearing grain in B.
- d. SAD pattern from c) showing [210] B2 zone with superimposed B8₂ spots.
- e. [100] B2 zone.
- f. CBED pattern showing 4m symmetry.

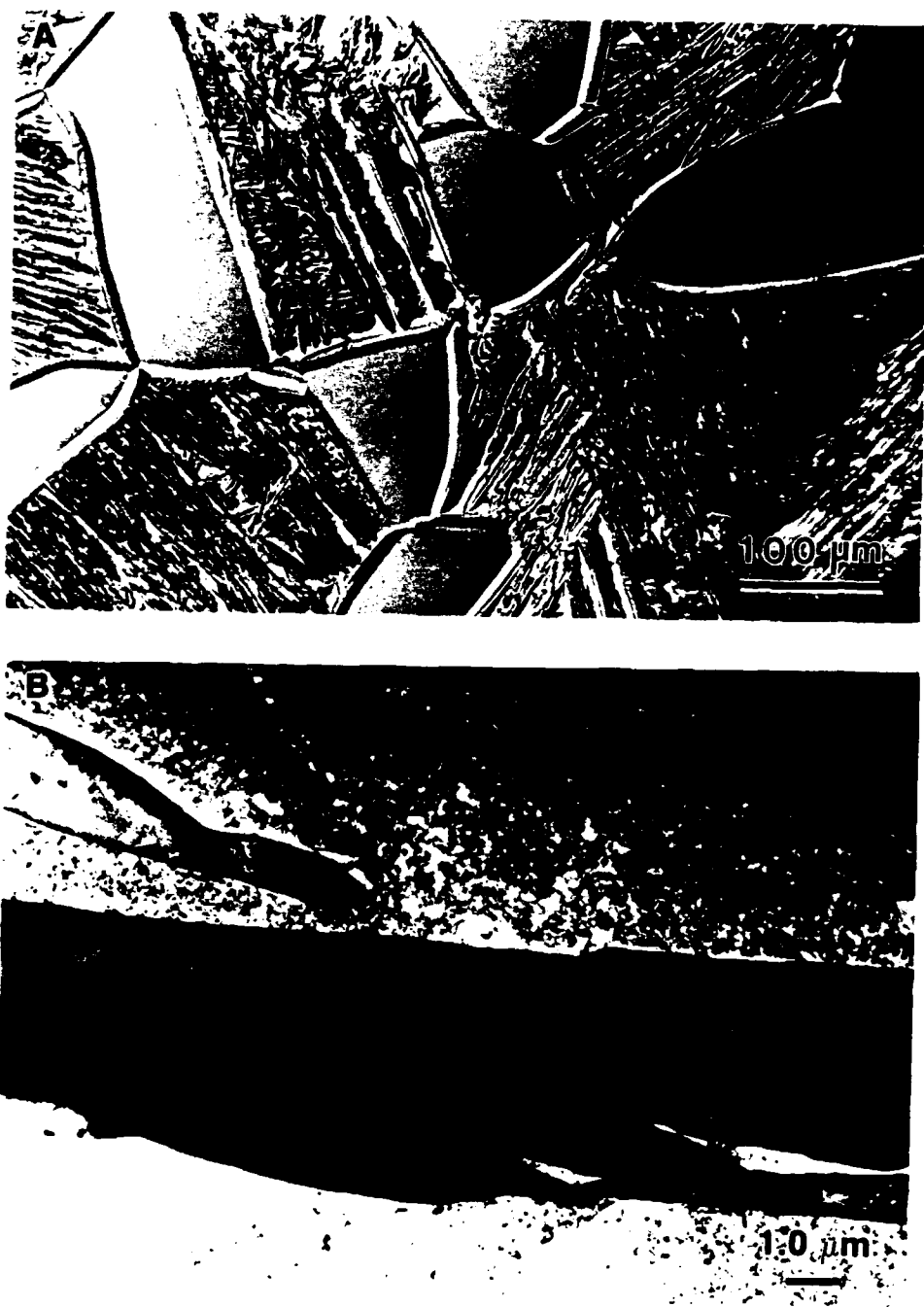


Figure 41 Structure in alloy 15
a. Optical micrograph
b. TEM micrograph of unsmooth grains in A.

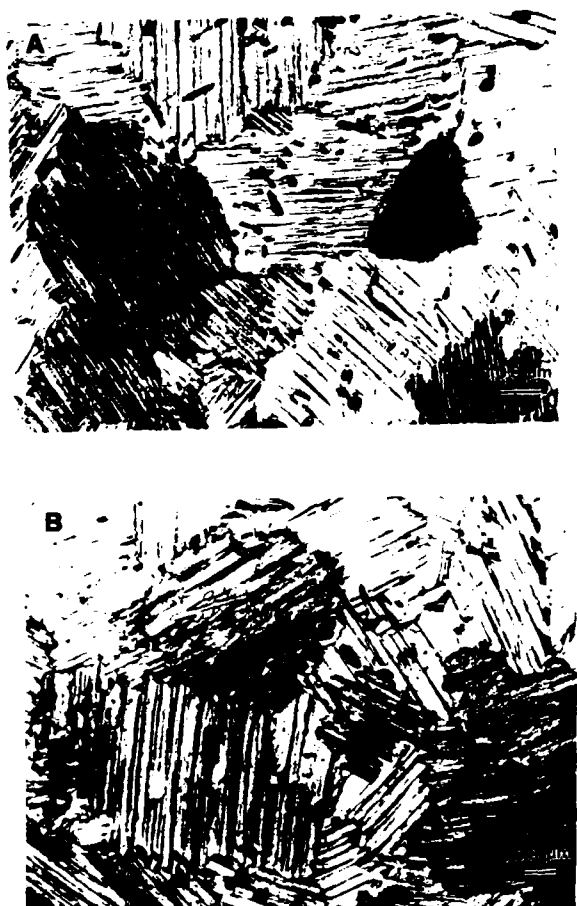


Figure 42 Optical micrograph of alloy 101 after
a. Slow cooling
b. Quenching

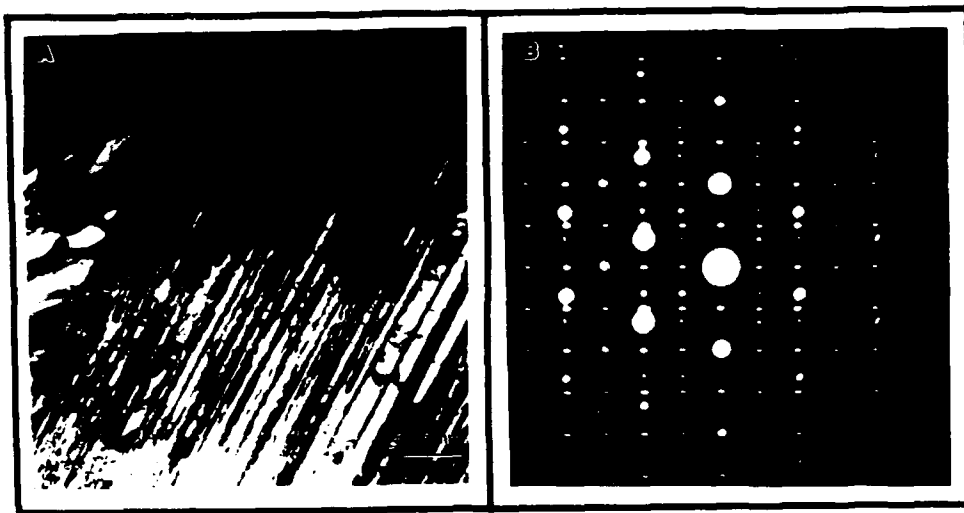


Figure 43 Lathe structure of alloy 101
a. TEM micrograph showing α_2/γ lathe structure
abutting a γ grain (upper left corner).
b. SAD pattern of α_2/γ lathe structure.



Figure 44

B2 phase in alloy 101

- a. TEM micrograph of 101 quenched. Regions a through g are B2.
- b. SAD.
- c. CBED of [111] B2 zone.
- d. SAD pattern of [100] B2 zone
- e. CBED pattern of [111] B2 zone

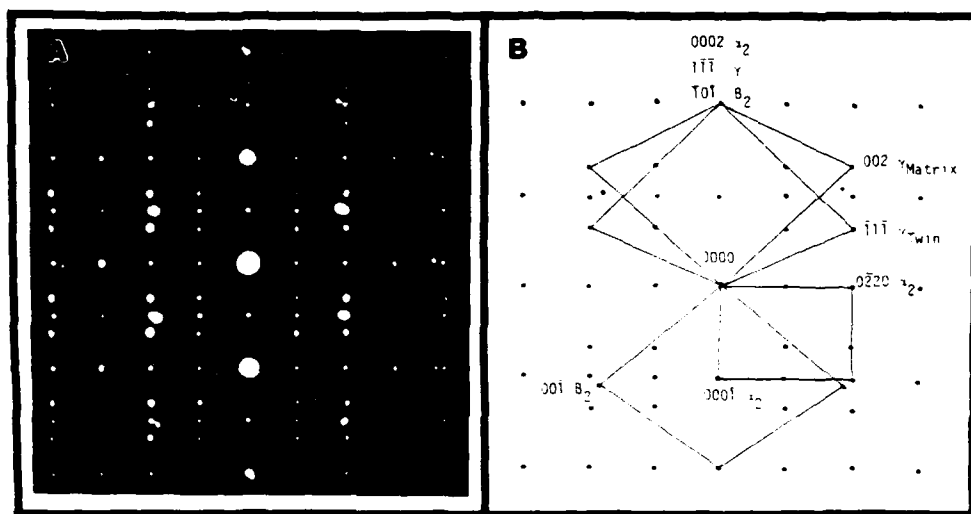


Figure 45 Structure Relationship of B2 to α_2 and γ
a. SAD pattern of α_2/γ lathe structure
and B2 grain.
b. Schematic of A. Showing [1120] α_2 , [110]
 γ , [110] γ_{TWIN} and [111] B2 zones superimposed.

Al₃Ti-Al₃Nb Pseudobinary System

A series of alloys with constant aluminum content were selected to investigate the phase equilibria of Al₃Ti-Al₃Nb pseudobinary system, (see Figure 46 and Table XIV). X-ray diffraction, optical microscopy and differential thermal analysis (DTA) have been used to determine the phase equilibria.

Similar X-ray diffraction patterns were obtained for the as-cast alloys. A representative X-ray trace is shown in Figure 47. Since Al₃Ti and Al₃Nb have identical crystal structures (D0₂₂, tetragonal) and nearly identical lattice parameters, the X-ray diffraction data suggests that the Al₃Ti-Al₃Nb pseudobinary alloys may form an isomorphous solid solution.

As-cast Al₃Ti showed some segregation or second phase (not identified) along the cell boundaries. Annealing of this alloy at 1200°C for 144 hours homogenized it completely. As-cast alloys with 2.5 to 10 at.% Nb showed dendritic segregation and required longer annealing times for homogenization at 1200°C. In some cases, even 492 hours of annealing did not homogenize these alloys completely. Figure 48 shows the as-cast and annealed microstructure of the alloy Nb₅Al₇₅Ti₂₀ (144 hours, 1200°C). The dendritic segregation seen in this alloy still existed even after 492 hours of annealing. Chemical analysis of some of the annealed alloys indicated an oxygen content less than 200 ppm, and Ti, Al and Nb contents close to the intended compositions. The dark areas in the annealed microstructure is the porosity which developed during annealing. As-cast alloys with 12.5 to 25 at.% Nb exhibited a cellular solidification morphology. After

annealing at 1200°C alloys in this range were completely homogenized. Interestingly the alloys with the higher Nb contents and higher solidus temperatures (as determined by DTA), required shorter homogenization times than those alloys with the lower Nb contents and lower solidus temperatures. This behavior is most likely due to the difference in the extent of solidification segregation in the as-cast alloys. One possible explanation for the development of dendritic segregation in the alloys on the Al₃Ti side and cellular-type microstructures in the alloys on Al₃Nb side could be the existence of a congruent melting point closer toward the Al₃Nb side.

If the Al₃Ti-Al₃Nb pseudobinary system forms a solid solution, then the solidus and liquidus temperatures should increase with increasing Nb content in Al₃Ti, since Al₃Nb has higher melting point. The Al₃Ti alloy showed a sharp melting signal at 1396°C. This is considerably higher than the value reported in the previous studies [Mis89]. Annealed Al₃Ti showed melting occurred at 1399°C, with a split endotherm due to peritectic melting i.e. ($\eta \rightarrow \epsilon + L$; ϵ is the high temperature Al₂₃T₁₉ phase). With an increase in the Nb content of the alloys the separation between the solidus and liquidus increased which would be expected for alloys that form solid solutions. The solidus and liquidus temperatures of the 2.5 at.% alloy were found to be 1400°C and 1461°C, respectively. Above 10 at.% Nb, the liquidus temperatures could not be measured. The DTA data obtained from these alloys is given in Figure 49 along with the estimated solidus and liquidus boundaries which indicate the development of

a congruent melting point.

Both Al_3Ti and Al_3Nb have limited solid solubility (<1 at.%) on either side of their binary stoichiometric compositions, however, they exhibit complete mutual solubility. In order to define the composition range of phase stability in the ternary system, the Al content was varied from 68 to 79 at.% along a compositional line normal to the pseudobinary at $\text{Nb}_{14}\text{Al}_{75}\text{Ti}_{11}$ as shown in Figure 46. The compositions of these alloys and annealing conditions are given in Table XV. Optical microscopy and X-ray diffraction of the annealed alloys showed $\text{Nb}_{14}\text{Al}_{75}\text{Ti}_{11}$ and $\text{Nb}_{15}\text{Al}_{73.5}\text{Ti}_{11.5}$ to be single phase η . Alloys with a lower Al content contained both the γ phase and η phase, while alloys with a higher Al content contained the Al and η phases. The presence of γ and Al phases in these alloys has been confirmed by DTA.

The alloy $\text{Nb}_{16}\text{Al}_{72}\text{Ti}_{12}$ was expected to be single phase η based on previous work [Jew89]. However, even after annealing for a total of 480 hours at 1200°C, a small amount of γ phase was detected with the η phase (see Figure 10). Electron microprobe analysis of this alloy showed the composition of η to confirm the earlier microprobe results [Jew89] and suggests a solubility range of about 4 at.% at this composition. Since γ and η have ordered crystal structures, diffusion is expected to be extremely slow and therefore expanded homogenization times will be necessary.

DTA showed a decrease in the melting temperatures of the γ phase in the alloys from 1486°C, to 1481°C, and then to

1460°C when increasing aluminum content from 68, to 70 and then to 72 at.% Al. As a result of the higher solidus temperatures of the η phase with Nb additions to the alloys the reactions could not be measured with the DTA. The solidus temperature of the alloy $\text{Nb}_{14}\text{Al}_{75}\text{Ti}_{11}$ was found to be 1540°C.

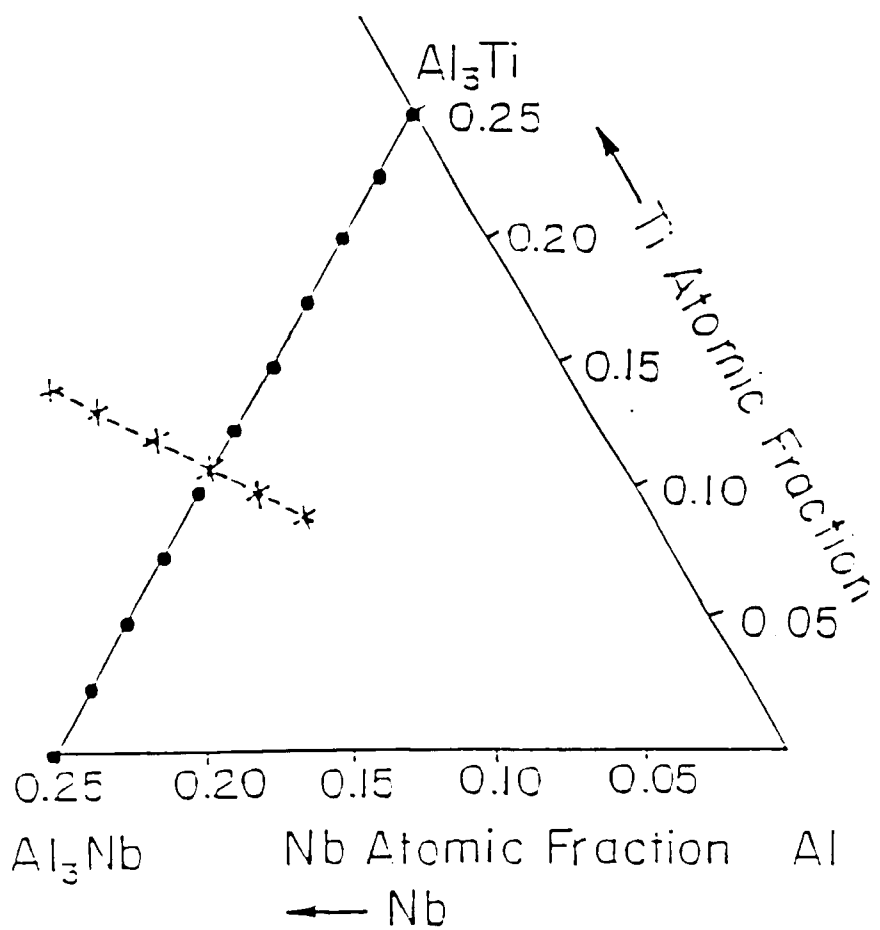
The variations of a , c , c/a and the atomic volume (a^2c) of η in these alloys were measured by X-ray diffraction and are summarized in Figure 50. These parameters varied considerably in the single η phase field. Since there is no discontinuity in the atomic volume with variation in the composition across the η single phase field, the variation of these parameters are believed not to be due to any change in the defect structure.

Table XIV
Compositions of Al_3Ti - Al_3Nb Pseudobinary Alloys
and Their Annealing Times

| Composition | Annealing Time (Hours, at 1200°C) |
|--|--------------------------------------|
| Al_3Ti | 144 |
| $\text{Nb}_{2.5}\text{Al}_{75}\text{Ti}_{22.5}$ | 144 |
| $\text{Nb}_5\text{Al}_{75}\text{Ti}_{20}$ | 492 |
| $\text{Nb}_{7.5}\text{Al}_{75}\text{Ti}_{17.5}$ | 372 |
| $\text{Nb}_{10}\text{Al}_{75}\text{Ti}_{15}$ | 348 |
| $\text{Nb}_{12.5}\text{Al}_{75}\text{Ti}_{12.5}$ | 372 |
| $\text{Nb}_{15}\text{Al}_{75}\text{Ti}_{10}$ | 108 |
| $\text{Nb}_{17.5}\text{Al}_{75}\text{Ti}_{7.5}$ | 372 |
| $\text{Nb}_{20}\text{Al}_{75}\text{Ti}_{5}$ | 348 |
| $\text{Nb}_{22.5}\text{Al}_{75}\text{Ti}_{2.5}$ | 372 |
| Al_3Nb | 336 |

Table XV
Compositions of $\text{Al}_{3+x}(\text{Ti}, \text{Nb})_{1+n}$ Alloys Shown in Figure 1,
Their Annealing Times and Phases Present in Them

| Compositions | Annealing Times (Hours at 1200°C) | Phases Present |
|--|--------------------------------------|--------------------|
| $\text{Nb}_{18}\text{Al}_{68}\text{Ti}_{14}$ | 240, 576 | $\eta + \gamma$ |
| $\text{Nb}_{17}\text{Al}_{70}\text{Ti}_{13}$ | 240, 588 | $\eta + \gamma$ |
| $\text{Nb}_{16}\text{Al}_{72}\text{Ti}_{12}$ | 144, 480 | $\eta + \gamma$ |
| $\text{Nb}_{15}\text{Al}_{73.5}\text{Ti}_{11.5}$ | 336 | η |
| $\text{Nb}_{14}\text{Al}_{75}\text{Ti}_{11}$ | 240 | η |
| $\text{Nb}_{13}\text{Al}_{77}\text{Ti}_{10}$ | 108, 444 | $\eta + \text{Al}$ |
| $\text{Nb}_{12}\text{Al}_{79}\text{Ti}_9$ | - | $\eta + \text{Al}$ |



Chemical Compositions of the Pseudobinary Alloys.

Figure 46 Chemical compositions of the pseudobinary alloys.

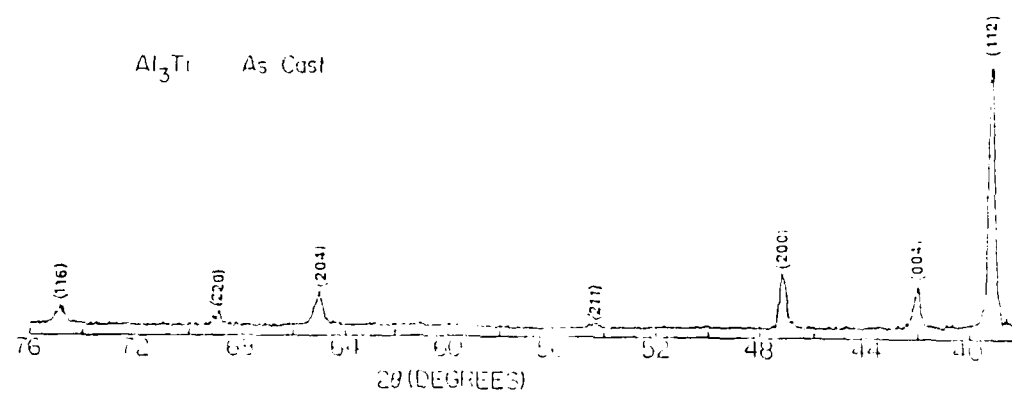


Figure 47 X-ray diffraction pattern of as cast single phase Al₃Ti.

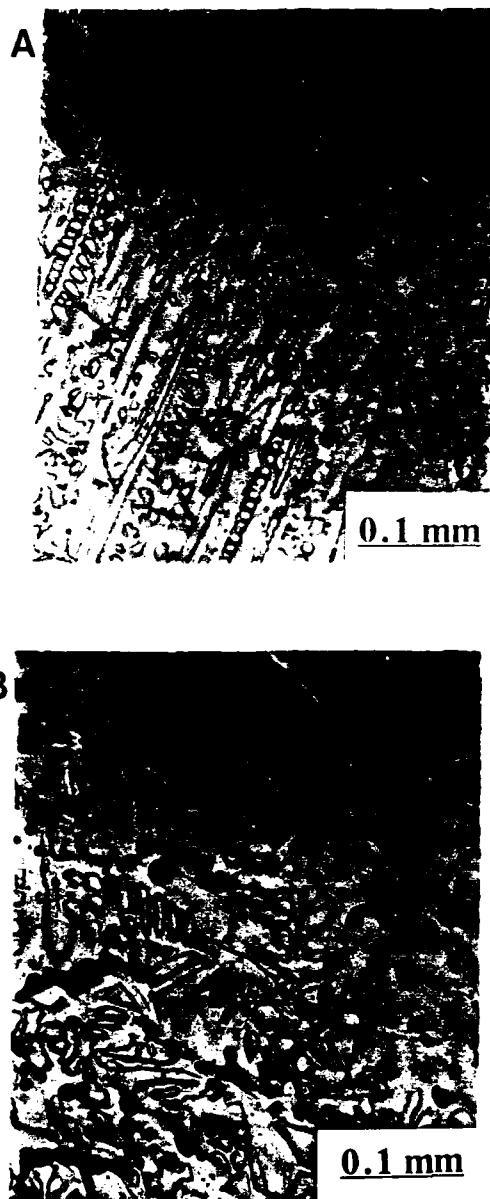


Figure 48

 $\text{Nb}_5\text{Al}_{75}\text{Ti}_{20}$

A. As-cast

B. Annealed at 1200°C for 144 hours.

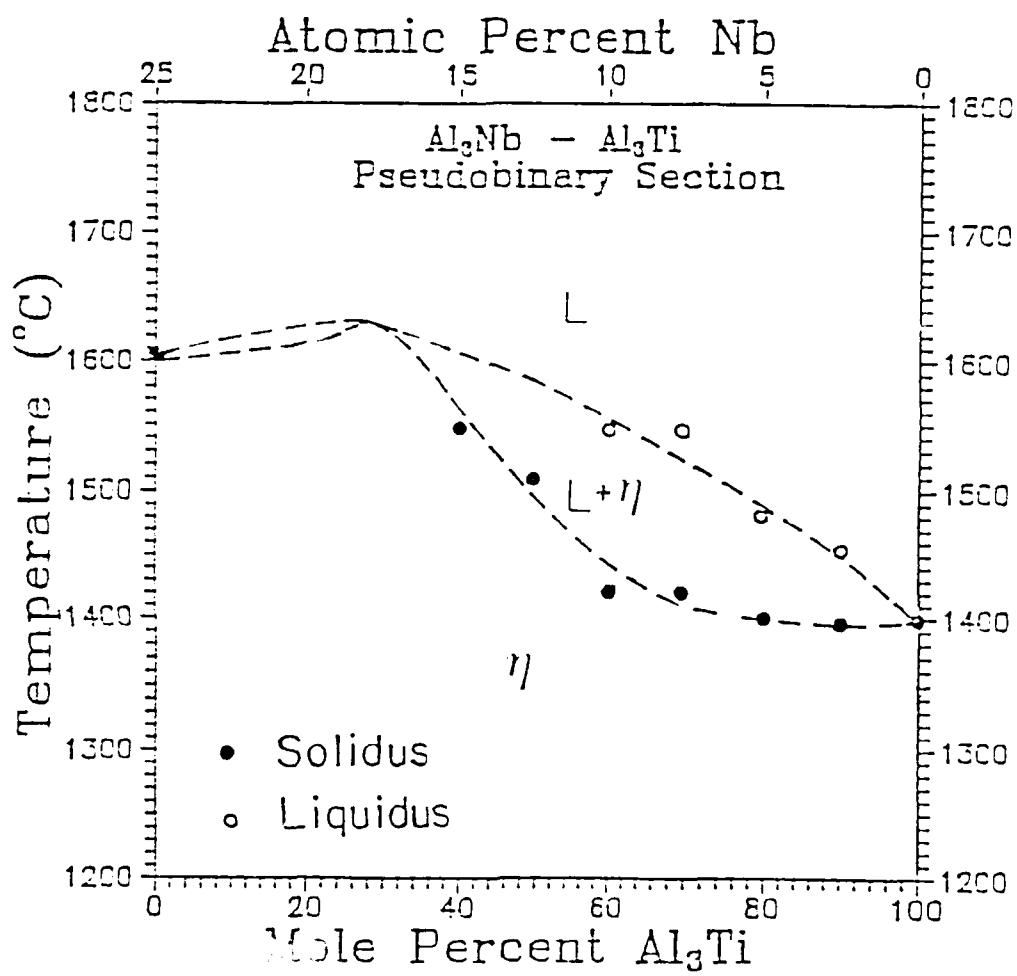


Figure 49

The $\text{Al}_3\text{Ti}-\text{Al}_3\text{Nb}$ pseudobinary section showing an estimated (dashed curve) solidus and liquidus boundaries along with the experimental points.

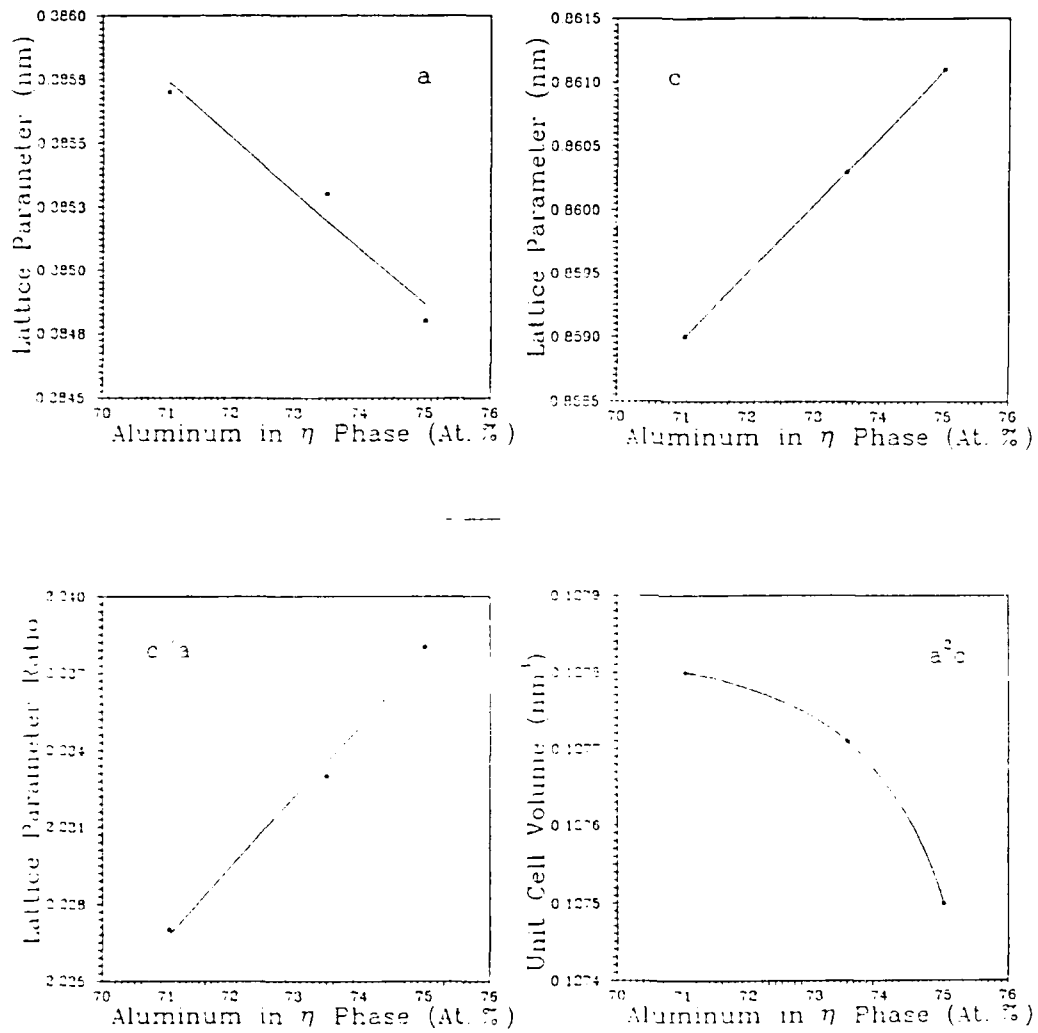


Figure 50 Variation of a , c , c/a and atomic volume of phase with Al content in the η phase of $\text{Al}_3(\text{Ti},\text{Nb})$ alloys.

Phase Equilibria in Nb-Rich Corner of the Nb-Al-Ti System

A preliminary investigation of the phase equilibria in Nb-rich Nb-Al-Ti alloys was conducted primarily by metallographic interpretation of as-cast and isothermally annealed samples. Alloy samples weighing approximately 10 g were prepared from the pure components by repeated arc melting (10 times) under an argon atmosphere. The as-cast ingots were sectioned and polished using standard metallographic techniques. Optical microscopy, scanning electron microscopy (SEM) with back-scattered electron imaging (BSEI) and x-ray diffraction (XRD) were then used to characterize the microstructure. Specimens examined with optical microscopy were etched with a solution of 30 ml HCl, 10 ml HNO₃, 10 ml HF and 10 ml H₂O₂.

The as-cast microstructure of sample 4 (Nb₅₄Ti₂₃Al₂₃) is shown in Figure 25. The optical micrograph (figure 25) shows the presence of large equiaxed grains with a second phase present at the grain boundaries. Structural analysis using XRD shows that the as-cast ingot consists of a bcc solid-solution with significant amounts of the δ-Nb₃Al phase (structure-type Al5). Three reflections which can be indexed as corresponding to the σ-Nb₂Al phase were also resolvable on the XRD scan indicating that some σ-phase was also present. The SEM micrograph of the same sample (Figure 25) at the same magnification shows a dendritic microstructure and no evidence of the grain boundary phase. The BSEI contrast exhibited by the sample arises from the dendritic segregation pattern and the concomitant variation in the mean atomic number, Z, (which varies with alloy composition)

across the dendrite. To observe variation in Z-contrast within the sample, some difference in Z must be present, and regions with the highest mean atomic number would appear brightest [Llo87]. In this case, the dendrite cores, which probably process the highest Nb content, and therefore the highest Z, appear brightest.

Based upon these results a likely phase transformation sequence during cooling from the liquid state can be proposed. The bcc solid-solution phase, β , crystallizes from the melt, and with further cooling in the solid-state, a second phase forms at the β grain-boundaries. If the grain-boundary-phase formed from the melt, possibly by a peritectic type reaction, one would expect an abrupt change in composition across the interface which would be resolved with BSEI imaging. A qualitative estimate of the relative volume fractions of the three phases present (β , δ and σ) suggests that the grain-boundary-phase is probably δ . The apparent absence of the δ -phase when imaging the sample using Z-contrast suggests that this phase processes the same composition as the parent β -phase and may therefore represent a massive transformation product. The existence of a massive β - δ transformation in the Nb-Al binary system has been well documented [Lun66] [Bor85].

The microstructure of a $\text{Nb}_{50}\text{Ti}_{25}\text{Al}_{25}$ alloy which was annealed in an argon atmosphere for 16 days at 1200°C is shown in Figure 37. The application of BSEI imaging shows the presence of three phases each of which is represented by a different shade of gray. There is also some porosity present in the sample (the

black spots) which formed during solidification of the arc melted ingot. The microstructure of this sample at low magnification (Figure 37a) shows some evidence of prior β dendrites (lighter regions). The micrograph of the same region at a higher magnification (Figure 37b) illustrates the equiaxed morphology of the three phases present in this equilibrated sample. Electron microprobe analysis was used to measure the compositions of the phases in equilibrium at 1200°C and therefore establish the three-phase field shown in Figure 27. Using the measured compositions and an estimate of the BSEI coefficients, η , for Nb, Ti and Al (0.369, 0.265 and 0.177 respectively [Hei64]), a weighted mean BSEI coefficient can be calculated for each phase. Based on these results, the phases appearing as light, medium and dark gray in Figure 37 represent δ , σ and β respectively.

Analysis of this sample using XRD also shows evidence for the presence of three phases (δ , σ and β) as is shown in Figure 38. A portion of an x-ray diffractometer scan (30-50 $^{\circ}2\theta$) shows that the sample consists primarily of δ and σ with smaller amounts of β in agreement with microstructural observations (Figure 37). Due the overlap of reflections corresponding to β with those of the more abundant δ and σ , only the β -(211) reflection could be used to verify the presence of the bcc phase.

The procedure used to measure the lattice parameters of the three phases is as follows. Apparent values of the lattice constant, a , were calculated for each reflection and plotted versus $\cot(\theta)$. This extrapolation function provides the widest range of linearity (a vs. $f(\theta)$) and is preferred for

diffractometer results where high angle reflections ($\theta > 80^\circ$) are not usually available and errors due to absorption are negligible [Nel45]. Extrapolation of the line fitted to the apparent a values using least squares to $\cot(\theta)=0$ ($\theta=90^\circ$) gave the actual value of the lattice constant, a_0 . The lattice constants of the tetragonal σ -phase were determined using the method outlined by King and Massalski [Kin61]. The measured values of the lattice constants are given in Table XVI, and the values for pure Nb and the binary Nb_2Al and Nb_3Al phases are shown for comparison. A decrease in the lattice constant(s) is observed in the case of the ternary alloy phases when compared to their binary counterparts.

The modification of the as-solidified microstructure which can be achieved with the application of rapid solidification processing (RSP) techniques was also investigated. BSEI micrographs of the $Nb_{50}Ti_{25}Al_{25}$ alloy in both the as-arc cast (Figure 51a) and splat quenched (Figure 51b) conditions illustrate the reduction in microstructural scale brought about through rapid solidification. The arc cast ingot shows a dendritic solidification pattern with a dendrite arm spacing of approximately $35 \mu\text{m}$. The microstructure of the splatted film ($53 \mu\text{m}$ thick) consists of fine columnar cells, with a spacing of less than $1 \mu\text{m}$, extending from the surface to a band of equiaxed cells ($8 \mu\text{m}$ thick) at the center of the splat. The x-ray diffraction pattern of the splat quenched sample exhibits only those reflections which can be indexed as corresponding to the β -phase ($a_0=3.256\pm0.001 \text{ \AA}$). Therefore, in addition to a reduction in the

microstructural scale resulting from solidification, rapid quenching from the liquid state also inhibits the subsequent solid state transformation of β to δ (illustrated in Figure 25 for a $\text{Nb}_{54}\text{Ti}_{23}\text{Al}_{23}$ alloy).

The microstructure of an as-arc melted $\text{Nb}_{50}\text{Ti}_{15}\text{Al}_{15}$ alloy also consists of a dendritic morphology, but with no evidence of the massive δ formation observed in the other two alloys. The x-ray pattern exhibits only those lines corresponding to a disordered bcc-phase indicating that the as-solidified ingot consists of the β solid solution.

In summary, all three of the alloys investigated apparently solidify as a β solid solution. In alloys with compositions in the vicinity of the β - σ two-phase field, evidence for a massive β - δ transformation is observed.

Table XVI
 β - δ - σ Three-Phase Equilibrium

| Phase | Composition | Lattice Constant(s) |
|----------|--|--|
| β | pure Nb $\text{Nb}_{47}\text{Ti}_{33}\text{Al}_{20}$ | $a_o = 3.3066$ $a_o = 3.26 \pm 0.01$ |
| δ | $\text{Nb}_{75}\text{Al}_{25}$ $\text{Nb}_{56}\text{Ti}_{24}\text{Al}_{20}$ | $a_o = 5.187$ $a_o = 5.170 \pm 0.001$ |
| σ | $\text{Nb}_{67}\text{Al}_{33}$ $\text{Nb}_{49}\text{Ti}_{23}\text{Al}_{28}$ | $a_o = 9.957$ $c_o = 5.167$ $a_o = 9.951 \pm 0.004$ $c_o = 5.140 \pm 0.005$ |

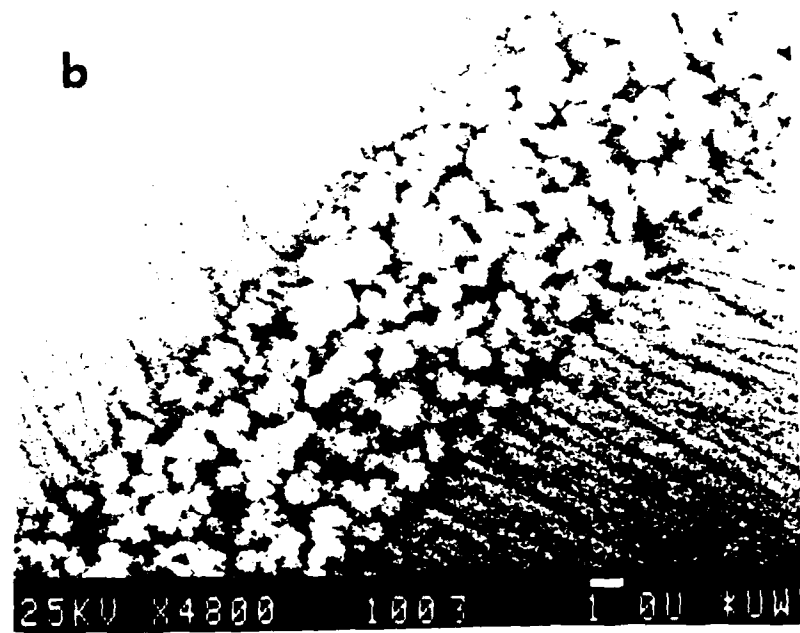
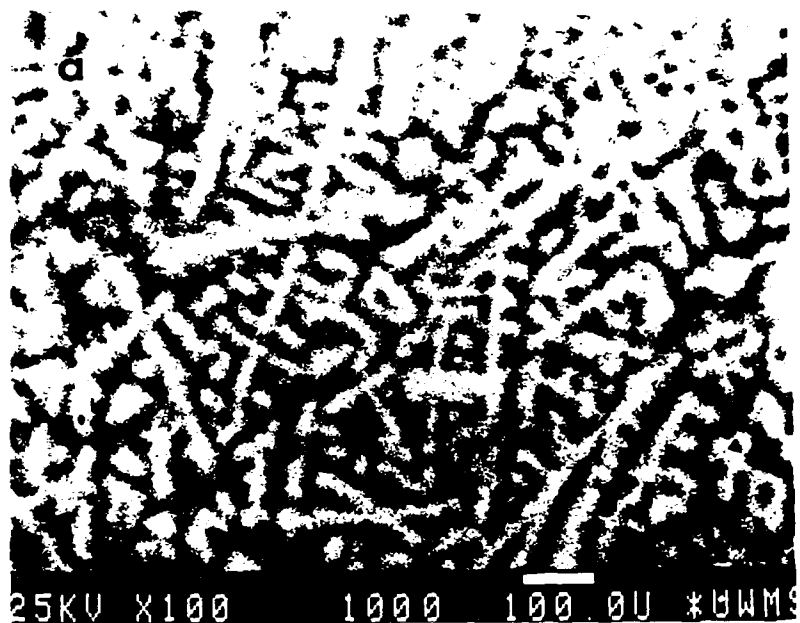


Figure 51 $\text{Nb}_{50}\text{Ti}_{25}\text{Al}_{25}$
A) As-arc melted
B) Splat quenched. SEM micrographs imaged with
BSEI.

3.2 Diffusion Couples - Kinetic Implications

Much of the recent activity in high temperature alloy studies has addressed the issue of thermal stability either in terms of external reactions with the environment or in terms of the internal stability of synthesized multiphase composites. In most composite systems of interest the kinetics of the chemical reactions and interdiffusional mixing at the composite particulate-matrix interface play a central role in determining the integrity of the overall structure and its mechanical performance. For example, it has been demonstrated that the fracture toughness of a brittle matrix can be improved in a composite with relatively weak bonding between the matrix and the composite particulate. For other applications of dispersion strengthening, it may be desirable to develop well bonded matrix-particulate mixtures.

In the present study, the interfacial reactions and interdiffusion between the $\gamma(L1_0)$ TiAl phase and $\beta(A_2)$ TiNb alloys were studied to determine the interaction products of a ductile phase in a γ matrix. By carefully monitoring the diffusional interaction it has been possible to obtain additional information on the ternary equilibria in Ti-Al-Nb alloys and new information on the diffusivities.

Experimental Procedure

Two compositions of β TiNb alloys, 30 and 44 at.% Nb, were deposited on γ -TiAl substrates using a sputter-deposition method. The thickness of the β phase varied from 100 to 150 microns. The interdiffusion experiments were carried out in

sealed, argon-filled quartz capsules. In order to minimize reaction between the samples and quartz capsules, the samples were coated with yttria and wrapped with tantalum foil. They were then annealed at a fixed temperature for a period of time and quenched in ice-water. The quenched samples were characterized by optical microscopy, SEM and EPMA.

Results and Discussion

The phase sequences of the couples after annealing at different temperatures are summarized in Table XVII. The results obtained for two couples, i.e. β -Ti₃₀Nb/ γ and β -Ti₄₄Nb/ γ , are similar. A layered α_2 (or α) phase grows at the β/γ interface. If equilibrium conditions (stable or metastable) are assumed at the interfaces, the compositions of the phases determined should correspond to those for a stable or metastable tie line. The tie line data are summarized in Table XVIII. Since the planer interface of β/α_2 which forms initially breaks down after further annealing at 1100°C, it is concluded that the β/α_2 interface may correspond to a metastable condition. A two-phase mixture in contact with α_2 forms after the breakdown of the planer β/α_2 interface. Figure 52 shows the morphology of the β Ti₃₀Nb/ γ couple annealed at 1100°C for 190 hours. The results of EPMA show that a constant composition for each phase has been reached in this couple. The same compositions were also found in the β (Ti₄₄Nb)/ γ couple. These results led us to believe that there exists a three-phase field. The crystal structures of these phases have not yet been determined. However, we believe this three-phase equilibrium to be the α_2 - β -B2 (see discussion on the

Nb-Al-Ti phase diagram).

In addition to the phase equilibrium data, kinetic information can be obtained from the diffusion couple results. In order to have the experimental conditions of the couples corresponding to semi-infinite boundary conditions, only short-term annealing at 1100°C was carried out. The Matano-Boltzmann analysis [Mat33] was used to obtain the diffusion flux profiles on the basis of composition profiles. Figure 53 shows the concentration profiles of the β -Ti₃0Nb/ γ couple annealed at 900°C for 96 hours and the corresponding diffusion flux profile obtained from an Matano-Boltzmann analysis. Using these flux and concentration profiles, the interdiffusion coefficients can be obtained from the following equations,

$$\tilde{J}_{Nb} = \tilde{D}_{Nb-Nb}^Ti \frac{dC_{Nb}}{dx} + \tilde{D}_{Nb-Al}^Ti \frac{dC_{Al}}{dx} \quad [1]$$

$$\tilde{J}_{Al} = \tilde{D}_{Al-Nb}^Ti \frac{dC_{Al}}{dx} + \tilde{D}_{Al-Al}^Ti \frac{C_{Nb}}{dx} \quad [2]$$

where \tilde{J}_{Nb} , \tilde{J}_{Al} are the interdiffusion flux for Nb and Al; C_{Nb} , C_{Al} are the concentrations for Nb and Al, x is the distance coordinate, \tilde{D}_{Nb-Nb}^Ti , \tilde{D}_{Al-Al}^Ti and interdiffusion coefficients for Nb and Al with reference to the component Ti, and \tilde{D}_{Nb-Al}^Ti , \tilde{D}_{Al-Nb}^Ti are the cross-interdiffusion coefficients. Since most of the diffusion occurs in the bcc phase, only the coefficients for this phase are obtained. These values are given in Tables XIX and XX. Although it is evident from these values that the interdiffusion coefficients are composition dependent the values

of the activation energies obtained for the two compositions,
i.e. 30 and 44 at% Nb, are the same within the uncertainties of
the data.

Table XVII
Phase Arrangements of the Diffusion Couples After Annealing

| Temp (°C) | Time (hr) | $\beta(\text{Ti}30\text{Nb})/\gamma$ | $\beta(\text{Ti}44\text{Nb})/\gamma$ |
|-----------|-----------|--------------------------------------|--------------------------------------|
| 900 | 24 | $\beta \alpha_2 \gamma$ | $\beta \alpha_2 \gamma$ |
| 900 | 72 | $\beta \alpha_2 \gamma$ | $\beta \alpha_2 \gamma$ |
| 900 | 96 | $\beta \alpha_2 \gamma$ | $\beta \alpha_2 \gamma$ |
| 900 | 168 | $\beta \alpha_2 \gamma$ | $\beta \alpha_2 \gamma$ |
| 1000 | 24 | $\beta \alpha_2 \gamma$ | $\beta \alpha_2 \gamma$ |
| 1000 | 48 | $\beta \alpha_2 \gamma$ | $\beta \alpha_2 \gamma$ |
| 1000 | 80 | $\beta \alpha_2 \gamma$ | - |
| 1100 | 18 | $\beta \alpha_2 \gamma$ | $\beta \alpha_2 \gamma$ |
| 1100 | 75 | $\beta_2+\alpha \alpha_2 \gamma$ | $\beta_2+\alpha \alpha_2 \gamma$ |
| 1100 | 190 | $\beta_2+\alpha \alpha_2 \gamma$ | $\beta_2+\alpha \alpha_2 \gamma$ |
| 1200 | 7 | $\beta \alpha \gamma$ | $\beta \alpha \gamma$ |

Table XVIII
Tie-line determined in the Ti-Al-Nb System

Table XIX
Interdiffusion Coefficients in the bcc Phase
of the Nb-Ti-Al System Obtained from the β -Ti₃₀Nb/TiAl Couples

| T (C) | $\sim D_{Nb-Nb}$ | $\sim D_{Nb-Al}$ | $\sim D_{Al-Al}$ | $\sim D_{Al-Nb}$ (cm^2/s) |
|----------|-----------------------|-----------------------|-----------------------|---|
| 1100 | 5.8×10^{-10} | 2.4×10^{-11} | 1.3×10^{-9} | 1.5×10^{-10} |
| 1000 | 1.0×10^{-10} | 5.4×10^{-12} | 2.1×10^{-10} | 2.3×10^{-11} |
| 900 | 1.4×10^{-11} | 1.2×10^{-12} | 2.2×10^{-11} | 2.5×10^{-12} |
| Q kJ/mol | 250 ± 20 | 210 ± 30 | 275 ± 20 | 270 ± 30 |

Table XX
Interdiffusion Coefficients in the bcc Phase of the
Nb-Ti-Al System Obtained from the β -Ti₄₄Nb/TiAl Couples

| T (C) | $\sim D_{Nb-Nb}$ | $\sim D_{Nb-Al}$ | $\sim D_{Al-Al}$ | $\sim D_{Al-Nb}$ (cm^2/s) |
|-------------|-----------------------|-----------------------|-----------------------|---|
| 1100 | 1.2×10^{-10} | 1.2×10^{-11} | 3.8×10^{-10} | 1.1×10^{-11} |
| 1000 | 2.0×10^{-11} | 2.4×10^{-12} | 5.2×10^{-11} | 1.5×10^{-12} |
| 900 | 2.5×10^{-12} | 3.7×10^{-13} | 5.0×10^{-12} | 1.5×10^{-13} |
| E (Kj/mole) | 260 ± 20 | 230 ± 30 | 290 ± 20 | 285 ± 30 |



Figure 52 Photomicrograph of a β -Ti₃₀Nb/ γ couple annealed at 1100°C for 190 hours.

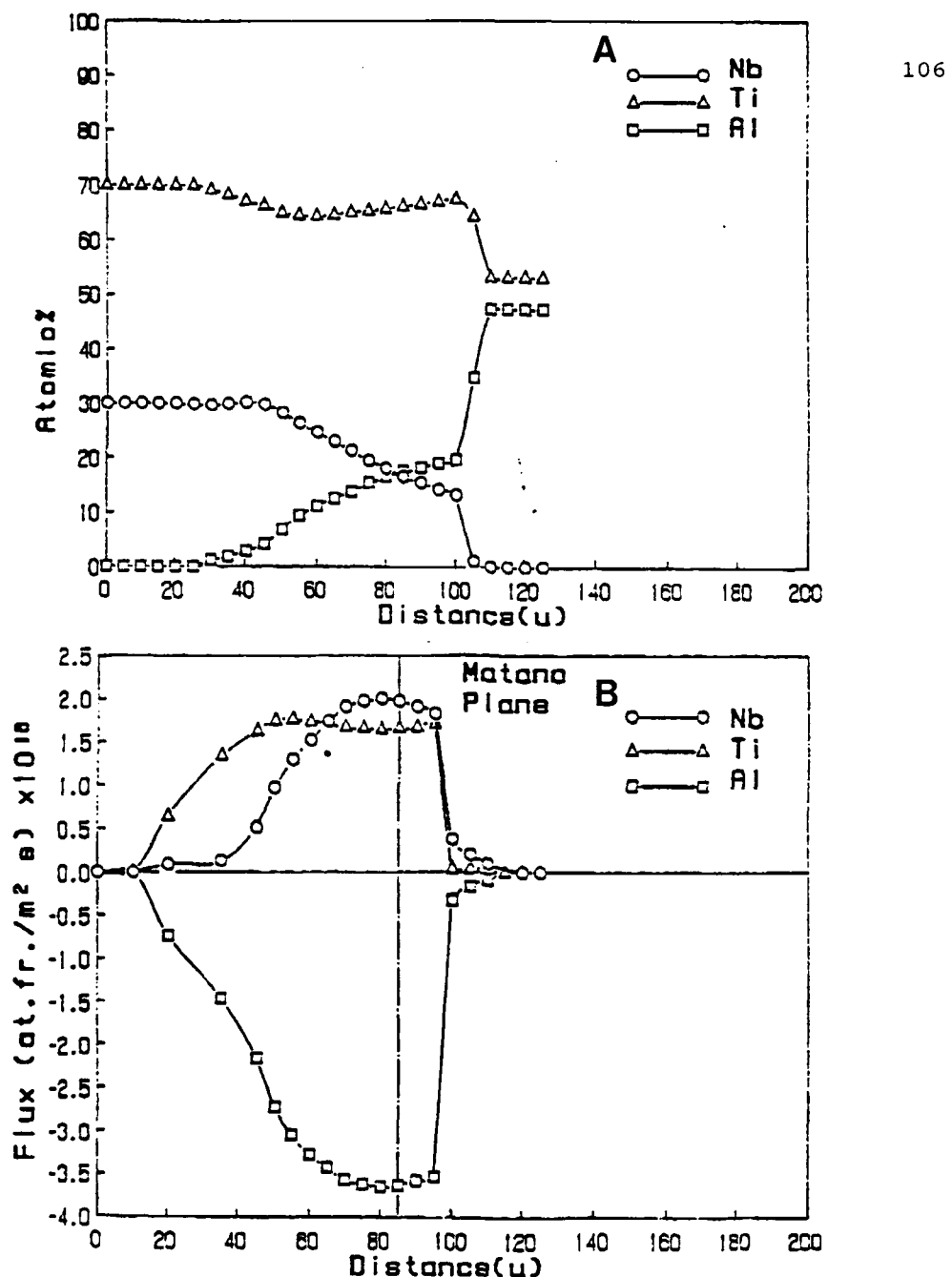


Figure 53 The results of a β -Ti₃₀Nb/ γ couple annealed at 1100°C for 2 hours.
 a. Concentration profile.
 b. Diffusion flux profile.

3.3 Model and Calculations for Ti-Al-Nb Ternary System

The experimental data obtained today will be essential in laying the foundations for the modeling parameters and future calculations. Calculations of the ternary phase equilibria is dependent on the binary phase equilibria, which are not yet finalized for the binary Ti-Al system. Current evaluations of the binary Ti-Al system have been sent to the NBS for use in ternary modeling. More detail will be provided at a later date.

3.4 Powder Processing

Ti₃Al+Nb Results-(Alloys B and C)

Two size ranges of powders, 5-20 and 20-38 μm were examined from sample C (Ti₃Al+11Nb), (see Table XXI) were examined. According to x-ray analysis, the structure of sample C(Ti₃Al+11Nb) was all β phase (see Figure 54). Since there were no significant trends of the lattice parameter based on powder size, an average lattice parameter was calculated. Recall the average lattice parameter for sample B (Ti₃Al+5Nb) was $a = 3.236 \pm 0.002 \text{ \AA}$. The average lattice parameter for sample C (Ti₃Al+11Nb) was $a = 3.246 \pm 0.004 \text{ \AA}$ (see Table XXII). With an increase in niobium content from 5 to 11 at.% the a lattice parameter increased by 0.01 \AA . No clear characterization of the surface texture of sample C could be made with SEM analysis due to the presence of a surface film on the powders and little depth to the surface relief.

Previous microstructural examination of powders from sample B (Ti₃Al+5Nb) revealed two main types of microstructures, a dendritic morphology and a featureless morphology. In general,

as the powder size decreased a slight increase in the number of featureless particles was observed, although featureless particles were observed even in the largest size powders (>177 microns). Microstructural examination of powders from sample C ($Ti_3Al+11Nb$) revealed that all powders exhibited a dendritic morphology (see Figure 55), with secondary dendrite arms orthogonal to the primary dendrite arms.

Additional work has been done on the Ti_3Al+5 at% Nb alloys to determine the cause for the featureless and dendritic microstructures. A special technique was developed to obtain a direct correlation between the external surface texture and the internal microstructure. Using a stereo microscope large diameter powders were sorted with tweezers by surface texture and aligned on double sided tape on a SEM pedestal. Ten dendritic particles, ten featureless particles and a dendritic-featureless pair were selected for analysis. The selected powders were assigned a coordinate system (see Figure 56). The SEM examination of the particles selected with the stereo microscope confirmed all the dendritic and featureless particles had the surface texture as assumed from the stereo microscope examination (see Figures 56-59). Three out of the ten dendritic particles and eight out of the ten featureless particles were found to have impact craters on their surface. Particle D5 had a small featureless satellite on it's surface. The samples were mounted in epoxy, polished and etched to reveal internal microstructures. Particle D6 was lost during the metallographic mounting process. Metallographic examination of the polished and etched powder

cross sections revealed all the particles which were dendritic on the surface had a dendritic microstructure in their interior and those that were featureless on the surface had a featureless microstructure in their interior (see Figures 60-64). Only one particle (D5) was found to contain a gas pocket. All of the featureless particles were similar to Figure 79b with only scratches from polishing visible, except for particle F1 (Figure 64) which contains a faint radiating dendritic structure.

Microprobe analysis of the 19 selected particles in the as polished condition revealed no significant chemistry variations between the dendritic particles and the featureless particles. The average composition of niobium in the dendritic particles was slightly higher by 0.105 at.%, but this was within both the deviation from particle to particle and the average error of the measurement technique for the species.

The thermal decomposition of sample C consisted of two exothermic reactions at 520 and 766°C (see Figure 65). The reaction started at around 466°C and completed around 766°C. No difference was noted in the thermograms between the two size ranges of Sample C. The post-DTA x-ray analysis of sample C revealed the structure consisted mainly of α_2 with some β phase present (see Figure 66 and Table XXII). The microstructure of sample C heated to 1255°C (2 times) (cooling rate 30°C/min) consisted of a primary phase in the grains with the possibility of small precipitates in the interior and a second phase at the grain boundaries (see Figure 67).

In an attempt to clarify the thermal decomposition of

sample C ($Ti_3Al+11Nb$), an X-ray unit equipped with a capillary furnace attachment and a position sensitive X-ray detector, centered over the 2θ range $25-62^\circ C$, were used to analyze the 20-38 micron size powder at 400, 600 and $800^\circ C$ (see Figure 68). At room temperature and $400^\circ C$, only two β peaks (110) and (200) could be detected. At $600^\circ C$, no identifiable peaks were observed above the noise. At $800^\circ C$, two α_2 peaks (002) and (201) were detected.

Discussion of Ti_3Al+Nb (Alloys B, and C)

The structure of the powder alloy B (26.95 Al, 4.93 Nb) was metastable β phase with two different microstructural morphologies, dendritic and featureless. The structure of alloy C (25.11 Al, 10.53 Nb) was also metastable β phase with only the dendritic morphology. No superlattice reflections were observed for either alloy which would indicate an ordered B2 structure. The dendritic morphology of the microstructures clearly shows the 90° orientations expected for β solidification. Thus, there was insufficient undercooling to alter the primary solidification structure from the equilibrium β phase. The presence of dendrites is an indication of either decreased diffusion rates or greater segregation as a result of solidification.

Compositional variations could not account for the two different morphologies (dendritic and featureless) observed in alloy B (26.95 Al, 4.93 Nb). The observed trend in the change in number of particles with featureless morphology with decreasing size was almost constant and what was not expected from the effect of nucleant isolation on undercooling. The

particles with dendritic solidification clearly show solidification shrinkage on the surface. A majority of the particles with no solidification shrinkage on the surface contained impact craters indicating particle interactions. It is likely the featureless particles solidified with a planer solidification front as a result of the undercooled melt colliding with a solid particle which acted as a heat sink and set off nucleation. An example of such a collision is shown in Figures 57 and 61. If the dendritic particle nucleated as a result of the collision from the point of impact then the dendrites should be radiating out from the point of impact or at least be perpendicular to a line through the particle centers. The temperature of the solid particle and the amount of liquid undercooling would vary and give rise to different solidification morphologies. Particles were observed which exhibited cellular structures, and radiating dendritic structure, with several of the larger particles having multiple grains, an indication of multiple nucleation sites. The β grain size was on the order of 60 to 70 microns which gives an estimated cooling rate of 2000°C/sec [Bom86].

The lack of the featureless morphologies observed in alloy C (25.11 Al, 10.53 Nb) can be accounted for by the lower probability of collision for the finer particle sizes (maximum size 38 microns) due to shorter molten droplet flight time and smaller diameter. It is also possible the increased niobium content makes plane front solidification less stable.

The metastable nature of the retained β phase in alloy B

(26.95 Al, 4.93 Nb) was demonstrated by the exothermic decomposition of β . A possible reaction path would be $\beta \Rightarrow \alpha \Rightarrow \alpha_2$. On cooling the structure returned to the predicted equilibrium phases α_2 and β [Str88] (see Figures 65 and 67).

The decomposition of the metastable β phase for alloy C (25.11 Al, 10.53 Nb) involved a two step decomposition. On cooling the structure returned to the predicted equilibrium phases α_2 and β (see Figures 11a-b, 81 and 85 a-b). Attempts to clarify the decomposition of the retained β phase using high temperature x-ray analysis was only partly successful. The β phase was observed prior to the exothermic reactions and α_2 after the exothermic reactions. The intermediate structure between the two exothermic reaction peaks was not distinguishable; no β nor α_2 peaks were observed. The possibility exist that the first exothermic reaction corresponds to B2 ordering followed by α_2 formation or a $\beta \Rightarrow \alpha$ martensitic decomposition followed by ordering to α_2 . Further work is needed to identify which possibility is more probable.

The "soccer ball" dendritic shrinkage pattern on the surface of the particles of alloy B (26.95 Al, 4.93 Nb) is the type of pattern (uniform hexagonal patches) that would be expected from an internal nucleation site with dendrites growing out and impinging on the surface of a sphere. In order to obtain the "soccer ball" surface texture as a result of surface nucleation, multiple surface nucleation events would be required to occur simultaneously around the powder's surface, a much lower probability of occurrence. Additional metallographic evidence for

this possibility is the appearance of dendrites originating from nonsurface areas. According to the nucleant isolation theory, the particles with the highest level of undercooling will be those particles that do not contain the potent internal nucleation sites, which would result in surface nucleation occurring. The presence of an internal nucleation site is an indication the potent nucleation sites have not been isolated, and the level of undercooling may be considered smaller than would be expected if surface nucleation had occurred.

Of particular interest is the suppression of the $\beta \Rightarrow \alpha'$ martensitic transformation as a result of solid state undercooling in both alloys B and C. This suggests a diffusional component to the martensitic transformation with the addition of niobium.

The solidification pathway for the Ti₃Al alloys with niobium additions is primary solidification of the β phase and retention of the β phase to room temperature. The level of undercooling experienced was insufficient to alter the primary solidification path from the β phase. On the other hand the level of solid state undercooling was sufficient to suppress the martensitic transformation of $\beta \Rightarrow \alpha$ and subsequent ordering reactions. Thus, the niobium addition results in the addition of a diffusional component to the martensitic transformation in the ternary Ti₃Al+Nb alloys. Other effects of the niobium additions include a decrease in the $\alpha \Rightarrow \beta$ transformation temperature (as was expected [Str88]), and slower diffusion rates and/or increased solidification segregation. Particle interactions (collisions)

resulted in significant morphological changes which are advantageous in reducing the segregation from solidification without decreasing the powder size.

Table XXI
Alloys Under Investigation

| ID# | Production Process | Alloy Composition |
|-----|--------------------|-------------------------|
| A | PREP | Ti ₃ Al |
| B | PREP | Ti ₃ Al+5Nb |
| C | PREP | Ti ₃ Al+11Nb |
| D | PREP | Ti-5Al-2Nb |
| E | PREP | Ti-50Al-5Nb |
| G | XRSR | Ti-48Al-2Nb |

Table XXII
Ti₃Al+Nb PREP Powder X-ray Data

| Alloy | Powder Size in microns | Phases Observed | Lattice Parameter A |
|--|------------------------|-----------------------------------|---|
| B(Ti ₃ Al+5Nb) | 177-105 | All β | a = 3.236 \pm 0.002 |
| B(Ti ₃ Al+5Nb) After DTA 1221°C | 177-105 | All α_2 | a = 5.780 \pm 0.003 c = 4.641 \pm 0.004 |
| C(Ti ₃ Al+11Nb) | 38-20 | All β | a = 5.757 \pm 0.015 |
| C(Ti ₃ Al+11Nb) After DTA 1160°C | 38-20 | Mainly α_2 Some β | a = 5.786 \pm 0.002 c = 4.661 \pm 0.002 a = 3.269 |

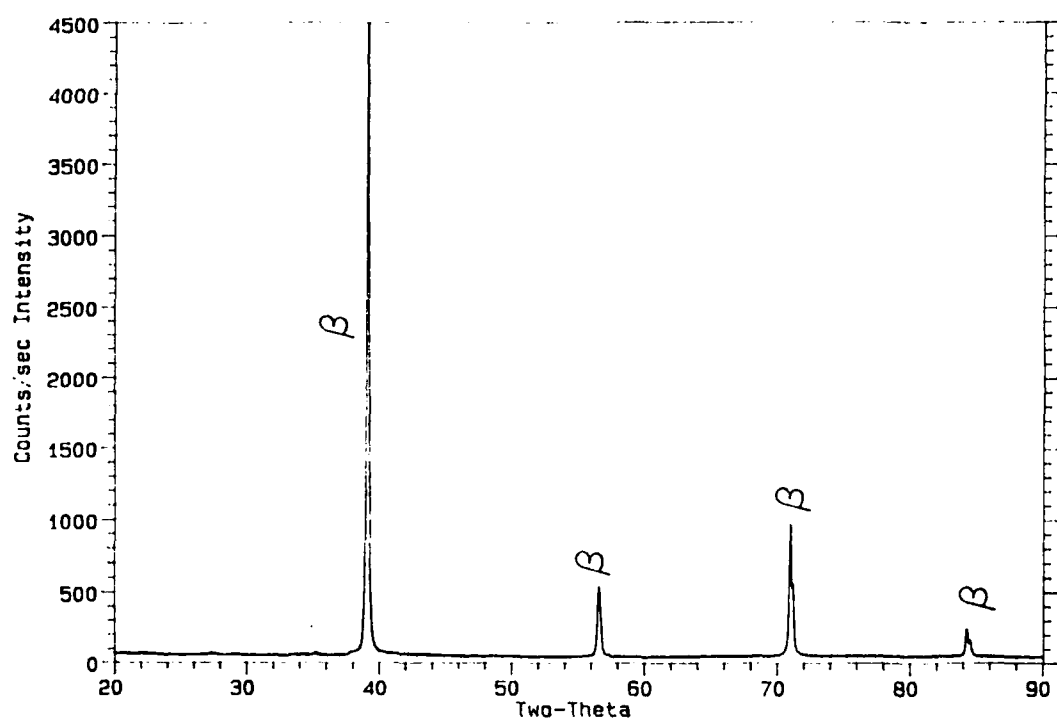
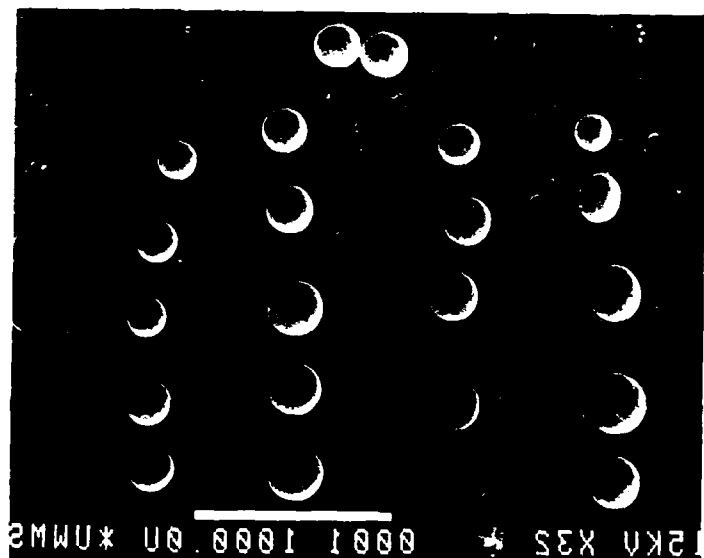


Figure 54 X-ray trace, alloy C ($Ti_3Al+11Nb$), 20-38 microns.



Figure 55 Microstructure, alloy C ($Ti_3Al+11Nb$), 20-38 microns, 90°C dendrite arms.



Coordinate System
F-D Twin

| | | | |
|-----|----|-----|----|
| F10 | F5 | D10 | D5 |
| F9 | F4 | D9 | D4 |
| F8 | F3 | D8 | D3 |
| F7 | F2 | D7 | D2 |
| F6 | F1 | D6 | D1 |

Figure 56 Surface Relief, Alloy B ($Ti_3Al+5Nb$), sorted particles, 10 dendritic, 10 featureless and coordinate system.

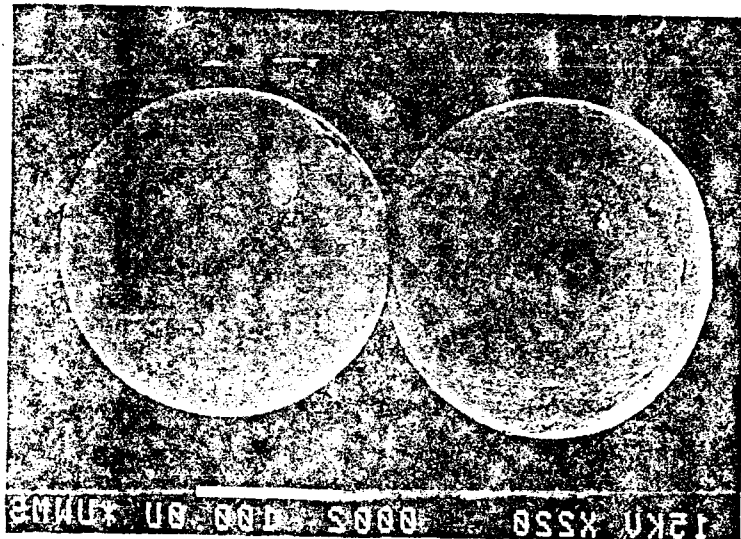
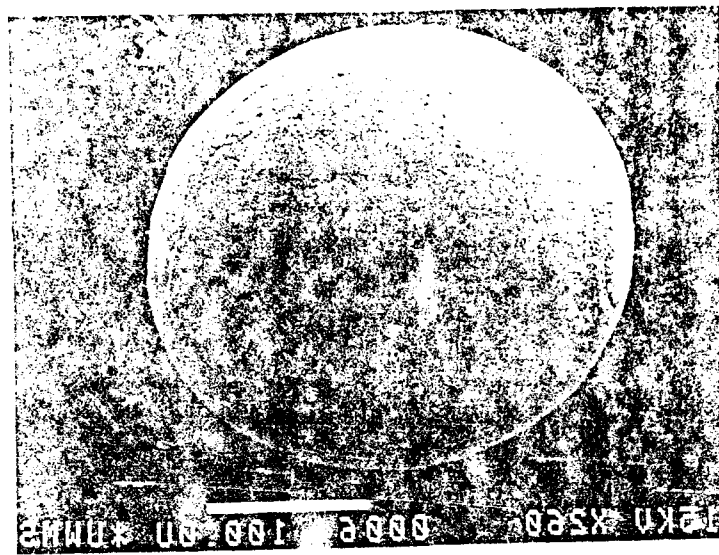


Figure 57 Surface relief, alloy B (Ti₃Al+5Nb), sorted particles, featureless-dendritic bonded pair.



120

Figure 58 Surface relief, alloy B ($Ti_4Al+5Nb$),
particle D3, dendritic surface relief.

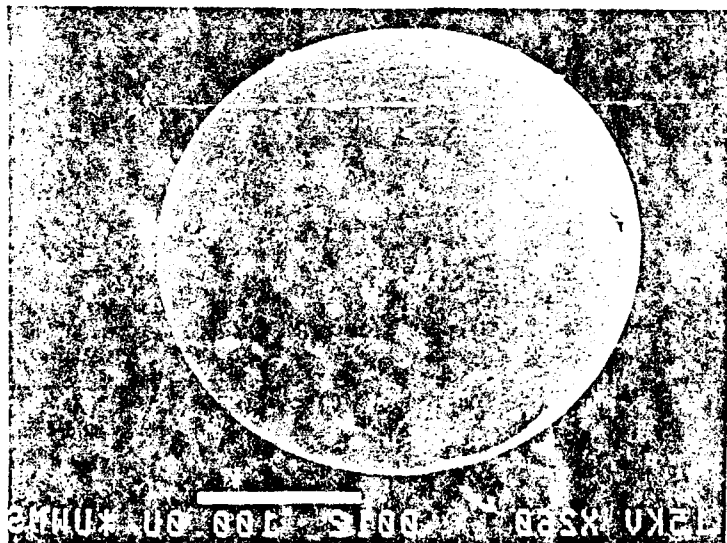
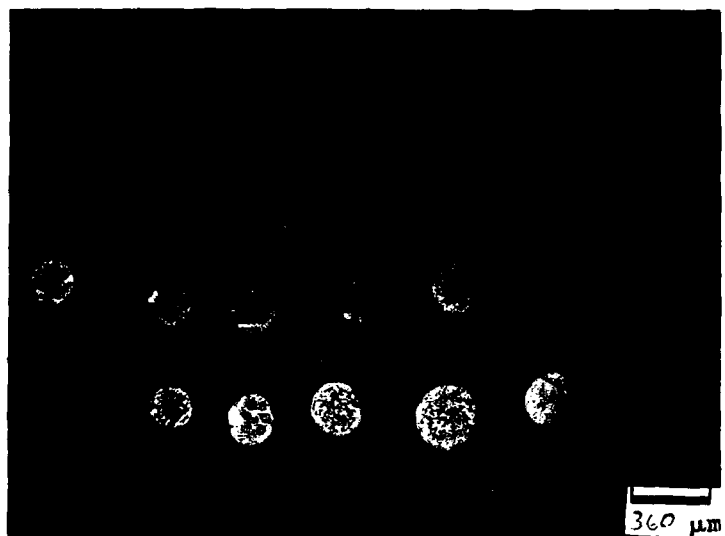


Figure 59 Surface relief, alloy B ($Ti_3Al+5Nb$),
particle F3, featureless surface.
Note: Impact crater on surface.



| Coordinate System | | | | | |
|-------------------|-----|----|----|----|----|
| Twin | F10 | F9 | F8 | F7 | F6 |
| - | F5 | F4 | F3 | F2 | F1 |
| D | D10 | D9 | D8 | D7 | -- |
| | D5 | D4 | D3 | D2 | D1 |

Figure 60 Microstructures, alloy B ($Ti_3Al+5Nb$), sorted particles, 9 dendritic, 10 featureless and coordinate system.

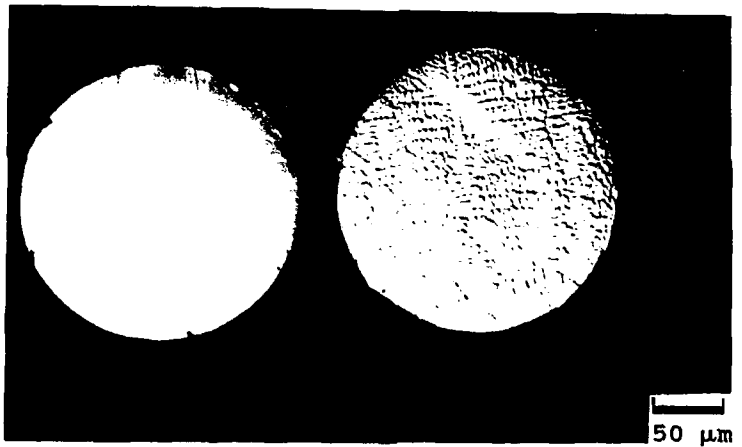


Figure 61 Microstructure, alloy B ($Ti_3Al+5Nb$), sorted particles, featureless-dendritic bonded pair.

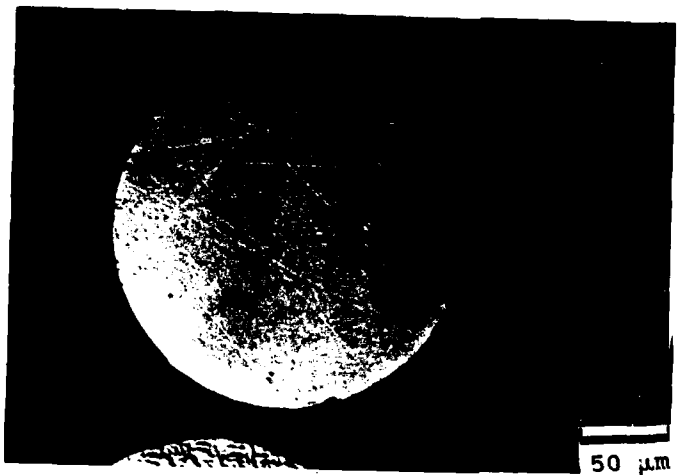


Figure 62 Microstructure, alloy B ($Ti_3Al+5Nb$), featureless particle from bonded pair.

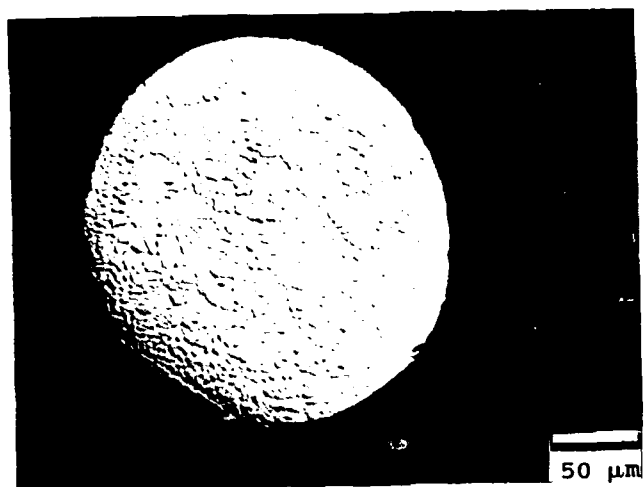


Figure 63 Microstructure, alloy B ($Ti_3Al+5Nb$),
particle D3.

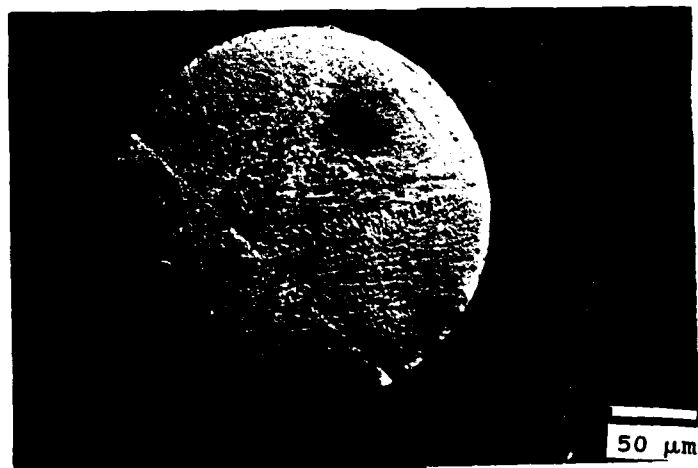


Figure 64 Microstructure, alloy B ($Ti_3Al+5Nb$),
particle F1, faint radiating dendrites.

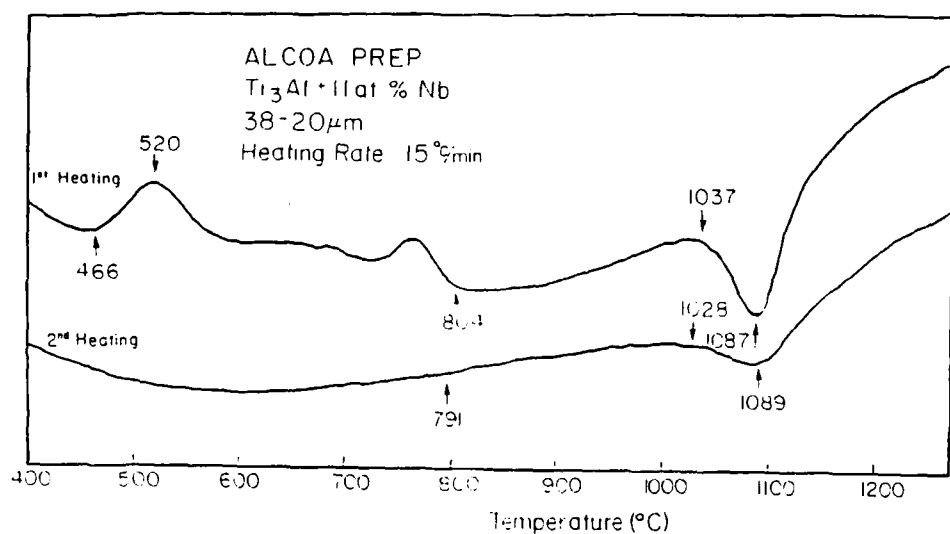


Figure 65 DTA thermogram, alloy C ($Ti_3Al + 11Nb$),
20-38 microns.

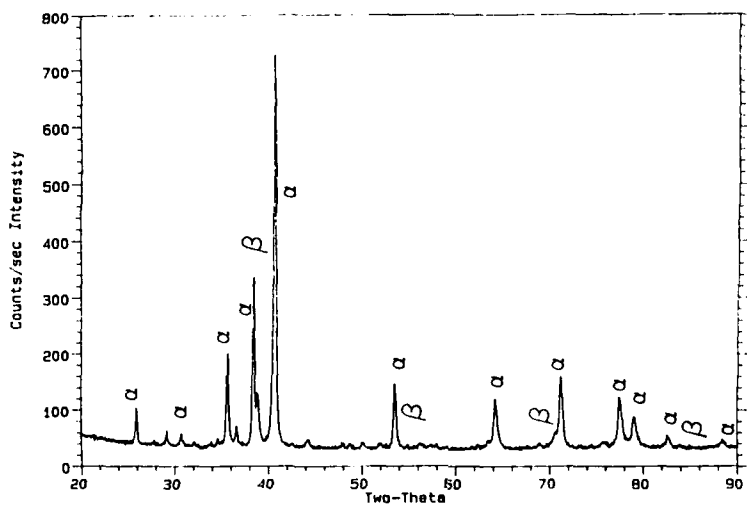


Figure 66 Post-DTA x-ray trace, alloy c ($Ti_3Al+11Nb$),
20-38 microns, $T_{max} = 1160^\circ C$ for 30 min.



Figure 67 Post-DTA microstructure, alloy C ($Ti_3Al+11Nb$).
Note: 2 cycles $T_{max} = 1255^\circ C$.

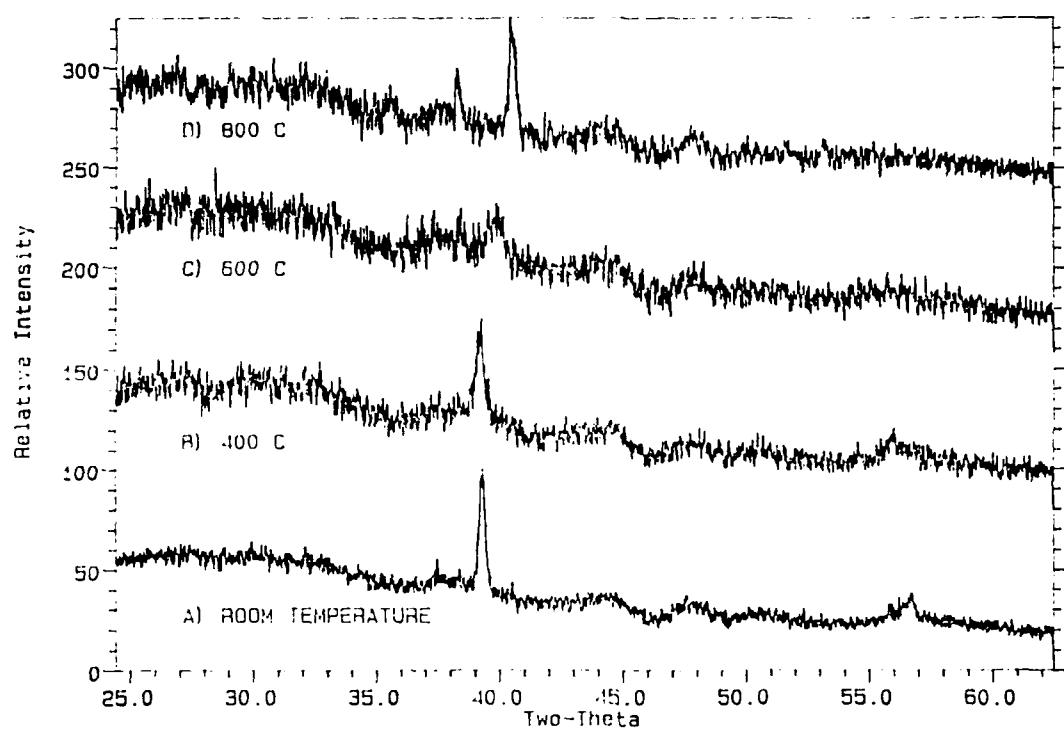


Figure 68 High temperature x-ray traces,
alloy C ($Ti_3Al+11Nb$), 20-38 microns.

TiAl+Nb Results (Alloys D, E and G)

The niobium additions to alloys D, and E were at the expense of the titanium, while the niobium addition to alloy G was at the expense of the aluminum (see Table XXI). Alloy G was produced by the XRSR process. The carbon content of alloy G was 0.233 wt.% C.

In all three alloys D, E, and G, x-ray analysis revealed both the α_2 phase and γ phase to be present in varying relative amounts depending on powder size (see Figures 69-71 and Table XXIII). The finer the powder the greater the amount of α_2 phase present. The trend in α_2 phase abundance with powder size observed in alloys D and E were similar. Alloy G showed a less consistent change with powder size, although the general trend was still present. Alloy G had more α_2 than the other alloys for the same size powder. Although some alloys show a change in lattice parameter with powder size, the observed changes were on the same order of magnitude as the estimated errors and thus not considered significant.

The SEM surface analysis of alloy D showed the main surface texture to be dendritic (see Figure 72). A few particle surfaces were smooth with surface striations visible at higher magnifications (see Figure 73 and Table XXIV). On several of the dendritic particles, 60°C orientations could be observed between the primary and secondary dendrite arms. The SEM surface analysis of alloy E revealed two main types of general surface textures: 1) dendritic with surface patterns ranging from coarse ("soccer ball"), to medium ("cauliflower") to fine ("golf ball"),

and 2) a generally smooth texture with surface striations (see Table XXIV). A few particles clearly indicate 60°C orientations between primary and secondary dendrite arms (see Figure 74). For the coarse "soccer ball" type particles, a 60° orientation between secondary and primary dendrite arms could occasionally be observed. Alloy G also possessed the dendritic and smooth particles. The surface textures for alloy G ranged from the "soccer ball" pattern to the "cauliflower" pattern. The number of smooth particles increased with decreasing powder size (for the 88-150 and 44-63 size ranges). Particle defects for alloy G included many fractured particles and a number of splat caps.

The microstructural examination of alloys D, E, and G revealed four general types of microstructural features: AM) uniformly dark etched area, BM) globular nonetched area; some of the areas appeared as coarse dendritic features, CM) nonetched fine dendritic areas with 60° orientation between primary and secondary dendrite arms, and DM) areas with no etching response.

Alloy D consisted primarily (85%) of a mixture of BM features in an AM matrix and CM features with interdendritic AM features (see Figures 75-79). About 5% of the particles consisted only of AM features. Examination of a polished sample under DIC conditions revealed the AM features consisted of very fine equiaxed grains. Another 5% of the particles consisted primarily of CM features with a very small amount of interdendritic AM. A total of four featureless particles were observed in alloy D and only in the smallest powders (105-5 micron range). No martensitic particles were observed. Except

for an increase in featureless particles, no significant trends were observed concerning changes in microstructural features with powder size for alloy D.

For alloy E the large size powders consisted mainly (70%) of a mixture of BM features in an AM matrix, with some (20%) consisting entirely of AM features (see Figures 81-84). The remaining 10% consisted of CM features in an AM matrix or were featureless. As the powder size decreased the number of particles with BM features in an AM matrix and particles entirely with AM features decreased (to 49% and 5% respectively), while the particles with CM features in an AM matrix and featureless characteristics increased (to 45% and 1% respectively). No martensitic particles were observed.

The microstructure of alloy G consisted of particles with CM features in an AM matrix and particles with BM features in an AM matrix (see Figures 85-86). In the larger size powders there are about the same number of particles with CM features as with BM features. As the powder size decreased, the number of particles with CM features increased, and the amount of AM matrix in a given particle decreased. In addition, the fraction of featureless particles increased (to 1%) as the particle size decreased. Particle defects such as fragmented particles, gas porosity, and splat caps on particles were observed in all size ranges.

In an attempt to determine the relationship between external surface texture and internal microstructure the "direct correspondence technique" was again employed. Alloy E (177-150

microns) was selected, since it exhibited the greatest variation in microstructural details compared to the other alloys. Using the stereo microscope, 14 featureless particles, 7 Coarse dendritic ("soccer ball"), 7 medium dendritic ("cauliflower head"), 7 fine dendritic ("golf ball"), and two pairs of particles bonded together were selected. The surface textures were uniform all around the particles. The selected particles were assigned a coordinate system (see Figure 87). The SEM examination revealed the featureless particles contained varying amounts of surface striations, and all 21 dendritic particles indeed had dendritic surfaces. Only one featureless particle (BF6) contained an impact crater. The surface relief patterns on the dendritic particles exhibited a continuous transition between the three categories of surface area patterns (coarse, medium and fine): i.e., the finest "soccer ball" pattern could also be classified as a large "cauliflower" pattern. A few of the very coarse "soccer ball" patterns clearly showed hexagonal dendrites on the surface and deviated more from the ideal spherical shape. Metallographic examination of the polished and etched powder cross sections revealed the particles which were generally featureless had an internal microstructure which consisted primarily (11 out of 14) of a uniformly dark etched area (AM type) (See Figure 88), while the other three particles had varying levels of nonetching areas (DM type) (see Figure 89) with some precipitates present. Examples of different particle surface types and corresponding internal microstructures are provided in Figures 90-94. In the as-polished condition the

uniformly etched particles consisted of very fine equiaxed grains (see Figure 90). Only one particle (BS7) contained a gas pore along with internal shrinkage porosity (see Figure 92b). All the dendritic particles consisted primarily of coarse nonetched primary dendritic areas (BM type) with an interdendritic uniformly etched phase (AM type). Some of the dendritic areas appeared to have an etching response similar to the interdendritic areas (for example, see Figure 79). Overall, the coarse pattern surface textured particles appeared to have more dendritic area (BM type) than the other particles with the finer dendritic surface patterns. However, the variation in amount of dendritic area versus interdendritic area was more of a function of the location of the cross section through the particle than the coarseness of the surface relief pattern (compare Figure 93b to 93c, and Figure 94b to 94c).

The DTA analysis of alloys D, E, and G resulted in similar thermograms consisting in general of one exothermic peak occurring around 600 to 700°C with an increased in magnitude of the peak with a decrease in powder size (see Figures 95 and 96 and Table XXV). No significant trends were noted concerning onset and peak temperatures with powder size. Alloy G contained an additional exothermic peak. The additional exothermic peak consisted of a slope change with two peaks overlapping. The peaks for alloy G were larger than those for the other alloys. X-ray analysis of the powders subjected to DTA analysis revealed the structure was γ phase in all the alloys (see Figure 97). The γ phase lattice parameters calculated for the alloys were

slightly larger (0.3\AA) than that reported for the pure titanium-aluminum composition (see Table XXVI). Microstructural examination of the post-DTA powders shows fine equiaxed grains in alloys D and E (see Figures 98 and 99). In alloy G the microstructure consisted of grains surrounded by intergranular phase.

In order to investigate whether the exothermic peaks, detected in the first heating cycle of the DTA analysis, correspond to either the decomposition of a metastable phase or the oxidation of the powder surfaces, high temperature x-ray analysis was performed at 200, 550 and 700°C for alloy E (105-74 microns). The heating rate used was $10^{\circ}\text{C}/\text{min}$, with a 1 hour hold at each temperature and the PSD centers at $47^{\circ} 2\text{-}\theta$. Both the γ and α_2 phases are distinguishable at room temperature and at 200°C . At 550°C the decomposition of the α_2 phase has already started as the primary (201) α_2 peak could not be detected. The presence of several other α_2 peaks the (200) at 36.28° and the (220) at 64.86° indicates some α_2 may have been present. Only the γ was present at 700°C . This experiment was repeated using $\text{K}(\alpha_1)$ molybdenum radiation to increase the penetration of x-rays through the sample and improve the signal to noise level. Alloy E (105-74 microns) was heated to 200, 400, and 700°C (see Figure 101). The heating rate used as $15^{\circ}\text{C}/\text{min}$, with a 40 minute hold at each temperature, a data collection time of 30 minutes and a PSD center of $32^{\circ} 2\text{-}\theta$. Both the α_2 and γ phases were present at room temperature, 200, and 400°C . At 700°C only the γ phase was present.

Discussion of TiAl+Nb for the Ti Alloys (D,E)

The solidification behavior of PREP powder alloys with niobium substitutions for titanium were very similar to the pure TiAl powders discussed previously [87Gra]. However, there are some differences in the interpretations of the results, due to differences in the binary Ti-Al phase diagram used previously. In addition no change in solidification behavior was observed by increasing the niobium content from alloy D (51.09 Al, 1.83 Nb) to alloy E (50.25 Al, 4.94 Nb). This result may be expected when one considers the fact that niobium atoms occupy the same lattice sites as titanium atoms. Several trends were observed as the particle size decreased (increased cooling rate): an increase in the amount of metastable β phase present (featureless microstructure), a decrease in the extent of thermal decomposition of $\beta \Rightarrow \alpha \Rightarrow \gamma$ (single phase γ particles), an increase in the amount of primary α phase, and an increase in the size of areas of dendritic surface relief (coarser surface texture).

The majority of the powders experienced primary dendritic α solidification with interdendritic γ formation. The particles which solidified with dendritic α clearly showed dendritic surface relief. In the larger diameter powders, some of the primary α dendrites decomposed to form γ , based on the presence of a dark etching response of hexagonal dendrites. Primary α solidification with interdendritic γ phase is the type of solidification behavior that is expected based on the binary Ti-Al phase diagram [Mis 89].

The particles with no surface solidification shrinkage

are believed to have undercooled sufficiently to form β from the melt instead of α , and most likely solidified under plane front solidification conditions. The main evidence for β solidification from the melt is the presence of surface striations on the particle surfaces. The only other time surface striation were observed was on the surfaces of the Ti₃Al powders that underwent a $\beta \Rightarrow \alpha'$ martensitic transformation. Microstructural evidence showed most of the larger diameter particles with primary β solidification decomposed during solid state cooling to the γ phase. The decomposition is most likely $\beta \Rightarrow \alpha' \Rightarrow \gamma$. No evidence was observed for the presence of martensitic microstructures. Once the martensite is formed it is likely easily decomposed to γ due to large number of nucleation sites. This explanation would also account for the fine grain size of the all γ phase particles. Since the particles consisting only of γ are the result of a subsequent solid state transformation then there is no evidence for primary γ solidification as previously thought. The microstructurally featureless particles observed in the very fine particle sizes and in greater abundance with higher niobium contents should be the metastable β phase retained to room temperature. There was an insufficient volume of these featureless particles to detect β phase either during x-ray analysis or thermal analysis. The featureless particles could form as a result of plane front solidification of the α phase, but that would not account for the formation of striations on the surface of the particles. TEM analysis is required to positively determine if any metastable β phase is present. It

should be pointed out no signs of particle interactions such as surface craters were observed with these P&W PREP powders.

Although α formation is the expected equilibrium solidification product it should decompose on cooling to form the γ phase [Mis 87]. Thus sufficient solid-state undercooling was obtained in the smaller diameter particles to retain the α_2 phase (following ordering of the α). The metastable nature of the α_2 phase was demonstrated by exothermic decomposition during differential thermal analysis. The exothermic decomposition was slightly higher (15°C) for alloy E than alloy D which is an indication niobium may be decreasing the diffusion rate. Confirmation that the exothermic reaction was due to the decomposition of α_2 as opposed to oxidation (expected to occur in the temperature range of the exothermic reaction, 600°C) was provided by high temperature x-ray analysis showing α_2 and γ phase stable at 400°C and only the γ phase at 700°C . The start of the decomposition of the metastable α_2 phase at 550°C during the first high temperature x-ray experiment gives an indication of the kinetic effect. Given sufficient time at temperature, the α_2 phase will decompose to γ phase at lower temperatures than indicated by the exothermic reaction observed in the thermograms. Examination of the decomposition product after thermal analysis revealed equiaxed grains of γ phase for both alloy D (51.09 Al, 1.83 Nb) and alloy E (50.25 Al, 4.94 Nb). The γ a lattice parameter was equal to the a lattice parameter for pure TiAl (± 0.002). The c lattice parameters increased by 0.003 and 0.009 Å with an increase in the niobium content to 1.83 and 4.94 at.%

Nb respectively, confirming niobium occupies titanium lattice sites.

The uniform dendritic shrinkage patterns on the surfaces of powders of alloy D (51.09 Al, 1.83 Nb) and alloy E (50.25 Al, 4.94 Nb) are the type of patterns (uniform hexagonal patches) that would be expected from an internal nucleation site with dendrites growing out and impinging on the surface of a sphere. In order to obtain the "soccer ball" surface texture with surface nucleation, multiple simultaneous surface nucleation events would be required with an increase in the number of nucleation events required for finer dendritic surface area spacing, a much lower probability of occurrence. The occurrence of internal nucleation is an indication the potent nucleation sites were not isolated and the level of undercooling not large, since surface nucleation would be expected if no potent internal nucleation site were present. Several particles do show signs of surface nucleation such as very large dendritic surface area patches with distinct secondary dendrite arm orientations visible, internal solidification shrinkage and an overall irregular spherical shape (see Figure 92). These particles should have higher levels of undercooling which could result in dendritic α particles with extended aluminum solubilities. Unfortunately the extended solubility of aluminum in the α phase would make it more prone to thermal decomposition to γ during solid state cooling.

A correlation appears to exist for alloy E (50.11 Al, 4.94 Nb) between a decrease in particle size and the increase in

the areas of the dendritic surface relief ("cauliflower" to "soccer ball"). Another trend with decreasing powder size is the higher levels of undercooling associated with the retention of more metastable α phase, observed for alloy E. It is believed for the alloys investigated a higher level of undercooling is associated with the coarser surface texture ("soccer ball") than the finer textures ("cauliflower"). The larger surface areas show more of the hexagonal surface relief and more internal α_2 phase present, which would be promoted by higher levels of undercooling. These coarser surface textures could be formed by a faster dendrite tip velocity resulting in fewer dendrite tips reaching the surface simultaneously. As opposed to the lower level of undercooling and slower dendrite tip velocity which would result in more dendrite tips impinging the surface. Another possibility is a greater number of nucleation events (more than one) occurred in the particles with the finer dendrite surface textures, which would also be an indication of lower levels of undercooling. If the correlation between surface features and undercooling (or nucleant effectiveness) can be verified then a number of possibilities exist for investigating undercooling/nucleation.

The solidification pathway for a majority of the TiAl alloys with niobium added at the expense of titanium is the solidification of primary α and interdendritic γ with partial decomposition of $\alpha \Rightarrow \gamma$ and ordering of the remaining $\alpha \Rightarrow \alpha_2$. A similar solidification pathway is observed in arc melted ingots. Undercooling in the powders extends the solubility of aluminum in

α and increases the amount of α present. With a decrease in powder size solid-state undercooling allows the retention of α which orders to α_2 . An alternate solidification pathway with sufficient undercooling (approximately 20°C based on β liquidus extension of the binary Ti-Al phase diagram [Mis 89]) is the solidification of the β phase, which decomposes in the larger size powders to α' and then to γ . In the finer size powder it is proposed the solid-state undercooling is sufficient to retain the metastable β phase. The only niobium effect observed was a slight decrease in the decomposition kinetics of the α_2 . No other significant niobium affects were observed with additions of up to 5 at.% Nb.

Discussion of TiAl + Nb for the Al Alloy (G)

Alloy G (48.02 Al, 1.99 Nb), had significantly more α_2 than the alloy D (51.09 Al, 1.83 Nb) and alloy E (50.25 Al, 4.94 Nb) in all powder size ranges. The solidification behavior appeared to be similar to alloys D and E except for the phase ratios (more α_2 , less γ). The trends observed with a decrease in powder size of alloys D and E were also observed for alloy G. An increase in the variation in these trends with powders size for alloy G was caused by the presence of the fractured particles, mixing solidification features from larger diameter powders with the finer size powders.

The behavior of alloy G compared to alloys D and E can readily be explained by a consideration of difference in the aluminum content and the binary Ti-Al phase diagram [Mis 89]. An alloy with 48 at.% Al would still solidify as the α

phase with the possibility of an initial primary β phase formation. The composition of primary α dendrites would be lower in aluminum and therefore, less prone to decompose to γ during solid state cooling. The solid state retention of α is greater in alloy G than in alloys D and E (no decomposed α dendrites were observed in alloy G). The hexagonal nature of the primary α dendrites are much clearer in alloy G than alloys D or E, although the same range of microstructural morphologies and surface solidification textures are present for all three alloys. The metastable nature of the α_2 phase in alloy G was demonstrated by its decomposition to form γ during thermal analysis.

It would be expected with less aluminum that undercooling to produce β phase with plane front solidification would be easier; especially with the XRSR process which is believed to provide a faster cooling rate than the PREP process. However, the number of particles with featureless microstructures and surface textures appeared to be less than or about the same as alloy E. What effect the high carbon content (0.233 wt.% C) has on the ability to solidify undercooled β phase can only be estimated based on the known effects of carbon on the Ti-Al alloys. A carbon content of 0.233 wt.% C would shift the $\alpha \Rightarrow \beta$ transformation temperature by about 20°C, the equivalent of the level of undercooling estimated to be required for β formation from the melt in alloys D and E. Alloy G may not be representative of solidification pathways for Ti-Al alloys with the niobium added at the expense of the aluminum due to the high carbon content. The solidification pathway of alloy G is similar

to that for alloys D and E except for the retention of more of the α_2 phase from decomposing to form γ .

Table XXIII
TiAl-Nb Powder X-ray Data

| Alloy | Powder Size in microns | Phases Observed Ratio** | Lattice Parameters α_2 (\AA)* | Lattice Parameters γ (\AA)* |
|---------------|------------------------------|-----------------------------------|---|---|
| D Ti-51Al-2Nb | 177-150 | α_2 : γ 1 : 3.48 | $a = 5.771 \pm 0.024$ $c = 4.605 \pm 0.032$ | $a = 3.998 \pm 0.002$ $c = 4.064 \pm 0.002$ |
| D Ti-51Al-2Nb | 150-105 | α_2 : γ 1 : 1.7 | $a = 5.770 \pm 0.022$ $c = 4.602 \pm 0.030$ | $a = 4.000 \pm 0.003$ $c = 4.061 \pm 0.004$ |
| E Ti-50Al-5Nb | 177-150 | α_2 : γ 1 : 2.53 | $a = 5.774 \pm 0.007$ $c = 4.609 \pm 0.005$ | $a = 3.997 \pm 0.003$ $c = 4.065 \pm 0.004$ |
| E Ti-50Al-5Nb | 150-105 | α_2 : γ 1 : 1.82 | $a = 5.780 \pm 0.005$ $c = 4.606 \pm 0.003$ | $a = 4.001 \pm 0.002$ $c = 4.067 \pm 0.003$ |
| E Ti-50Al-5Nb | 105-74 | α_2 : γ 1.58 : 1 | $a = 5.760 \pm 0.001$ $c = 4.604 \pm 0.002$ | $a = 4.001 \pm 0.003$ $c = 4.060 \pm 0.004$ |
| E Ti-50Al-5Nb | 74-53 | α_2 : γ 3.66 : 1 | $a = 5.775 \pm 0.029$ $c = 4.595 \pm 0.035$ | $a = 4.002 \pm 0.013$ $c = 4.056 \pm 0.016$ |
| E Ti-50Al-5Nb | 53-20 | α_2 : γ 2.7 : 1 | $a = 5.772 \pm 0.037$ $c = 4.629 \pm 0.025$ | $a = 4.005 \pm 0.008$ $c = 4.057 \pm 0.010$ |

* = Parameters from regression analysis of $\sin^2(\theta)$ with an assumed error function.
 ** = Ratio based on 100% α_2 peak (41°) and 60% γ peak (45°).

Table XXIII Continued
TiAl-Nb Powder X-ray Data

| Alloy | Powder Size in microns | Phases Observed Ratio ** | Lattice Parameters α_2 (Å)* | Lattice Parameters γ (Å)* |
|---------------|------------------------|---------------------------------|--|--|
| G Ti-48Al-2Nb | >150 | $\alpha_2 : \gamma$ 3.74 : 1 | $a = 5.743 \pm 0.003$ $c = 4.612 \pm 0.003$ | $a = 4.011 \pm 0.022$ $c = 4.051 \pm 0.029$ |
| G Ti-48Al-2Nb | 150-88 | $\alpha_2 : \gamma$ 16.2 : 1 | $a = 5.747 \pm 0.003$ $c = 4.613 \pm 0.003$ | $a = 4.004 \pm 0.040$ $c = 4.047 \pm 0.040$ |
| G Ti-48Al-2Nb | 88-63 | $\alpha_2 : \gamma$ 10.7 : 1 | $a = 5.739 \pm 0.002$ $c = 4.613 \pm 0.001$ | $a = 4.015 \pm 0.029$ $c = 4.051 \pm 0.034$ |
| G Ti-48Al-2Nb | 63-44 | $\alpha_2 : \gamma$ 18 : 1 | $a = 5.731 \pm 0.005$ $c = 4.604 \pm 0.007$ | $a = 4.017 \pm 0.036$ $c = 4.052 \pm 0.029$ |
| G Ti-48Al-2Nb | 44-30 | $\alpha_2 : \gamma$ 11.3 : 1 | $a = 5.742 \pm 0.004$ $c = 4.616 \pm 0.003$ | $a = 4.003 \pm 0.029$ $c = 4.041 \pm 0.070$ |
| G Ti-48Al-2Nb | 30-20 | $\alpha_2 : \gamma$ 19.9 : 1 | $a = 5.747 \pm 0.001$ $c = 4.617 \pm 0.001$ | $a = 4.039 \pm 0.043$ $c = 4.063 \pm 0.034$ |

* = Parameters from regression analysis of $\sin^2(\theta)$ with an assumed error function.

** = Ratio based on 100% α_2 peak (41°) and 60% γ peak (45°).

Table XXIV
Surface Textures from SEM Analysis
For TiAl+Nb Alloys

| Alloy | Powder Size Microns | "Soccer Ball" Dendritic | "Cauli- flower" Dendritic | Smooth With Surface Striations |
|---------------|---------------------------|-------------------------------|---------------------------------|--------------------------------------|
| D Ti-51Al-2Nb | 177-150 | 60 94% | | 4 6% |
| D Ti-51Al-2Nb | 150-105 | 61 89.7% | | 7 10.3% |
| E Ti-50Al-5Nb | 150-105 | 26 45.6% | 27 47.4% | 4 7% |
| E Ti-50Al-5Nb | 105-74 | 50 65.8% | 19 25% | 7 9.2% |
| G Ti-48Al-2Nb | 150-88 | Yes* | Yes* | Yes* <1% |
| G Ti-48Al-2Nb | 63-44 | Yes* | Yes* | Yes* >1% |

* = Observations using stereo microscope

Table XXV
DTA Results#
For TiAl+Nb Alloys

| Alloy | Powder Size Microns | Max. Temp. (°C) | Exothermic Reaction* (°C) | Endothermic Reactions (°C) |
|---------------|---------------------------|-----------------------|---------------------------------|----------------------------------|
| D Ti-51Al-2Nb | 177-150 | 1032 | O: 603 P: 658 | None |
| D Ti-51Al-2Nb | 150-105 | 1377 | O: 605 P: 664 | None |
| E Ti-50Al-5Nb | 177-150 | 1003 | O: 621 P: 686 | None |
| E Ti-50Al-5Nb | 150-105 | 1010 | O: 617 P: 681 | None |
| E Ti-50Al-5Nb | 105-74 | 1399 | O: 603 P: 678 | O: 1325 P: ---- |
| E Ti-50Al-5Nb | 105-74 | 994 for 90 min## | O: 600 P: 672 | None |

* = Peaks occurred during the first heating cycle only.

O = Onset Temperature

= Heating rate 15°C/min.

S = Slope Change Temperature

= Heating rate 10°C/min.

P = Peak Temperature

Table XXV Continued
DTA Results#
For TiAl+Nb Alloys

| Alloy | Powder Size Microns | Max. Temp. (°C) | Exothermic Reaction* (°C) | Endothermic Reactions (°C) |
|---------------|---------------------------|-----------------------|---------------------------------|----------------------------------|
| G Ti-48Al-2Nb | 150-88 | 1440 | O: 680 P: 716 | O: 1255 P: ---- |
| G Ti-48Al-2Nb | 150-88 | 930 | O: 691 P: 735 | None |
| G Ti-48Al-2Nb | 88-63 | 956 | O: 650 P: 742 P: 864 | None |
| G Ti-48Al-2Nb | 63-44 | 957 | O: 645 P: 740 | None |
| G Ti-48Al-2Nb | 44-30 | 909 | O: 661 S: 705 P: 735 | None |

* = Peaks occurred during the first heating cycle only.

O = Onset Temperature

= Heating rate 15°C/min

S = Slope Change Temperature

= Heating rate 10°C/min

P = Peak Temperature

Table XXVI
Post DTA X-ray Data
TiAl-Nb Powders

| Alloy | Powder Size in Microns | Maximum Temperature (°C) | Lattice Parameter γ (Å*) |
|---------------|------------------------------|--------------------------------|---------------------------------------|
| D Ti-51Al-2Nb | >177 | 1012 2 cycles | a = 3.999±0.002 c = 4.079±0.003 |
| D Ti-51Al-2Nb | 177-150 | 1032 2 cycles | a = 3.998±0.002 c = 4.078±0.002 |
| E Ti-50Al-5Nb | 150-105 | 1010 2 cycles | a = 3.998±0.001 c = 4.083±0.001 |
| E Ti-50Al-5Nb | 105-74 | 994 for 30 min. | a = 3.997±0.002 c = 4.084±0.003 |
| G Ti-48Al-2Nb | 150-88 | 930 1 cycle | a = 4.003±0.002 c = 4.075±0.003 |
| G Ti-48Al-2Nb | 63-44 | 957 1 cycle | a = 4.007±0.003 c = 4.078±0.004 |

* = Parameters obtained from regression analysis of $\sin^2(\theta)$ values
and an assumed error function

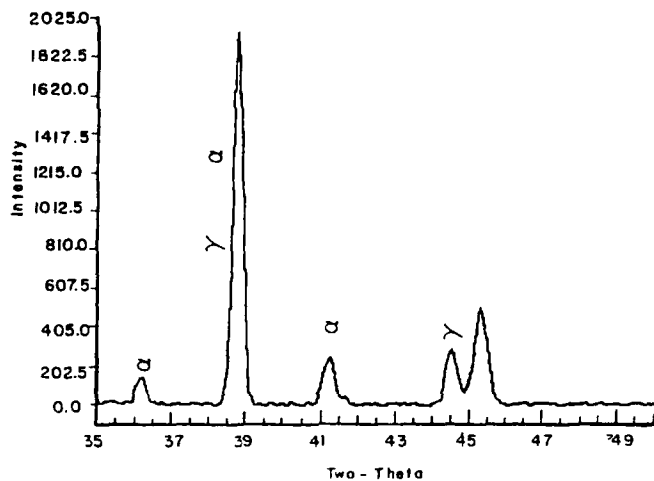


Figure 69a X-ray trace, alloy D (Ti47-Al51-Nb2),
150-177 microns.

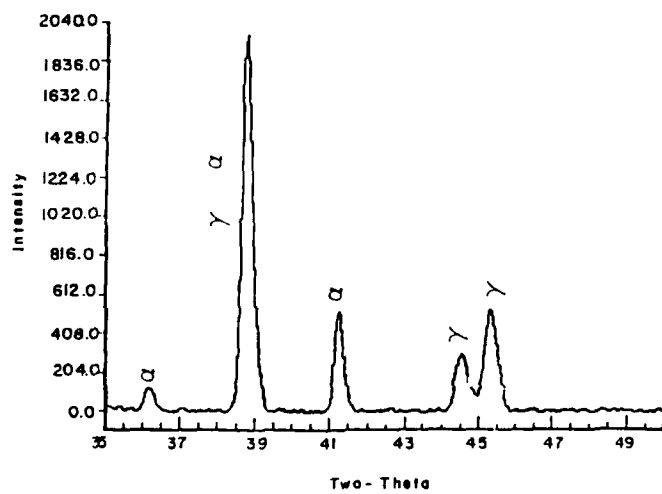


Figure 69b X-ray trace, alloy D (Ti47-Al51-Nb2),
105-150 microns.

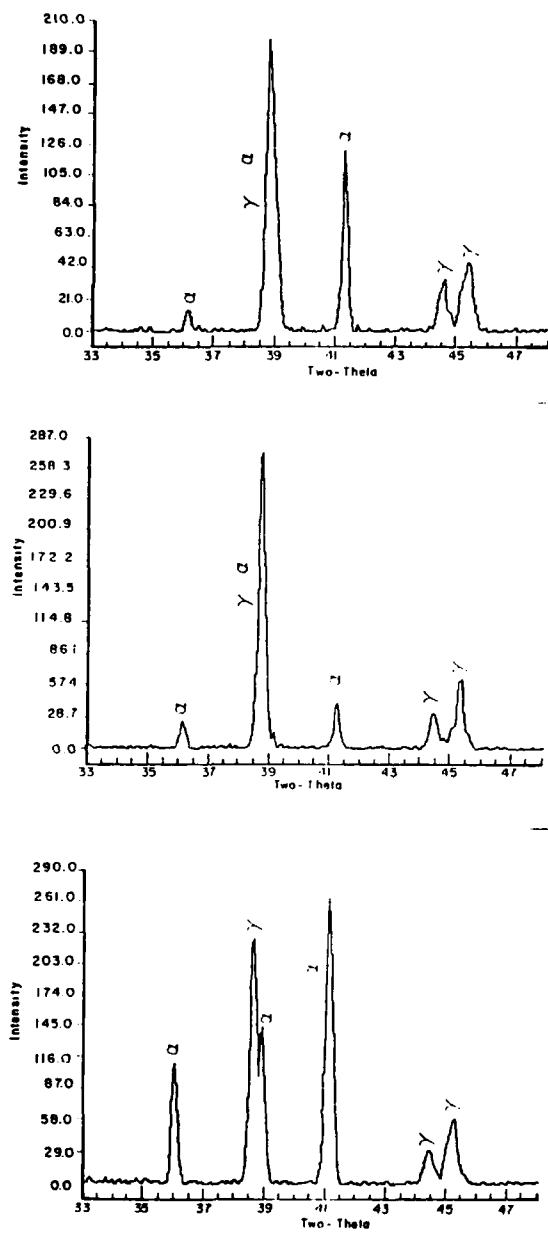


Figure 70 X-ray trace, alloy E (Ti45-Al50-Nb5),
 a) 150-177 microns.
 b) 74-105 microns.
 c) 20-53 microns.

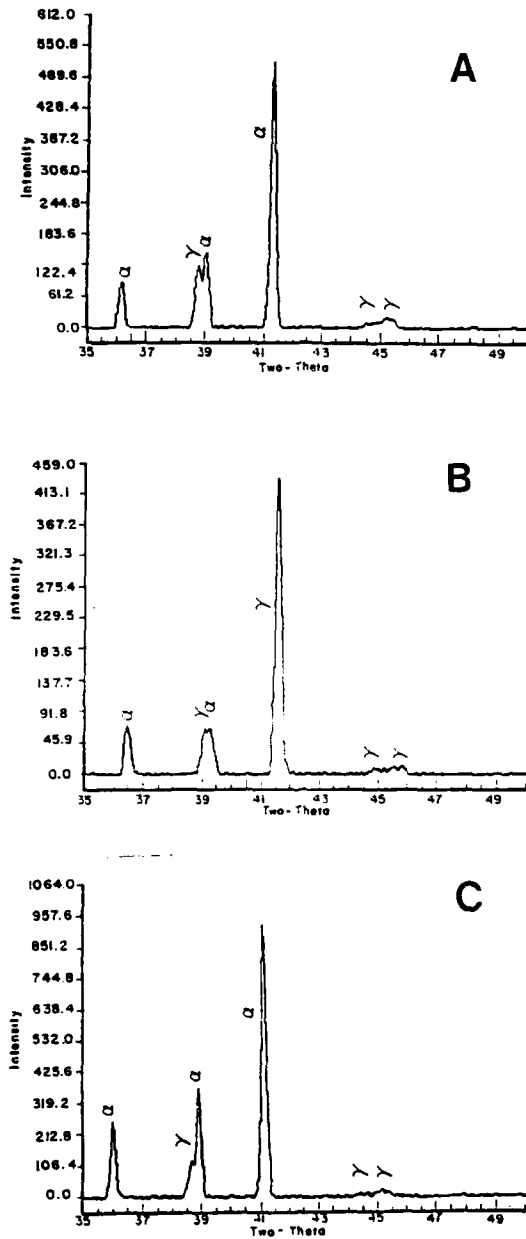
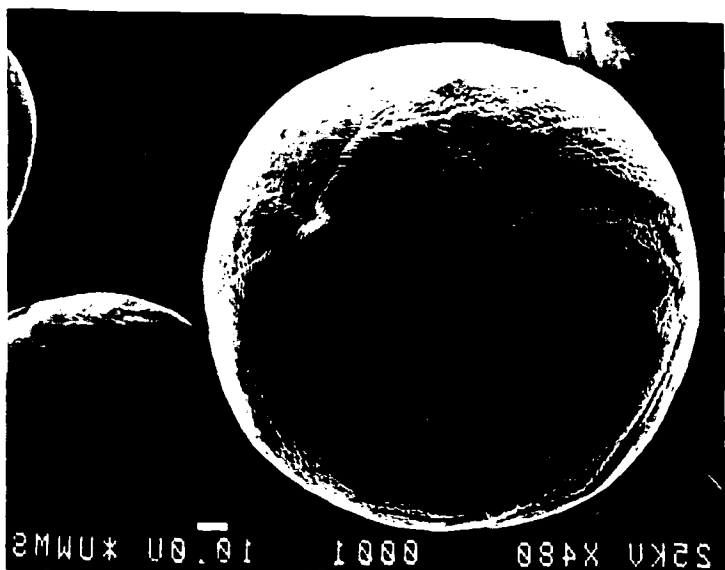


Figure 71 X-ray trace, alloy G (Ti₅₀-Al₄₈-Nb₂),
 a) 177-150 microns.
 b) 44-63 microns.
 c) 20-30 microns.



150



Figure 72 Surface relief, alloy D (Ti47-Al51-Nb2),
dendritic surface texture.

Figure 73 Surface relief, alloy D (Ti47-Al51-Nb2),
smooth surface with surface striations.

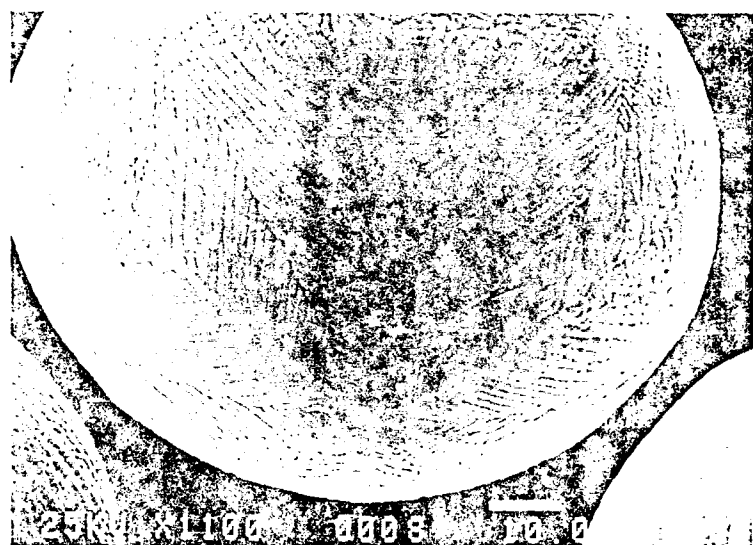


Figure 74 60° dendrite orientations on surface,
alloy E (Ti45-Al50-Nb5).

152



Figure 75 Microstructure, alloy D (Ti47-Al51-Nb2),
BM and CM features in AM matrix, 105-150 microns.

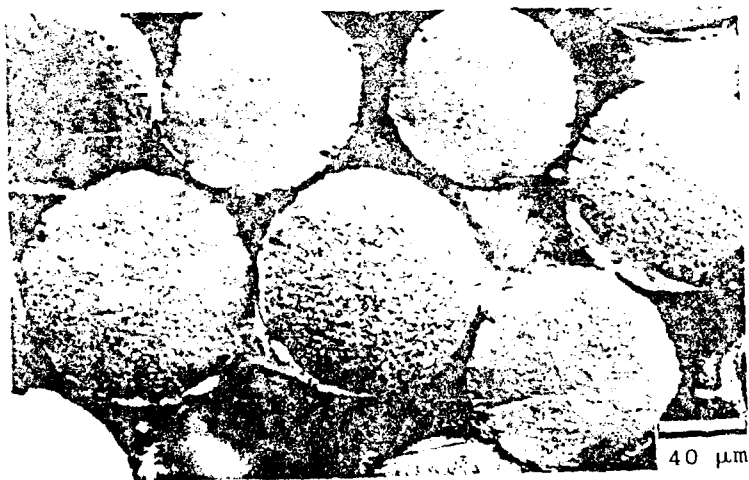


Figure 76 Microstructure, alloy D (Ti47-Al51-Nb2),
small grain size in AM type particles,
5-105 microns.

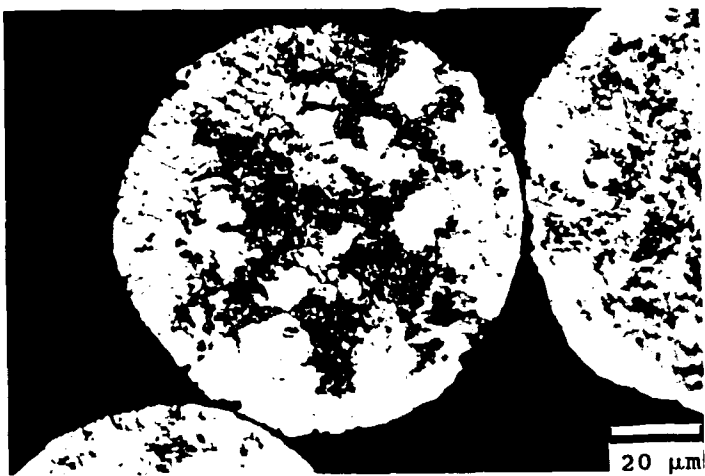


Figure 77 Microstructure, alloy D (Ti47-Al51-Nb2),
BM features in AM matrix, 5-105 microns.



Figure 78 Microstructure, alloy D (Ti47-Al51-Nb2),
CM features in AM matrix, 5-105 microns.
Note: 60° dendrite orientations.

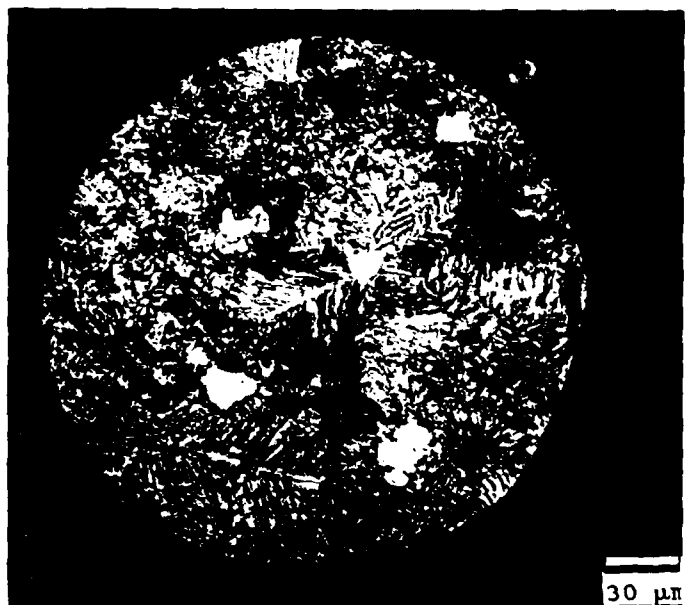


Figure 79 Microstructure, alloy D (Ti47-Al51-Nb2),
CM features in AM matrix.
Note: etching response of dendrites.

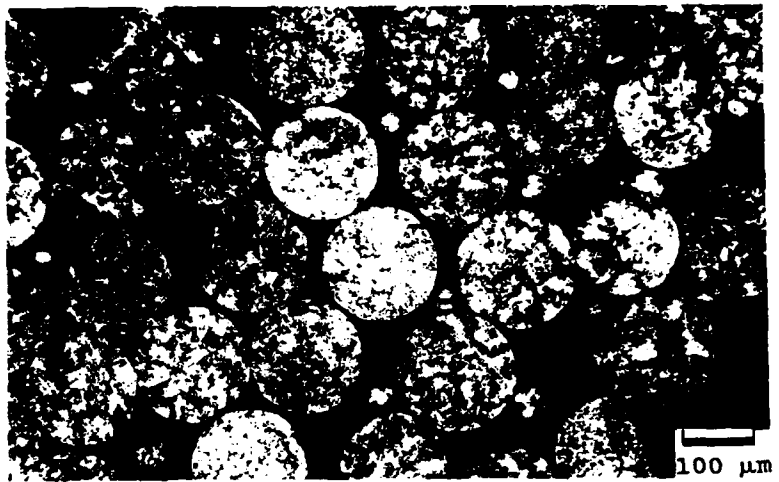


Figure 80 Microstructure, alloy E (Ti45-Al50-Nb5), variation in microstructures, 150-177 microns.

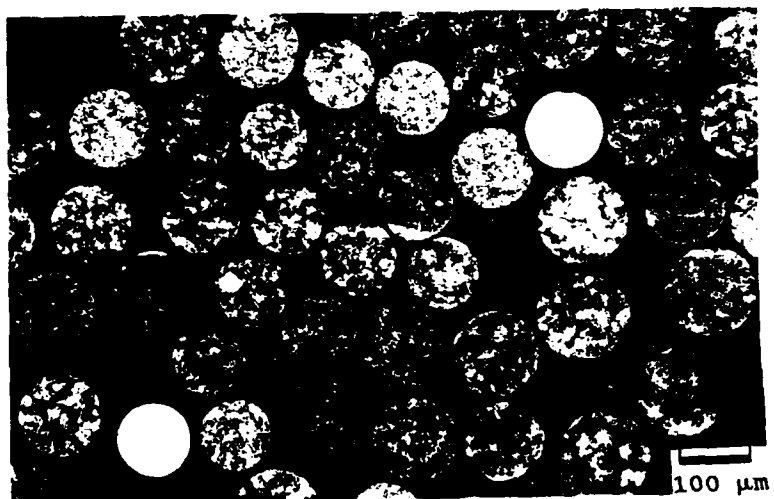


Figure 81 Microstructure, alloy E (Ti45-Al50-Nb5), variation in microstructures, 105-150 microns.
Note: increase in featureless particles.

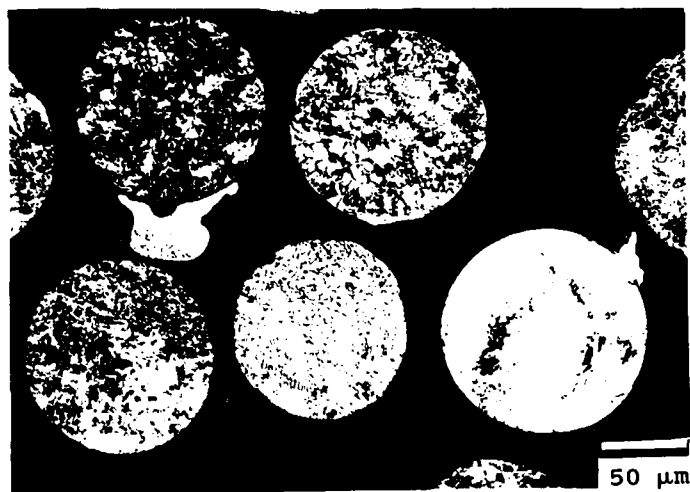


Figure 82 Microstructure, alloy E (Ti45-Al50-Nb5),
AM, BM, CM and DM, features, 105-150 microns.



Figure 83 Microstructure, alloy E (Ti45-Al50-Nb5),
Fine grain size in AM type particles,
105-150 microns.

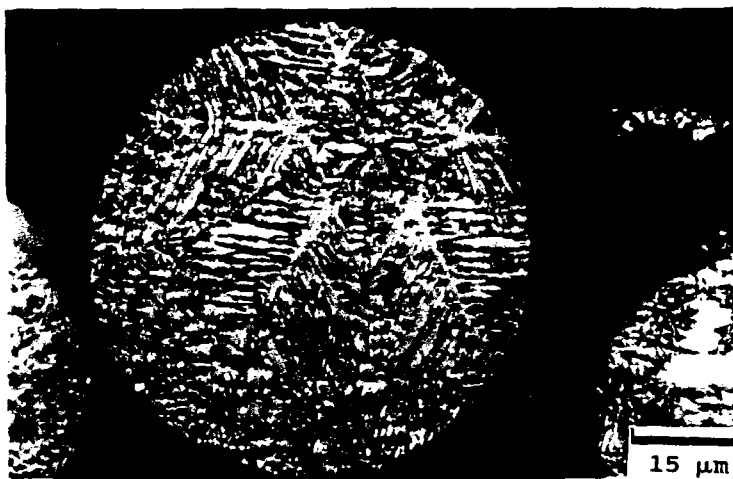


Figure 84 60° orientation of dendrites, alloy E
(Ti45-Al50-Nb5), 53-74 microns.

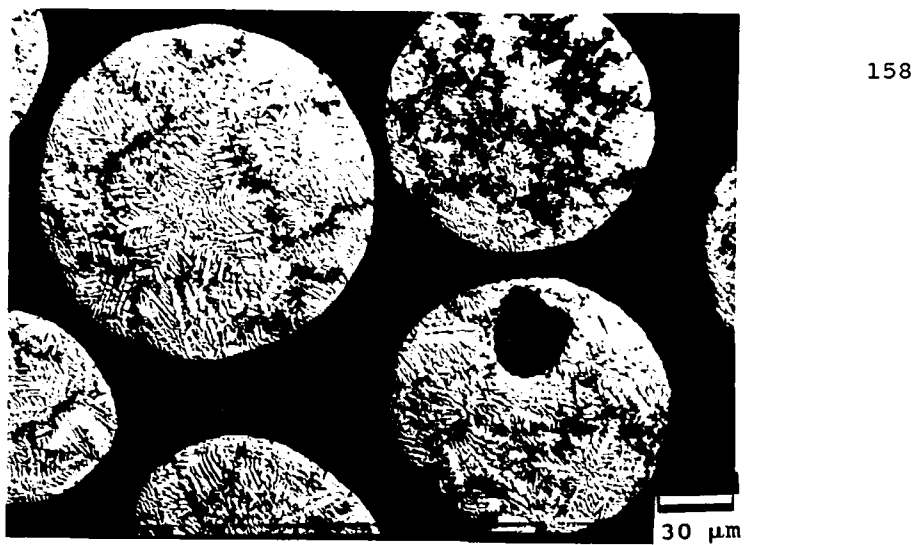


Figure 85 Microstructure, alloy G (Ti50-Al48-Nb2),
CM features in AM matrix, 88-150 microns.

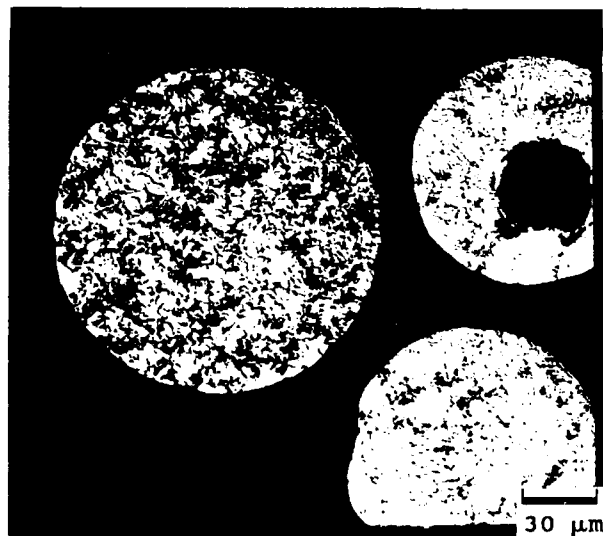
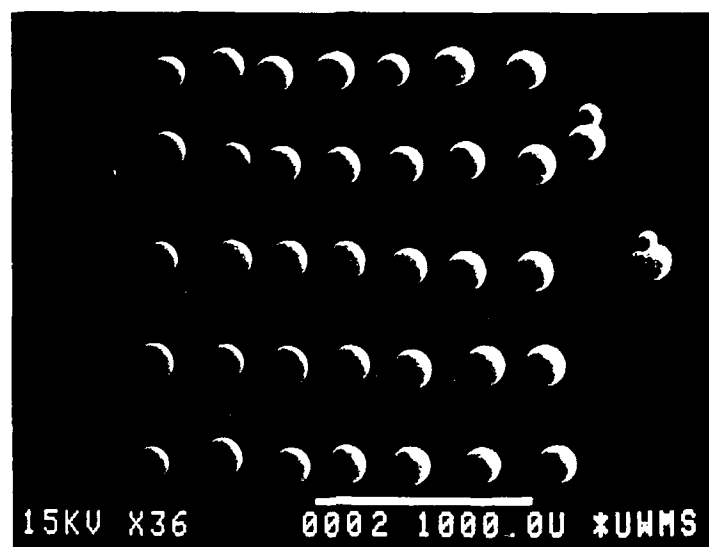


Figure 86 Microstructure, alloy G (Ti50-Al48-Nb2),
BM features in AM matrix, 88-150 microns.

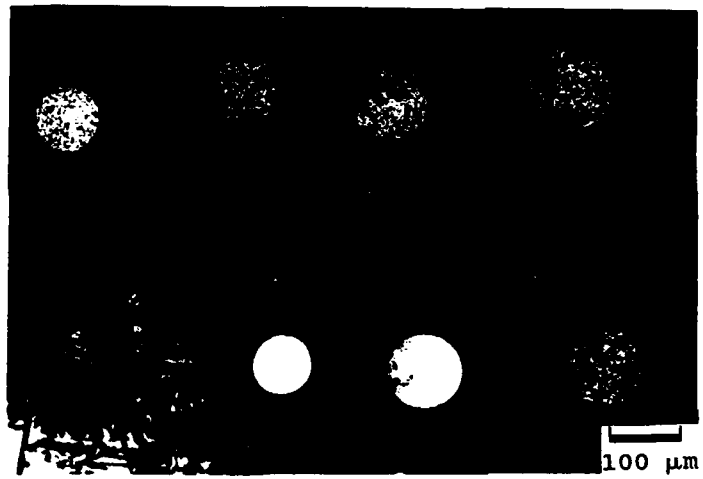


Coordinate System

| | | | | |
|----|----|----------------|-----|----------------|
| S1 | G1 | C1 | FS | F1 |
| S2 | G2 | C2 | F9 | F2 |
| S3 | G3 | C3 | F10 | F3 |
| S4 | G4 | C4 | F11 | F4 |
| S5 | G5 | C5 | F12 | F5 |
| S6 | G6 | C6 | F13 | F6 |
| S7 | G7 | C7 | F14 | F7 |
| | | T ₂ | | T ₁ |

Figure 87

Surface relief, alloy E (Ti45-Al50-Nb5),
sorted particles, 7 "soccer ball", 7 "golf ball",
7 "cauliflower", 14 featureless, and coordinate
system, 150-177 microns.



Coordinate System
F1 F2 F3 F4
F8 F9 F10 F11

Figure 88 Microstructures, alloy E (Ti45-Al50-Nb5), sorted particles, 8 featureless, and coordinate system, 150-177 microns.

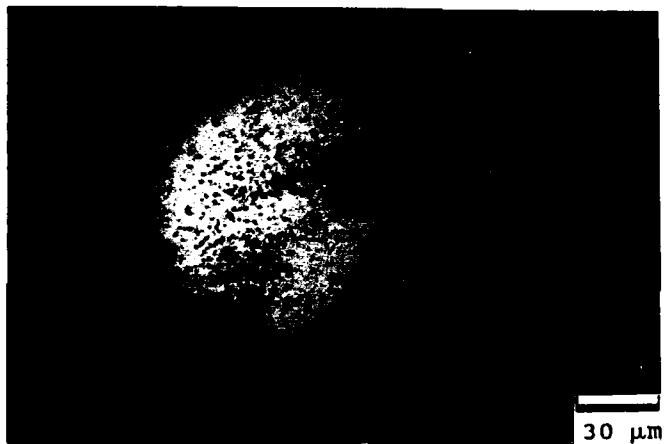


Figure 89 Microstructures, alloy E (Ti45-Al50-Nb5),
particle F10, type DM features.

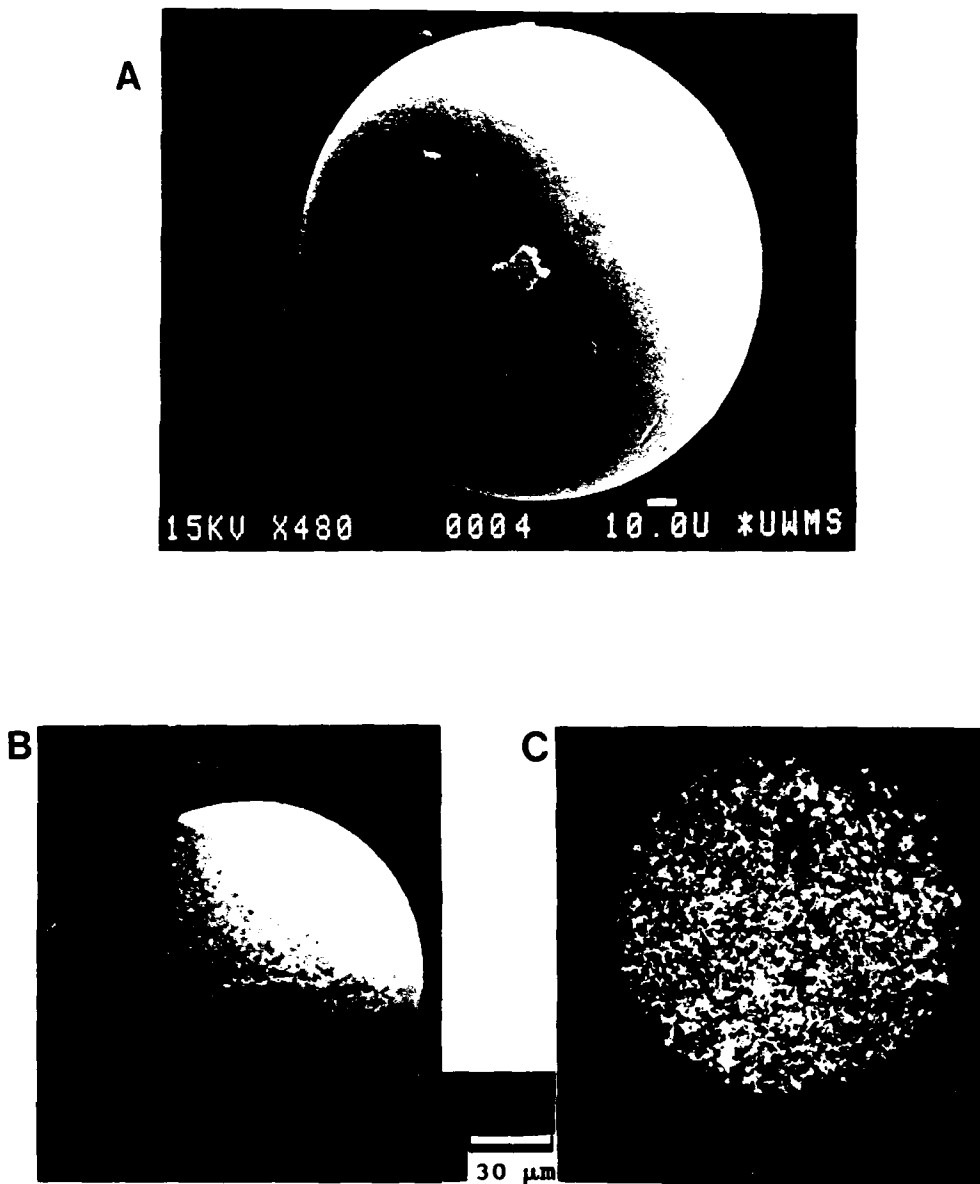
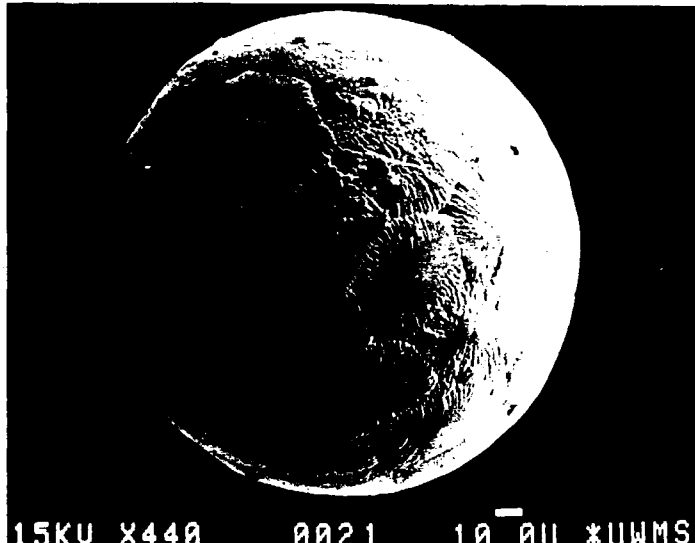


Figure 90

Alloy (Ti45-Al50-Nb), Particle F5
a) Surface relief, smooth + surface striations
b) Microstructure, Unetched DIC contrast
Note: fine grain size.
c) Microstructure, Etched, type AM features.

163



15KV X440 0021 10.0U *UWMS

Figure 91a Surface relief, alloy E (Ti45-Al50-Nb5),
particle S3, dendritic "soccer ball".

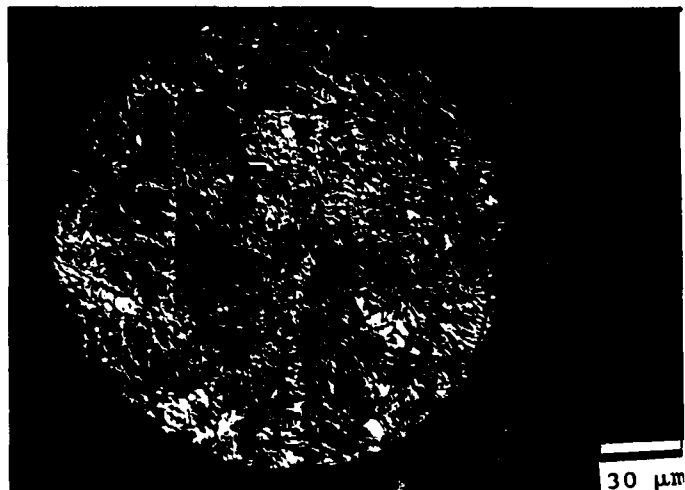
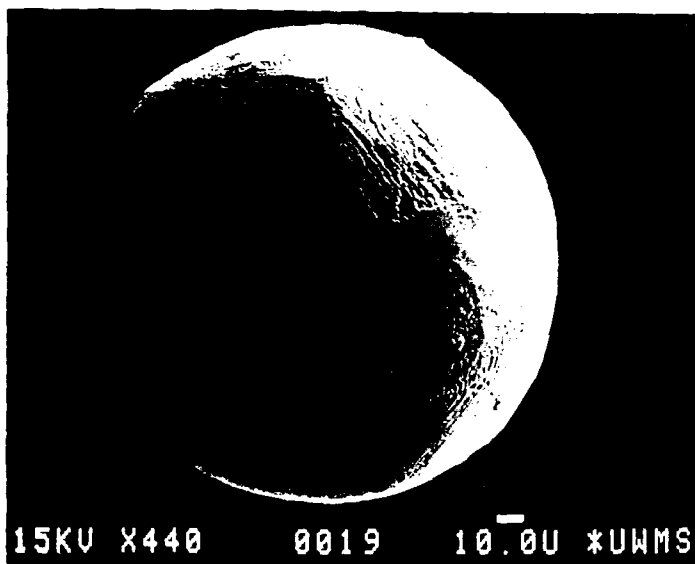


Figure 91b Microstructures, alloy E (Ti45-Al-50-Nb5),
particle S3, AM and BM features.



164

Figure 92a Surface relief, alloy E (Ti45-Al50-Nb5),
 particle S7, dendritic "soccer ball".

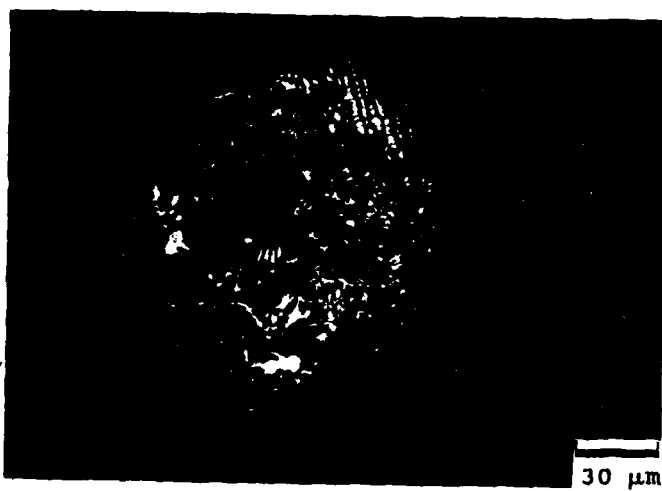


Figure 92b Microstructures, alloy E (Ti45-Al50-Nb5),
 particle S7, type CM features. Note: Gas pore,
 and internal solidification shrinkage
 (indicated by arrows).

165

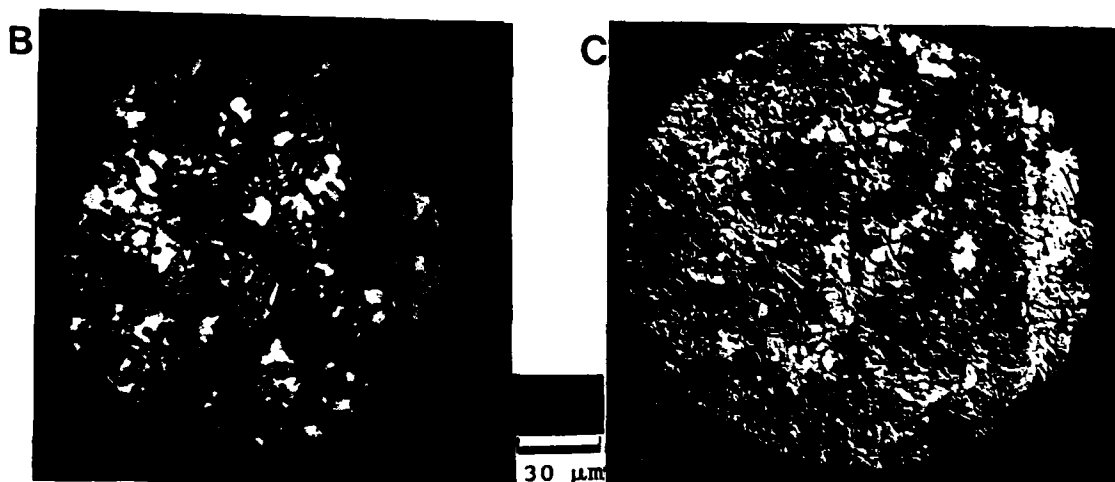
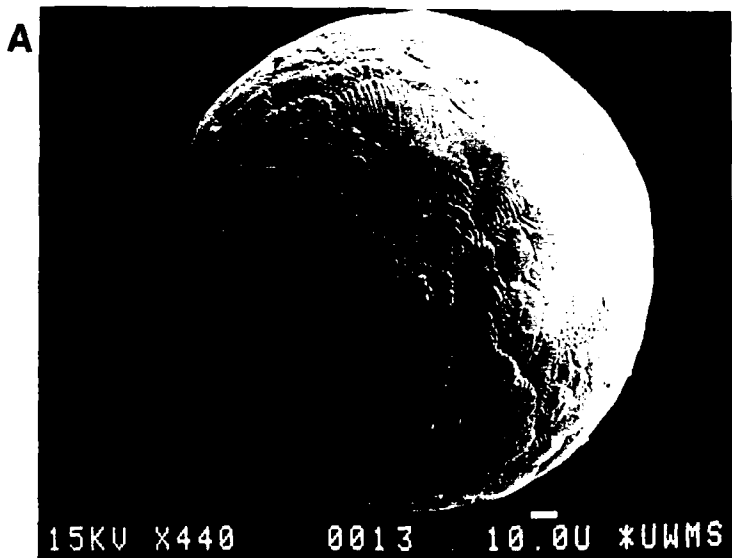
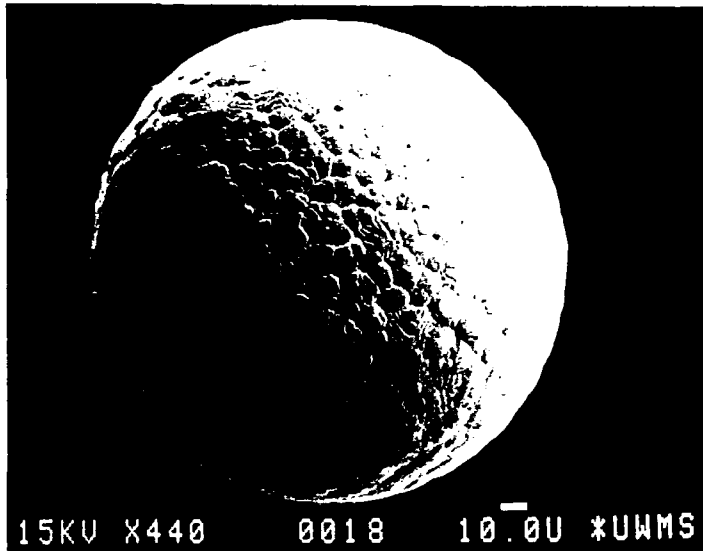


Figure 93

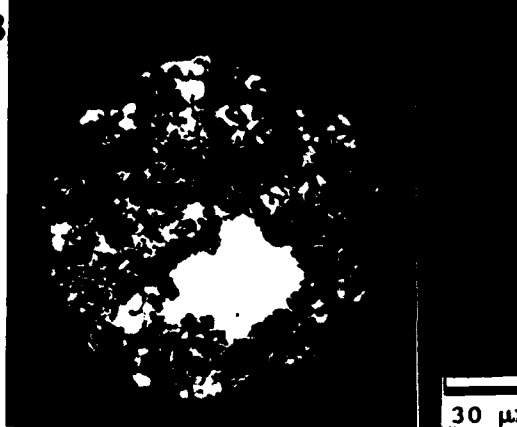
Alloy E (Ti45-Al50-Nb5), Particle C6
a) Surface relief, dendriti 'cauliflower'.
b) Microstructure, BM and AM features,
1st cross section.
c) Microstructure, BM and AM features,
2nd cross section.

166

A



B



C

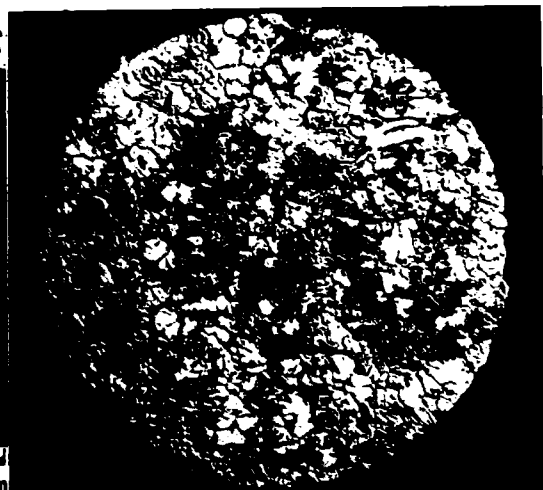


Figure 94 Alloy E (Ti45-Al50-Nb5), G Type Particle
a) Surface relief, particle G4,
dendritic "golf ball".
b) Microstructure, particle G5,
BM and AM features, 1st cross section.
c) Microstructures, particle G5,
BM and AM features, 2nd cross section.

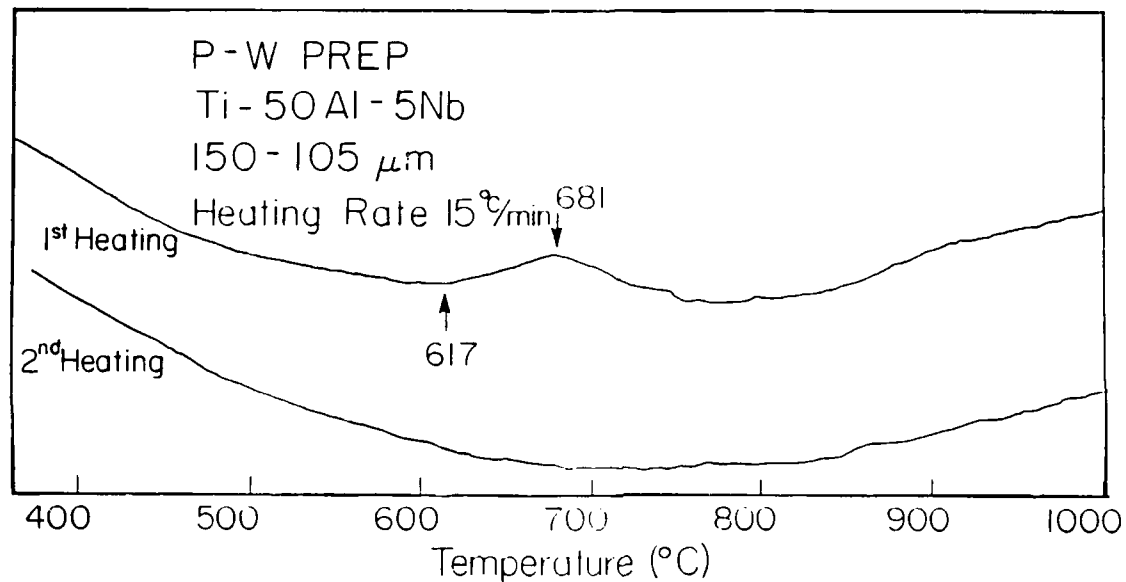


Figure 95a DTA thermogram, alloy E (Ti45-Al50-Nb5),
105-150 microns.

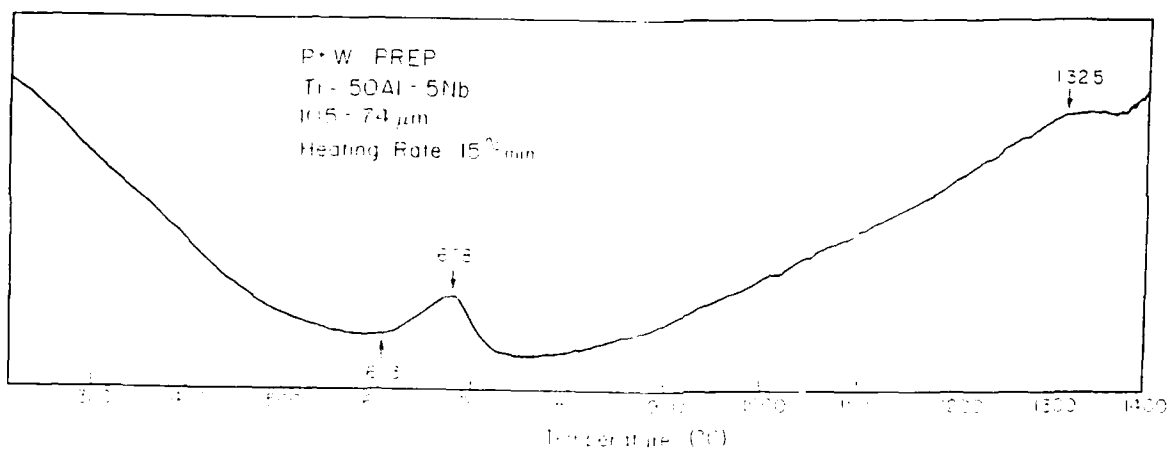


Figure 95b DTA thermogram, alloy E (Ti45-Al50-Nb5), 74-105 microns.

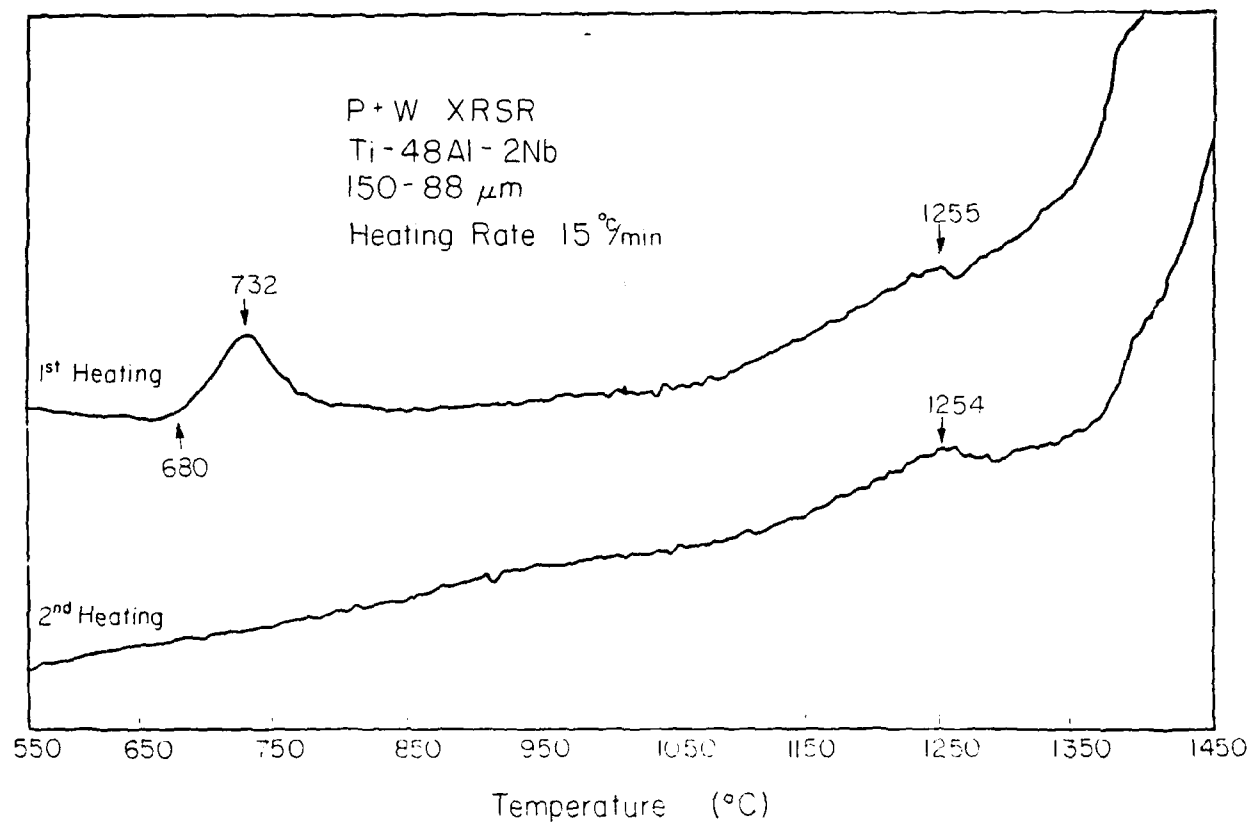


Figure 96a

DTA thermogram, alloy G (Ti₅₀-Al₄₈-Nb₂),
88-150 microns.

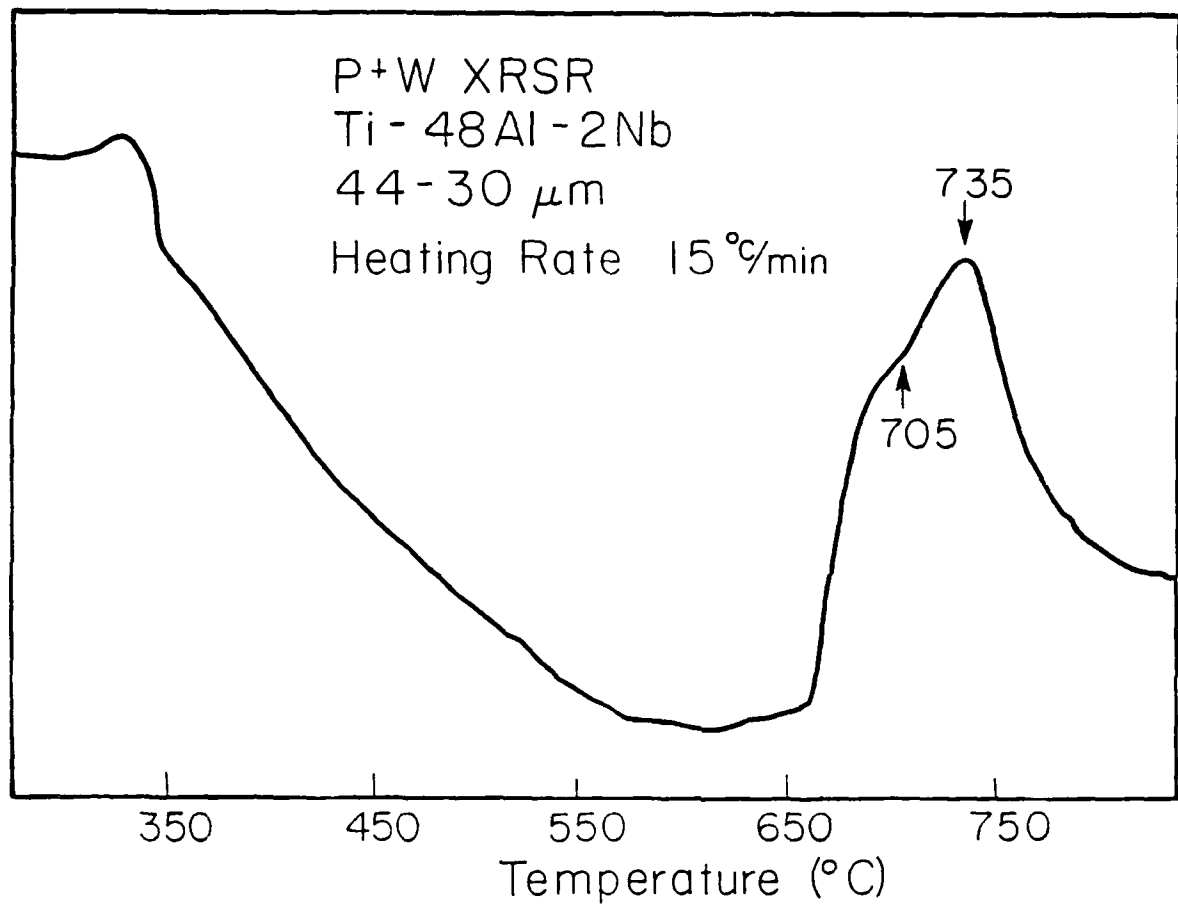


Figure 96b DTA thermogram, alloy G (Ti50-Al48-Nb2),
30-4 μ microns.

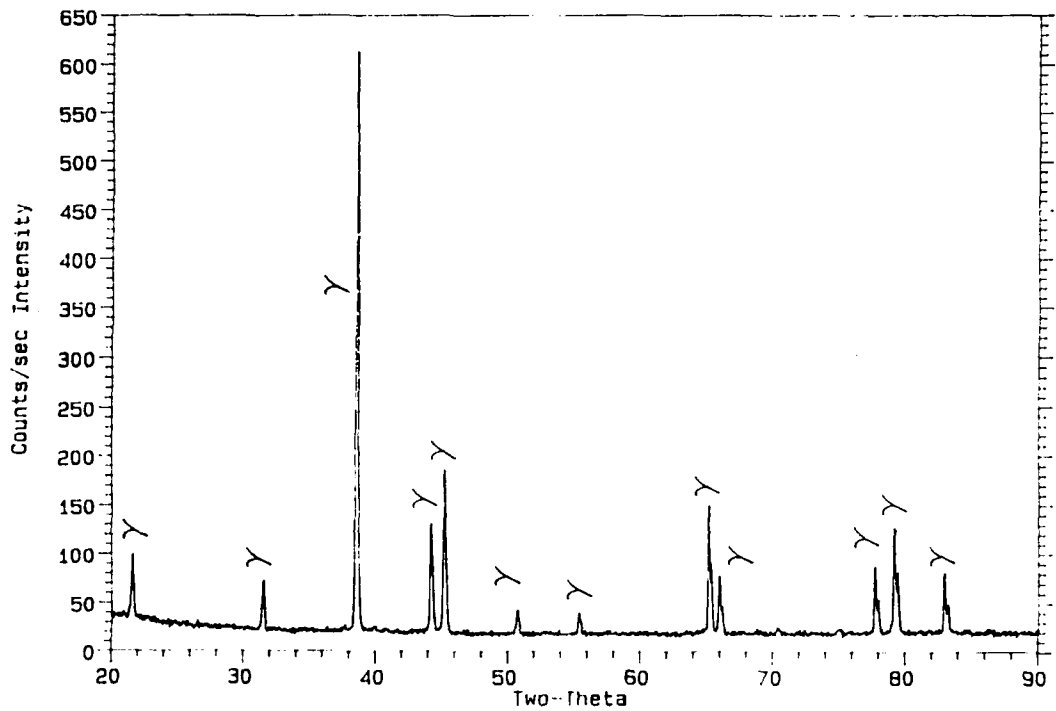


Figure 97 Post-DTA x-ray trace, alloy E (Ti45-Al50-Nb5),
74-105 microns, $T_{max} = 994^\circ\text{C}$ for 30 min.



Figure 98 Post-DTA microstructure, alloy D (Ti47-Al51-Nb2).
Note: 2 cycles Tmax = 1375°C.



Figure 99 Post-DTA microstructure, alloy E (Ti45-Al50-Nb5).
Note: Tmax = 994°C for 30 min.

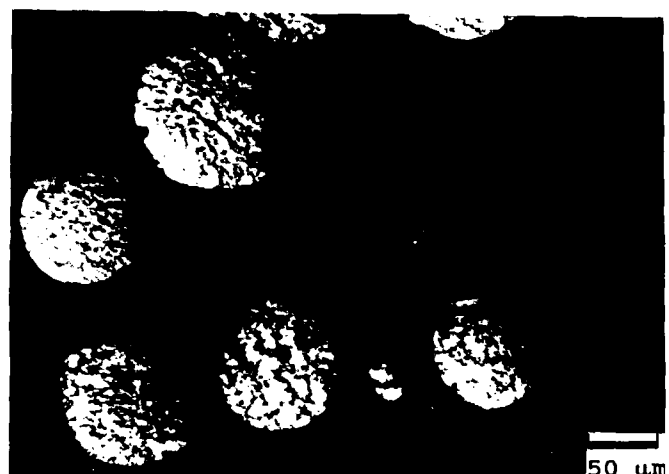


Figure 10J Post-DTA microstructure, alloy G (Ti₅₀-Al₄₈-Nb₂).
Note: Tmax = 925°C.

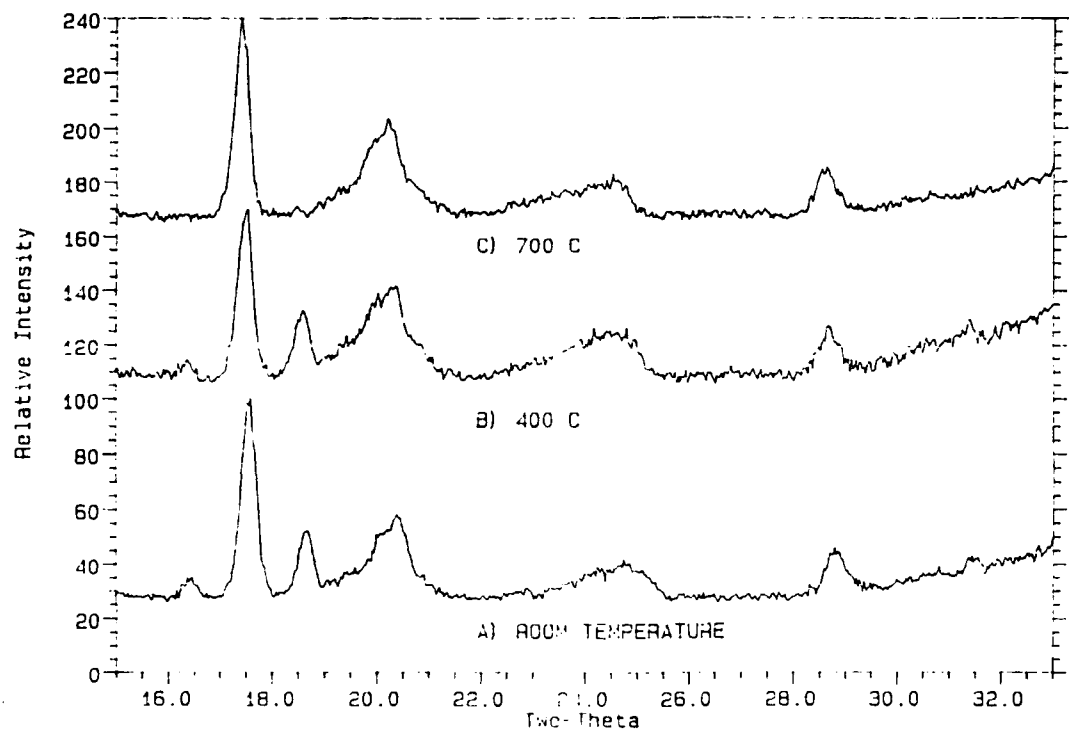


Figure 101 High temperature x-ray traces,
alloy E (Ti45-Al50-Nb5), 74-105 microns.
Note: Mo K_α x-ray source.

Summary of Powder Processing Results

For the Ti_3Al alloys produced by the PREP process, the level of melt undercooling proved to be insufficient to alter the solidification pathway from β phase formation. The most dramatic undercooling effects were observed in subsequent solid state transformations. Solid state undercooling resulted in the partial retention of disordered α' in the binary Ti_3Al alloy. Suppression of the martensitic transformation in the binary alloy Ti_3Al was not possible. In the Ti_3Al alloys with niobium additions, the martensitic transformation could be suppressed and metastable β phase retained to room temperature, indicating a diffusional component in the martensitic transformation for the ternary alloys. The retention of metastable β phase is significant for controlling microstructural development and for use during subsequent consolidation.

Particle interactions in the binary Ti_3Al alloys with 5 at.% niobium have been shown to lead to higher solidification front velocities and homogeneous featureless microstructures. Thus, variations in particle morphologies can also occur as a result of particle interactions.

For the $TiAl$ alloys with niobium additions up to 5 at.% the binary Ti-Al phase diagram [Mis89] could be used to describe the solidification behavior by treating the alloy as if it were a binary and using the aluminum content of the ternary alloy. The solidification behavior starts with primary α solidification with the undercooling extending the solubility of the α phase, followed by interdendritic solidification of γ .

During subsequent solid state cooling decomposition of some of the metastable α phase to equilibrium γ occurred with subsequent ordering of the remaining $\alpha = \alpha_2$. Solid state undercooling was sufficient to retain the metastable α phase with decreasing powder size, but not to prevent ordering of α to α_2 . An alternate solidification pathway for the TiAl alloys with niobium additions was identified which only required an estimated 20°C of undercooling (extension of the β liquidus). This solidification pathway involved initial β solidification, which in the finer powder sizes is believed to have been retained down to room temperature. In the larger size powders the β phase is believed to decomposed to α' and then to γ . The undercooling needed to form metastable β phase was obtained even in the larger size powders.

4.0 Summary and conclusions

Experimental work on the binary Ti-Al system is nearly complete except for a few experiments to verify the phase diagram modeling currently in progress. The experimental results have helped fill the gaps in our understanding of the Ti-Al phase equilibria. The adjustments to the modeling parameters are nearly complete, and a finalized calculated diagram is expected in the near future. Establishment of the binary phase equilibria and the initial experimental work in the ternary system will benefit the current efforts toward modeling the ternary system. A preliminary copy of the current calculations of the binary system have been forwarded to NBS for use on the ternary model.

With the establishment of the preliminary liquidus surface and 1200°C isothermal section, significant progress has been made in expanding our knowledge of the ternary system. Much work is still needed to clarify areas of uncertainty. However, a basis has been established to move forward, and it is now possible to identify some new research opportunities. For example, identification of the solidification pathways for the powder processed ternary alloys of Ti-Al-Nb system with Nb additions up to 5 at.% provides a basis for extending this work to higher niobium additions.

References

[Ban87] D. Banerjee, T. Naudi and A.K. Gogia, *Scripta Met.*, 21 (1987) 597.

[Ban88] D. Banerjee, A.K. Gogia, T.K. Naudi and V.A. Joshi, *Acta Met.* 36 (1988) 871.

[Ben89] L.A. Bendersky and W.J. Boettinger, *Mat.Res. Soc. Symp. Proc.*, 133 (1989) 45.

[Bla69] M. J. Blackburn, in the *Science, Technology, and Application of Titanium*, R. I. Jaffee and N. E. Promisel, eds., Pergamon Press, NY (1969) 633.

[Bla78] M. J. Blackburn, and M. P. Smith, "The Understanding and Exploitation of Alloys Based on the Compound TiAl (γ Phase)", Air Force Technical Report AFML-TR-78-78, (Period May 74 - Mar 77), WPAFB, Dayton, Ohio, June 1978.

[Boe89] W. J. Boettinger, L. A. Bendersky, J. W. Cahn and U. R. Kattner, Semi-annual Technical Report for the period October 1, 1988 to March 31, 1989.

[Bom86] H. B. Bomberger and F. H. Froes, "Prospects for Developing Novel Titanium Alloys Using Rapid Solidification", Proceedings 4th Symposium on Titanium Rapid Solidification Technology, New Orleans, Louisiana, USA, March 2-6 (1986); Titanium Rapid Solidification Technology, Ed. F. H. Froes and D. Eylon, pp. 21-43 (1986).

[Bor85] R. Bormann, D.-Y. Yu, R.H. Hammond, A. Marshall and T. H. Geballe, In "Rapidly Quenched Metals V", Edited by S. Steeb and H. Warlimont, Elsevier Sci. Pub. (1985) 879.

[Bor88] R. J. Borg and G. J. Dienes, An Introduction to Solid-State Diffusion, Academic Press, Inc., NY, 1988, p. 173.

[Cha79] Y. A. Chang, J. P. Neumann, A. Mikula and Goldberg, INCRA Monograph VI *Phase Diagrams and Thermodynamic Properties of Ternary Copper-Metal Systems*, The International Copper Research Ass'n, Inc., New York, 1979.

[Gar65] M. Garfinkle and H. M. Davis, "Reaction of Liquid Titanium with Some Refractory Compounds", *Trans. ASM*, vol. 58, pp. 520-530, (1965).

[Gra87] J. A. Graves, "Rapid Solidification of High Temperature Aluminide Compound", PhD Thesis, University of Wisconsin-Madison (1987).

[Hei64] K. J. F. Heinrich, *Adv. X-ray Anal.*, 7, 325 (1964).

[Jew89] T. J. Jewett, J. C. Lin, K. C. Hsieh, N. R. Bonda, Y. A. Chang and J. H. Perepezko, *Mat. Res. Soc. Symp. Proc.*, 133 (1989) 69.

[Kin61] H. W. King and T. B. Massalski, *J. Inst. Metals*, 90, 486 (1961-62).

[Kir57] J. S. Kirkaldy, *Can.J. Phys.* 36, (1957) 435.

[Kon86] D.G. Konitzer, I.P. Jones and H.L. Fraser, *Scripta Met.*, 20 (1986) 265.

[Lip85] H.A. Lipsitt. *Mat. Res. Soc. Symp. Proc.*, (1985) 351.

[Llo87] G. E. Lloyd, *Mineral. Mag.*, 51, 3 (1987).

[Lun66] C.E. Lundin and A. S. Yamamoto, *Trans. AIME*, 236 (1966) 863.

[Lyo73] S. R. Lyon, S. Inouye, C. A. Alexander and D. E. Niesz, "The Introduction of Titanium with Refractory Oxides", Proceedings 2nd International Conference on Titanium, Cambridge, Massachusetts, USA, May 2-5 (1972); Titanium Science and Technology, Ed. R. I. Jaffee and H. M. Burte, vol. 1, pp. 271-284, (1973).

[Mat33] C. Matano, *Jpn. J. Phys.*, 1933, 8, 109.

[McC88] C. McCullough, J. J. Valencia, H. Mateos, C. G. Levi, and R. Mehrabian, "The High Temperature α Field in the Titanium- β minum Phase Diagram", *Scripta Metallurgica*, vol. 22, pp. 1131 -136 (1988).

[McC89] C. McCullough, J.J. Valencia, C.G. Levi and R. Mehrabian, *Acta Met.* 37 (1989) 1321.

[Mis89] J. C. Mishurda, J. C. Lin, Y. A. Chang, and J. H. Perepezko, in High-Temperature Ordered Intermetallic Alloys III (Eds.: C. T. Liu, A. I. Taub, N. S. Stoloff and C. C. Koch), MRS Symposium Proc., 1989, 133, 57.

[Mur89] K. Muraleedharan and D. Banerjee, *Met. Trans.*, 20A (1989) 1139.

[Nel45] J. B. Nelson and D. P. Riley, *Proc. Phys. Soc.*, 57, 160 (1945).

[Rhi56] F. Rhines, "Phase Diagrams in Metallurgy", Their Development and Application, McGraw-Hill, NY 1956.

[Sas77] S.M.L. Sastry and H.A. Lipsitt, *Met. Trans.*, 8A (1977) 1543.

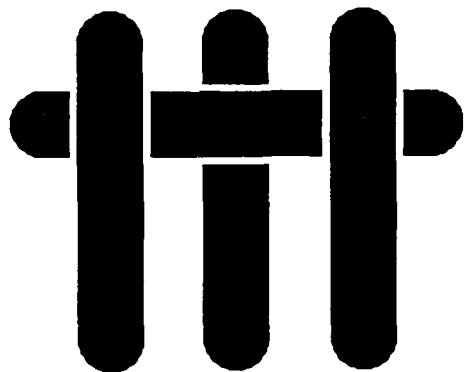
[Shu84] R. D. Shull, A. J. McAlister and R. C. Reno, "Phase Equilibria in the Titanium-Aluminum System", Proceedings 5th International Conference on Titanium, Munich, FRG, Sept. 10-14 (1984); Titanium Science and Technology, Ed. G. Lutjering, U. Zwicker, and Bunk, vol. 3, pp. 1459-1466, (1985).

[Sir86] S. Sircar, K. Narasimhan, and K. Mukherjee, "An Investigation of the Ordered D019 Phase Formation in the Ti-Al System", Journal of Materials Science, vol. 21, pp. 4143-4146, (1986).

[Str88] R. Strychor, J.C. Williams and W.A. Soffa, Met. Trans., 19A (1988) 1321.

[Web57] B. C. Weber, W. M. Thompson, H. O. Bielstein, and M. A. Schwartz, "Ceramic Crucible for Melting Titanium", Journal of the American Ceramic Society, vol. 40, No. 11, pp. 363-373, (1957).

M A T E R I A L S



MICROSTRUCTURAL ANALYSIS OF RAPIDLY SOLIDIFIED Ti-Al-X POWDERS

by

C.McCullough, J.J.Valencia, C.G.Levi and R.Mehrabian.

Materials Department
College of Engineering
University of California
Santa Barbara, CA 93106

ABSTRACT

Microstructural evolution in Ti-48%Al powders with additions of Ta and C is analyzed with the aid of levitation melting/solidification experiments on Ti-48%Al and Ti-45%Al alloys with and without additions of C, where the supercooling can be quantified and related to the observed microstructures. Supercoolings up to 258K were achieved in the binary alloys; in all cases the primary solidification phase was β , and the relative amount of γ segregate decreased with increasing ΔT . Analysis of PREP and XSR powders of nominally identical composition revealed major differences in the primary phase selection. The PREP powders showed evidence of β formation at all particle sizes, while the XSR powders were overwhelmingly α in the coarser powder sizes, with the proportion of primary β increasing with decreasing particle size. This effect was ascribed primarily to the carbon contamination introduced in the XSR process. C appears to shift the phase equilibria so that α is the stable primary phase in the ternary alloys. There is evidence of Ti_2AlC formation if the C content is larger than ~1% (0.3wt%), but the carbide appears to have a marginal role in the phase selection process. Even at the higher carbon contents, the phase selection reverts to primary β at high supercoolings, presumably due to a kinetic preference for the latter phase. The decomposition of the α_2 phase--resulting from solid-state transformations of the primary dendrites--into the $(\alpha_2 + \gamma)$ lath microconstituent, appears to be suppressed by Ta additions and the increased cooling rate associated with reduction in powder particle size. It was also observed that martensite forms in segregate-free powders, presumably because the particles solidify completely as single phase β . When martensite is formed, the room temperature microstructure is disordered α , rather than the α_2 or $(\alpha_2 + \gamma)$ commonly observed in the dendritic powders.

1. INTRODUCTION

In pursuit of a new generation of materials for high temperature aerospace applications, attention has recently focused on alloys based on titanium aluminides. Of these intermetallics, γ -TiAl (L1₀) offers the best combination of high temperature stiffness, creep and oxidation resistance, but its development is hindered by its low room-temperature toughness [85Lip]. Tensile ductility of the base material is somewhat improved (up to ~2%) in alloys slightly leaner in Al than the stoichiometric compound (e.g. 48%Al)¹, where small amounts of α_2 -Ti₃Al (DO₁₉) are introduced in the microstructure [87Bla, 88Sas]. Further toughening approaches under investigation include compositing schemes wherein ductile phase particles are blended with rapidly solidified TiAl powders and consolidated by powder metallurgy [88Ell], or the intermetallic is deposited by plasma spraying onto coated fibers to produce frictionally-constrained fiber-reinforced composites. In either case, the alloy droplets undergo rapid solidification prior to or during the compositing step.

Potential benefits of rapid solidification processing (RSP) of intermetallics include microstructural refinement, reduction of harmful segregation, increased solid-solubility of ternary additions and the production of metastable phases which may facilitate consolidation and forming. Microstructural evolution is usually elucidated from extensive characterization of the resulting powder, and rationalized on the basis of changes in cooling rate (and less frequently supercooling) as a function of particle size. Experimental verification of these variables during atomization, however, is extremely difficult, if not impossible.

This paper deals with the use of supercooling experiments as an essential component of the characterization of rapidly solidified powders. Electromagnetic levitation/melting was used to produce rapidly solidified microstructures under known conditions of supercooling (and cooling rate). An experimental phase selection map may be developed in this manner and compared with the thermodynamic hierarchy deduced from the phase diagram [88Val]. The knowledge thus acquired can be used to improve our understanding of phase selection in the rapidly solidified powders on a more

¹All compositions in atomic percent unless specified otherwise.

quantitative basis. The base alloy selected for the study was Ti-48%Al, which should consist of $\gamma + \alpha_2$. The effect of small amounts of ternary additions, one substitutional (Ta) and one compound-former (C) was also investigated. The latter is of interest because C is an impurity introduced in some atomization processes and has been claimed to form a carbide which catalyzes the formation of metastable α -(Ti) in this alloy composition [88Gra].

The starting point for understanding microstructure evolution in RSP powders should be an analysis of phase equilibria and conventional (i.e. near equilibrium) solidification of the Ti-Al alloys. Recent work on the Titanium-Aluminum system [88McC, 88McV, 88Sch, 88Wat, 88JoK] has proved conclusively that the high temperature ($\beta + \gamma$) field shown by the current phase diagram [86Mur] does not exist. It has been established that there is a high temperature α -(Ti) phase field, and the liquid-solid equilibrium in this composition range includes a double peritectic cascade of $L + \beta \rightarrow \alpha$ and $L + \alpha \rightarrow \gamma$, as depicted in Figure 1 [88McC, 88McV]. Hence, a baseline for predicting the conventional solidification behavior of these alloys is now available.

Solidification experiments reported elsewhere [88McC] indicate that, in the absence of supercooling, the primary phase evolving from the liquid changes from β -(Ti) to α -(Ti) at ~49%Al, as suggested by Figure 1. In either case, γ -TiAl appears only as a segregate for alloy compositions between 46 and 55%Al. Furthermore, supercooling experiments on Ti-Al alloys between 45 and 50%Al revealed that β is always kinetically preferred at high supercooling (typically below the $L \rightarrow \beta$ T_0 curve) even though thermodynamics would predict a larger driving force for the formation of α and/or γ [88Val].

2. EXPERIMENTAL

Alloys for the supercooling experiments were produced by arc-melting in a slightly pressurized atmosphere of gettered argon containing less than 0.1ppb oxygen. The starting materials were high purity Ti buttons, (200 ppm O), 99.99% Al pellets and 99.9%C graphite rods.² In order to minimize Al losses, the ternary Ti-Al-C alloys were produced by first making

² Pure Ti buttons were supplied by TIMET, Al pellets by Alfa/Morton Thiokol and graphite rods by Union 76

a Ti-C master alloy and then adding the aluminum, following the procedure developed for Ti-Al-B alloys [88Hym]. The buttons were flipped over and remelted six times to ensure complete homogenization. Nine alloy compositions were produced in this manner, namely:

Ti-48Al
 Ti-48Al + (0.38, 0.76, 1.0 and 1.5)%C³
 Ti-45Al + (0.32, 0.64, 1.05 and 1.5)%C³

In addition, all alloys contained ~500 ppm oxygen by weight.

Pieces of the above materials were melted and supercooled in a electromagnetic levitation apparatus driven by a 20 kW, 450 kHz radiofrequency generator. The specimen temperature was continuously monitored using an Ircon-Maxline two-color pyrometer with a response time of 25 ms and a minimum target size of 2 mm; the data was recorded in a microcomputer. The experimental set-up has been described in greater detail elsewhere [88Val]. Briefly, the temperature of the sample was controlled during heating by a small flow of gettered argon (<0.1ppb O₂) mixed with high purity He (<5 ppm O₂). The Ti-48%Al binary alloy samples were superheated 100 - 125 K, while the alloys containing carbon were superheated in the range of 150-200 K to ensure complete carbide dissolution in the liquid⁴. While still levitated, the liquid droplet was cooled with a high flow of He gas until rescalescence and complete solidification occurred. The power was then cut off to allow the sample to fall and cool in the He environment. The supercooled specimens were sectioned into thin slices for chemical analysis and for microstructural characterization by optical metallography, scanning and transmission electron microscopy.

Titanium aluminide powders were produced elsewhere⁵ by centrifugal atomization (XSR) and the plasma-rotating electrode process (PREP) [84 Sav]. Alloy compositions investigated are given in Table I. The powders were sieved and samples from three size ranges, coarse (106-150 µm), medium (75-90 µm) and fine (< 25µm), were separated for microstructural

³ Carbon content measured by fusion gas analysis

⁴ Additional superheating may result in slight Al losses, ~0.5%

⁵ Powders were kindly provided by Pratt & Whitney Aircraft (XSR) and McDonnell Douglas (PREP)

characterization by X-ray diffraction, optical microscopy, SEM and TEM.

Metallographic specimens of powders and supercooled droplets were etched with a solution containing: 20 g Benzalkonium chloride, 80 ml Ethanol, 100 ml Glycerin, 20 ml Hydrofluoric acid (50%), and 10 g Oxalic acid. The response to the etchant was much faster in the powder specimens, which were only etched for ~1 s, whereas the supercooled droplets were etched for 10-30s.

TEM specimens of the supercooled droplets were prepared by conventional mechanical thinning of 3 mm discs and twin-jet polishing in a solution of 3.5% perchloric acid (70%), 35% 1-butanol, and 61.5% methanol using currents of 20-22 mA at 8-15V and temperatures <250 K. The thin foils were then washed in the manner suggested by Hu and Cline [68 HuC] using consecutive baths of: i) 75% nitric acid in water, ii) 200ml of 25% nitric acid in water containing 60 g of anhydrous zinc chloride, and iii) methanol.

Powders were prepared for TEM using a modified version of a technique first employed by Field and Fraser [78Fie]. A monolayer of powder was first placed on a titanium sheet substrate. The powder could be left loose inside a retaining ring, or spread over a conducting cement, with the object of achieving a high packing density within the monolayer. This arrangement was then electroplated with nickel, using a commercially available nickel sulfamate solution. A low current density, 5-10 mA cm⁻² was used to ensure good adherence of the nickel plating to the powders, and plating was performed overnight (12-14 hrs) producing a compact ~600μm thick. This was removed from the substrate with no further plating necessary. From this compact, 3 mm discs were cut and mechanically thinned to 50-100μm thickness depending on the powder size range under examination. Twin-jet polishing was then undertaken using a solution of 7% sulphuric acid in methanol [88Kon] at 95-100mA. This solution polished the powders faster than the plating material, thus ensuring the production of electron transparent areas within the powders. The coarse XSR powders contained many large shrinkage cavities (~50μm diameter) which precluded the manufacture of good TEM specimens by electropolishing. In this case, dimpling to <5μm followed by ion-milling, using argon gas, produced good quality thin foils.

3. RESULTS AND DISCUSSION

This part is organized in three sections to facilitate the discussion. Firstly, we introduce the structures formed during solidification of the binary Ti-48%Al alloy at various levels of supercooling. The influence of supercooling and cooling rate upon primary phase selection and the final microstructural features (scale, segregation) are addressed. Microstructural development in Ti-48%Al powders is discussed in the second section, with regard to the influence of atomization technique (PREP vs XSR) and alloying additions. A comparison of the structures developed in the supercooled droplets with microstructural observations made on atomized powders, provides a framework for deducing the thermal history and solidification path for the latter.

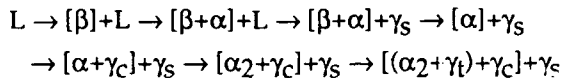
The final section deals with the microstructural effects of controlled additions of carbon to Ti-48%Al and Ti-45%Al alloys. Potential roles of heterogeneous nucleating species during solidification are discussed in the light of the supercooling experiments, together with the implications for atomized powders.

3.1 Supercooling Effects on Ti-48%Al

The microstructure resulting from conventional solidification of this alloy is depicted in Figure 2. The solidification path has previously been established [88McC] and may be reviewed with the aid of the phase diagram, Figure 1.

In the absence of significant supercooling, e.g. in arc buttons and ingots, solidification starts with the formation of primary β -(Ti) as evidenced by the orthogonal symmetry of the dendrites in Figure 2. The Al content of this alloy is sufficiently high to permit the system to go through the double peritectic cascade, whereupon the primary β dendrites are first surrounded by α -(Ti) and subsequently by γ -TiAl which appears as the final segregate. According to the phase diagram, solid state cooling causes the primary β to transform to α , producing a microstructure of α dendrites surrounded by segregate of γ . Since the α phase also becomes metastable upon cooling through the $(\alpha + \gamma)$ field, Figure 1, γ grows epitaxially from the segregate and partially consumes the original dendrite, forming a "cellular" constituent

[87Val, 88McC]. Further cooling results in the ordering of α to α_2 , with concomitant formation of stacking faults and APB's. From these, plates of γ grow with the $\{111\}_{\gamma}$ parallel to the basal plane of the α_2 , as proposed by Blackburn [70Bla, 88McC]. Hence, the final microstructure consists of transformed β dendrites, which now contain alternating phases of γ and α_2 , surrounded by segregate of γ . Thus, the complete solidification and solid state transformation path may be summarized as:



where γ_s refers to γ segregate, γ_c to cellular γ formed at the dendrite / segregate interface, γ_t to the twin related γ variants formed during the decomposition of α_2 , and the square brackets indicate phases within the initial dendrites.

The maximum supercooling achieved in this alloy was 258K or $0.14T_L$. The microstructures developed in the supercooling experiments are presented in Figure 3. At ΔT of up to 88K there is still clear evidence for the formation of β dendrites, as in the arc button, Figure 3(a). However, the amount of segregate decreased with increasing supercooling, as seen by comparing Figures 2(b) and 3(a). At the maximum supercooling there is no evidence of segregate and the microstructure consists of large equiaxed grains, $\sim 500\mu m$ in diameter. In all cases, striations corresponding to the $(\alpha_2 + \gamma_t)$ lath structure are observed. In addition, Table II shows that the solute content of the dendrites increases, and the segregate spacing decreases, due to the reduction in available time for coarsening.

In the TEM, the microstructures observed contain the usual $(\alpha_2 + \gamma_t)$ lath structure with a spacing of 50-100 nm, Figure 4. There are areas of γ segregate (10-20 μm across) in the sample obtained at $\Delta T \sim 0$, Figure 4(a), and the cellular constituent γ_c is observed at the interface between lath and segregate, growing epitaxially from the latter in a manner similar to that seen in Ti(48-50)%Al arc buttons [88McC, 88McV]. No segregate was observed in the highly undercooled sample, Figure 4(b) which contained only grains of the $(\alpha_2 + \gamma_t)$ lath structure.

In conclusion, these experiments suggest that β is formed as the primary solidification phase at supercoolings up to 258K , with the proportion

of γ segregate reduced by increasing supercooling. This is in accordance with the results of similar experiments on compositions between 45-55%Al [88Val]. A cursory examination of the phase diagram at this alloy composition, Figure 1, reveals that the thermodynamic hierarchy of phase selection changes from β to α at very modest supercoolings and eventually to γ at $\Delta T \sim 150K$. Thus, the consistent selection of β at supercoolings of up to 258K must be due solely to a kinetic preference for this phase, presumably due to the lack of suitable nucleation sites for α in the liquid droplet, and the more sluggish nucleation and growth kinetics anticipated for the ordered γ [88Val].

3.2 Powders

The structures developed in the Ti-48%Al powders change with particle size (and hence with supercooling and cooling rate). While most of the effort was focused on the XSR powders, we will discuss the results for the PREP powders first, since they behave essentially as expected from the supercooling experiments while the XSR powders do not. Results are presented for powder diameter ranges representing coarse (106-150 μm), medium (75-90 μm) and fine ($< 25\mu m$). Over 200 powders were examined for each size range; the proportions of different structure types are presented in Table III.

3.2.1 Ti-48.%Al PREP Powders

Of the powders examined in the range 106-150 μm , 93% are dendritic, but only 6% exhibit a clearly developed cubic symmetry, Table III. Figures 5(a) and (b) show surface and cross-sectional views of the latter, where the dendrite arms are orthogonal to one another, characteristic of growth of the cubic β -phase from the liquid. Most (87%) of the powders were clearly dendritic, Figures 5(c) and (d) but the growth is equiaxed and the grains rather small (~20 μm) to show a distinct crystallographic pattern. The surface morphology of these powders reveals equiaxed rosettes very similar to those seen in titanium aluminide buttons in which the primary phase was clearly shown to be β [88McC, 88Val]. Since the hexagonal symmetry characteristic of α dendrites is quite distinctive on the powder surface, even in the case of small equiaxed crystals -- see, for example, Figure 6(b)--it was inferred that

these "indistinct" dendritic powders are more likely the result of primary β growth.

A significantly different microstructure is shown in Figures 5(e) and (f) in which martensitic relief is evident on the exterior of the powder, and the cross section is essentially featureless. These powders account for 7% of the total examined. Since the presence of α' martensite, (which is hexagonal as described later), is indicative of a transformation from a parent β -phase, it was concluded that β was also the primary phase in these powders. Less than 1% of the powders appeared to have any sign of hexagonal α forming from the liquid. Hence, virtually all the powders in the range 106-150 μm , seem to have formed primary β -phase during solidification, but only about 7% achieved sufficient supercooling to prevent the formation of γ segregate.

The smallest powders produced by the PREP process lie in the size range from 75 to 90 μm . The majority (91%) are of the indistinct dendritic type, as in Figures 5(c) and (d), with no powders showing a developed orthogonal symmetry. The remainder of the powders (9%) have a martensitic surface relief, with a featureless cross-sectional microstructure. No hexagonal structures were observed. Therefore, this again suggests that all the powders solidified by forming primary β .

SEM analyses did not provide any evidence for the $(\alpha_2 + \gamma_t)$ lath structure in the dendritic powders. Presumably the microstructure contains dendrites of α_2 , transformed from the β , and a segregate phase of γ . As with the supercooled droplets, it appears that β is formed during solidification at all supercoolings. The dendritic powders seem to have experienced a supercooling of ≤ 100 K, judging from the scale and amount of segregate present, while the segregate-free martensitic powders must have achieved supercoolings of ~ 250 K or higher. The presence of martensite indicates that the powders experienced a faster cooling rate in the solid-state than the levitated and supercooled samples, reflecting the higher rate of heat removal from the smaller atomized liquid droplets.

3.2.2 Ti-48% Al XSR Powders

For the size range 106-150 μm , the predominant powder morphology was equiaxed dendritic, Table III, and most of these (85%) revealed a clear

hexagonal symmetry as shown by Figures 6(a) and (b); thus, the primary phase forming from the liquid was α . In the cross-section, Figure 6(c), there was little development of long dendrite arms, although at the edges of the powder some dendrites are seen with arms lying 60° to one another, as expected for the α -phase. The remaining 15% of the powders were equiaxed dendritic but with no distinct symmetry (presumably β).

In moving to the smaller size range, 75-90 μm , similar structures were observed but the proportion of indistinct dendritic powders increased from 15% to 25% as noted in Table III. This trend continues in the smallest powders, <25 μm diameter. Here 46% of the powders are clearly hexagonal, Figure 6(d), and 43% are dendritic but with no clear symmetry, Figure 6(e). The remaining 11% of powders have the exterior martensitic relief, Figure 6(f) and featureless cross-sections. Hence, in the small powders there is evidence for the formation of both primary α (hexagonal dendrites) and primary β (martensite). Clearly in moving to smaller powders, and presumably larger supercoolings, there is a trend which favors the formation of β at the expense of α .

A TEM examination of the coarser (106-150 μm) powders revealed well defined dendrite arms with segregate spacings of $\sim 4\mu\text{m}$, Figures 7(a) and (b), reasonably consistent with those observed in the SEM, e.g. Figure 6(c). Electron diffraction shows the majority of the dendrite arms to be α_2 , from the $[1\bar{2}10]\alpha_2$ zone axis in Figure 7(e), although higher magnification micrographs, e.g. Figure 7(c), indicate some fine and limited precipitation of the γ_t lath phase. Segregate areas are γ , as shown by the $[101]\gamma$ diffraction pattern in Figure 7(f). These areas often contain fine twins, and the interface with the dendrite is jagged and sinusoidal as depicted in Figure 7(d). It is believed this represents the regrowth of cellular γ into the dendrite during solid-state cooling, as previously described [88McC, 88McV, 88 Val]. However the scale of the cells is much finer in the powders (~ 50 nm) than in the supercooled Ti-48%Al droplets ($\sim 1 \mu\text{m}$); see Figure 4(a). In addition, the width of the cellular zone is also smaller in the powders, as expected from the higher solid state cooling rate. Energy Dispersive Spectroscopy (EDS) performed in the TEM, yielded average compositions for the dendritic and

segregate areas of 45.9%Al and 51.8%Al, respectively.⁶

In the fine powder (<25 μm) both dendritic and martensitic structures were observed by TEM, Figures 8 and 9. The dendritic powders have somewhat finer microstructures than the corresponding coarse powders with segregate spacings of 2-3 μm . Figure 8(a) shows a partially transformed dendrite with some regions containing only α_2 , see diffraction pattern in Figure 8(c), and others containing the ($\alpha_2 + \gamma_t$) lath constituent, Figures 8(b) and (d).

A peculiar feature of Figure 8(a) is the lath constituent growing into the dendrite from the interface with the γ segregate. Since γ_t is supposed to nucleate and grow from stacking faults in the parent α_2 , and these should be randomly distributed within the dendrite, there must be an additional factor promoting the preferential formation of the lath near the dendrite-segregate interface. This could simply be due to more favorable nucleation conditions at the interface, or could also be influenced by microsegregation of Al within the dendrite, i.e. the dendrite edge is slightly richer in the Al than the core. The lath in Figure 8(b) is only 5-10 nm wide, much finer than any lath morphology seen hitherto. In addition, no evidence was found for regrowth of cellular γ into the dendrites. EDS analysis gave average compositions of 46%Al and 51%Al for the dendrite and segregate regions respectively, similar to the coarse powders.

Figure 9 shows a TEM view of the martensitic powders. The microstructure is composed of plates of a hexagonal phase, and electron diffraction suggests this is disordered α and not the ordered α_2 phase.

Electron diffraction in Figures 9(b) and (c) show [1 $\bar{2}$ 10] and [1213] zone axes for the disordered α phase which are unambiguously different from corresponding α_2 zone axes, due to the absences of both superlattice spots and expected α_2 diffraction spots. This was the first direct TEM evidence of suppression in the ordering reaction $\alpha \rightarrow \alpha_2$, in these titanium aluminide alloys. It has previously been reported that this may occur in powders of Ti-40%Al, which showed a mixed α/α_2 spectrum using X-ray diffraction spectrum [88Mis]. Figure 9(a) shows alternating laths of the martensite, some of which contain striations parallel to the basal plane of α . These striations

⁶ 0.5at.%Fe was also detected in the segregate (obviously an impurity), but was absent from the dendrite arms.

are as yet unidentified.

It is interesting to note that within the segregated dendritic powders the actual dendrites contain α_2 or the $(\alpha_2 + \gamma_t)$ lath structure, whereas martensite appears to form only in the powders that are segregate-free. Powders with primary α dendrites readily transform to α_2 and $(\alpha_2 + \gamma_t)$ during solid state cooling. On the other hand, dendritic powders that start with solidification of β at moderate supercoolings, recalesce and are subsequently surrounded by a layer of α as they go through the $L + \beta \rightarrow \alpha$ peritectic. Hence, the dendrites are composed of both phases just below the melting range. Solid state cooling of the dendrites destabilizes the β as the system moves into the $(\beta + \alpha)$ field and subsequently into the single phase α region, see Figure 1. Since α is already in contact with β , it may readily serve as a site for the start of the $\beta \rightarrow \alpha$ transformation, i.e. there is no need for separate nucleation of α . Powders that solidify in a segregate-free manner start solidification at high supercoolings and may form just single phase β from the liquid. Recalescence and subsequent cooling into the single phase α field requires separate nucleation of α within the β . This is obviously a more difficult process and the microstructure may find it easier to transform martensitically to α .

3.2.3 Ti-48%Al-2%Ta XSR Powders

In the coarse powder range (106-150 μm), there is a greater proportion of the hexagonal dendritic structure (94%) than in the binary alloy powders. Again clearly equiaxed dendrites, 20-30 μm inside, were observed on the surface and cross-section of the powders. The remaining structures appeared to be cubic dendritic (1%) and dendritic of indistinct symmetry (5%). No martensite was observed.

Fine powders ($<25 \mu\text{m}$) contained essentially the same structures as the fine binary alloy XSR powders, i.e. hexagonal dendritic, indistinct dendritic (presumably β), and martensitic. The proportions of the respective structures were 35% hexagonal, 40% indistinct dendritic and 25% martensitic. This represents a large drop in the fraction of hexagonal dendritic powders from the coarse size range and a significant increase in the fraction of martensitic powders relative to the binary alloy. Clearly β is being increasingly favored as the primary phase with decreasing particle size.

TEM examination of the coarse powders revealed the dendritic microstructure shown in Figure 10. The electron diffraction information from the $[0001]\alpha_2$ and $[112]\gamma$ zone axes in Figures 10(c) and (d), shows the interior of the dendrite to be α_2 and the segregate to be γ . No γ_t formation was observed within the dendrites, only APB contrast from the α_2 was noted, Figure 10(b). EDS analysis gave the composition of the dendrite as 44.5%Al-1.5%Ta, while the segregate contained 53.3%Al-0.6%Ta (The seemingly low mass balance for tantalum merely reflects the difficulty of accurate measurement of low elemental fractions in the SEM). The aluminum partitioned to γ a little more strongly than in the binary alloy, while the tantalum concentrated preferentially in the primary α -phase. The tantalum seems to suppress completely the formation of the lath constituent which is frequently observed in the binary alloy, even in the smallest powders, i.e. those experiencing the highest cooling rate. Since the $\alpha_2 \rightarrow (\alpha_2 + \gamma_t)$ transformation involves the redistribution of alloying elements by diffusion at the α_2/γ_t interface, its kinetics are likely to be slowed down by additions of elements which partition strongly to one of the phases.

In the fine powders, the dendritic structures proved to be very similar to those of the coarse powders: the dendrites contained α_2 with no lath constituent present and the segregate phase was γ . Martensitic structures were also observed as shown in Figure 11. As in the binary alloy martensite, electron diffraction shows these to be the disordered α phase. Furthermore, the diffraction pattern in Figure 11(c) shows there are two $[0\bar{1}11]\alpha$ zones which are twin-related, suggesting that neighboring martensite plates may be twins.

A comparative analysis of the XSR powders with and without Ta was performed by X-ray diffraction. The results revealed the presence of just two phases: α_2 and γ^7 . The changes in their relative amounts were followed by monitoring the intensity ratio of two adjacent major peaks of the two phases, i.e., $(02\bar{2}1)\alpha_2 / (111)\gamma$. The results are given in Table III. In both alloys, the amount of γ is reduced by decreasing the particle size. This would be due to the concomitant decrease in volume fraction of segregate and greater

⁷ No distinction was made at this point between the predominant α_2 and the disordered α found in the martensitic powders.

proportion of segregate-free powders. The addition of tantalum also causes a significant increase in the α_2/γ ratio in both the coarse and fine powders. From the TEM observations this can largely be attributed to the suppressed decomposition of α_2 into the $(\alpha_2 + \gamma_t)$ lath microstructure. Moreover, the fine powders with tantalum contain a greater proportion of the martensitic microstructure, whose X-ray diffraction maxima corresponding to the α -phase, were not clearly distinguishable from those of α_2 .

3.3 Effect of Carbon

Previous work on powder solidification in this system [87Gra], indicated that Ti-50%Al powders formed primary α on solidification and only formed β at small powder sizes. Since α is known to be the equilibrium phase of the Ti-50at%Al composition [88McC, 88McV], one can thus infer that β is metastable at large supercoolings, in agreement with controlled supercooling experiments on this alloy [88Val]. On the other hand, β is the primary phase that forms during conventional solidification of Ti-48%Al alloy, with a transition from β to α at ~49%Al. The PREP powders in this work appear to have formed primary β at all powder sizes, whilst most of the XSR powders clearly started solidification by forming α , and only formed β at the larger supercoolings (small powder size). In principle, one could attempt to rationalize this change in phase selection based on differences in process parameters like cooling rate, superheat, etc. A more obvious choice, however, is the difference in impurity level of these powders, especially in the amount of carbon picked up from the graphite crucible and nozzle used in the XSR process, but absent in the "containerless" PREP atomization.

Given the location of the 48%Al alloy in the phase diagram, it is anticipated that the α -phase would become thermodynamically feasible at supercoolings of the order of 20-40 K - see Figure 1. As a matter of fact, one could readily show that the α phase should be thermodynamically favored over β at this composition if solidification were to take place in a partitionless

fashion⁸. Thus, very modest catalysts might be needed to shift the phase selection from β to α . To assess the relative potency of C on α nucleation, we conducted both arc-button and levitation melting/supercooling experiments on Ti-45%Al and Ti-48%Al alloys with controlled additions of carbon. The Ti-45%Al + C alloys were included since the thermodynamic driving force for α formation is significantly smaller for this alloy than for Ti-48%Al at comparable supercoolings. Carbon concentrations studied ranged from the 0.3% (0.1 wt%), characteristic of our powder specimens, to 1.5% (~0.5wt%).

The microstructures of Ti-45%Al ingots with compositions between 0.32-1.05%C are presented in Figures 12(a) to (c). With 0.32%C, the matrix contains cubic dendrites and no carbide phase, Figure 12(a), as in the corresponding binary alloy button [88McC]. Increasing the carbon to 0.64% results in the formation of hexagonal dendrites of α in the matrix and a small fraction of a carbide phase, Figure 12(b). In the sample containing 1.05%C, Figure 12(c), the dendrites are still α and there is a greater number of long carbides plates. Similar structures were also observed in the an alloy containing 1.5%C, with more of the carbide phase present.

Figures 12(d) to (f) show the effect of adding between 0.38-1.0%C to the Ti-48%Al alloy. In all cases the matrix is seen to contain dendrites displaying a hexagonal symmetry, indicating primary solidification of α -(Ti). This is clearly different from the primary cubic β -phase described earlier in the alloy with no carbon, Figure 2. The addition of $\geq 1\%$ carbon forms long carbide plates, seen in Figure 12(f), which always appear inside the primary phase. Given the size of these plates (up to 500 μm long), it is likely these formed directly from the liquid and not by solid-state precipitation. These were not observed in the alloys with carbon levels below ~1%, Figures 12(d) to (e). This was also confirmed by TEM analysis. A button containing 1.5%C also showed hexagonal structures and large carbide plates, in a greater proportion than in the 1% C alloy.

The large plates observed in Figure 12 were investigated by TEM, Figure 13. EDS analysis detected only titanium and aluminum with a Ti:Al

⁸ If the 48%Al alloy falls to the right of the peritectic composition as depicted in Figure 1, then the intersection of the α and β equilibrium liquidi will be above 48%Al but the T_0 curves for these phases will cross below 48%Al. Thus, β would be thermodynamically favored if solidification takes place with local interfacial equilibrium, but α would exhibit a larger driving force for partitionless solidification.

ratio of 2:1, and electron diffraction resulted in patterns consistent with Ti₂AlC, which is a hexagonal phase (hP8, P6₃/mmc) with $a=305.6\text{pm}$ and $c=1362.3\text{pm}$ [85Vi]. The c-axis lies perpendicular the habit plane of the carbide, which is the basal plane of Ti₂AlC. Some (<20%) of these plates were aligned with the ($\alpha_2 + \gamma_t$) lath structure, Figure 13, and these seemed to have an orientation relationship with the matrix. Electron diffraction shows:

$$\begin{aligned}[0\bar{1}10]_{\text{Ti}_2\text{AlC}} &\parallel [112]_{\gamma_t} \\ [1\bar{2}10]_{\text{Ti}_2\text{AlC}} &\parallel [1\bar{2}10]_{\alpha_2} \parallel [1\bar{1}0]_{\gamma_t}\end{aligned}$$

From these it may be shown that:

$$\begin{aligned}\{2\bar{1}\bar{1}0\}_{\text{Ti}_2\text{AlC}} &\parallel \{1\bar{1}0\}_{\gamma_t} \\ \{0001\}_{\text{Ti}_2\text{AlC}} &\parallel \{1\bar{1}1\}_{\gamma_t}\end{aligned}$$

and also:

$$\begin{aligned}\{0001\}_{\text{Ti}_2\text{AlC}} &\parallel \{0001\}_{\alpha_2} \\ \{2\bar{1}\bar{1}0\}_{\text{Ti}_2\text{AlC}} &\parallel \{2\bar{1}\bar{1}0\}_{\alpha_2}\end{aligned}$$

This reveals that the face of the carbide plate, i.e. the basal plane, lies parallel to the basal plane of the α_2 . Hence, during solidification the basal planes of the α phase evolve parallel to that of the carbide. Indeed, Graves [88Gra] hypothesized that Ti₂AlC would have a low degree of disregistry with the α (Ti) phase and should be a favorable nucleation site for the latter, although he reported that this carbide was not detected in his powders. One should also point out that the majority of the plates were not aligned with the lath microstructure and did not follow any consistent orientation relationship.

Some of the Ti-48%Al buttons containing 0.38%C and 1.0%C were remelted into small pieces and supercooled in the electromagnetic levitation device. For the lower C alloy, α dendrites may still be seen at supercoolings up to ~60K, Figure 14(a), but cubic β dendrites are observed at supercoolings of ~100K and larger, Figure 14(c). No carbide was detected in any of these

samples, as expected from the ingot microstructure, leading to the conclusion that any effects on the phase selection in this alloy were due to the carbon in solution.

Two supercoolings are also shown for the alloy containing 1.0% C in Figures 14(b) and (d): $\Delta T \sim 0$ and 117 K, respectively. In the former, hexagonal dendrites and large carbide plates may be seen. Small supercoolings always occurred when the samples were superheated less than 150 K and not subjected to multiple melting/solidification cycles. Large supercoolings (up to 207 K) were achieved with larger superheats and cycling of the droplets, presumably because the carbides were able to dissolve completely in the liquid. Figure 14(d) shows the dendrite symmetry changes to cubic β at $\Delta T = 117$ K, and the large carbide plates are clearly absent. However, occasional smaller equiaxed particles may be seen. Results of an EDS analysis from these detected only titanium, suggesting they may be the metastable TiC reported by Graves [88 Gra]. There is also a clear reduction in the volume fraction of carbide, which is probably due to supersaturation of carbon during supercooling since chemical analysis showed no loss of carbon.

Supercooling experiments were also performed on the 45% Al-1.05% C alloy. As expected from the button microstructures, Figure 12(f), α formed as the primary phase at low supercoolings together with plates of the ternary carbide, Figures 15(a) and (b). At larger supercoolings (≥ 100 K) β formed as before but, contrary to the 48% Al alloy, occasional carbide phases are still observed, Figures 15(c) and (d). The amount of carbide decreases with increasing supercooling as more of the carbon is taken into solution.

It is clear from these experiments that carbon does play a role in changing the phase selection from primary β to primary α during solidification. It appears, however, that this process can occur even in the absence of a carbide as in the Ti-48% Al-0.38% C, and at negligible supercoolings, suggesting that α is indeed an equilibrium primary phase for this composition.⁹. One may thus conclude that carbon additions shift the transition from β to α from ~49% in the binary system to lower Al contents in

⁹On the other hand, the 45% Al alloy with a similar carbon content forms primary β , as does the binary alloy of the same Al content.

the ternary.¹⁰

A catalytic effect of the Ti₂AlC on the formation of α may be postulated, since the latter is accompanied by the presence of carbide in the Ti-45%Al alloy with carbon contents above 0.64%. Note, however, that β does form in the presence of Ti₂AlC when the supercooling is sufficiently high, showing that the catalytic effect, if any, is dominated by the faster solidification kinetics of the β phase which has been observed in the binary alloys [88Val].

4. CONCLUSIONS

Supercooling experiments are an invaluable tool in elucidating the microstructure evolution of rapidly solidified powders and should be an important component of the characterization process.

It was shown that the Ti-48%Al alloy, whose equilibrium configuration at room temperature consists of γ -TiAl plus small amounts of α_2 -Ti₃Al, starts solidification with the formation of β -(Ti) dendrites at all supercoolings ranging from zero to 258K. Since thermodynamics indicates that the phase with the largest driving force for solidification changes from β -(Ti) to α -(Ti) and finally to γ as supercooling increases, it was concluded that the selection of primary β at high supercoolings must be due solely to kinetic factors. At low ΔT solidification proceeds with surrounding of the β dendrites, first by α and subsequently by γ , as the system goes through the double peritectic cascade indicated in the revised phase diagram. Increasing the supercooling refines the microstructure and reduces the amount of γ segregate which is completely absent at $\Delta T = 258K$.

Microstructures of the PREP powders are in general consistent with the trends established by the supercooling experiments, as there is only evidence of primary β formation in all powder sizes studied. A small fraction of the powders exhibited a segregate-free martensitic structure, suggesting that they reached supercoolings of the order of 250K before nucleation of β .

The XSR powders, on the other hand, reveal unequivocal evidence of primary α formation from the liquid in all powder sizes. Primary α is

¹⁰Furthermore, the evolution of primary β at the higher supercoolings is consistent with the trend observed for the binary Ti-50%Al alloy, which shows a change from primary α to β as supercooling increases [88Val].

predominant (85% of the particles) in the larger powder sizes, but its proportion decreases as the number of particles exhibiting primary β increases with decreasing particle size. Since the nominal composition of the PREP and XSR powders is the same, the differences in phase selection were ascribed to the higher impurity content of the latter, especially with regard to C.

Supercooling experiments revealed that C additions do promote the formation of primary α from the melt, although the phase selection reverts to β at high supercoolings. Large carbide plates were observed in alloys with C contents above 1% (~0.3wt%), but they do not appear to play a major role in the nucleation of α . Thus, the effect appears to be mainly associated with a shift in the intersection of the β and α liquidus from ~49%Al in the binary to lower Al concentrations in the ternary.

The major effect of the cooling rate in the powders appears to be the partial suppression of the $\alpha_2 \rightarrow \alpha_2 + \gamma_t$ transformation and progressive refinement of the resulting lath microconstituent. Additions of Tantalum seem to slow down the kinetics of the α_2 decomposition to the point that no lath structure was detected in the powders. This was ascribed to the need for redistribution of Ta between the phases during the transformation, since this element appears to partition strongly to the α_2 .

Finally, it was shown that the martensite formed in the finer XSR powders has the disordered hexagonal structure of α . In addition, the martensite laths appear to be twin related.

ACKNOWLEDGMENTS

The support of the Defense Advanced Research Projects Agency (DARPA) through the contract URI-N00014-86-K-0753, supervised by Dr. B. Wilcox and monitored by Dr. S.G. Fishman of the Office of Naval Research, is gratefully acknowledged. The authors would like to thank Dr. R. Anderson and his group at Pratt and Whitney (Florida) and Dr. S.M.L. Sastry at McDonnell Douglas (St. Louis) for providing the powder samples. Further thanks are due to Drs. R. Martin and J. McCarthy (P&W) for discussions regarding the chemical analysis and the preparation of TEM specimens from powders, and Dr. J. Graves (Rockwell International Science Center) for discussions regarding the effects of carbon.

REFERENCES

68HuC H. Hu and R.S Cline, Trans. AIME., 242 (1968), p. 1013.

70Bla M.J. Blackburn, in "The Science, Technology, and Application of Titanium", eds. R.I. Jaffee and N.E. Promisel, Pergamon Press, London (1970), p. 633.

78Fie R.D. Field and H.L. Fraser, Metall. Trans., 9A (1978), p. 131-2.

84Sav S.J. Savage and F.H. Froes, J. of Metals, 36 (4), (1984), pp. 20-33.

85Lip H.A. Lipsitt, in "High Temperature Ordered Intermetallic Alloys", MRS Symposia Proceedings vol. 39, ed. by C.C. Koch, C.T. Liu and N.S. Stoloff, MRS, Pittsburgh, PA (1985), 351-364.

85Vil P. Villars and L.D. Calvert, in Pearson's Handbook of Crystallographic Data for Intermetallic Phases, ASM, Metals Park, OH, 1985, p. 553.

86Mur J.L Murray, in Binary Alloy Phase Diagrams, ed T.B. Massalski, ASM, Metals Park, OH, (1986), p.173.

87Bla M.J. Blackburn, presentation to the URI Winter Study Group on High Temperature, High-Performance Composites. Santa Barbara, CA 1987.

87Gra J.A. Graves, J.H. Perepezko, C.H. Ward and F.H. Froes, Scripta Metall., 21 (1987), p. 567-72.

87Val J.J. Valencia, C. McCullough, C.G. Levi and R. Mehrabian, Scripta Metall., 21 (1987), pp. 1141-6.

88Ell C.K. Elliott, G.R. Odette, G.E. Lucas and J.W. Scheckard in High Temperature/High Performance Composites, MRS Symposium Proceedings Vol. 120, eds. by F.D. Lemkey, S.G. Fishman, A.G. Evans, and J.R. Strife, Materials Research Society, Pittsburgh, PA (1988) pp. 95-102.

88Gra J.A. Graves, Ph.D thesis, U. of Wisconsin-Madison, (1988).

88Hym M.E. Hyman, C. McCullough, J.J. Valencia, C.G. Levi and R. Mehrabian, accepted for publication in Metallurgical Transactions.

88JoK S.A. Jones and M.J. Kaufman, presented at the AIME Fall Meeting, Chicago, IL (1988).

88Kon D.G. Konitzer, J.P.A. Lofvander, S.A. Court, R. Kirchheim and H.L. Fraser, Acta Metall., 36 (1988), 1595-1606.

88McC C. McCullough, J.J. Valencia, C.G. Levi and R. Mehrabian, accepted for publication to Acta Metall.

88McV C. McCullough, J.J. Valencia, H. Mateos, C.G. Levi, R. Mehrabian and K.A. Rhyne, Scripta Metall., 22 (1988), pp. 1131-6.

88Mis J.C. Mishurda, J.H. Perepezko, J.A. Graves, R. Bonda and D.J. Thoma, U. of Wisconsin-Madison, Second annual report to the University Research Initiative, University of California at Santa Barbara, (1988).

88Sas S.M.L. Sastry, R.J. Lederich and T.C. Peng, J. of Metals 40 (9) (1988), pp.11-13.

88Sch R.D. Schull and J.P. Cline, presented at the TMS-AIME Fall Meeting, Chicago, Il(1988)

88Val J.J. Valencia, C. McCullough, C.G. Levi and R. Mehrabian,
submitted for publication to Acta Metall.

88Wat R.M. Waterstrat, U.S. Dept. of Commerce, NISTIR 88-3856,
(1988).

TABLE I

Compositions of Powders in Atomic Percent*

| Powder | Al | Ta | O | C |
|--------------|------|------|------|------|
| 48Al PREP | 48 | - | n.a. | - |
| 48Al XSR | 48 | - | 0.25 | 0.31 |
| 48Al-2Ta XSR | 47.8 | 1.98 | 0.37 | 0.47 |

* balance Ti

TABLE IIMicrostructural Features of Levitated
and Supercooled Ti-48%Al Droplets

| $\Delta T/K$ | Composition (%Al) | | γ_s | Volume Fraction | Segregate Spacing (μm) |
|--------------|-------------------|-------------------------|------------|-----------------|----------------------------------|
| | Bulk | $(\alpha_2 + \gamma_l)$ | | | |
| 0 | 48.0 | 47.0 | 54.9 | 6.2 | 30 |
| 88 | 48.1 | 47.3 | 54.2 | 1.7 | 10-20 |
| 110 | 48.1 | 47.5 | 54.0 | 1.0 | 5-15 |
| 258 | 48.1 | 48.1 | -- | 0 | -- |

TABLE III

Proportions of Structures in Powder Samples

| Powder | Size Range <u>(μm)</u> | Dendritic Symmetry | <u>Hexagonal</u> | <u>Cubic</u> | <u>Indistinct (1)</u> | <u>Martensite</u> | $\alpha_2/\gamma(2)$ Ratio |
|------------------|---|--------------------|------------------|--------------|-----------------------|-------------------|-------------------------------|
| PREP 48Al(3) | 106-150 | - | - | 6% | 87% | 7% | n.d. (4) |
| | 75-90 | - | - | - | 91% | 9% | n.d. |
| XSR 48Al | 106-150 | 85% | - | - | 15% | - | 1.7 |
| | 75-90 | 75% | - | - | 25% | - | n.d. |
| XSR 48Al -2Ta | <25 | 46% | - | - | 43% | 11% | 4.4 |
| | 106-150 | 94% | 1% | - | 5% | - | 3.3 |
| | <25 | 35% | - | - | 40% | 25% | 6.0 |

(1) dendritic but with no clear symmetry; believed to be cubic

(2) intensity ration $(02\bar{2}1)\alpha_2/(111)\gamma$ from X-ray diffraction(3) no PREP powders <25 μm

(4) n.d. = not determined

FIGURE CAPTIONS

Figure 1. Section of the recently modified Ti-Al phase diagram in the vicinity of the γ phase field. The existence of the high temperature α -phase field was verified by both solidification and high temperature in-situ X-ray experiments [88McC].

Figure 2. Dendritic microstructures of a Ti-48%Al alloy solidified in absence of a significant supercooling; the presence of orthogonal dendrites is evidence of β -(Ti) primary phase. (a) SEM view of a shrinkage cavity and (b) Optical view of the cross-section.

Figure 3. Metallographic sections of supercooled Ti-48%Al alloy: (a) $\Delta T = 88K$ and (b) $\Delta T = 258K$. Note the orthogonal symmetry of the dendrites in (a), and the absence of γ segregate in (b).

Figure 4. TEM views of Ti-48%Al microstructures supercooled: (a) $\Delta T \sim 0K$ and (b) $\Delta T = 258K$. Note the cellular growth of γ_c into the primary phase in (a), and the usual $(\alpha_2 + \gamma_t)$ lath structure in (b).

Figure 5. SEM views of surface and cross-sections of Ti-48%Al PREP powders: (a) and (b) show orthogonal dendrites typical of the primary β -phase; (c) and (d) are equiaxed dendrites, with no distinct crystallographic pattern; and (e) and (f) reveal martensitic relief on the exterior and a featureless cross-section.

Figure 6. SEM microstructures of Ti-48%Al XSR powders: (a) to (c) from coarse particles ($106\text{-}150\mu\text{m}$) clearly showing the hexagonal growth symmetry at the surface in (a) and (b), and at the edges of the cross-section in (c). (d) to (f) are from fine powders ($<25\mu\text{m}$) showing: hexagonal growth (d), indistinct dendrites (e) and martensite (f).

Figure 7. TEM views of Ti-48%Al XSR coarse powders ($106\text{-}150\mu\text{m}$); (a) and (b) are dendritic microstructures showing the γ -segregate, (c) reveals incipient precipitation of the γ_t lath phase, and (d) interface showing the regrowth of cellular γ into the dendrite. The zone axis patterns in (e) and (f) are: $[1\bar{2}10]\alpha_2$ and $[101]\gamma$, respectively.

Figure 8. TEM microstructures of Ti-48%Al XSR fine powder (<25 μ m): (a) α_2 dendrite partially transformed to ($\alpha_2 + \gamma_t$), surrounded by the γ -segregate; (b) very fine ($\alpha_2 + \gamma_t$) lath within the dendrite. The zone axis patterns are; (c) [1210] α_2 and (d) [1210] α_2 // [110] γ_t for the untransformed and transformed regions, respectively.

Figure 9. TEM microstructure of Ti-48%Al martensitic XSR powders: (a) martensite laths of a disordered hexagonal phase as shown by the zone axis patters in (b) [1210] α and (c) [1213] α .

Figure 10. TEM views of Ti-48%Al-2%Ta XSR coarse powders: (a) dendritic region showing the γ -segregate, (b) APB contrast within α_2 but no evidence of γ lath. The diffraction zone axes are: (c) [112] γ for the segregate, and (d) [0001] α_2 for the dendrite.

Figure 11. Martensitic microstructures in Ti-48%Al-2%Ta XSR powder: (a) and (b) show martensite laths and (c) is the ZAP showing twin related [0111] α orientations of neighboring laths.

Figure 12. Metallographic sections of Ti-45%Al and Ti-48%Al ingots with carbon additions: Ti-45%Al containing (a) 0.32, (b) 0.64 and (c) 1.05%C, and Ti-48%Al containing (d) 0.38, (e) 0.76 and (f) 1.0%C. Note the absence of carbide plates in (a), (b) and (d), and the clearly hexagonal symmetry in all the micrographs except for (a), which shows cubic dendrites.

Figure 13. TEM microstructure of Ti-48%-1.5%C alloy ingot showing a carbide plate, identified as hexagonal Ti_2AlC crystal, and the corresponding diffraction pattern with a [0110] Ti_2AlC zone axis, which is parallel to a [112] zone axis of γ .

Figure 14. Microstructures of supercooled Ti-48%Al containing 0.38 (left) and 1.0%C (right). The leaner carbon alloy was supercooled: (a) $\Delta T = 60K$ and (c) $\Delta T = 100K$, and the higher carbon composition (b)~0K and (d) $\Delta T = 117K$. In each composition the primary phase changes from α to β with increasing supercooling.

Figure 15. SEM and optical micrographs of supercooled Ti-45%Al -1.05at%C $\Delta T \sim 0$ in (a) and (b), $\Delta T \sim 100K$ in (c) and (d). The primary phase changes from α to β with increasing supercooling.

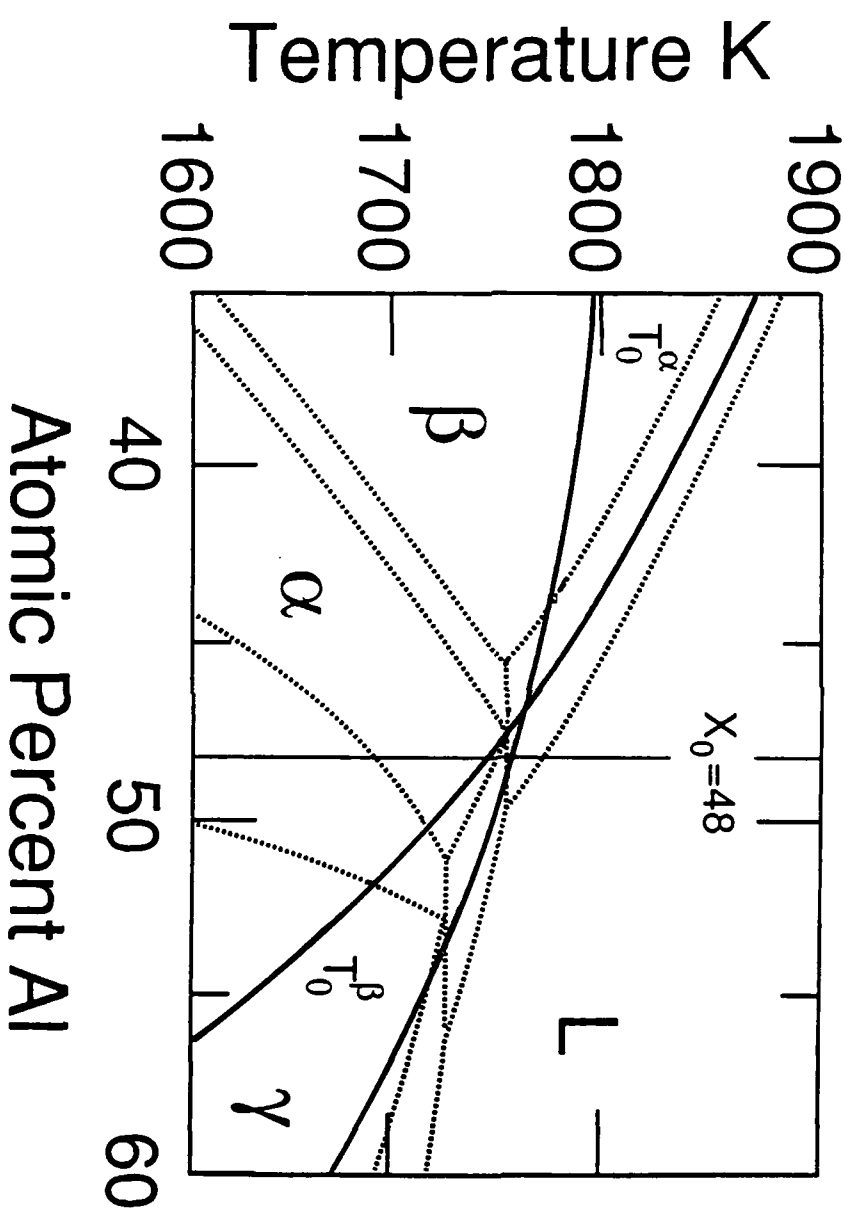


Figure 1. Section of the recently modified Ti-Al phase diagram in the vicinity of the γ phase field. The existence of the high temperature α -phase field was verified by both solidification and high temperature in-situ X-ray experiments.

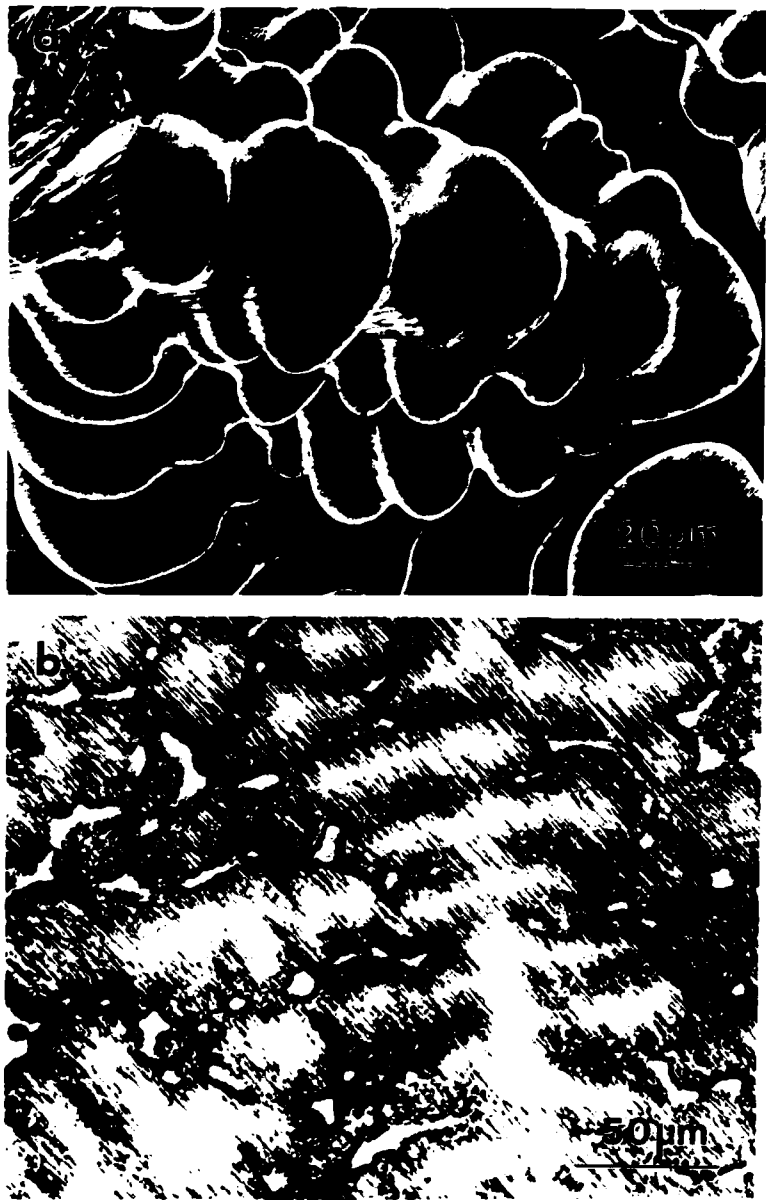


Figure 2. Dendritic microstructures of a Ti-48%Al alloy solidified in absence of a significant supercooling; the presence of orthogonal dendrites is evidence of β -(Ti) primary phase.
(a) SEM view of a shrinkage cavity and (b) Optical view of the cross-section.

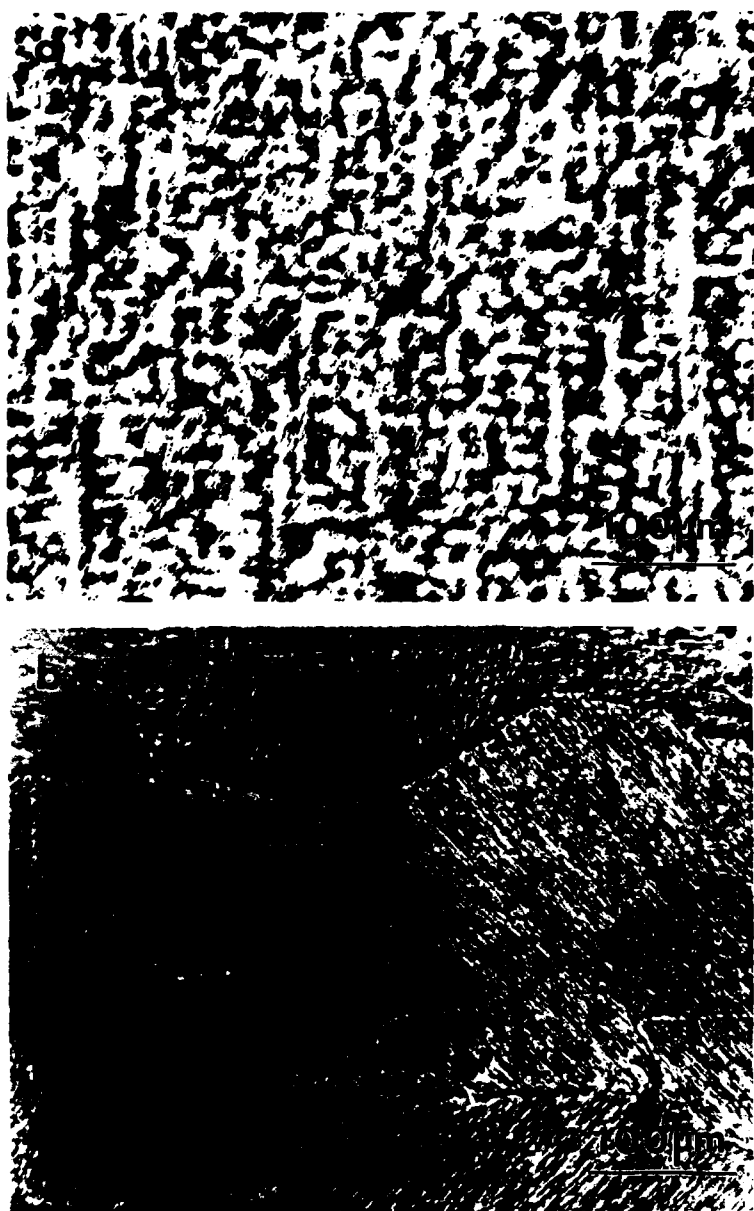


Figure 3. Metallographic sections of supercooled Ti-48%Al alloy:
(a) $\Delta T = 88\text{K}$ and (b) $\Delta T = 258\text{K}$. Note the orthogonal symmetry of the dendrites in (a), and the absence of γ segregate in (b).



Figure 4. TEM views of Ti-48%Al microstructures supercooled:
(a) $\Delta T \sim 0K$ and (b) $\Delta T = 258K$. Note the cellular growth
of γ_c into the primary phase in (a), and the usual
 $(\alpha_2 + \gamma_t)$ lath structure in (b).

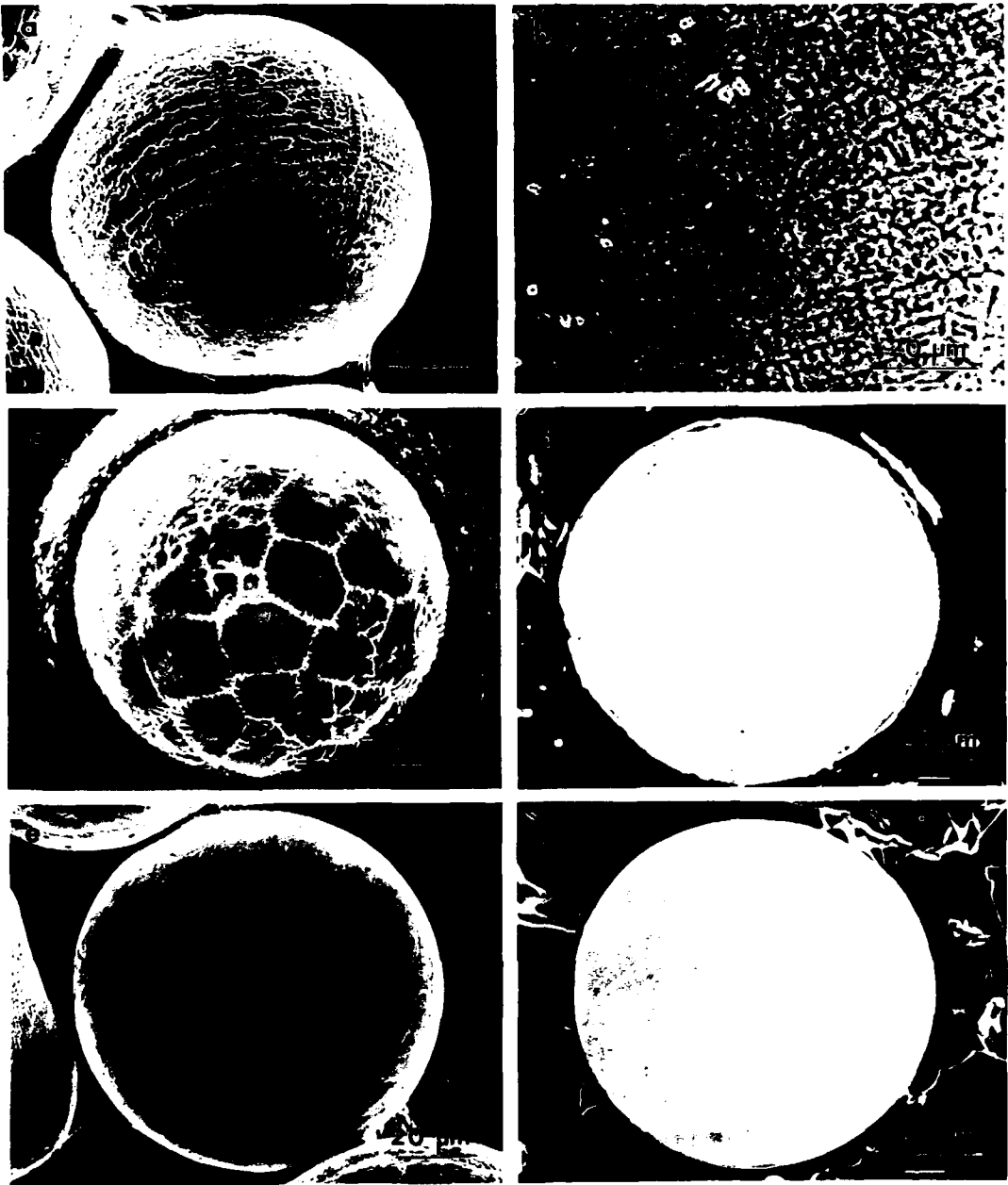


Figure 5. SEM views of surface and cross-sections of Ti-48%Al PREP powders:
(a) and (b) show orthogonal dendrites typical of the primary β -phase;
(c) and (d) are equiaxed dendrites, with no distinct crystallographic
pattern; and (e) and (f) reveal martensitic relief on the exterior and a
featureless cross-section.

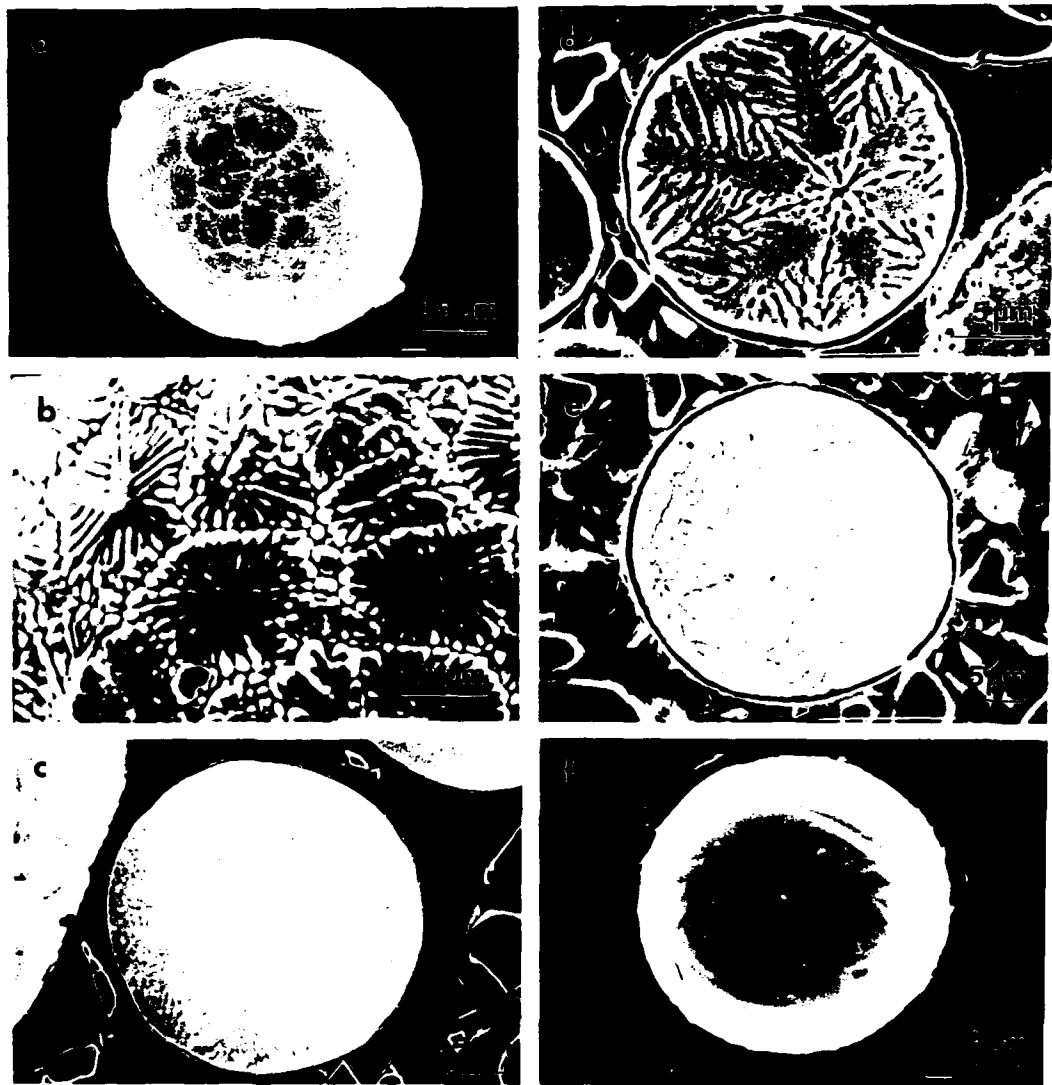


Figure 6. SEM microstructures of Ti-48%Al XSR powders: (a) to (c) from coarse particles ($106\text{--}150\mu\text{m}$) clearly showing the hexagonal growth symmetry at the surface in (a) and (b), and at the edges of the cross-section in (c). (d) to (f) are from fine powders ($<25\mu\text{m}$) showing: hexagonal growth (d), indistinct dendrites (e) and martensite (f).

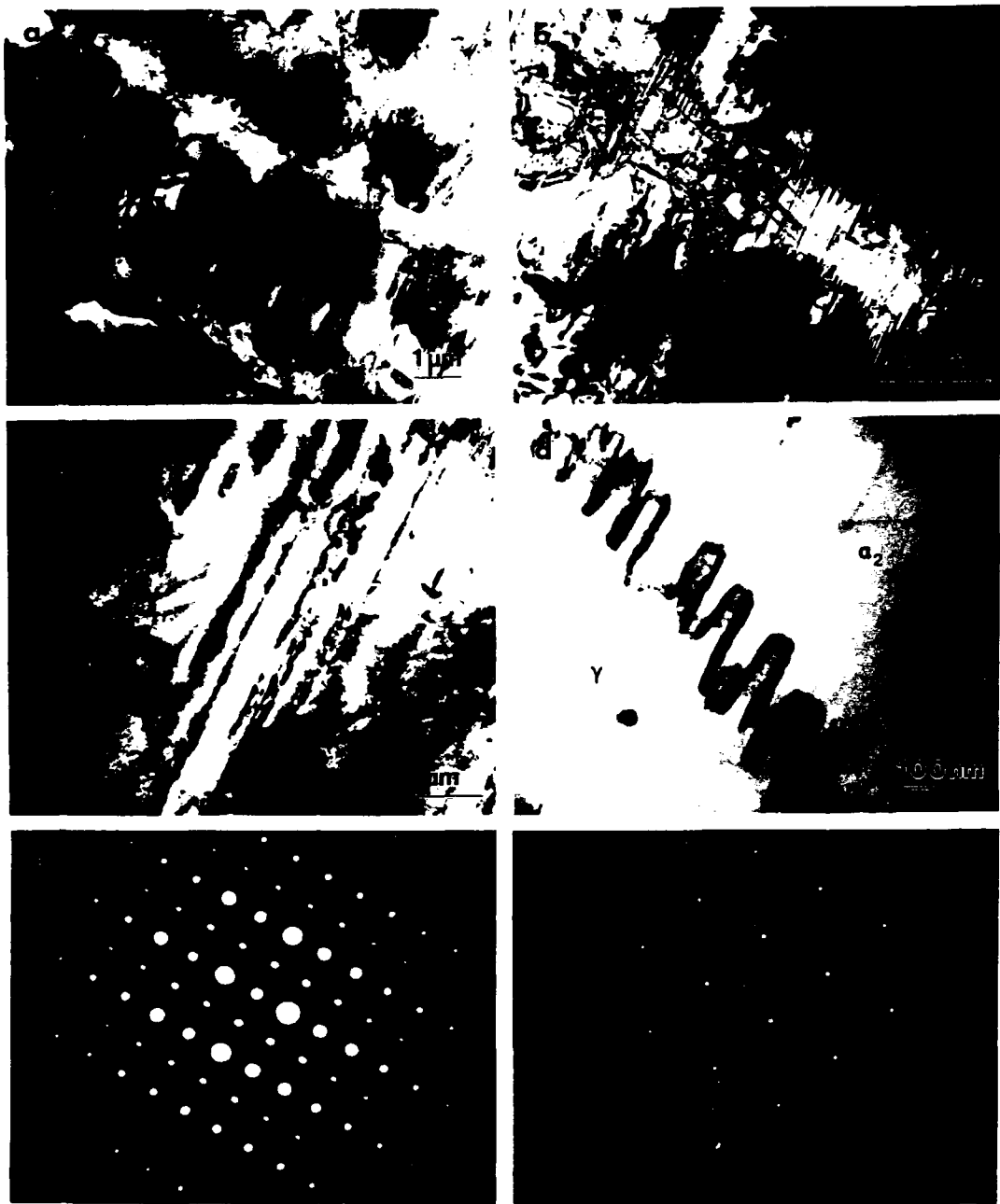


Figure 7. TEM views of Ti-48%Al XSR coarse powders (106-150 μm); (a) and (b) are dendritic microstructures showing the γ -segregate, (c) reveals incipient precipitation of the γ_t lath phase, and (d) interface showing the regrowth of cellular γ into the dendrite. The zone axis patterns in (e) and (f) are: [1210] α_2 and [101] γ , respectively.

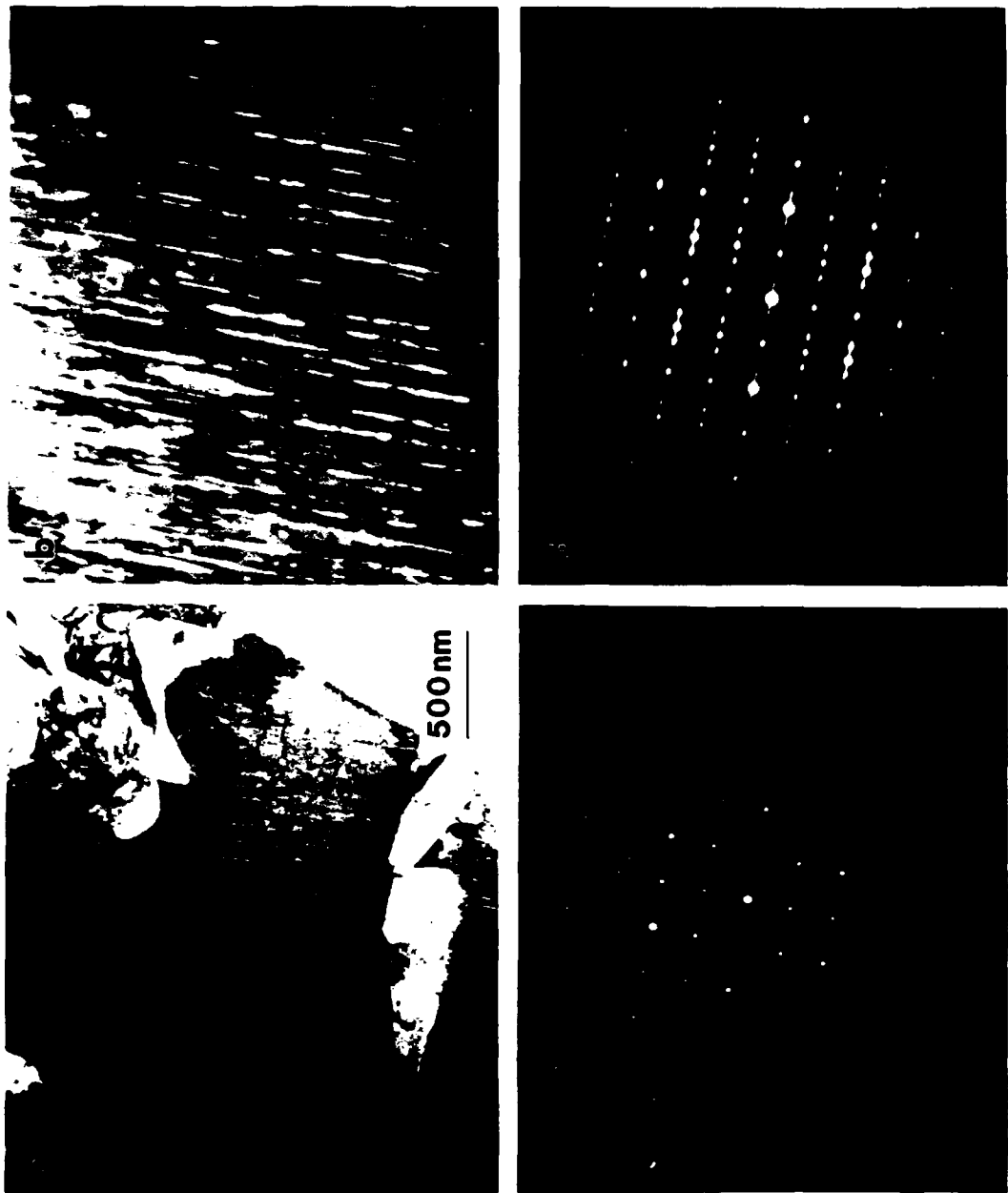


Figure 8. TEM microstructures of Ti-48%Al XSR fine powder ($<25\mu\text{m}$): (a) α_2 dendrite partially transformed to $(\alpha_2 + \gamma)$, surrounded by the γ -segregate; (b) very fine $(\alpha_2 + \gamma)$ lath within the dendrite. The zone axis patterns are: (c) $[1\bar{2}0]\alpha_2$ and (d) $[1\bar{2}0]\alpha_2 // [1\bar{1}0]\gamma$ for the untransformed and transformed regions, respectively.

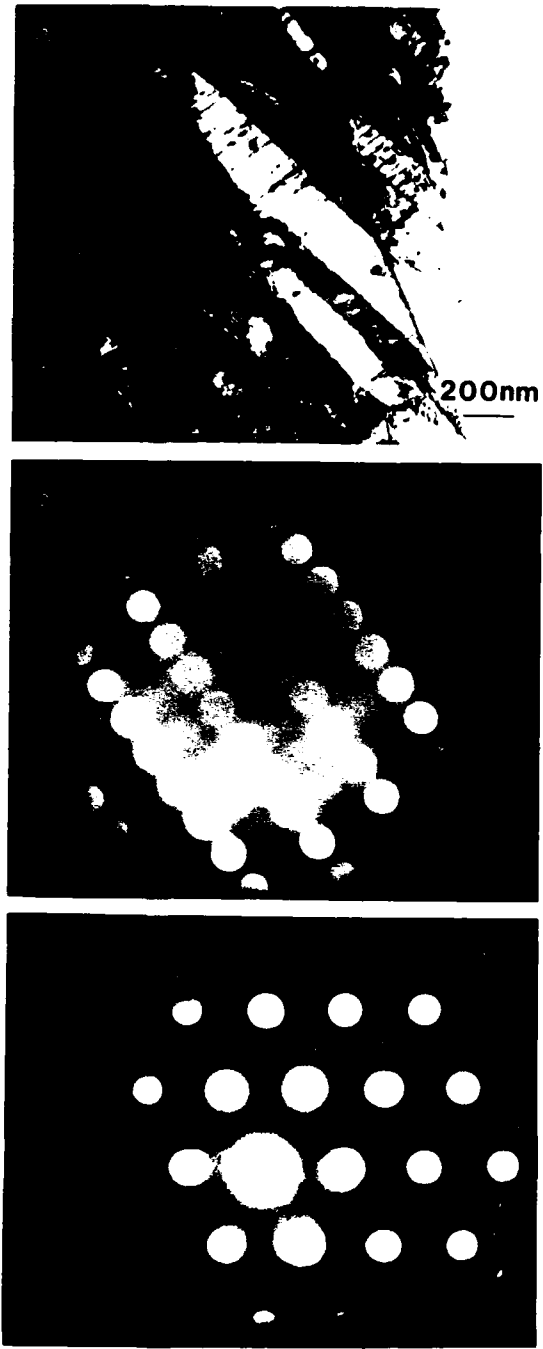


Figure 9. TEM microstructure of Ti-48%Al martensitic XSR powders: (a) martensite laths of a disordered hexagonal phase as shown by the zone axis patterns in (b) $[1\bar{2}10]\alpha$ and (c) $[1\bar{2}13]\alpha$.

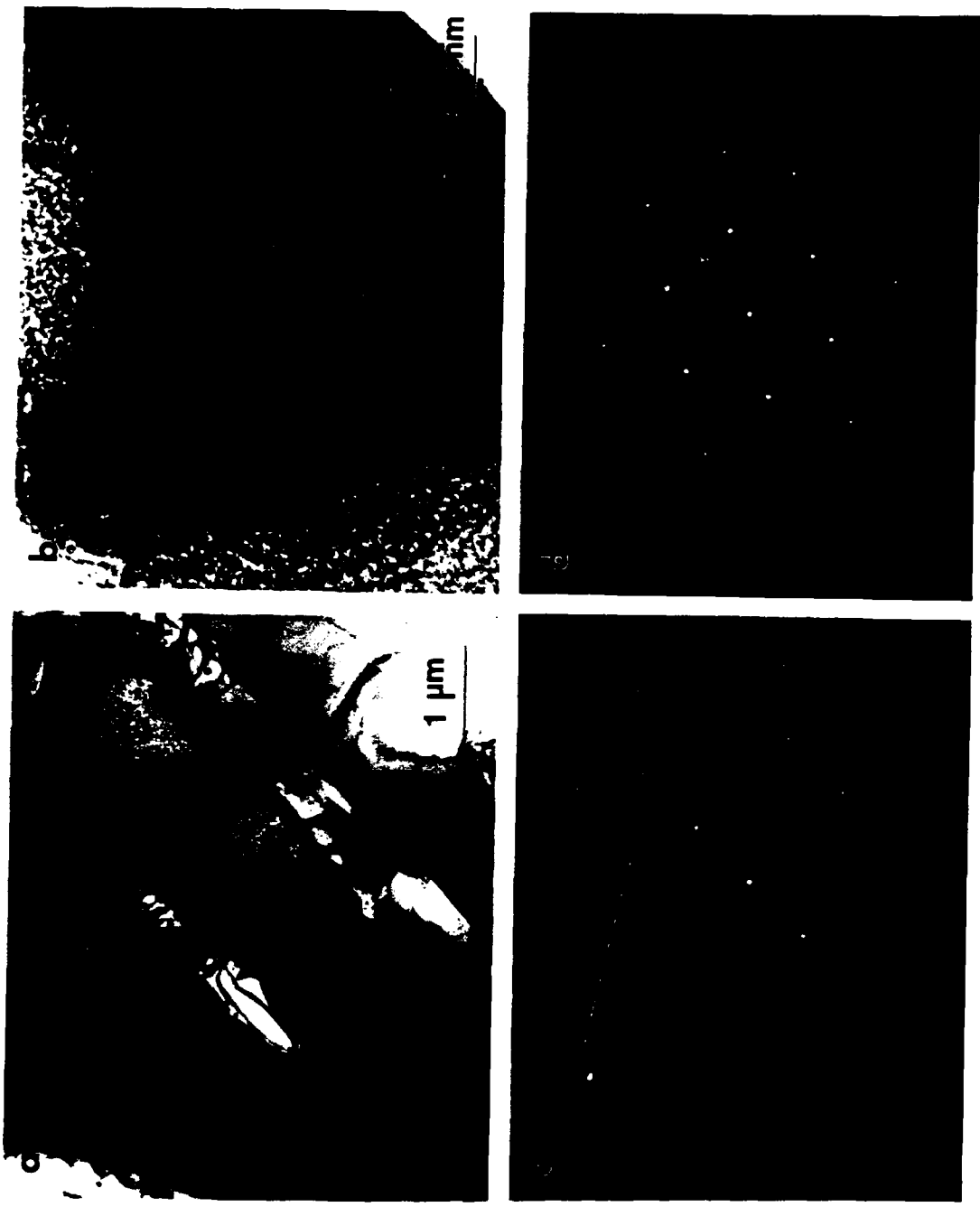


Figure 10. TEM views of Ti-48%Al-2%Ta XSR coarse powders: (a) dendritic region showing the γ -segregate, (b) APB contrast within α_2 but no evidence of γ lath. The diffraction zone axes are: (c) $[112]\gamma$ for the segregate, and (d) $(0001)\alpha_2$ for the dendrite.

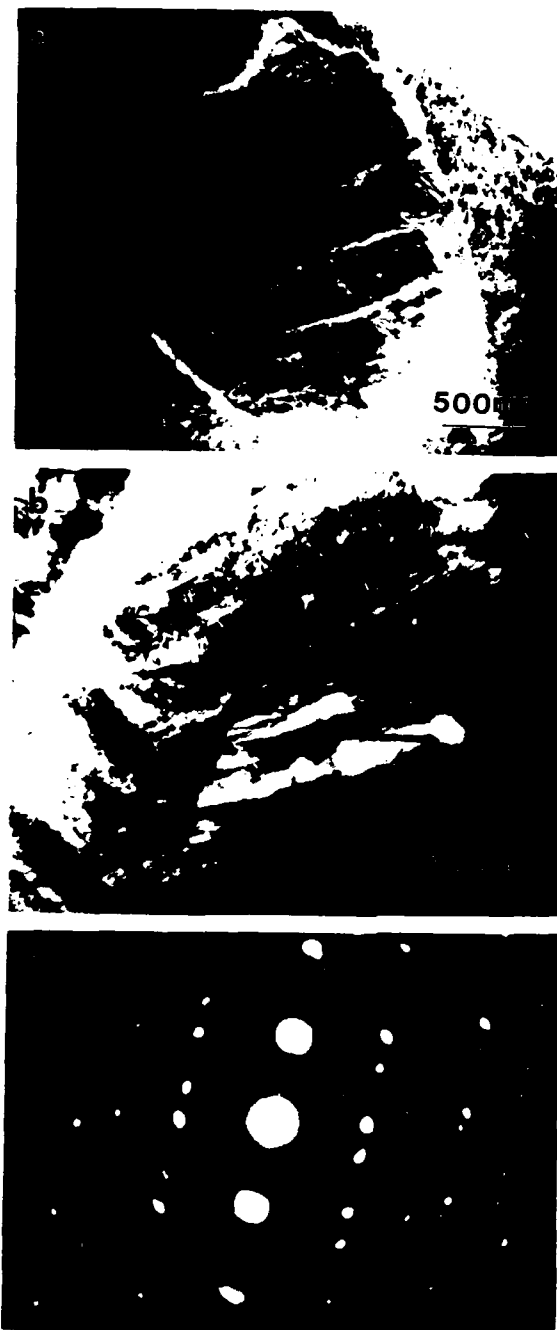


Figure 11. Martensitic microstructures in Ti-48%Al-2%Ta XSR powder:
(a) and (b) show martensite laths and (c) is the ZAP
showing twin related $[0\bar{1}11]\alpha$ orientations of neighboring
laths.

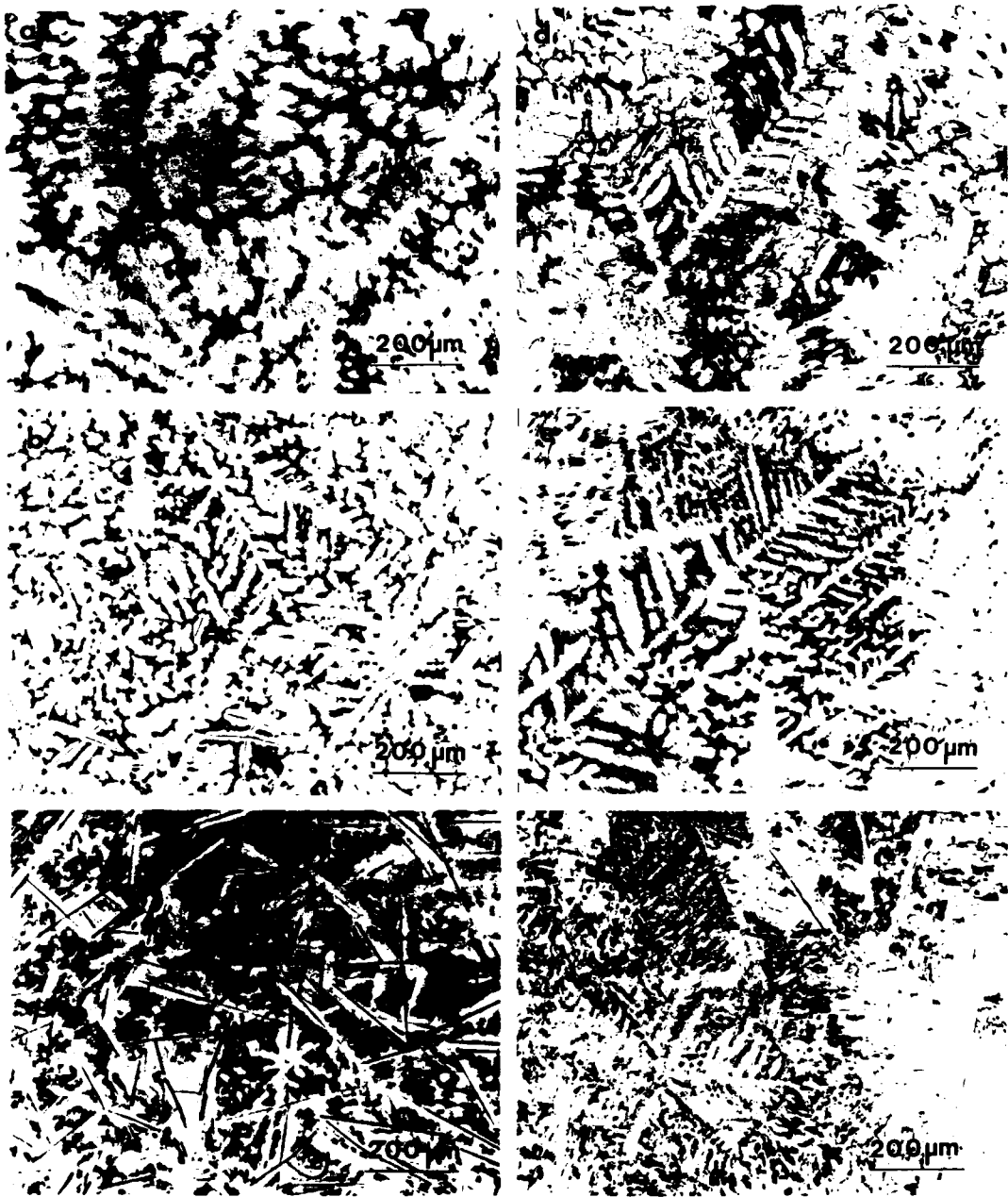


Figure 12. Metallographic sections of Ti-45%Al and Ti-48%Al ingots with carbon additions: Ti-45%Al containing (a) 0.32, (b) 0.64 and (c) 1.05% C, and Ti-48%Al containing (d) 0.38, (e) 0.76 and (f) 1.0% C. Note the absence of carbide plates in (a), (b) and (d), and the clearly hexagonal symmetry in all the micrographs except for (a), which shows cubic dendrites.

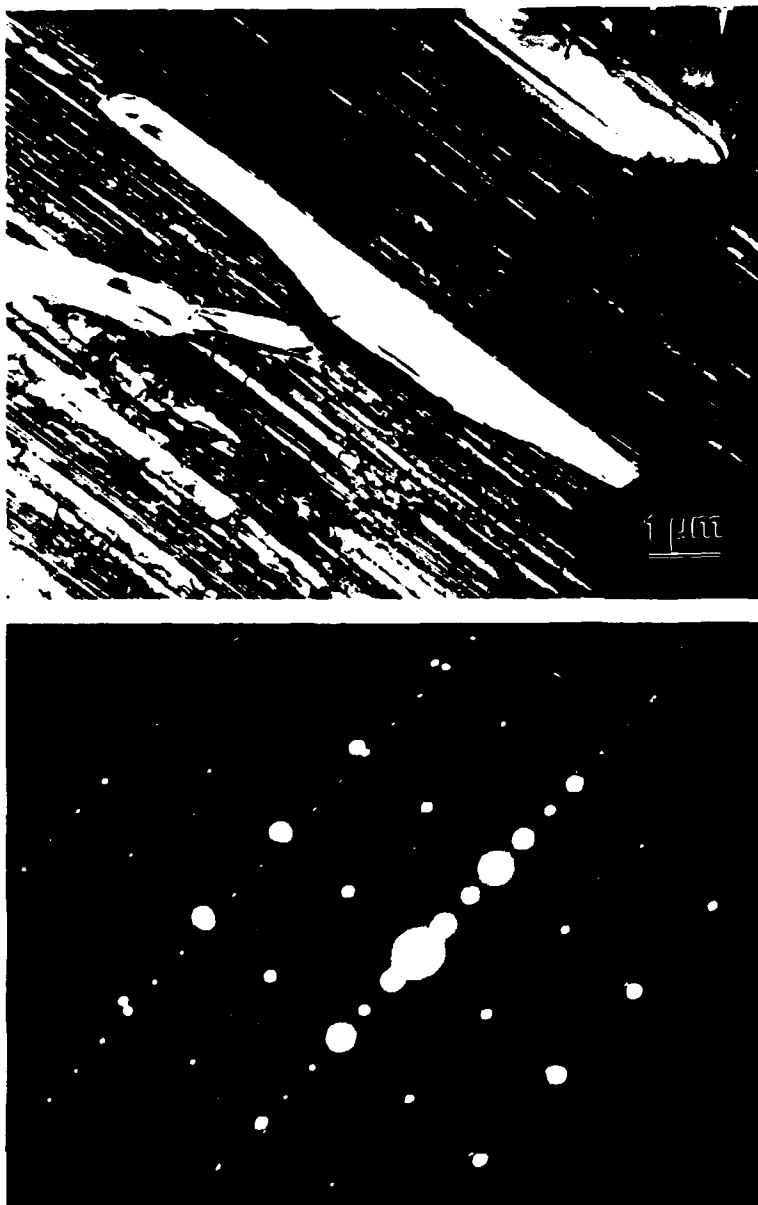


Figure 13. TEM microstructure of Ti-48%-1.5% C alloy ingot Ti_2AlC crystal, and the corresponding diffraction pattern with a $[0\bar{1}10]\text{Ti}_2\text{AlC}$ zone axis, which is parallel to a $[112]$ zone axis of γ .

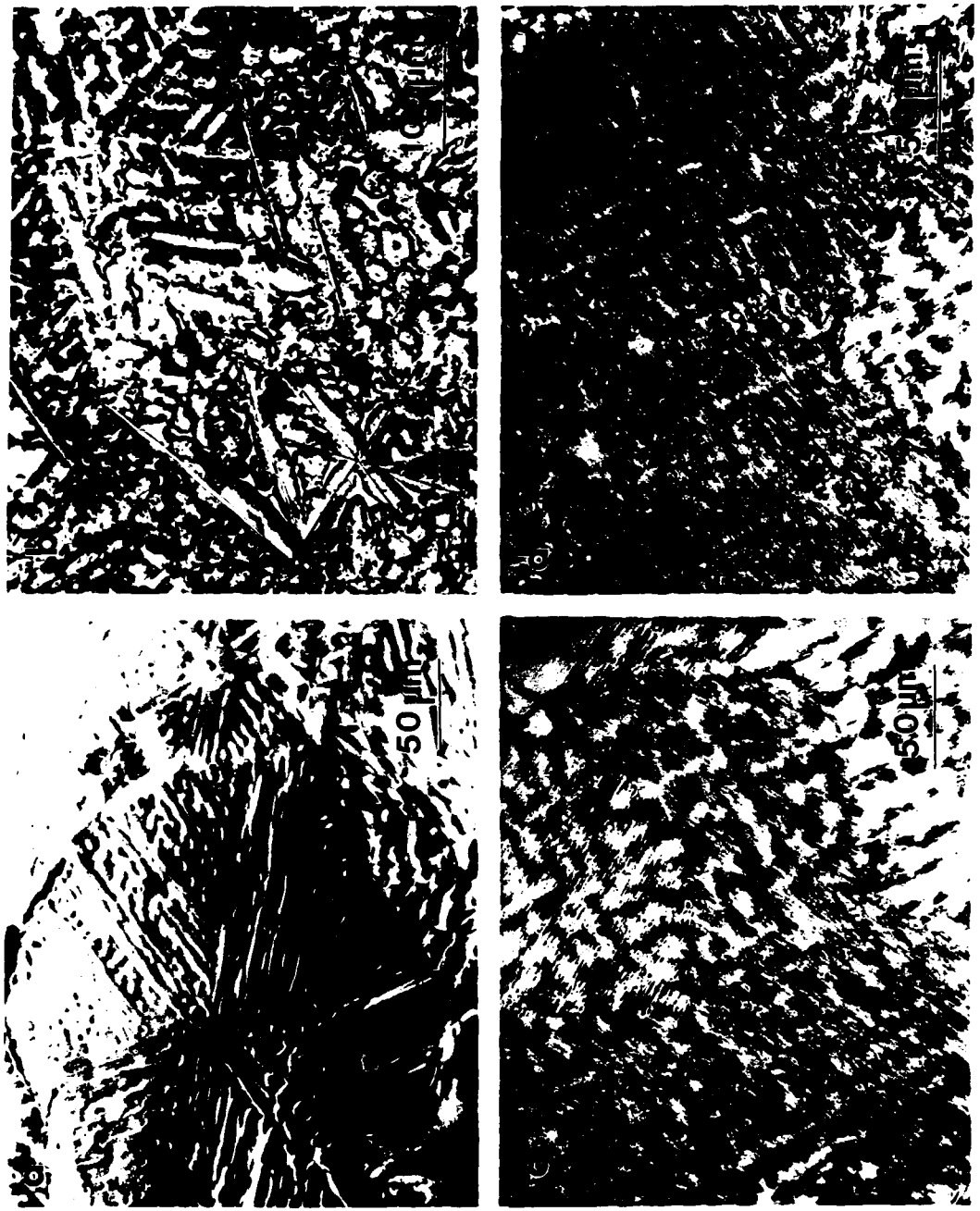


Figure 14. Microstructures of supercooled Ti-48%Al containing 0.38 (left) and 1.0% C (right). The leaner carbon alloy was supercooled: (a) $\Delta T = 60\text{K}$ and (c) $\Delta T = 100\text{K}$, and the higher carbon composition (b) $\Delta T = 60\text{K}$ and (d) $\Delta T = 117\text{K}$. In each composition the primary phase changes from α to β with increasing supercooling.

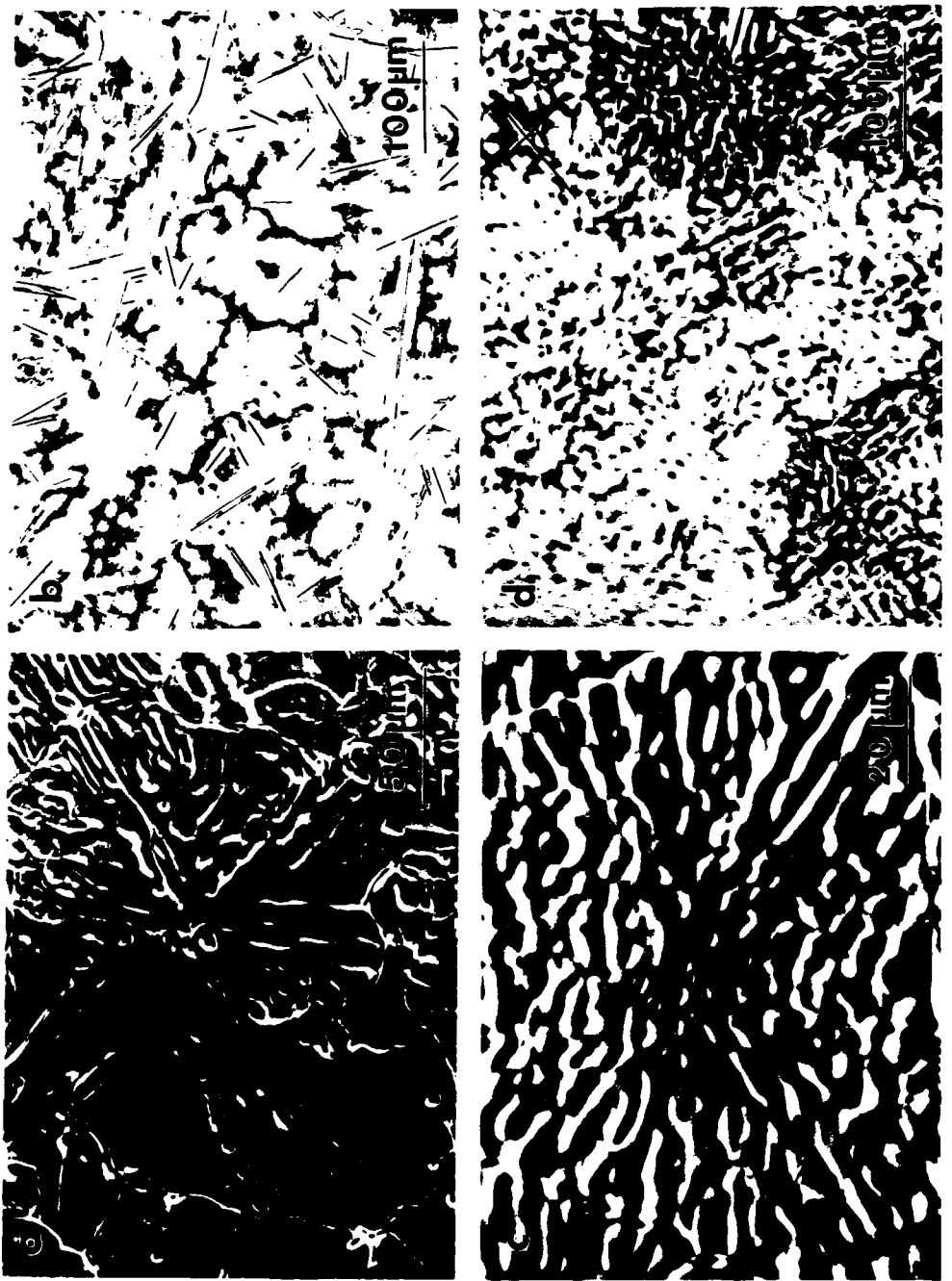
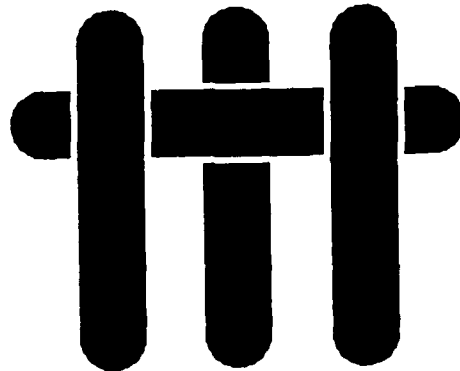


Figure 15. SEM and optical micrographs of supercooled Ti-45%Al-1.05at%Cr at $\Delta T \sim 0$ in (a) and (b), $\Delta T \sim 100\text{K}$ in (c) and (d). The primary phase changes from α to β with increasing supercooling.

M A T E R I A L S



SOLIDIFICATION PATHS IN Ta-Ti-Al ALLOYS

by

C.McCullough, J.J.Valencia, C.G.Levi, R.Mehrabian,
M. Malone* and R. Hecht*.

Materials Department
College of Engineering
University of California
Santa Barbara, CA 93106

* Pratt and Whitney Aircraft Co.
Government Engine Business
West Palm Beach, Fl 33410-9600

ABSTRACT

Microstructure evolution during solidification, and high temperature phase equilibria were investigated for Ta-Ti-Al alloys based on γ -TiAl containing up to 32%Ta. Examination of dendrite morphologies and segregation profiles were coupled with TEM analysis of the final microstructures to deduce the phase sequences during solidification and in the subsequent solid-state transformations. In situ high temperature X-ray diffraction and isothermal annealing experiments were conducted to study the phases present at elevated temperatures. For low Ta concentrations (7%) the primary phase in local equilibrium with the liquid was α as in the binary alloys, but with higher Ta levels (>10%) the primary phase was β . The latter were highly cored leading to different microstructures in the core and bulk dendrite regions. The segregate formed was always γ . In the solid state, the dendrites decomposed through various single, two and three fields, which at high temperatures usually involved the α phase. In low Ta alloys (<15%), ($\alpha_2 + \gamma_t$) lath formed in the bulk due to the decomposition of low Ta α , with σ precipitating the core (>10%Ta). With increasing Ta levels the lath is gradually replaced by polycrystalline γ from growth of the segregate into the dendrite bulk, and the core decomposes into a lamellar ($\gamma + \sigma$) microstructure from the decomposition of high Ta α . The γ segregate does not transform further.

INTRODUCTION

Titanium aluminides are currently the focus of a major research effort for prospective use in the next generation of aerospace materials. The most promising alloys are based on the γ -TiAl (L1₀) which has attractive stiffness and oxidation resistance at high temperature, but inadequate creep strength and room temperature toughness. Current microstructural design approaches involve adding ductile phase particles to give toughness and fibers to enhance the creep strength. However, the highest potential service temperature of these materials will ultimately be limited by the melting point of the matrix.

Alloying elements such as niobium and tantalum added in significant amounts offer the potential for increasing the refractoriness of γ -TiAl. Tantalum is particularly attractive, due to its higher melting temperature (2996°C) and an apparent increase in oxidation resistance of the aluminides, although there is also an attendant penalty of a higher density than in the case of Nb. On the other hand, these alloys segregate heavily during solidification leading to detrimental effects on the mechanical behavior and environmental resistance. Understanding the solidification behavior is thus critical to the alloy development effort.

A fundamental limitation to the solidification understanding is the relative lack of information on the Ti-Ta-Al system. The available diagram is from Nowotny et al. [61Not,83Sri], but it is questionable since two of the binaries have since been revised. The Ti-Ta diagram [85Mur] is the only well documented system and consists of a continuous high temperature bcc solid solution (β) between Ti and Ta with a low temperature hexagonal α phase at higher Ti contents. The Ti-Al system has recently been re-evaluated and the most current version is shown in Figure 1 [89Cha]. Many problems still exist for the Ta-Al diagram, primarily regarding the number and crystallographic nature of the phases present. A recent experimental study [89Mir] may have resolved some of the disagreement; the proposed diagram is shown in Figure 2. The equilibrium phases reported are σ -AlTa₂ (tetragonal, tP30), AlTa (cubic)[89Mir2], Al₂Ta (unidentified) and Al₃Ta (tetragonal, tI8). This is contrary to the previous version [85Shu] which showed no AlTa or Al₂Ta, and an additional phase in Al₃Ta₂. Interestingly, Miracle [89Mir] shows the X-ray diffraction evidence for Al₂Ta to essentially match that reported for the high temperature orthorhombic form of Al₃Ta₂ reported by Schuster [85Shu]. Furthermore

equilibration at 1150°C for 500 hours failed to produce evidence of any low temperature phase which was reported by Schuster to be hexagonal Al₃Ta₂.

Recent studies have also shown the possibility of a ternary phase around the composition Ti₂AlTa [89Per] based on a B2 structure [89Per,89Abb], although it is not clear at present if this is an equilibrium or a metastable phase. It is likely however, that this phase forms by transformation of the β phase, rather than directly from the liquid. Moreover there is evidence that this demands high quenching rates to avoid decomposition into other phases, which masks the evidence of its existence. Thus it is anticipated that all the phases that may form during solidification will be based on those already existing in the binaries.

Before the ternary Ta-Ti-Al alloys can be understood, it is convenient to review the solidification behavior of the binary TiAl alloys. The phase equilibria [89Cha,89McC,88McC] and solidification paths are well characterized for the α_2 - γ region [87Val,88McC,89McC,88Gra], see Figure 1. Between 40-45% Al* the b.c.c. β forms as the primary phase, which is then surrounded with the hexagonal α by solidification through a peritectic $L + \beta \rightarrow \alpha$. Solid state cooling transforms the β to α producing a single phase α at high temperature. Further cooling results in ordering of α to α_2 (DO₁₉) and γ (L1₀) phase precipitates within as twin related plates, γ_t , such that the close packed planes and directions of each phase are parallel [70Bla,87Val,89McC]. With contents of 46-49% Al, β still forms as the primary phase, and α again forms via the above peritectic solidification. There is also a third phase formed from the liquid, γ , produced as segregate by a further peritectic solidification of $L + \alpha \rightarrow \gamma$. In the solid state the β and α transform much as before but the γ segregate remains unchanged. Additionally as the α becomes less stable, the γ segregate begins to consume the edge of the dendrite corresponding to the alloy entering an ($\alpha + \gamma$) phase field (Figure 1). This produces an equiaxed γ morphology at the edge of the dendrite, termed a cellular morphology, γ_c [88McC,89McC]. Alloys between 49-55% Al form α as the primary phase, and γ forms as segregate, again through the peritectic solidification of $L + \alpha \rightarrow \gamma$. Further solid state decomposition follows the paths described above.

This paper aims to elucidate the solidification paths of a range of alloys based on the γ -TiAl phase with additions of up to 32% Ta. Extensive characterization of arc melted buttons was performed to establish the phases and segregation patterns formed from solidification. Further studies were conducted by high temperature X-

* all compositions are given in atomic percent.

ray diffraction to follow phase transformations as a function of temperature, and isothermal annealing experiments were performed to map the phase fields developed. From these it was possible to gain some insight into the phase sequencing from both the liquid and the solid states.

EXPERIMENTAL

A range of arc melted buttons of Ti-Al-Ta alloys were made with the compositions shown in Table I. Large buttons (250g) of alloys 2 to 4 were provided by Pratt and Whitney (West Palm Beach Laboratories). These were prepared under vacuum by first melting Ti and Ta together and then introducing the Al into the edge of the melt, and allowing it to soak into the liquid to produce the final alloy. The remaining alloys (20g) were made from high purity Ti (200 ppm O), Ta (99.99%) and Al (99.99%) by arc-melting in a purified argon atmosphere (< 0.1 ppb oxygen). To minimize the evaporation of Al in these smaller buttons, two master alloys were first produced for each alloy composition, one of Ti-Al and the other of Ti-Ta. These were then subsequently melted together to produce the final ternary alloy. In all cases the buttons were flipped several times and remelted to ensure mixing of the constituents.

Samples were cut from the as cast buttons by electrodischarge machining and characterized using high temperature X-ray diffraction, TEM (transmission electron microscopy) and SEM (scanning electron microscopy). The latter was operated in a backscattered imaging mode to obtain strong atomic number contrast, ideal for imaging segregated structures. Quantitative chemical information was acquired with a Tracor EDS (electron dispersive spectroscopy) system, calibrated with standards. Thin foils of the as cast buttons were prepared for TEM by twin jet-electropolishing as described elsewhere [89McC,89McX].

The high temperature X-ray diffraction studies were carried out on polished samples ~ 300-400 μm thick (Table II). During the experiments these samples were supported on a Ta stage and heated step-wise to various temperatures in a gettered argon atmosphere (~0.1 ppb oxygen) at a pressure between 0.9 - 1.0 atm. Diffraction spectra were then obtained at different temperatures, after the sample had been at temperature for ~15 minutes. Afterwards the samples were analyzed by EDS for any Al evaporation, which is common in such experiments and generally of the order of 1-2%Al. This technique has been successfully applied by the authors to the binary Ti-Al system [88McC,89McC], to elucidate the phase transformations during heating

and cooling, and providing information on the phase fields existing at high temperature.

Isothermal annealing experiments were carried out on buttons listed in Table III. These were placed in a vacuum furnace and heat treated at 1100°C for 48 hours, followed by furnace cooling. These samples were first examined in a microprobe to elicit the composition and distribution of the phases, and then studied in a X-ray diffractometer for phase identification. From all the above data, insight may be gained into the evolution of the microstructure during solidification.

RESULTS

Results are presented below for the alloys listed in Table I. This consists of three sections, the first detailing the solidification microstructure of the as cast materials, the second outlining the solid state phase transformation microstructures, and the third describing the transformations and phase sequencing as monitored by high temperature X-ray diffraction. A further section is presented dealing with a group of alloys (Table III) annealed at 1100°C for 48 hours, in order to map a partial isothermal section of the ternary system.

Solidification Microstructures

The alloys investigated seem to lie on three different regions of the liquidus surface. Alloys 1 and 8 exhibit dendrites with a six-fold symmetry (Figure 3), which are usually associated with growth of phases with a hexagonal crystal structure from the liquid. The primary phase in Alloy 1 is believed to be α -Ti, but that in Alloy 8 is more likely to be based on one of the intermetallics in the Ta-Al binary system. Note that the stoichiometry of the dendrites in the latter alloy (see Table I) suggests the recently reported AlTa as the primary phase, but the crystallography of that phase has tentatively been identified as cubic [89Mir2] and so is not consistent with the appearance of dendrites exhibiting hexagonal symmetry. The only hexagonal phase reported near this composition is Al_3Ta_2 [85Shu], but is a low temperature phase which transforms to an orthorhombic phase before melting, and thus would not be expected to give rise to these dendrites. Hence only the unidentified Al_2Ta or a metastable phase seem a likely candidate for the dendritic phase. Alloys in this

composition range remain under investigation. The segregate constituent is γ in Alloys 1-7 and probably Al_2Ta or Al_3Ta in Alloy 8.

The largest group (Alloys 2-7) exhibit orthogonal dendrites characteristic of the formation of β -Ti as the primary phase. Figure 4 shows four of these alloys. Within all of the dendrites (grey regions) there is a strong coring pattern as shown by the white regions at their centers., and surrounding these is a segregate phase (black regions), identified later as γ . The secondary dendrite arm spacing was found to be 20-25 μm in alloy 2 and smaller in alloys 3 and 4 (15-20 μm). The remaining alloys (5-7) had similar spacings. The proportion of segregate was ~ 10.5 % in alloy 2, climbing to ~15% in alloy 3 and falling to ~7 % in alloy 4; the latter is lower probably because of a relatively lower Al content (Table I).

The primary phases observed are helpful in defining the approximate boundaries of the α and β regions on the liquidus surface which are estimated in Figure 5. The results suggest that the α liquidus, which ranges from 49 to 55 at%Al on the binary system, is shifted to lower aluminum contents with the initial additions of Ta but is encroached by the β and γ liquidus as the Ta content increases above ~10at%. It is interesting to note that the α liquidus behaves in a similar manner in the Ti-Al-Nb system [89Cha2].

All alloys that form primary β exhibit strong partitioning of Ta toward the dendrite cores. The average compositions of the core and segregate regions as measured for many dendrites are given in Table I, and an individual dendrite arm of Alloys 2-4 are shown in Figure 6. Composition profiles across these dendrites reveal that the Ta concentration at the core is 10-20% higher than that in the bulk of the dendrite, and even higher when compared to the segregate. Aluminum segregates in the opposite way to tantalum. The Ta appears primarily associated with a σ (white) phase (see below) in the final microstructure which corresponds to the "spike" in the composition profile. As the Ta content of the alloys increases so too does the Ta levels in all parts of the microstructure. In addition, the microstructures can exhibit multiple constituents within the same dendrite, suggesting that different regions in the dendrite go through different transformation paths in the solid state. Figure 6 shows that the core region enlarges with increasing Ta content, and eventually evolves into a two phase structure in the high Ta alloys (Figure 6e). This causes the fluctuations in Ta seen in the core (Figure 6f). This microstructure will be described further below. The γ segregate does not transform further during cooling.

Solid State Transformation Microstructures

Extensive TEM characterization was performed on Alloys 2-4. The major phase present in all cases is polycrystalline γ , with σ and/or α_2 in minor proportions. The pattern of coring can also be seen in alloys of low Ta content, Figure 7a, in which the darker regions are areas richer in tantalum, due to the greater scattering effect of tantalum. Such areas delineate dendrites with arms at right angles to each other, consistent with the morphologies described previously. Within the dendrites of Figure 7a striations may frequently be observed (as also seen in Figures 4a and 4b), and Figure 7b shows these are characteristic of the $(\alpha_2 + \gamma_t)$ lath microstructure developed in the binary Ti-Al system. This consists of alternating layers of α_2 and γ_t which evolves from the ordering of α to α_2 and the further precipitation of γ_t on basal stacking faults of the α_2 phase[70Bla,87Val,88McC,89McC]. The spacing of the γ lath is ~300nm. Electron diffraction from this area (Figure 7c) revealed the presence of two twin related γ_t variants as in the equivalent binary alloy but there was no α_2 detected. The α_2 may be present but only as very thin layers (few atoms thick) at the lath boundaries, and hence the diffraction is weak enough relative to γ to be unobserved in Figure 7c. On the other hand the α_2 may have been totally consumed by the precipitation of the γ_t constituent. Figure 7a also shows the laths lie at 45° to the dendrite arm growth directions, which is consistent with the formation of β dendrites during solidification, given the crystallographic considerations of microstructure evolution in the binary Ti-Al system [89McC].

Figure 8a shows the segregate grains of polycrystalline γ , identified by the $[101]_\gamma$ zone axis in figure 8b. These grains are not restricted to the segregate alone, but may also be found within some of the dendrites (as in Figure 7a), and the γ grain size in these areas are of the same order as the γ segregate. This may be due to partial homogenization during the melting procedure, or more likely because of some epitaxial regrowth of the segregate back into the dendrite, in much the same manner as reported for binary Ti-50%Al [89McC,87Val]. After solidification the β dendrite transforms to α and then with further cooling the dendrite would like to transform to $(\alpha + \gamma)$. Since the γ segregate is in intimate contact with the edge of the dendrite, the latter is consumed by the segregate thus eliminating the need for any separate γ nucleation. The extent of regrowth is much greater than for the binary alloys, often consuming entire secondary arms. This is probably because additions of Ta stabilize the γ phase in the ternary alloys (see later section), thus increasing the driving force

for the regrowth reaction. As the Ta content of the alloys increases, the amount of lath microconstituent decreases and that of the polycrystalline γ increases. In addition the dendrite cores enlarge and decompose into a two phase mixture.

Figure 9a shows a TEM micrograph of the two phase region at the dendrite core of Ta rich alloys (e.g. figure 6e). The light regions are the γ phase and the dark regions σ . The two phase ($\gamma + \sigma$) lamellar are grouped in "packets" of different orientations, all within a matrix of polycrystalline γ . At the boundary between these constituents there is a thick σ layer enveloping the lamellar component, which has a similar orientation to the σ in the neighboring packets of the ($\sigma + \gamma$) core. However, the polycrystalline γ has a quite different orientation from any of the γ within the core. It is interesting to note that polycrystalline γ exists in all areas of the microstructure outside of the core region, suggesting that the γ segregate grows back and consumes all of the original dendrite outside of the Ta enriched center. Suitable orienting of the two phase region enables the lamellae to be viewed edge on, producing a morphology reminiscent of a eutectoid type or cellular type decomposition product (figure 9b).

Figure 10a shows the two phases coexist as a plate structure inside the core. Electron diffraction from this structure (figure 10b), resulted in the elucidation of a clear and repeatable orientation relationship between these phases. The diffraction pattern contains a single σ zone axis and two twin related γ zone axes, and the orientation relationship was determined as;

$$[11\bar{3}]_{\sigma} // [110]_{\gamma} // [110]_{\gamma t}$$

$$(\bar{1}10)_{\sigma} // (\bar{1}11)_{\gamma} // (\bar{1}11)_{\gamma t}$$

$$(332)_{\sigma} // (1\bar{1}2)_{\gamma} // (1\bar{1}2)_{\gamma t}$$

where γt refers to the twinned γ variant. The habit planes of the plates are $(\bar{1}10)_{\sigma}$ and $(\bar{1}11)_{\gamma}$. These planes have only a small mismatch since the d-spacings for these particular planes are such that $(\bar{1}10)_{\sigma} \sim 3 (\bar{1}11)_{\gamma}$, i.e. there is very little misfit between the planes. Figure 10a shows contrast at the interface between the plates indicative of

periodically spaced dislocations that would accommodate this misfit. The $\{111\}_\gamma$ planes are the closest packed planes for γ and inspection of the unit cell of σ suggests that $(\bar{1}10)_\sigma$ is also the closest packed plane. Hence in this structure the closest packed planes of each phase are parallel. Dark field imaging shows the alternating layers of γ (figure 10c) and σ (figure 10d), with the layers ~80 nm thick, and imaged using $g = (\bar{1}11)_\gamma + (\bar{1}11)_{\gamma\text{f}}$ for γ and $g = (1\bar{4}1)_\sigma$ for σ .

The σ phase also appears as two other morphologies. One as small discrete precipitates and the other as strings. The first of these, the small discrete precipitates (figure 11a), are 100-500 nm in diameter. In leaner alloys (10-15% Ta) they occur at the dendrite core within the $(\alpha_2 + \gamma_t)$ lath ~15 μm apart, while in Ta rich alloys (25%) these precipitates form in the bulk of the dendrites as depicted in figure 10a. Also in the high Ta alloys, within areas of the γ matrix close to the two phase ($\sigma + \gamma$) core there are strings of σ (figure 11b). The strings and the thick σ envelope have identical orientations although there was no constant relation between the σ strings and the polycrystalline γ .

An understanding has now been reached regarding the nature and morphologies of the phases formed from solidification. In order to understand how these evolved, it is necessary to obtain information on the phase transformations and phase equilibria at various temperatures and compositions. This may be accomplished by using high temperature X-ray diffraction.

High Temperature X-Ray Diffraction

The relevant phase fields for various temperatures, as well as the transformations that may occur during post-solidification cooling may be determined from the data collected during these experiments. These are summarized in Table II.

Alloy 1 shows γ at low temperature, which transforms to $(\alpha + \gamma)$ and eventually becomes $(\alpha + L)$, the latter determined from both the X-ray spectrum and evidence of incipient melting of the sample. No σ was detected. Interestingly no α_2 was detected either at low temperature although it may be present in small

quantities as outlined earlier for alloy 2[†] (figure 7b). Alloy 2 shows σ at the start of the run but since this was not detected during the cooling cycle, the σ signal is probably attributable to undissolved precipitates formed from the Ta segregation in the ingot. Again ($\alpha + \gamma$) is detected at high temperature, but the σ disappears as the α appears. Alloy 3 is clearly ($\gamma + \sigma$) at low temperature, but transforms through a three phase ($\alpha + \gamma + \sigma$) field before eventually forming single phase α^{\ddagger} at high temperature. Alloys 4 and 6 behave similarly in that they contain ($\gamma + \sigma$) at low temperature, but transform through a ($\alpha + \sigma$) field and eventually form ($\alpha + \beta$) at high temperature. Above these temperatures solidification evidence shows that alloys 2-7 lie on a ($L + \beta$) region on the liquidus surface.

All alloys contain γ as the predominant phase at low temperatures, with σ and/or α_2 as second phases. σ is more evident as the Ta content increases, and reappears upon cooling in the richer Ta alloys (alloys 3,4,6), but not in the 10% alloy (alloy 2). The latter is believed to be close to the $\gamma/(\gamma + \sigma)$ boundary and thus exhibits non-equilibrium σ in the as-cast condition as a result of precipitation in the Ta-rich dendrite cores. The presence of α_2 in the leaner Ta alloys (1-3) was deduced from the microstructural evidence[†], but the proportion is so small that it is not detected by the X-ray diffraction technique.

The α solid solution appears in all alloys at high temperature ($T > 1300^{\circ}\text{C}$), while γ and/or σ gradually disappear. This suggests that the α^{\ddagger} field extends significantly into the ternary diagram, even though the liquidus surface is probably truncated at a fairly low Ta content. As expected, the β phase is detected in the richer Ta alloys at the maximum testing temperature (1500°C).

Since no transformations appear to take place below 1200°C (see Table II), an isothermal annealing study was conducted to elucidate the general shape and scope of the phase fields at 1100°C .

[†] as noted previously the α_2 may also have been totally consumed by the precipitation of the γ lath.

[‡] although a trace signal from γ was detected at 1450°C , the highest temperature studied for this alloy.

Heat Treatment

A range of alloys were subject to heat treatment at 1100°C for 48 hours, and then furnace cooled. These are shown in Table III. The furnace cooling was not expected to greatly change the information obtained (versus quenching) as only slight composition shifts are likely and no further phase transformations will occur (see previous section). Microprobe examination obtained quantitative composition measurements for the different phases present, and these are also displayed in Table III.

The data from Table III is plotted in Figure 12 as tie lines. These results seem to fall into three separate phase regimes, of (i) a two phase $\gamma + \sigma$ field, (ii) a three phase $\gamma + \text{Al}_3(\text{Ti,Ta}) + (\text{AlTa or } \sigma)$ field, (iii) a two phase α_2 /ternary (T) + σ , or a three phase $\alpha_2 + \sigma + \text{T}$ field.

Figure 13a shows an example of an alloy (4) containing the two phases $\gamma + \sigma$. The σ phase is the light phase, present as a blocky network and string morphology in a matrix of γ . For the four alloys (3,4,9,10) that exhibit $(\gamma + \sigma)$, the σ phase was always positively identified by X-ray diffraction, and the γ in two instances where it constituted the major phase. From the plot in figure 12, it is clear that these alloys lie in a two phase $(\gamma + \sigma)$ field.

The two alloys 11 and 12 were found to contain three phases, and these are plotted as the three phase triangles in figure 12. X-ray diffraction identified two phases as γ and $\text{Al}_3(\text{Ti,Ta})$ with some signals remaining that could not be indexed. An example of one of the alloys (12) is given in figure 13b, which shows the dark matrix of $\text{Al}_3(\text{Ti,Ta})$ (area A) and between this and the light phase (area C) is a grey phase (area B) which compositionally corresponds to the γ . Figure 12 also offers some guidance into the nature of the light phase (area C), which lies in the vicinity of both the σ and AlTa fields. Compositionally this phase contains approximately equal proportions of Al and Ta with a small Ti dissolution (Table III), suggesting that the AlTa phase might penetrate 8-10%Ti into the ternary system. However, if the light phase were σ , which has a solubility of ~42%Al in the binary (Figure 2), then the single phase σ region would have to be distorted sharply across the diagram. This need not be the case if the unidentified phase is AlTa. At present this issue remains unresolved.

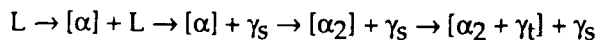
The third group of alloys (13,14), are a little more difficult to interpret. X-ray diffraction identifies only σ , with some unidentified peaks in both alloys which were thought to arise in part from α_2 . Figure 13c shows the microstructure from alloy 13

showing the light σ phase (area C) and two unidentified phases in the matrix. The composition of the dark phase (area B) appears to correspond to α_2 but the grey phase (area A) has a composition nearer that for the reported ternary Ti_2AlTa phase. Hence these two alloys may be mixtures of $\sigma + \alpha_2$ and/or Ti_2AlTa . A similar set of data acquired at 1200°C [89Ale], suggests little difference from 1100°C and the data in figure 12.

The high temperature X-ray diffraction results were combined with the microchemical analysis to estimate the phase boundaries at certain temperatures of interest. The 1100°C isothermal section (Figure 14) depicts the phase fields which are relevant to these alloys at the lower temperatures. Below this temperature the phase fields are not expected to change significantly. The diagram is constructed using data drawn from (i) Chang and Perepezko [89 Per2] for the α_2 and β fields, (ii) Miracle [89Mir] for the Ta-Al binary, (iii) annealing experiments and X-ray results of this study. The areas of uncertainty lie firstly at the Ti-rich end where the possible presence of a B2 ternary phase based on Ti_2AlTa make it difficult to construct phase fields at present. The second area of uncertainty lies near the $AlTa$ and Al_2Ta compounds since no data is available on how these project into the ternary system.

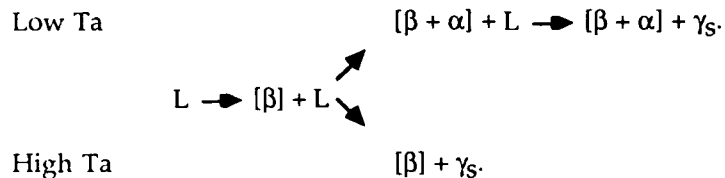
DISCUSSION

The paths of microstructure evolution elucidated from the information presented are discussed below. Alloy 1 is the only alloy that solidifies with α as the primary phase. Phase sequencing becomes essentially the same as for binary Ti-Al alloys in the range 49-55% Al, and may be summarized as:



where the phases in square brackets are inside the initial dendrites, and γ_S refers to the γ segregate. Following this path, the α dendrites form from the liquid, and are surrounded with segregate of γ phase after solidification through a peritectic of the type $L + \alpha \rightarrow \gamma$. The α orders to α_2 and then γ_t plates form within producing a final microstructure of an $(\alpha_2 + \gamma_t)$ lath constituent inside the original α dendrite, surrounded by γ segregate. Alloy 8 remains largely unidentified, other than it forms a primary phase that exhibits growth with a hexagonal symmetry.

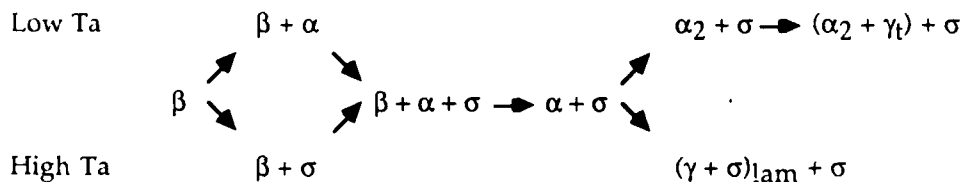
The remaining alloys studied all start solidification with β as the primary phase and only these are considered below. Those lean in Ta solidify through a double peritectic cascade $L + \beta \rightarrow \alpha$, and $L + \alpha \rightarrow \gamma$, as in the equivalent binary Ti-Al alloys (45-48% Al). As the Ta content increases the α liquidus is pinched-off and the alloys appear to solidify through a $L + \beta \rightarrow \gamma$ peritectic. In all the alloys γ is formed both as a segregate phase and by the solid state transformation of the dendrites (discussed later). Hence solidification in these alloys may be summarized as follows:



where the β is heavily cored, γ_s is the γ segregate which does not transform upon cooling, and the square brackets indicate phases inside the initial dendrites.

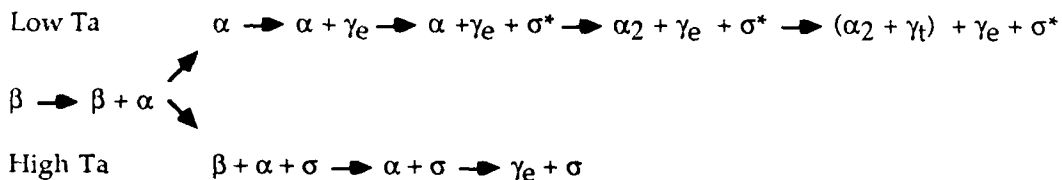
The primary β dendrites exhibit significant Ta segregation as a result of partitioning during solidification and solid state transformations. Depending on the local Ta content which is set by solidification, different regions of the dendrite may transform, through a series of single, two, and three phase fields, into different microconstituents during solid state cooling. Hence the core and bulk areas of the dendrites need to be considered separately. Since the local compositions are known, and the high temperature X-ray diffraction results give some guidance as to the positions of the phase fields at various temperatures, some insight into the microstructural evolution can be gained.

The solid state transformation of the Ta-rich, Al-poor, core regions during cooling may be described as follows:



where lam refers to the lamellar constituent. For alloys of low Ta content (e.g. 10%), the core contains 25-30% Ta. The β partially decomposes on cooling to α and then further to σ , producing a three phase mixture of $(\beta + \alpha + \sigma)$. The σ forms as small precipitates. With further cooling the β completely transforms to $(\alpha + \sigma)$, the α orders to α_2 and γ_t plates form within, as in the binary Ti-Al system. Hence the final core microstructure in Ta lean alloys consists of $(\alpha_2 + \gamma_t)$ lath[†] which contains small σ precipitates. As the Ta content of the alloy increases (e.g. >15%), the core of the β dendrite contains more Ta (35-40%) and so probably transforms first to $(\beta + \sigma)$ and then to $(\beta + \alpha + \sigma)$. This then transforms fully to $(\alpha + \sigma)$, but as the α becomes unstable upon further cooling, it cannot transform to α_2 since this phase is not stable at these higher Ta concentrations. Instead the α apparently undergoes a eutectoid-like or cellular-like decomposition to produce the final lamellar ($\gamma + \sigma$) constituent.

The bulk of the dendrites (i.e. those regions outside of the core) transform differently due to their much lower Ta content relative to the core. Phase sequencing during cooling may be expressed as follows:



where γ_e refers to equiaxed polycrystalline γ transformed from the dendrite by epitaxial regrowth of the γ segregate, and the asterisk refers to the fact that σ may be absent at low Ta contents.

For the lower Ta alloys, (<15%), the dendrite transforms in a similar fashion to the binary Ti-Al alloys, except for the extra consideration of some slight σ precipitation. In these cases β decomposes to single phase α , and as this becomes unstable relative to γ , the edges of the transformed dendrites are consumed by the epitaxial regrowth of γ (γ_e) from the segregate. With further cooling, the α may also decompose to σ if there is sufficient Ta enrichment (e.g. 15%, alloy 3). At the ordering temperature the α orders to α_2 and any further formation of γ is then

[†] as noted previously the α_2 may also have been totally consumed by the precipitation of the γ lath.

competitive between the growth of γ_t plates and regrowth of the γ_e . Hence the final microstructure in the dendrite bulk consists of the $(\alpha_2 + \gamma_t)$ lath structure, some σ precipitates (given sufficient Ta) and γ_e from growth of the segregate into the dendrite. At higher Ta contents, the β probably transforms via $(\beta + \alpha)$ to a three phase $(\beta + \alpha + \sigma)$, with the σ precipitating as small precipitates or strings. Eventually the β transforms fully to $(\alpha + \sigma)$. With further cooling, the α would like to transform to γ and σ , and this is achieved by extensive epitaxial regrowth of γ_e , which consumes the entire bulk of the dendrite up to the core region, with σ appearing as more precipitation and as some contribution to the σ envelope around the core. Hence the final microstructure in the dendrite bulk contains γ_e with strings and precipitates of σ .

SUMMARY

Additions of Ta to γ -TiAl modify both the solidification behavior and phase equilibria from those of the binary alloys. An understanding of these changes has been achieved by combining studies of solidification microstructures and in-situ determinations of phase equilibria.

Small additions of Ta (7%) do not appear to alter the solidification path; α still forms as the primary phase with γ as segregate. Higher Ta concentrations (10-15%) lead to the formation of β as the primary phase, which is superseded by peritectic α as solidification proceeds and finally γ is again produced as segregate. Alloys with larger amounts of Ta (15-25%) follow a similar path but with the omission of peritectic α , since the α liquidus surface is pinched off by the encroachment of the β and γ liquidus.

The alloys solidifying with β as the primary phase, also exhibit significant coring leading to Ta enrichment at the dendrite cores 10-20% above the bulk. This causes the dendrite bulk and core regions to transform quite differently during solid state cooling. With increasing Ta contents the dendrite cores contain increasing amounts of σ and ultimately form a lamellar $(\sigma + \gamma)$ microstructure due to the decomposition of a high temperature α phase. Bulk dendrite microstructures at lower Ta contents are dominated by the formation of the $(\alpha_2 + \gamma_t)$ lath, but this diminishes with increasing Ta levels, to be replaced by polycrystalline γ formed by epitaxial growth of the γ segregate into the dendrite.

It was established that the α -phase penetrates far into the ternary diagram at elevated temperatures ($>1300^{\circ}\text{C}$), and tends to lie above those fields containing σ , which itself becomes unstable at similar temperatures. γ remains as a single phase field ($<1200^{\circ}\text{C}$) even when ~10%Ta is present, but further Ta leads to the formation of a two phase ($\gamma + \sigma$) field.

ACKNOWLEDGEMENTS

The authors would like to thank Dr. Dan Miracle (WRDC/MLLM, Wright-Patterson AFB, Ohio) for permitting us to reproduce his Ta-Al phase diagram. Also fruitful discussions with Professors Y. A. Chang and J. H. Perepezko (University of Wisconsin-Madison) are gratefully acknowledged. The support of the Defense Advanced Research Projects Agency (DARPA) through the grant URI-N00014-86-K-0753, supervised by Dr. B. Wilcox and monitored by Dr. S.G. Fishman of the Office of Naval Research, is gratefully acknowledged.

REFERENCES

- [61Not] H. Nowotny, C. Brukl and F. Benesovsky, Monatsh. Chem., 92, 116-127 (1961)
- [83Sri] S. Sridharan and H. Nowotny, Z. Metallkde., 74, 468, (1983)
- [85Mur] J. L. Murray, in Binary Alloy Phase Diagrams, vol. 2, ed. T.B. Massalski, ASM, Metals Park, OH, 2099-2100 (1986)
- [85Shu] J.C. Schuster, Z. Metallkde "6, 724-727, (1985)
- [89McC] C. McCullough, J.J. Valencia, C.G. Levi and R. Mehrabian, Acta Metall., 37, 1321-1336 (1989)
- [89Cha] J.C. Mishurda, J.-C. Lin, Y.A. Chang and J.H. Perepezko, Mat. Res. Soc. Symp. Proc. Vol. 133, 57-62, MRS (1989)
- [88McC] C. McCullough, J.J. Valencia, C.G. Levi and R. Mehrabian, Scripta Metall., 22, 1131-1136 (1988)

[87Val] J.J. Valencia, C. McCullough, C.G. Levi and R. Mehrabian,
Scripta Metall., 21, 1341-1346 (1987)

[88Gra] J.A. Graves, L.A. Bendersky, F.S. Biancaniello, J.H. Perepezko
and W.J. Boettinger, Mat. Sci. Eng., 98 (1988) p. 265-268.

[70Bla] M.J. Blackburn, in "The Science, Technology, and Application of
Titanium", eds. R.I. Jaffee and N.E. Promisel, Pergamon Press, London
(1970), p. 633.

[89Mir] P.R. Subramanian, D.B. Miracle and S. Mazdiyasni, accepted for
publication in Met. Trans. (1989)

[89Mir2] D.B. Miracle, S. Mazdiyasni, and R. Subramanian, "TEM and X-Ray
Investigations of the Intermetallic Compound AlTa", presented at the
TMS/ASM Fall Meeting, Indianapolis, 1-5 Oct. (1989)

[89Per] J.C. Lin, Y.A. Chang and J.H. Perepezko, "Interdiffusion and Reactions at
the Interface between TiAl and Another Phase", presented at the
TMS/ASM Fall Meeting, Indianapolis, 1-5 Oct. (1989)

[89Abb] Y.S. Kim, K.R. Javed and G.J. Abbaschian, private communication,
University of Florida (1989)

[89McX] C. McCullough, J.J. Valencia, C.G. Levi and R. Mehrabian, accepted for
publication in Mat. Sci. Eng. (1989)

[89Cha2] J.H. Perepezko, Y.A. Chang, L.E. Seitzman, J.-C. Lin, N.R. Bonda, T.J. Jewett
and J.C. Mishurda, "High-Temperature Phase Stability in the Ti-Al-Nb
System", presented at the TMS/ASM Fall Meeting, Indianapolis, 1-5 Oct.
(1989)

[89Per2] J.H. Perepezko, J.-C. Lin, T.J. Jewett and Y.A. Chang, third annual report to
the University Research Initiative, of the University of California at Santa
Barbara, University of Wisconsin-Madison (1989)

[89Ale]

D. Alexander, private communication, Pratt and Whitney Aircraft Corporation (1989)

TABLES

Table I Composition of the Ta-Ti-Al arc-melted buttons (atomic %) and their microconstituents

Table II High temperature X-ray diffraction data for the Ta-Ti-Al alloys

Table III Composition of the phases resulting from heat treatment at 1100°C for 48 hours.

FIGURE CAPTIONS

Figure 1 Section of the recently assessed Ti-Al phase diagram [89Cha], showing the high temperature α field and two peritectics about the equi-atomic composition.

Figure 2 Experimentally determined Ta-Al phase diagram from Miracle[89Mir], showing a series of intermetallic compounds and an array of peritectics.

Figure 3 SEM micrographs of dendrites which exhibit hexagonal symmetry
(a) alloy 1 containing primary α phase dendrites, surrounded by a γ phase segregate
(b) alloy 8 containing unidentified dendrites.

Figure 4 Cubic dendrites of primary β phase in (a) alloy 2, (b) alloy 3, (c) alloy 6 and (d) alloy 4. All dendrites contain a Ta enriched core, which enlarges as the Ta content of the alloys increases, and γ is the segregate phase.

Figure 5 Estimated liquidus surface of the Ta-Ti-Al system, showing the dominance of the β liquidus and the pinching off of the α liquidus. The aluminum rich corner has been left incomplete due to lack of data.
Alloys 1-8 are marked by the circles.

Figure 6 Individual dendrite arms and associated Ta/Al segregation profiles determined from EDS measurements, (a-b) alloy 2, (c-d) alloy 3, (e-f) alloy 4. The cores are enriched in Ta and depleted in Al relative to the dendrite bulk and segregate.

Figure 7 TEM micrographs of the $(\alpha_2 + \gamma_t)$ lath morphology.
(a) lath within the dendrites, surrounded by polycrystalline γ segregate,
(b) alternating plates of γ and a twin related γ_t variant, with probable fine α_2 between,
(c) diffraction pattern showing two twin related $[1\bar{1}0]_\gamma$ zones.

Figure 8 (a) Polycrystalline γ segregate, (b) diffraction pattern showing a $[101]_{\gamma}$ zone.

Figure 9 (a) Core morphology in Ta rich samples consisting of $(\gamma + \sigma)$ lamellae with a surrounding envelope of σ , and a matrix of polycrystalline γ from regrowth of the segregate into the dendrite,
(b) lamellae oriented edge on.

Figure 10 (a) Bright field image of lamellar constituent. Note the interface contrast arising from elastic strain and misfit dislocations,
(b) diffraction pattern showing a single $[11\bar{3}]_{\sigma}$ zone and two twin related $[110]_{\gamma}$ zones,
(c) dark field of image of γ plates, $g = (\bar{1}11)_{\gamma} + (\bar{1}11)_{\gamma t}$,
(d) dark field of image of σ plates, $g = (1\bar{4}1)_{\sigma}$.

Figure 11 (a) equiaxed σ precipitate morphology,
(b) string morphology of σ .

Figure 12 Composition data from 1100°C annealing experiments plotted as tie lines and three phase triangles. This gives the position and approximate boundaries of the phase fields for the alloys studied.

Figure 13 SEM micrographs of samples annealed at 1100°C for 48 hours.
(a) alloy 4 containing σ (light regions) in a matrix of γ ,
(b) alloy 12 containing $Al_3(Ti,Ta)$ (region A), γ (region B) and either σ or $AlTa$ (region C),
(c) alloy 13 containing a possible ternary phase (region A), α_2 (region B) and σ (region C).

Figure 14 Estimated isothermal section at 1100°C.

Composition of the microconstituents in
Ta-Ti-Al arc-melted buttons (atomic %)

| Alloy | Average composition | | | Dendrite core | | | Segregate region | | |
|-----------|---------------------|------|------|---------------|------|------|------------------|------|------|
| | Ta | Ti | Al | Ta | Ti | Al | Ta | Ti | Al |
| 1 T0746** | 7.0 | 47.0 | 46.0 | 9.2 | 48.0 | 42.8 | 3.5 | 47.2 | 49.3 |
| 2 P224* | 10.2 | 41.8 | 48.0 | 25.8 | 40.6 | 33.6 | 3.7 | 42.5 | 53.8 |
| 3 P205* | 15.2 | 36.9 | 47.9 | 26.0 | 38.5 | 35.5 | 5.9 | 39.6 | 54.5 |
| 4 P208* | 27.0 | 27.5 | 45.5 | 35.0 | 26.7 | 38.3 | 9.9 | 33.6 | 56.5 |
| 5 T1742 | 17.0 | 40.9 | 42.1 | 31.3 | 38.2 | 30.5 | 6.0 | 42.4 | 51.6 |
| 6 T2341 | 23.6 | 33.9 | 42.5 | 34.0 | 34.2 | 31.8 | 8.7 | 38.8 | 52.5 |
| 7 T2743 | 27.5 | 29.7 | 42.8 | 40.5 | 26.7 | 32.8 | 14.7 | 33.1 | 52.2 |
| 8 T3155** | 31.6 | 13.5 | 54.9 | 41.8 | 12.4 | 45.8 | 23.5 | 13.2 | 63.3 |

(*) Alloys provided by Pratt and Whitney
 (***) Alloys do not contain a dendrite core

Table II: High temperature X-ray diffraction of Ta-Ti-Al Alloys

| Alloy Composition | 1 | 2 | 3 | 4 |
|-------------------|--------------------|--------------------|--------|------|
| | Ta | Al | Ta | Al |
| Before | 7.0 | 46.0 | 10.2 | 48.0 |
| After | | | 10.4 | 47.5 |
| 25°C | | | | |
| 1100°C | γ | γ+σ ⁽²⁾ | γ+σ | γ+σ |
| 1200°C | γ | γ+σ | γ+σ | γ+σ |
| 1300°C | γ | γ+σ | γ+σ | γ+σ |
| 1350°C | γ | γ+α+σ* | γ+σ | γ+σ |
| 1400°C | γ | γ+α | γ+α+σ* | γ+σ |
| 1425°C | γ+α | α+γ | α+γ+σ* | γ+σ |
| 1450°C | γ+α | α+γ* | α | α+σ* |
| 1475°C | α+γ | — | — | α+σ |
| 1500°C | α+L ⁽¹⁾ | — | — | α+β |
| 1450°C | γ+α? | — | — | α+β |
| 1400°C | γ | — | α+γ+σ* | γ+σ |
| 1350°C | — | γ | γ+α+σ* | — |
| 1300°C | — | — | γ+α+σ* | γ+σ |
| 1200°C | — | γ | γ+σ | γ+σ |
| 1100°C | γ | — | — | γ+σ |
| 25°C | γ | γ | γ+σ | γ+σ |

* trace signal
 (1) from microstructural evidence
 (2) probably from undissolved precipitates

Table III: Composition of the Phases Resulting from Heat Treatment at 1100°C for 48hrs.

| Alloy | Alloy Composition* | | | Phase | Phase Composition (%) | | |
|-------|--------------------|----|----|-------------------------|-----------------------|------|------|
| | Ta | Ti | Al | | Ta | Ti | Al |
| 3 | 15 | 35 | 50 | γ | 11.7 | 39.5 | 48.8 |
| | | | | σ | 43.2 | 20.8 | 36.0 |
| 4 | 25 | 25 | 50 | γ | 13.6 | 32.8 | 53.6 |
| | | | | σ | 42.9 | 17.2 | 39.9 |
| 9 | 35 | 25 | 40 | γ | 16.7 | 35.7 | 47.6 |
| | | | | σ | 40.6 | 22.1 | 37.3 |
| 10 | 36 | 26 | 38 | γ | 19.1 | 36.7 | 44.2 |
| | | | | σ | 39.9 | 24.6 | 35.5 |
| 11 | 23 | 23 | 54 | γ | 15.2 | 26.0 | 58.8 |
| | | | | σ /AlTa? | 43.4 | 9.8 | 46.8 |
| | | | | Al ₃ (Ti,Ta) | 12.8 | 16.6 | 70.6 |
| 12 | 25 | 15 | 60 | γ | 17.2 | 23.4 | 59.5 |
| | | | | σ /AlTa? | 45.8 | 7.9 | 46.3 |
| | | | | Al ₃ (Ti,Ta) | 16.4 | 13.5 | 70.1 |
| 13 | 20 | 47 | 33 | σ | 35.8 | 30.8 | 33.4 |
| | | | | α_2 ? | 9.7 | 54.5 | 35.8 |
| | | | | T? | 15.0 | 51.0 | 34.0 |
| 14 | 39 | 28 | 33 | α_2 ? | 15.5 | 49.1 | 35.4 |
| | | | | σ | 35.1 | 29.3 | 35.6 |

all alloys were furnace cooled

* nominal target alloy composition

T - ternary phase

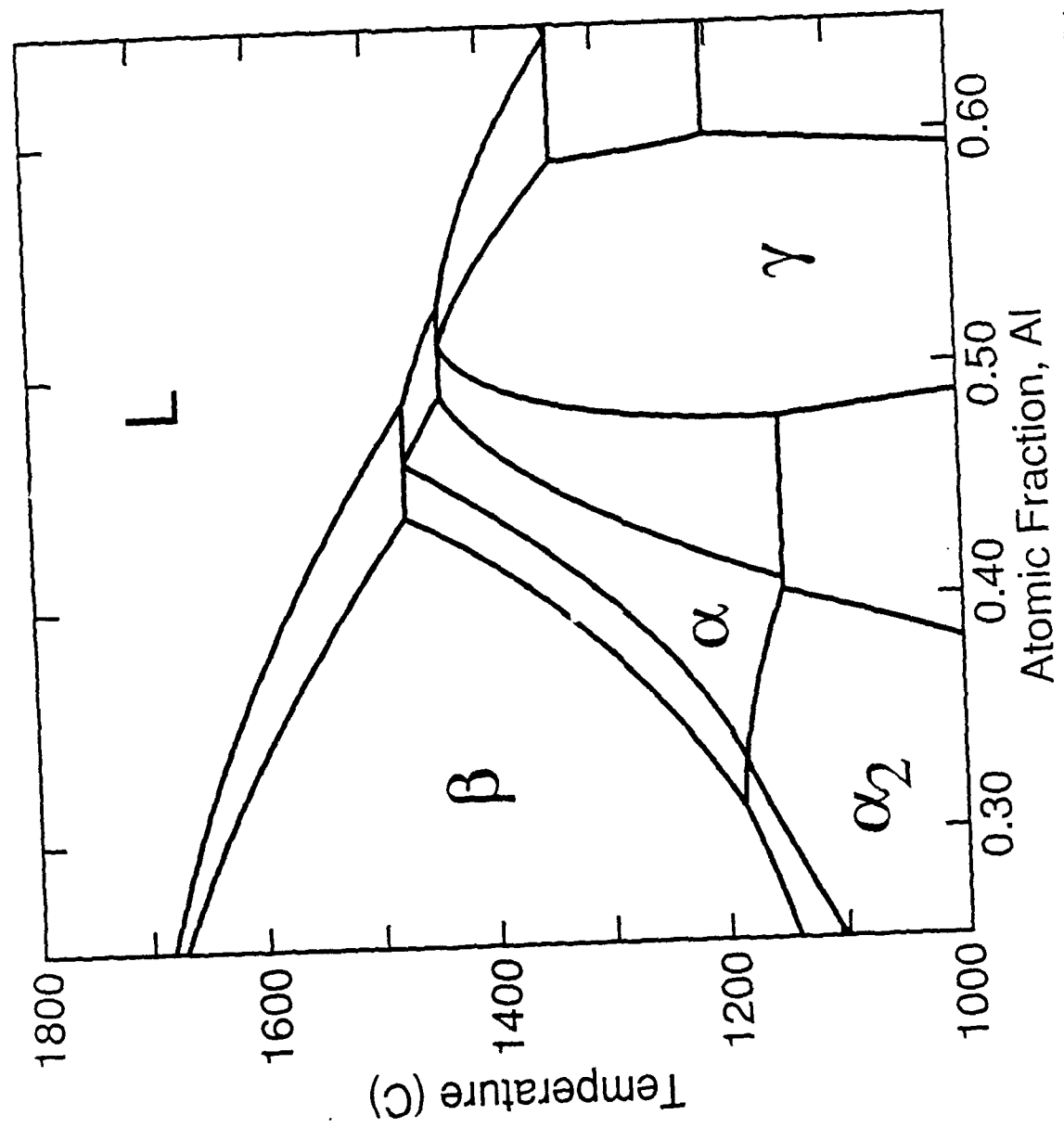


Figure 1. Section of the recently assessed Ti-Al phase diagram [89Chal], showing the high temperature α field and two peritectics about the equi-atomic composition.

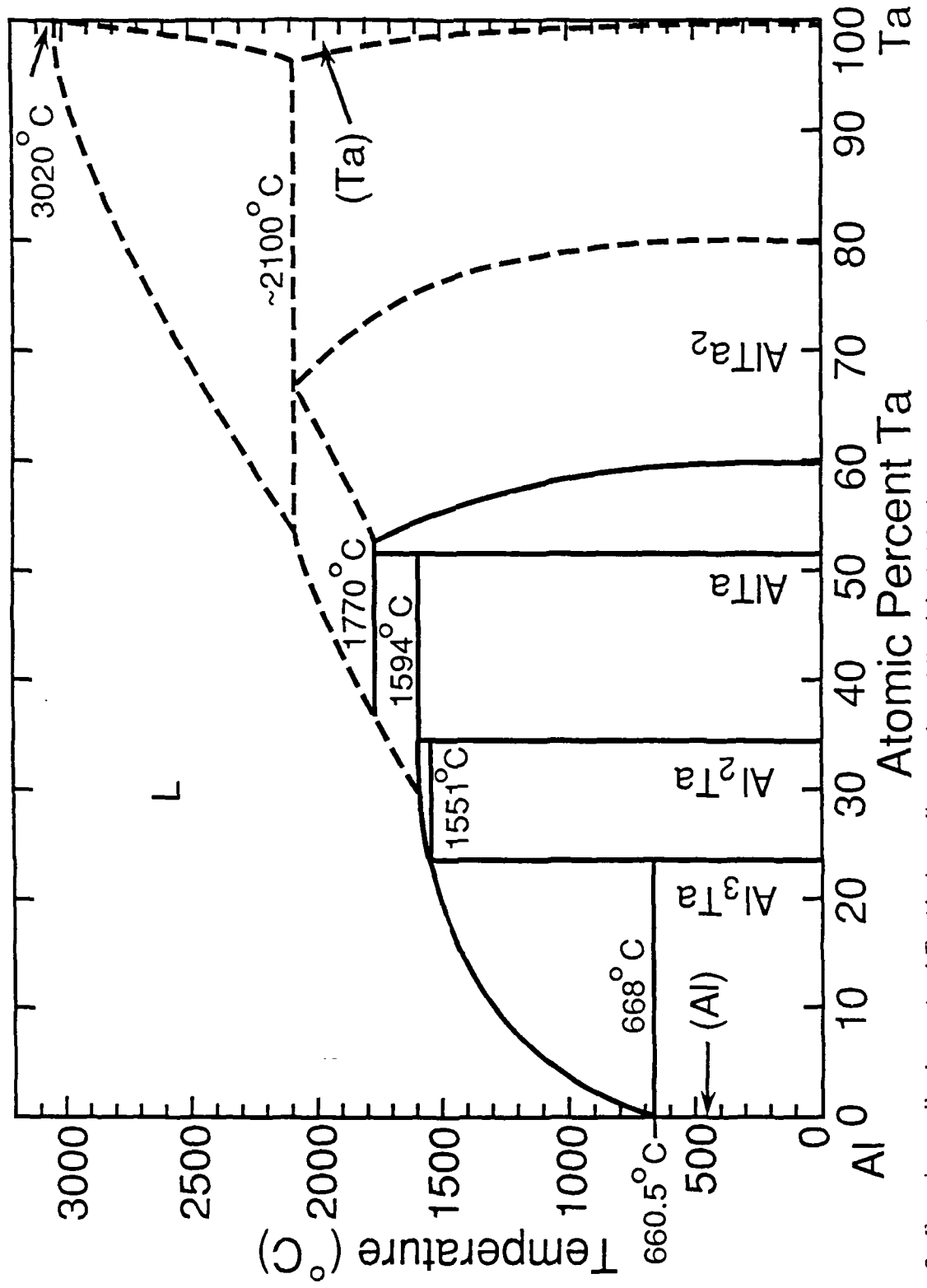


Figure 2. Experimentally determined Ta-Al phase diagram from Miracle[89Mir], showing a series of intermetallic compounds and an array of peritectics.

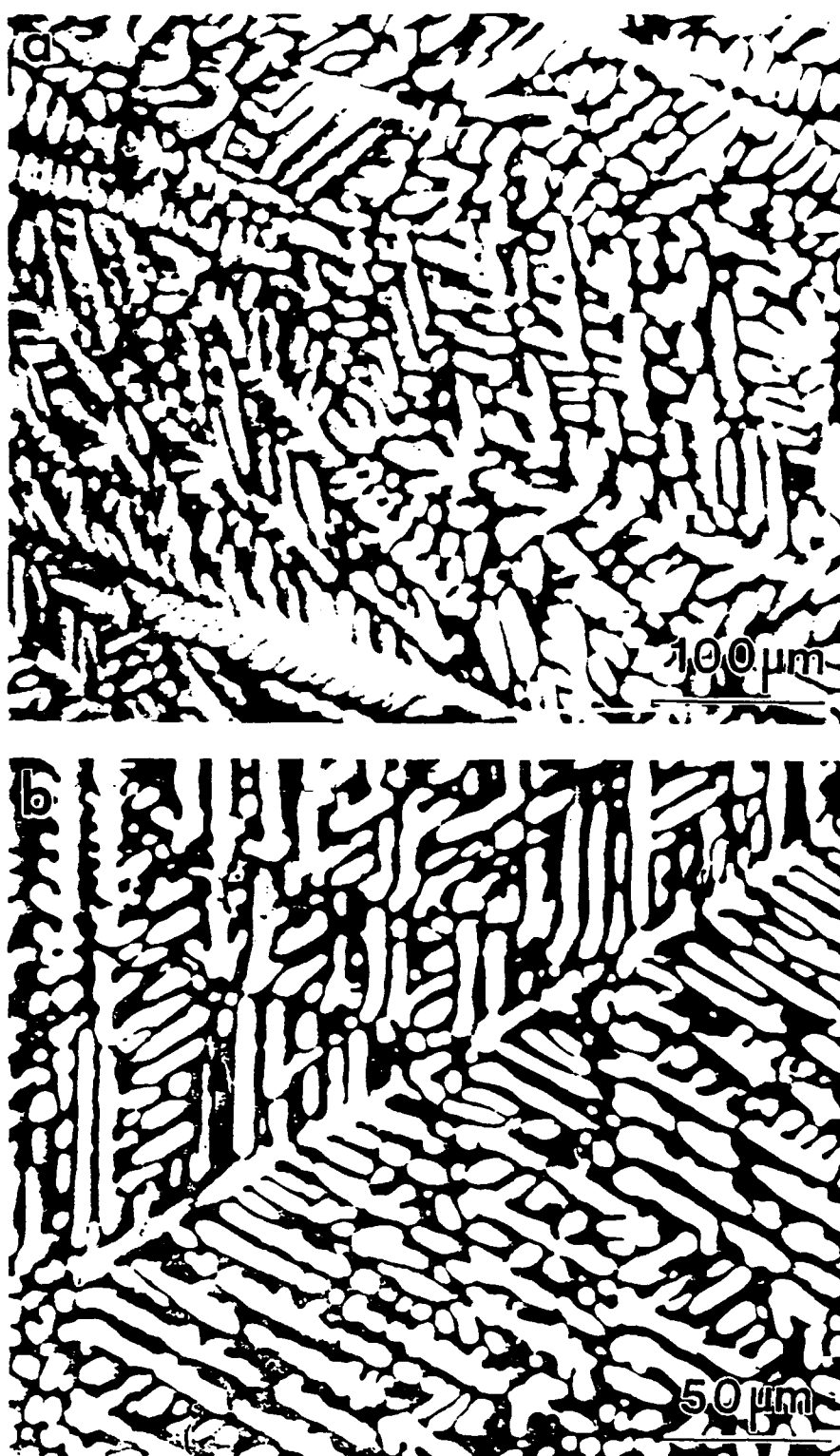


Figure 3. SEM micrographs of dendrites which exhibit hexagonal symmetry
(a) alloy 1 containing primary α phase dendrites, surrounded by a γ phase segregate (b) alloy 8 containing unidentified dendrites.

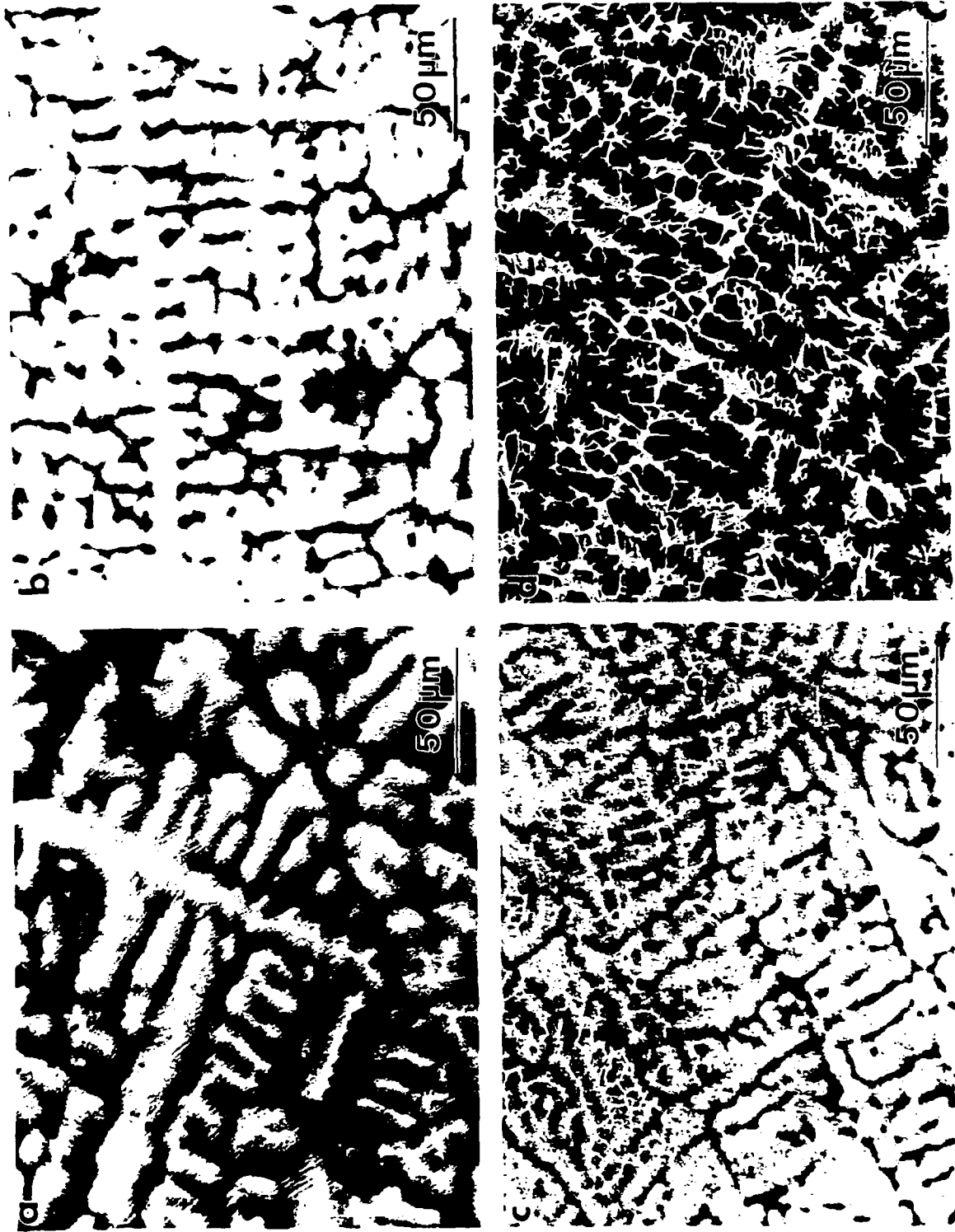


Figure 4. Cubic dendrites of primary β phase in (a) alloy 2, (b) alloy 3, (c) alloy 6 and (d) alloy 4. All dendrites contain a Ta enriched core, which enlarges as the Ta content of the alloys increases. γ is the segregate phase.

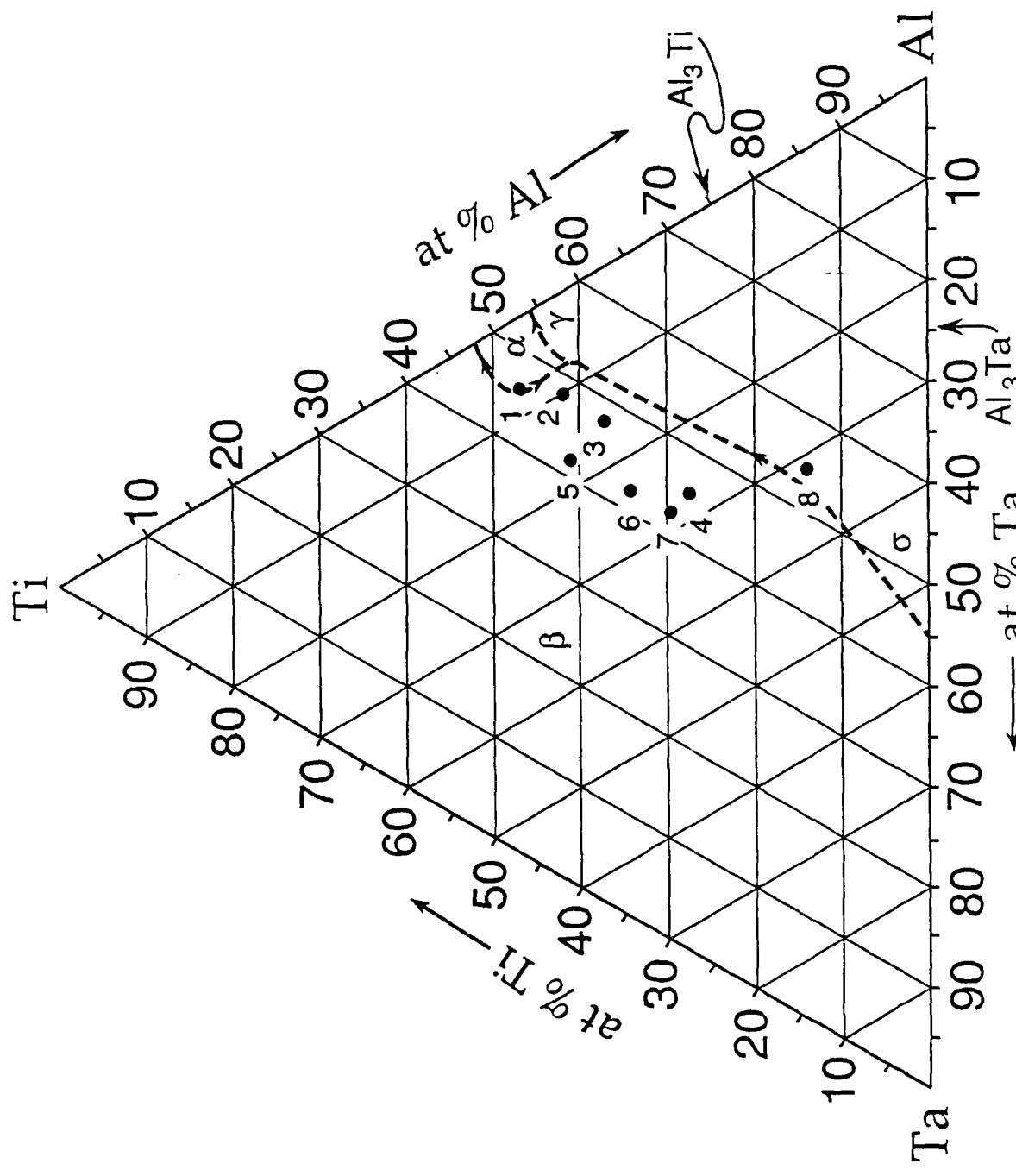


Figure 5. Estimated liquidus surface of the Ta-Ti-Al system, showing the dominance of the β liquidus and the pinching off of the α liquidus. The aluminum rich corner has been left incomplete due to lack of data. Alloys 1-8 are marked by the circles.

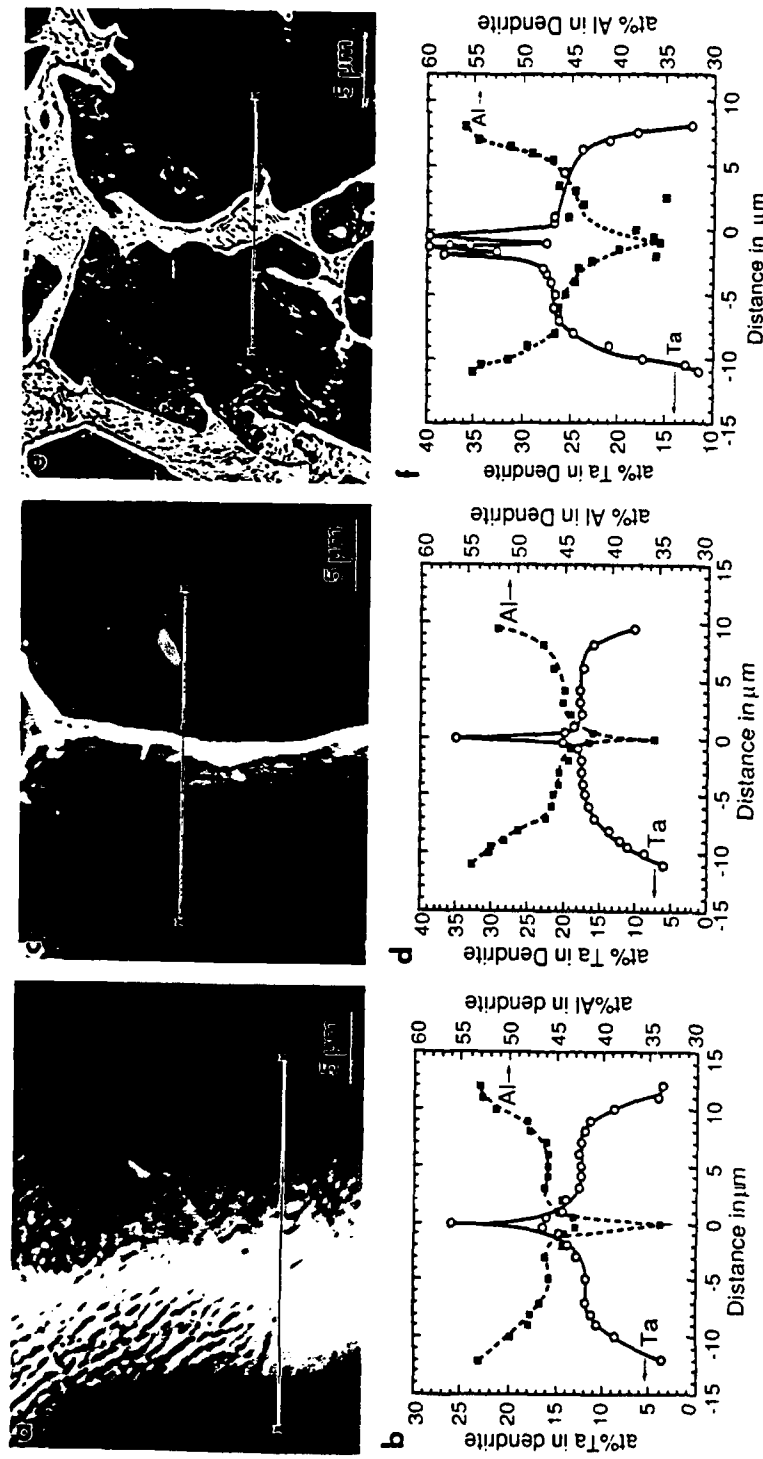


Figure 6. Individual dendrite arms and associated Ta/Al segregation profiles determined from EDS measurements, (a-b) alloy 2, (c-d) alloy 3, (e-f) alloy 4. The cores are enriched in Ta and depleted in Al relative to the dendrite bulk and segregate.



Figure 7. TEM micrographs of the $(\alpha_2 + \gamma_t)$ lath morphology. (a) lath within the dendrites, surrounded by polycrystalline γ segregate, (b) alternating plates of γ and a twin related γ_t variant, with probable fine α_2 between, (c) diffraction pattern showing two twin related $[110]_\gamma$ zones.

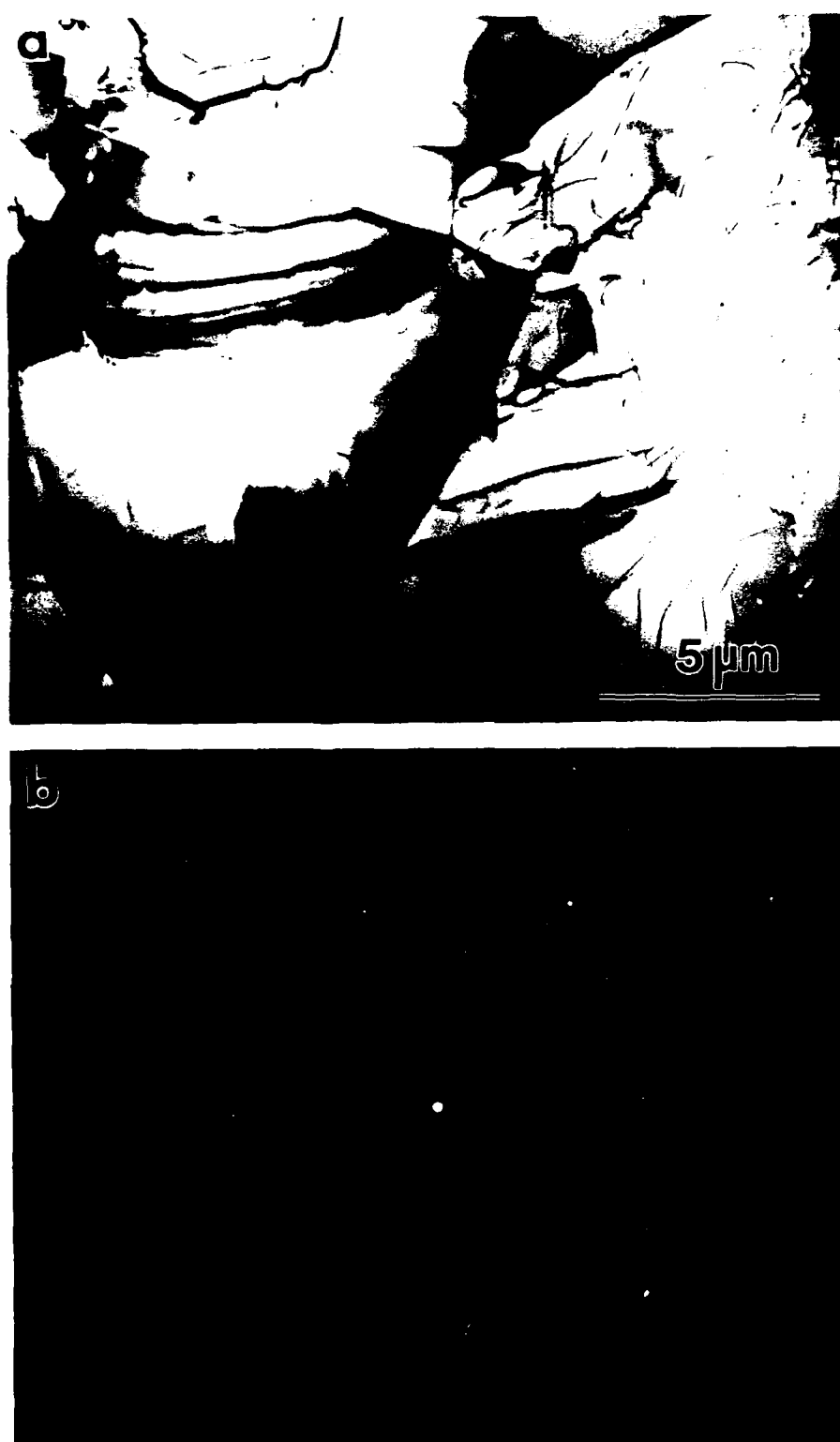


Figure 8. (a) Polycrystalline γ segregate, (b) diffraction pattern showing a $[101]\gamma$ zone.

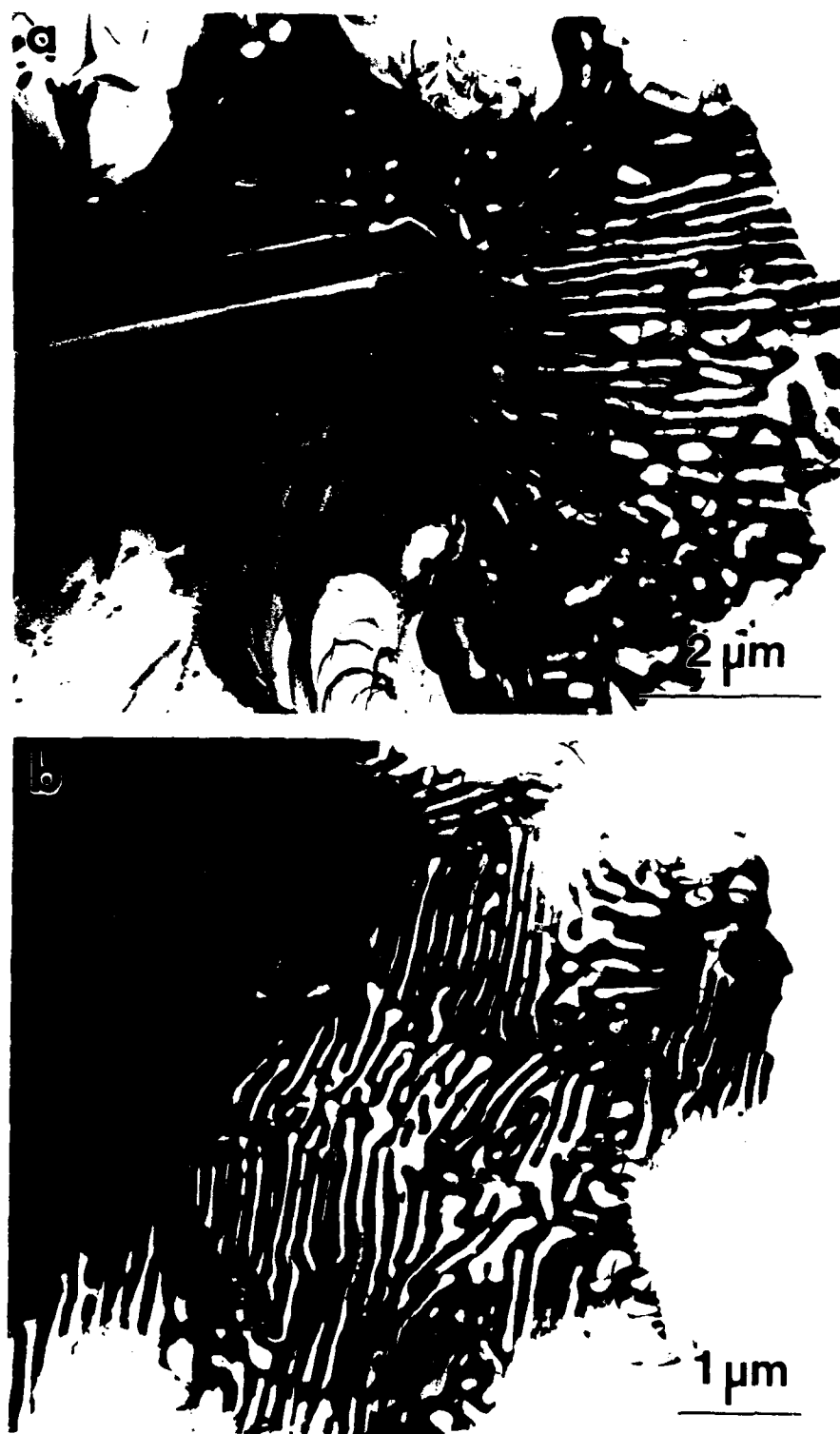


Figure 9. (a) Core morphology in Ta rich samples consisting of $(\gamma + \sigma)$ lamellae with a surrounding envelope of σ , and a matrix of polycrystalline γ from regrowth of the segregate into the dendrite, (b) lamellae oriented edge on.

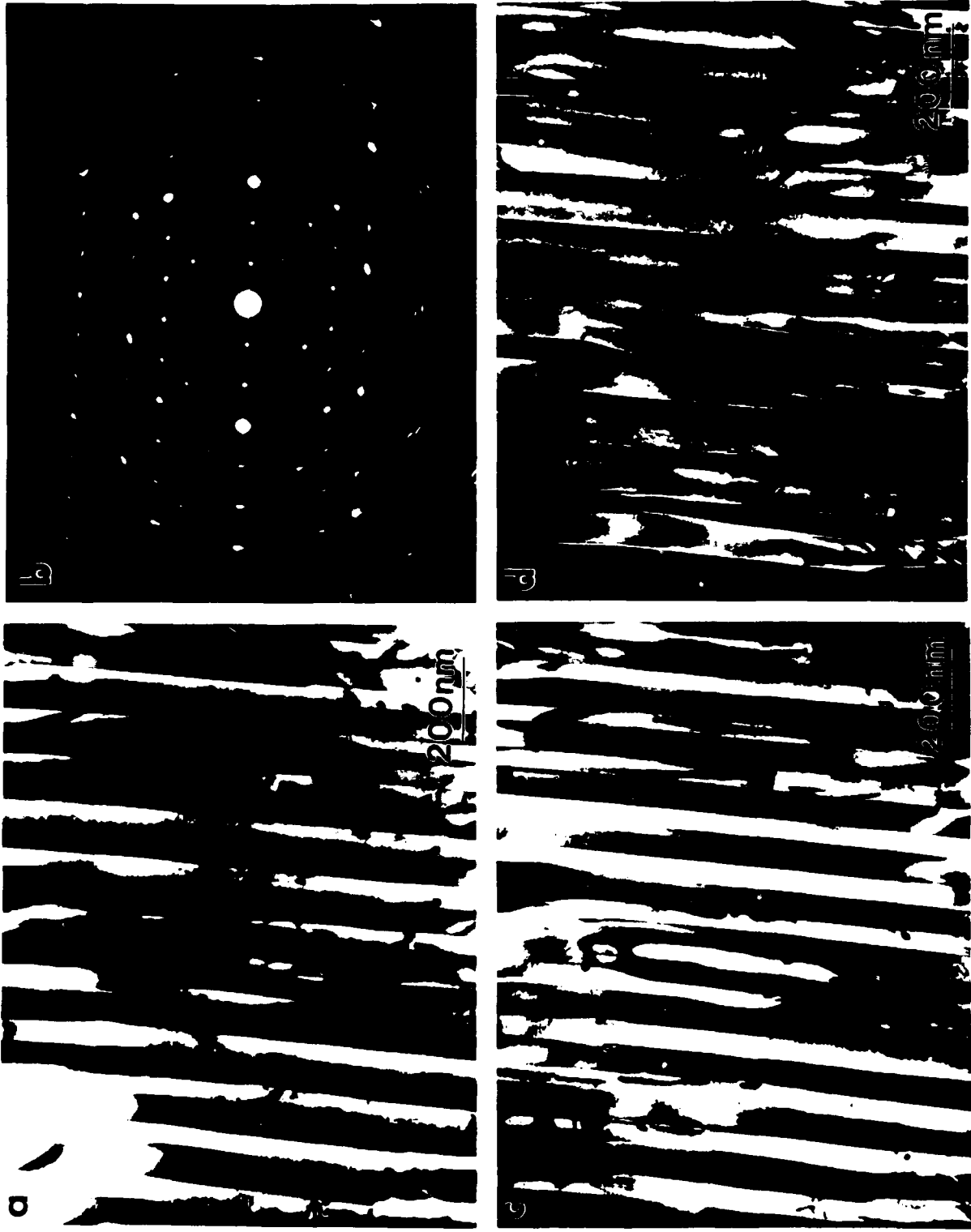


Figure 10. (a) Bright field image of lamellar constituent. Note the interface contrast arising from elastic strain and misfit dislocations, (b) diffraction pattern showing a single $[113]_{\sigma}$ zone and two twin related $[110]_{\gamma}$ zones, (c) dark field of image of γ plates, $\mathbf{g} = (111)_{\gamma} + (\bar{1}\bar{1}1)_{\gamma}$, (d) dark field of image of σ plates, $\mathbf{g} = (141)_{\sigma}$.

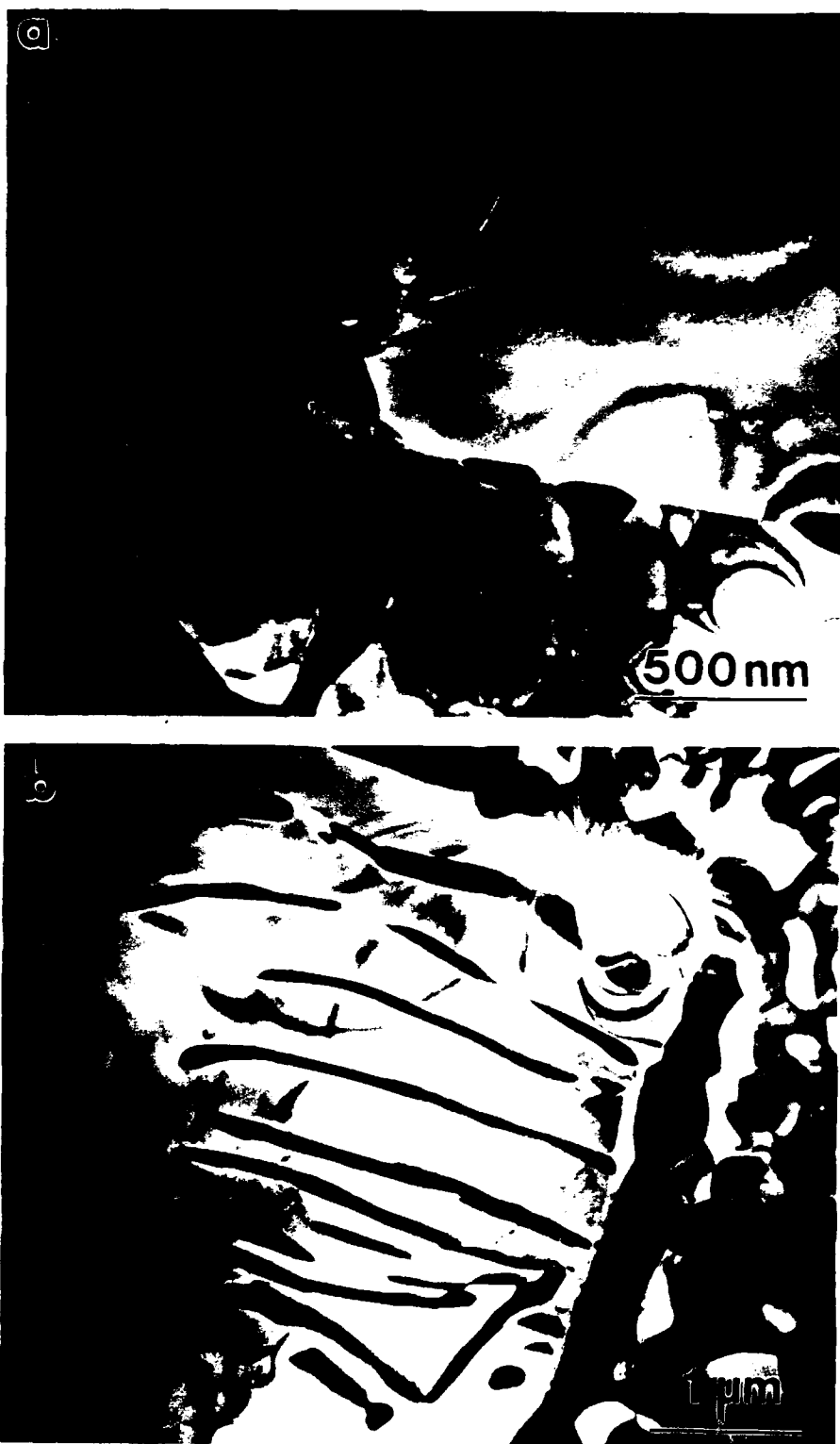


Figure 11. (a) equiaxed σ precipitate morphology, (b) string morphology of σ .

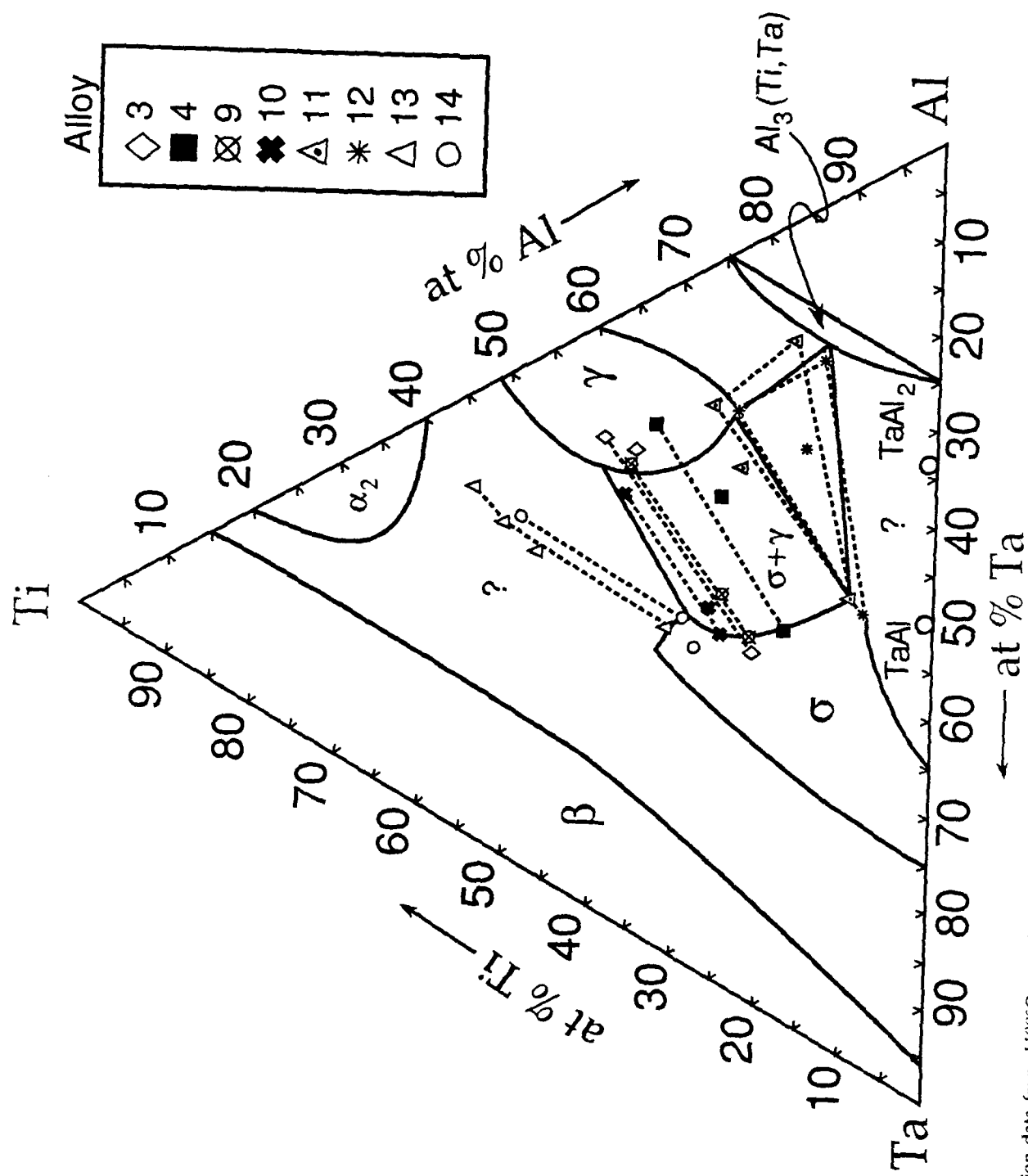


Figure 12. Composition data from 1100°C annealing experiments plotted as tie lines and three phase triangles. This gives the position and approximate boundaries of the phase fields for the alloys studied.

021 A89-1176-616

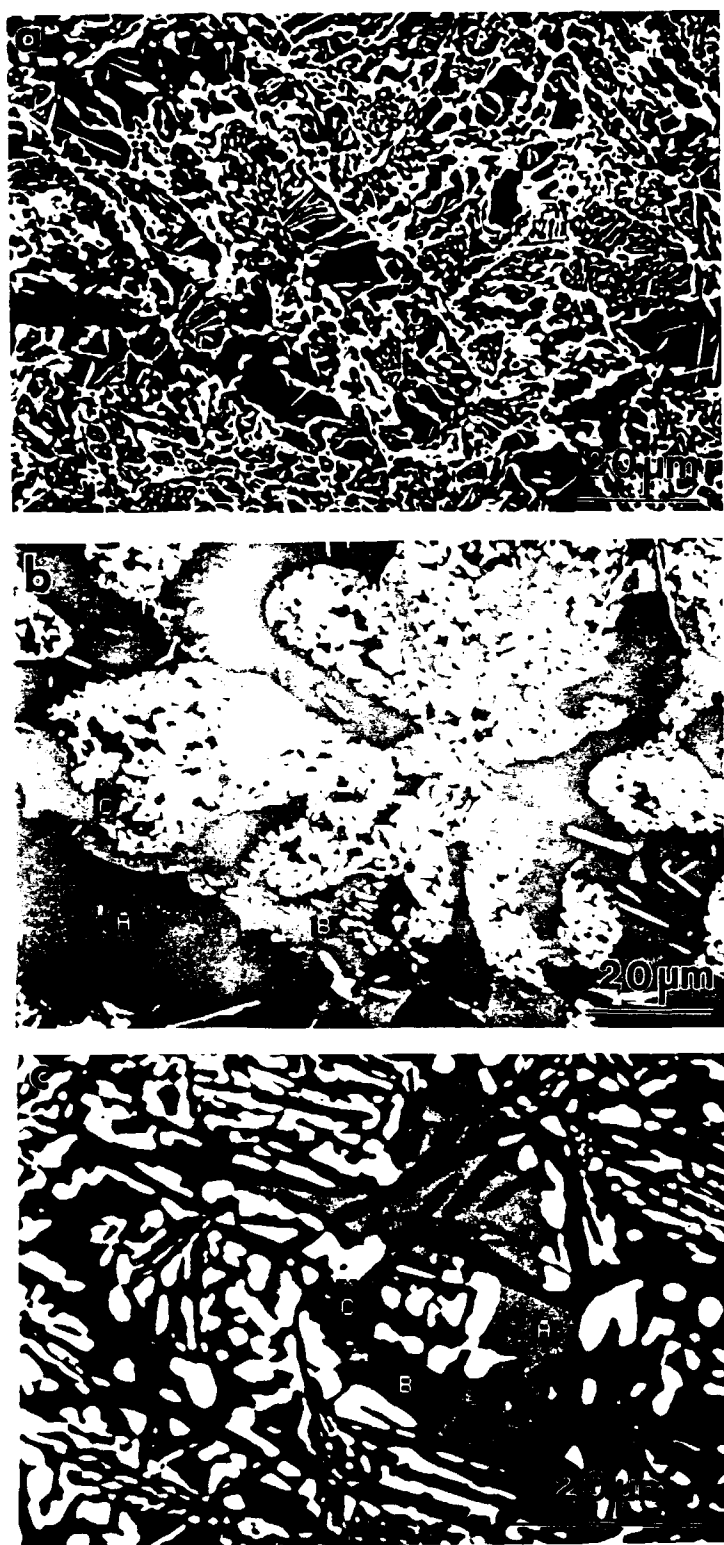


Figure 13. SEM micrographs of samples annealed at 1100°C for 48 hours. (a) alloy 4 containing σ (light regions) in a matrix of γ , (b) alloy 12 containing $\text{Al}_3(\text{Ti},\text{Ta})$ (region A), γ (region B) and either σ or AlTa (region C), (c) alloy 13 containing a possible ternary phase (region A), α_2 (region B) and σ (region C).

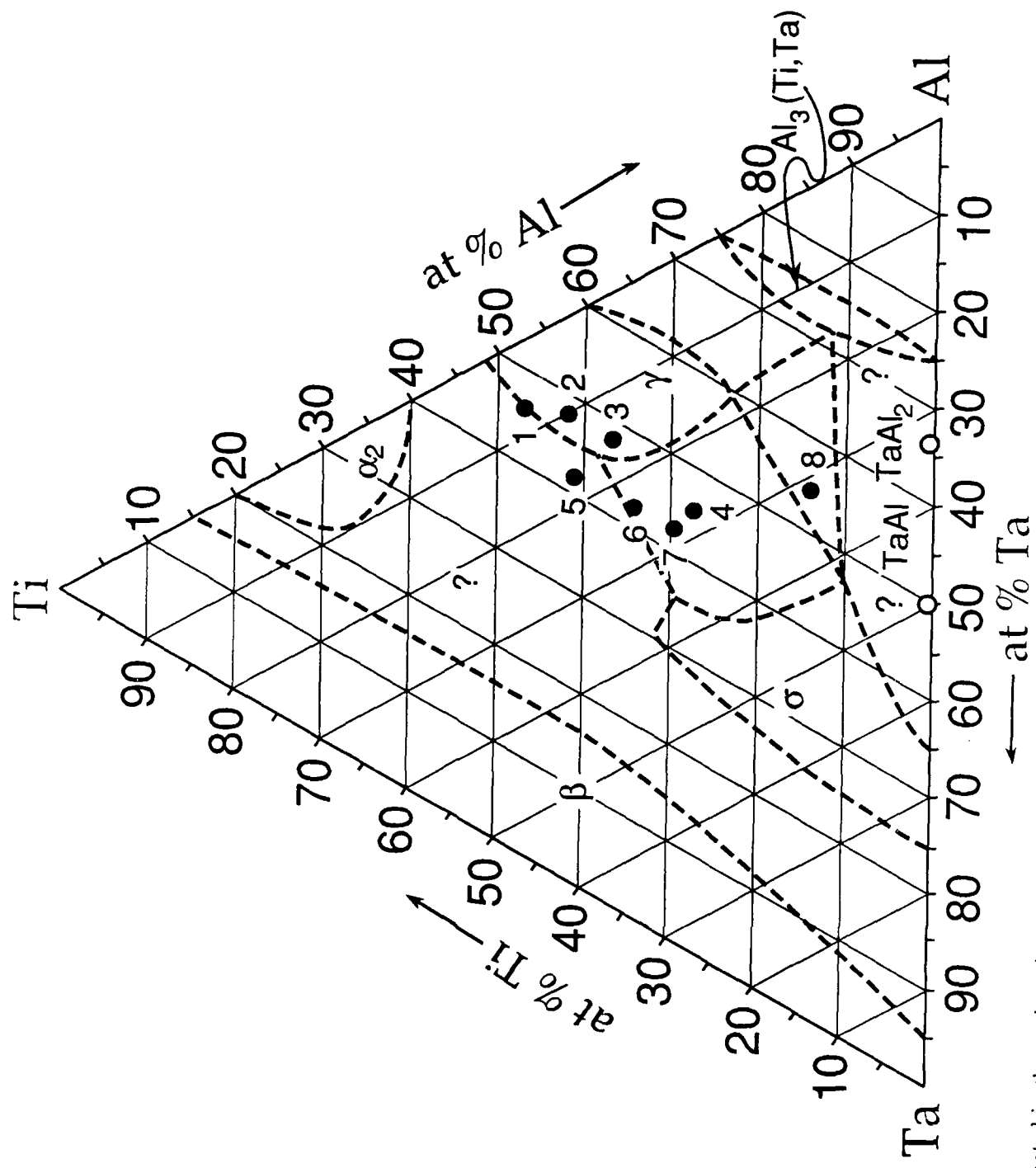


Figure 14. Estimated isothermal section at 1100°C.

Part 2 of Section 4
continues in
Book 6